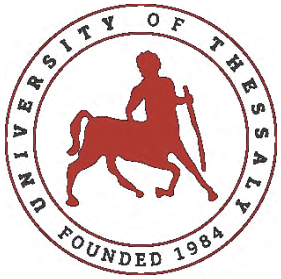

UNIVERSITY OF THESSALY
Faculty of Engineering
Department of Mechanical Engineering

EXPERIMENTAL AND NUMERICAL INVESTIGATION OF GAS JETS IN TURBULENT ENVIRONMENTS

by

NIKOLAOS TSANTOUKLAS
Diploma in Aeronautical Engineering, Hellenic Airforce Academy, 2011
M.Sc. in Mechanical Engineering, University of Thessaly, 2014

Submitted in partial fulfillment of the requirements for the degree of Doctor of Philosophy in Mechanical Engineering at the University of Thessaly

Volos, 2023

The Examination Committee:

Advisor	Dr. Georgios Charalampous, Assistant Professor, Department of Mechanical Engineering, University of Thessaly
Member	Dr. Anastasios Stamatelos, Professor, Department of Mechanical Engineering, University of Thessaly
Member	Dr. Nikolaos Pelekasis Professor, Department of Mechanical Engineering, University of Thessaly
Member	Dr. Nikolaos Andritsos, Professor, Department of Mechanical Engineering, University of Thessaly
Member	Dr. Antonios Tourlidakis, Professor, Department of Mechanical Engineering, University of West Macedonia
Member	Dr. Zinon Vlachostergios, Associate Professor, Department of Production and Management Engineering, Democritus University of Thrace
Member	Dr. Dimitrios Tziourtzioumis, Assistant Professor, Department of Industrial Engineering and Management, International Hellenic University

Acknowledgements

The research described in this thesis was performed under the supervision of Assistant Professor Dr. G. Charalampous. Without his scientific guidance and technical assistance, the completion of this doctoral thesis would not have been possible. More specifically, I am grateful to him for showing trust in me in the first place and undertaking the task of supervising me as a doctoral student in a time when the scope of my academic efforts seemed to have been disoriented. His contribution to reorganizing the project and introducing me to the proper methods of conducting research and writing a scientific manuscript was immense. The utilization of the PIV system was a cornerstone in the continuation of the research since it was the only option after the LDV system was deemed impossible to use due to serious malfunction. Without Dr. Charalampous's experience and time dedication the utilization of the PIV, which until that time remained inert would not have happened. Furthermore, I want to thank him for understanding the difficulties that I had to confront in my efforts to combine the requirements of the research with my duties as a Hellenic Air Force Engineering Officer.

On a second level, the moral and administrative support from Prof. A. Stamatelos were also two elements indispensable to the fulfilment of this thesis, especially during the late stages of completing the research and writing the manuscript. Moreover, it would be inappropriate not to mention the contribution of Prof. E. Stapountzis for introducing me to the field of turbulent flows during my post graduate studies and sparking the idea of the thesis topic.

I also need to express my gratitude to Mr. A. Dafereras and Mr. I. Marinos, technical staff of the Department of Mechanical Engineering. The first one, through his electronics expertise provided the necessary solution for the continuous seeding of the flow by implementing a suitable device and contributed to the assembly of the amplifier-frequency generator-loudspeakers arrangement. The latter helped a lot during the modification of the originally built Box of Turbulence frame.

On a personal level, I must thank my family for their moral support and help in everyday issues emerging from my limited time resulting from trying to combine my academic interests with professional activity.

Abstract

Opposed jet flows is a special category of shear flows with applications ranging from natural phenomena to mechanical systems and chemical industries. Several studies have been published which investigate the fluid dynamics of such applications. These studies consider the surroundings of the opposed jets as a quiescent environment. However, in practical applications the surrounding environment is often characterised by significant mean flow and turbulent fluctuations that interact with the opposed jets and affect their development. To understand the effect of the surrounding environment in the development of the opposed jets, it is essential to separate the effect of the mean flow to that of turbulence. This thesis undertakes the task of investigating the effects of background turbulence on the evolution of an opposed jets flow. As a foundation for the influence of background turbulence on opposed jet development, the effect of background turbulence on the development of simple axisymmetric jets is examined first.

The background turbulence was approximately homogeneous and isotropic turbulence (HIT) with fluctuating velocities greater than the background mean flow in a domain of about 200mm x 200mm. For this purpose, a box of turbulence facility utilizing eight synthetic jets was employed. Velocity measurements for the characterization of the background flow, the single and opposed jets were conducted by means of Particle Image Velocimetry (PIV).

Single jets, were investigated for Reynolds numbers in the range of 10^3 and 10^4 and for an extend of up to 16 jet nozzle diameters. Background turbulence was found to have an additive effect in the turbulence intensity of the jet and also increased the spreading rate and mass flow entrainment. Moreover, the anticipated self-similar behavior changed significantly.

Opposed turbulent jets were investigated for Reynolds numbers in the region of $5 \cdot 10^3$ to 10^4 at two nozzle separation distances of 5 and 7.5 nozzle diameters. The background turbulence had a more significant impact on the lower Reynolds number cases, which was mitigated as the jets Reynolds number approached the upper limit. The velocity decay constants around the stagnation plane decreased in the presence of HIT, while the turbulence intensity was amplified along the centerline. The formation of radial free jets was verified in the case of a quiescent environment. These radial jets exhibited larger spreading rates and absence of self-similarity in the presence of background turbulence.

Περίληψη

Οι ροές αντικρουόμενων δεσμών είναι μια ειδική κατηγορία με εφαρμογές που εκτείνονται από φυσικά φαινόμενα μέχρι μηχανικά συστήματα και χημικές βιομηχανίες. Αρκετές μελέτες έχουν δημοσιευτεί οι οποίες διερευνούν τη δυναμική ρευστών τέτοιων εφαρμογών. Οι μελέτες αυτές θεωρούν το περιβάλλον των αντικρουόμενων δεσμών ως ήρεμο. Εντούτοις, σε πρακτικές εφαρμογές το περιβάλλον χαρακτηρίζεται συχνά από σημαντική μέση ροή και τυρβώδεις διακυμάνσεις που αλληλεπιδρούν με τις αντικρουόμενες δέσμες και επηρεάζουν την ανάπτυξή τους. Για να κατανοηθεί η επίδραση του περιβάλλοντος στην ανάπτυξη των αντικρουόμενων δεσμών, είναι απαραίτητο να διαχωριστεί η επίδραση της μέσης ροής από αυτή της τύρβης. Η παρούσα διατριβή επιφορτίζεται με το έργο να διερευνήσει την επίδραση της τύρβης του περιβάλλοντος στην εξέλιξη μιας ροής αντικρουόμενων δεσμών. Ως βάση για την επίδραση της περιβαλλοντικής τύρβης στην ανάπτυξη αντικρουόμενων δεσμών, εξετάζεται αρχικά η επίδραση περιβαλλοντικής τύρβης στην ανάπτυξη μιας μονής αξονοσυμμετρικής δέσμης.

Η περιβαλλοντική τύρβη ήταν κατά προσέγγιση ομογενής και ισότροπη με διακυμάνσεις της ταχύτητας μεγαλύτερες από τη μέση ροή σε μια περιοχή περίπου 200mm x 200mm. Μια διάταξη κυβικού θαλάμου τύρβης χρησιμοποιώντας οκτώ συνθετικές δέσμες χρησιμοποιήθηκε προς αυτό το σκοπό. Μετρήσεις πραγματοποιήθηκαν με χρήση Particle Image Velocimetry (PIV) για το χαρακτηρισμό της περιβαλλοντικής τύρβης, της μονής αξονοσυμμετρικής δέσμης και των αντικρουόμενων δεσμών.

Οι μονές δέσμες διερευνήθηκαν για αριθμούς Reynolds στο εύρος 10^3 έως 10^4 και για απόσταση μέχρι 16 διαμέτρους ακροφυσίου. Η περιβαλλοντική τύρβη βρέθηκε να έχει ενισχυτική επίδραση στην ένταση της τύρβης της δέσμης και αύξησε επίσης το ρυθμό εξάπλωσης και πρόσληψης μάζας. Επιπρόσθετα, η αναμενόμενη ασυμπτωτική συμπεριφορά μεταβλήθηκε σημαντικά.

Τυρβώδεις αντικρουόμενες δέσμες διερευνήθηκαν για αριθμούς Reynolds στην περιοχή $5{\cdot}10^3$ έως 10^4 για δύο διαφορετικές αποστάσεις 5 και 7.5 διαμέτρων ακροφυσίου. Η περιβαλλοντική τύρβη είχε πιο σημαντική επίδραση στις περιπτώσεις χαμηλότερων αριθμών Reynolds, η οποία υποχωρούσε όσο ο αριθμός Reynolds των δεσμών προσέγγιζε το ανώτερο όριο. Οι σταθερές μείωσης της ταχύτητας γύρω από το επίπεδο ανακοπής μειώθηκαν υπό την παρουσία της ομογενούς και ισότροπης τύρβης, ενώ η ένταση της τύρβης ενισχύθηκε κατά μήκος της αξονικής γραμμής. Η δημιουργία ελεύθερων ακτινικών δεσμών επιβεβαιώθηκε στην περίπτωση ήρεμου περιβάλλοντος. Οι ακτινικές δέσμες αυτές παρουσίασαν μεγαλύτερους ρυθμούς εξάπλωσης και απουσία ασυμπτωτικής συμπεριφοράς υπό την παρουσία περιβαλλοντικής τύρβης.

Table of Contents

List of Figures

List of Tables

Nomenclature

A	Spreading rate of jet	-
B	jet's velocity decay constant	-
B_C	jet's concentration decay constant	-
C_{cl}	mean jet's centerline concentration	-
C_e	mean jet's exit concentration	-
C_m	jet's mass flow entrainment constant	-
d_e	jet exit nozzle diameter	L
f	frequency	T^{-1}
H	slit exit width for a planar jet	L
KE	mean flow kinetic energy	L^2T^{-2}
k_t	turbulent kinetic energy (tke)	L^2T^{-2}
l	integral length scale of a turbulent flow	L
L	inter-nozzle separation of opposed jets	L
L_o	synthetic jet's blowing cycle fluid column	L
L_p	Jet's potential core length	L
L_S	Synthetic jet stroke length ratio	
l_u	streamwise integral length scale of a turbulent flow	L
l_v	cross-stream integral length scale of a turbulent flow	L
m_0	Mass initial flow rate	MT^{-1}
q	jet's flowrate	L^3T^{-1}
q_e	jet's exit flowrate	L^3T^{-1}
$r_{1/2}$	jet half-width	L
r_e	nozzle's jet radius	L
Re	Reynolds number	
$r_{ii}(\Delta t)$	temporal autocorrelation coefficient (in the x_i direction)	-
$R_{ii}(\Delta t)$	temporal autocorrelation function (in the x_i direction)	L^2T^{-2}
$r_{ii}(\Delta x)$	spatial autocorrelation coefficient (in the x_i direction)	-

$R_{ii}(\Delta x)$	spatial autocorrelation function (in the x_i direction)	L^2T^{-2}
s'_{ij}	Fluctuating rate of strain tensor	T^{-1}
S_{ii}	mean rate of strain tensor	T^{-1}
s_{ii}	Rate of strain tensor	T^{-1}
$S_{ii}(k)$	energy spectrum (in the x_i direction)	L^3T^{-2}
T_0	initial temperature of jet	K
T_{cl}	centerline temperature of jet	K
T_{ij}	stress tensor including Reynolds stresses	$ML^{-1}T^{-2}$
u'_i	fluctuating velocity component (in the x_i direction)	LT^{-1}
U_{cl}	Jet centerline velocity	LT^{-1}
U_e	mean jet exit velocity	LT^{-}
u_i	instantaneous velocity component (in the x_i direction)	LT^{-1}
U_i	mean velocity (in the x_i direction)	LT^{-1}
$u_{i,rms}$	root mean square of velocity fluctuation (in the x_i direction)	LT^{-1}
V	mean cross-stream velocity (in the y direction)	LT^{-1}
v'	fluctuating radial velocity (in the y direction)	LT^{-1}
δ	jet average diameter	L
ε	turbulent kinetic energy dissipation rate	L^2T^{-3}
η_{KOL}	Kolmogorov length microscale	L
θ'	fluctuating temperature of jet	K
λ	Taylor length microscale	L
μ	dynamic viscosity	$ML^{-1}T^{-1}$
ν	kinematic viscosity	L^2T^{-1}
ρ_s	surrounding fluid density	ML^{-3}
ρ_o	jet's fluid density	ML^{-3}
Σ_{ij}	mean stress tensor	$ML^{-1}T^{-2}$
σ'_{ij}	fluctuating stress tensor	$ML^{-1}T^{-2}$
σ^2	variance	-
σ_{ij}	stress tensor	$ML^{-1}T^{-2}$

τ_{ij}	Reynolds stress tensor	$ML^{-1}T^{-2}$
τ_{KOL}	Kolmogorov time microscale	T
υ_{KOL}	Kolmogorov velocity microscale	LT^{-1}
ω	cyclic frequency	T^{-1}
Re_{λ}	Reynolds number based on Taylor microscale	-
T	integral time scale	T

Acronyms

ADV	Acoustic Doppler Velocimetry
CCD	Charged-Couple-Device
CFD	Computational Fluid Dynamics
CIJR	Confined Impinging Jets Reactors
CSTOJ	Closely Spaced Turbulent Opposed Jets
DNS	Direct Numerical Simulation
ESP	Eulerian stagnation plane
EWT	Enhanced Wall Treatment
FHW	Flying Hot Wire
GST	Grid Stirred Tank
HIT	Homogeneous Isotropic Turbulence
HWA	Hot Wire Anemometry
LDV	Laser Doppler Velocimetry
LES	Large Eddy Simulation
LSP	Lagrangian Stagnation Plane
NIF	Near to Intermediate Field
OMB	Opposed Multiple Burners
PDA	Particle Dynamics Analyzer
PIV	Particle Image Velocimetry
POD	Proper Orthogonal Decomposition
PSF	Planar Symmetric Forcing
RANS	Reynolds Averaged Navier-Stokes
RASJA	Randomly Actuated Synthetic Jet Array
RIM	Reaction Injection Molding
RJA	Random Jet Array
RSM	Reynolds Stress Model

SF	Symmetric Forcing
SSF	Spherically Symmetric Forcing
SWF	Standard Wall Function
UAV	Unmanned Arial Vehicle
ZEF	Zone of Established Flow
ZFE	Zone of Flow Establishment
ZNMF	Zero-Net-Mass-Flux

1. Introduction

Jets are a fundamental type of flow where a stream of fluid is discharged from a nozzle or an orifice into another fluid environment which may be at rest or in motion. They are ubiquitous in natural flows and industrial applications and are encountered in many different configurations. The archetypal configuration is that of a single axisymmetric jet discharging in a quiescent environment. In practical applications more complex configurations are commonly found, such as the case of opposed jets where two jets meet head on and spread radially, the case of coaxial jets where the environmental flow is parallel to the direction of injection reducing the shear between the jet and the environment or even accelerating the jet, or the case of a jet in cross flow where the environmental flow is normal to the direction of injection and deflects the jet.

Considerable attention has been given to the study of the most fundamental configuration, that of axisymmetric turbulent jets in a quiescent environment, which can serve as a baseline for more complex jet flows. The majority of studies for this case have focused on the velocity field evolution, the spreading and mixing mechanisms of the jets. The region of interest of these studies focused on the developed region of the jet, far from the jet exit, which is called Zone of Established Flow (ZEF) where the jet flow has become self-similar. Moreover, in order to ensure a fully turbulent profile the Reynolds numbers involved were large, $Re>10^4$. Additionally, in most cases, a contoured exit nozzle was used, producing a uniform velocity profile. More recent studies have unveiled deviations from a universal behavior for jet flows resting on the initial conditions which include the nozzle exit shape, the exit Reynolds number and the properties of the surrounding fluid domain. The first two parameters (exit shape and Reynolds number) affect primarily the near to exit field of the jet, namely the Zone of Flow Establishment (ZFE), with the existing information relating to this Zone being sporadic and leading to contradicting conclusions.

The more applied opposed jets configuration is a special arrangement of single axisymmetric jets. The flow behavior is dictated by the characteristics of the ZFE, since their inter-separation distance is commonly smaller than 10 exit diameters. Such configurations are of high importance in today's industry, with applications including Closely Spaced Turbulent Opposed Jets (CSTOJ) burners for gaseous, Opposed Multiple Burners (OMB) for coal gasification, Confined Impinging Jet Reactors (CIJR) in pharmacology and biology and Reaction Injection Molding (RIM) or polymerization processes. The straining of the flow and the turbulence intensity generated in the stagnation plane formed by the impingement of the opposed streams are crucial parameters in terms of reaction or mixing

performance of such devices. These parameters are affected in turn by the exit conditions including the Reynolds number and nozzle shape in conjunction with the separation distance between the jets.

For both single and opposed jets, during injection into an industrial environment the jet development is complicated by additional considerations related to the environment besides the jet's own properties. These include the mean flow and the turbulence in the environment. When the environmental turbulence and mean flow act simultaneously on the jet, it is difficult to account for the effect of each separately due to the compounding of their contributions. Therefore, in order to study their individual contributions, each needs to be examined separately without interference from the other. The contribution of the environmental turbulence on the development of single and opposed jets is of primary interest as it can provide a basis on which the effect of the mean environmental flow can be subsequently compounded. This can be accomplished by injecting single and opposed jets into an environment that is dominated by turbulence where the mean flow is minimum.

The ideal flow for the investigation of jets in turbulence without mean flow is produced by Spherically Symmetric Forcing (SSF) facilities where actuators (synthetic jets, fans or vortex ring generators) are placed symmetrically at the corners of a cubic chamber or of a more complicated polyhedron. The symmetric forcing of the flow at the center of the facility from all directions results to near zero mean flow and produces satisfactory levels of 3D isotropy and homogeneity.

Based on the above, the objective of this investigation was to experimentally investigate the development of single and opposed round jets, by means of Particle Image Velocimetry, in terms of mean and fluctuating velocities, for jet Reynolds numbers $Re<10^4$, in the near nozzle region using a fully developed pipe velocity profile and at two different opposed jets nozzle separations, namely 5.0 and 7.5 nozzle diameters. Two types of environments were considered, a quiescent environment and an environment of homogenous and isotropic turbulence with low mean flow, which allows the investigation of the contribution of environmental turbulence on the jet development isolated from the effects of advection. The investigation was supplemented by numerical simulation of the development of single and opposed jets in quiescent environments as a means of additional information on jet development process.

Fundamental to the investigation was the generation of an environment of a homogenous and isotropic turbulence with near zero mean flow. For this purpose, a facility of 8 synthetic jet actuators was employed. The flow at the center of the facility was characterized to confirm the generation of homogenous and isotropic turbulence with near zero mean flow within a region of interest of 200mm x 200 mm. The turbulence Reynolds number within the region of interest was found to be Re_λ =184.

For the case of single jets in particular, the aim is to evaluate the effect of turbulence on the characteristics of the flow in terms of survivability of the jet coherence, the radial and axial mean and fluctuating velocities, the spreading rate and self-similar behavior and compare them to the known literature. For the particular task jets of Reynolds numbers in the range of 10^3 and 10^4 were considered and for an extend of up to 16 jet nozzle diameters.

For the case of opposed jets, the aim is to investigate the effect of environmental turbulence for fully turbulence opposed jets with Reynolds numbers in the region of $5.5 \cdot 10^3$ to 10^4 and at two nozzle separation distances of 5 and 7.5 nozzle diameters which is sufficiently long to prevent modification of the velocity profile at the nozzle exit. The characteristics of the opposed jets are investigated in terms of the radial and axial mean and fluctuating velocities, the spreading rate, and self-similar behavior of the main jet and of the radial jet.

The remaining of the thesis is structured in five chapters. In the second chapter the scientific background and literature review are presented in detail.

Chapter 3 describes the experimental facility, the measurement techniques employed and the computational tools used for the numerical simulations. The setup of an open Box of Turbulence is presented and the characteristics of the generated Homogeneous and Isotropic Turbulence with nearly zero mean velocity are provided. The configurations of single and opposed jets are described in detail. The principles of the Particle Image Velocimetry technique are explained, and the implementation of the current PIV system is given. The choice of the CFD models used for the simulations is discussed, accompanied by an analysis of the approach followed for building a high-quality mesh and reaching converged solutions.

Chapter 4 presents the results for the case of a single axisymmetric jet in terms of mean and fluctuating velocities both in a quiescent and HIT environment. The variation of these properties along the centerline of the jet is presented, while cross-stream profiles of the flow components are employed to assess the self-similarity of the jets. The influence of HIT on the spreading and entrainment mechanisms is also presented and discussed.

Chapter 5 presents the results for the case of the opposed jets; the results are included in for two different separation distances under both a quiescent and a HIT environment. The mean and rms velocities are presented both along the centerline and the cross-stream direction at the stagnation plane formed. The variation of the axial and radial strain rates with Re and separation distance is discussed. The formation of free radial jets around the stagnation line is presented and their characteristics are examined in terms of self-similarity and spreading rate.

Chapter 6 summarizes the conclusions of this study and provides directions for further investigation related to the topic.

2. Background and Literature Review

2.1 Turbulence

Most flows that we come across in the natural environment and in the technical world are turbulent. Few examples of flows that reside in the first category are the natural convection inside a room, winds, atmospheric and ocean currents, the water currents below the ocean such as the gulf stream, the flow of water into the rivers and natural gas into pipelines, the motion of cumulus clouds, even the air flowing in and out of our lungs. Other turbulent motions that are considered not so ordinary subjects for the average person but concern the natural sciences are the liquid core of the earth and its turbulence that maintains the terrestrial magnetic field. This magnetic field shields the earth from the turbulent solar wind, composed by flakes that result from the vigorous motion on the surface of the sun. At the same time, turbulence pervades a large quantity of engineering fields. In fact, the cases of laminar flow such as the flow of lubricating oil in a bearing are the exceptions. In civil engineering, the turbulent air loads that are exerted onto the buildings or bridges need to be taken into consideration during design. In transportation, turbulence controls the aerodynamic drag on cars, trains, or airplanes. In chemical engineering, the homogenization of mixtures and the acceleration of the chemical reactions are defined by the level of turbulence of gases or fluids. The contribution of turbulence in the above engineering applications may be either beneficial or counterproductive. For example, in combustion devices, the presence of turbulence increases the mixing rates of the reactants but at the same time produces noise and efficiency losses. In the same way, a turbulent boundary layer on an airplane wing increases parasite drag but at the same time adds kinetic energy to the flow preventing the early separation of the flow and the subsequent stall.

Bearing in mind the profound impact of turbulence on so many natural or human activities, it is easy to perceive why turbulent flows have been investigated for more than one and a half century and hold a unique place in the field of classical mechanics. However, even though the equations of motion have been well established for a long time, no unified theory for the solution of problems exists and there is still little we can predict with relative certainty. Furthermore, despite our everyday encounters with turbulence (everyone can observe a thermal plume emanating from an industrial chimney), it has been proven arduous to produce an unambiguous definition. As a result, in lieu of providing such a definition, it is more convenient and productive to identify its characteristics:

- Irregularity: The fluid motion in turbulent flows is characterized by disorderly complex fluid structures. The dependent flow field quantities (velocity, pressure, temperature, etc.) contain

significant fluctuations, even when steady boundary conditions are imposed. These fluctuations present irregular, chaotic, and unpredictable behavior. As a result, it is not possible to study turbulence in a deterministic manner; instead, we rely on statistical methods.

- Nonlinearity-Large Reynolds numbers: The initiation of turbulence is often attributed to instabilities of laminar flows in conjunction with large Reynolds number. The advection acceleration term renders the generic solution of momentum conservation equation as non-linear even in ideal flows and pressure depends on the square of the velocity. Turbulence itself is considered as a further manifestation of this nonlinearity and occurs when the value of the relevant nonlinearity parameter; the Reynolds number is exceeded. Thus, the superposition principle used in ideal flows cannot be employed for turbulent flows. Turbulence causes the time and length scales of the flow's initial and boundary conditions to collapse into fluctuations having continuous spectrum containing a large range of frequencies and wave numbers.
- Three-dimensional vorticity fluctuations: Turbulence is rotational and three dimensional and is characterized by high levels of fluctuating vorticity. The velocity fluctuations are three dimensional and in such flows the production mechanism of vorticity called vortex stretching is present. If the velocity fluctuations were two-dimensional, random vorticity fluctuations that characterize turbulence would be absent since they could not be self-maintained.
- Diffusivity: Within a turbulent flow, the predominancy of fluctuations and vortical overturning motions, known as eddies, augments remarkably the mixing process of chemical species and diffusion of momentum and heat that is orders of magnitude faster in relation with the molecular transport in equivalent laminar flows with the absence of such fluctuations and vortical motions. Diffusivity is responsible for the increased rate of heat transfer in heat exchangers, the fast dispersion of pollutants into the atmosphere and the flow resistance in pipelines.
- Dissipation: Part of the kinetic energy of the flow is continuously transformed (dissipated) into internal energy of the fluid (heat) through the action of viscous shear stresses. Thus, a continuous supply of energy from an imposed velocity or pressure difference is necessary, in order for this energy loss to be compensated and turbulence to be persisted.
- Continuum: Turbulence is governed by the equations of fluid mechanics. The mean free path of the molecules is very much smaller than the average (statistically) motion of the smallest scales (eddies) occurring in a turbulent flow. Molecular transport effects may be represented by transport coefficients like viscosity and heat conductivity. The turbulence flow cannot be

characterized by such local coefficients since they are meant to be for a fluid and not for a flow. Turbulence characteristics depend on its environment. However, turbulence dynamics are the same in all fluids.

As a synopsis, a particular flow to be considered turbulent creates the necessity to exhibit at the same time the features of non-linearity, vorticity, dissipation and vorticity. This is why certain flows such as failing rain, internal waves in the ocean or the atmosphere and wind driven ocean-surface waves are excluded from this category, since they do not fulfil the three above requirements. Although imperfect, a simple definition of turbulence as a dissipative flow state characterized by nonlinear fluctuating three-dimensional vorticity seems appropriate.

The absence of sufficiently powerful nonlinear concepts and mathematical tools make turbulence research both laborious and challenging, being one of the most prominent issues in science that remain unsolved until today. Nevertheless, due to its immense importance in physics and engineering, turbulence remains a first-rate subject in modern fluid dynamics research. The scientific background of the current studies in the field relies on a framework established by the advances and achievements of several of the most prominent physicists of the last one and half century.

The first systematic work is found in the experiments of Osborne Reynolds in 1883, who demonstrated that when the dimensionless ratio $Re=UD/\nu$ surpasses a critical value in an initially laminar pipe flow, a transition to turbulence or irregularity occurs. This ratio was later named Reynolds number in his honor. The concept of turbulent stresses coming from the separation of flow-field variables into mean and fluctuating components is attributed to him.

Prandtl is credited with semi-empirical theories of turbulence, with the mixing length theory being the most successful among them (1920s). By estimating an appropriate form for the mixing length, Prandtl reached out to the conclusion that the average turbulent velocity profile near a solid wall is logarithmic. This is considered one of the most credible products of the turbulent flows research.

In 1922, the British meteorologist Lewis Richardson was the first to propose the concept of viscous dissipation, stating that the kinetic energy of the fluctuations is continually transferred from larger to smaller eddies, until it is converted into heat under the action of viscosity. This first qualitative description of the energy cascade remains until today one of the foundations for decoding the nature of turbulence.

In 1935-1936, Taylor laid the basis of the statistical description of turbulence and introduced the concepts of homogeneous and isotropic turbulence and of a turbulence spectrum. Although real

turbulent flows do not exhibit isotropy, the mathematical techniques employed have proven their usefulness for analyzing the small structures of turbulence, which are considered nearly isotropic.

The Russian mathematician Kolmogorov gave quantitative shape to the idea of a spectral energy cascade proposed by Richardson. He claimed that the statistics of the small scales are isotropic and depend on only two parameters, namely ν, the kinematic viscosity, and ε, the average rate of kinetic energy dissipation per unit mass of fluid and derived the size of the smallest scales $\eta_{KOL}=(\nu^3/\varepsilon)^{1/4}$. His second contribution was the hypothesis of an intermediate range which includes eddy sizes much smaller than large scale motions represented by a scale *l* and much larger than η_{KOL}. In this region which is called "inertial sub-range" kinematic viscosity ν has no influence on the turbulence evolution and the statistics depend only on the single parameter ε (kinetic energy dissipation rate). Based on this hypothesis, in 1941 Kolmogorov and Obukhov independently derived that the spectrum in the inertial sub-range must be proportional to $\varepsilon^{2/3}k^{-5/3}$, where k is the wave number describing the eddies motions.

Some of the above concepts will be analyzed in more detail in the course of this chapter, based on the needs and purposes of the thesis.

2.1.1 Reynolds decomposition and average equations of motion

A turbulent flow in each instant satisfies the Navier-Stokes equations. The equations of motion in tensor notation for an incompressible fluid are:

$$\frac{\partial u_i}{\partial t}+u_j\frac{\partial u_i}{\partial x_j}=\frac{1}{\rho}\frac{\partial}{\partial x_j}\sigma_{ij} \tag{1.1}$$

$$\frac{\partial u_i}{\partial x_i}=0 \tag{1.2}$$

If the fluid is Newtonian, the stress tensor σ_{ij} is given by:

$$\sigma_{ij}=-p\delta_{ij}+2\mu s_{ij} \tag{1.3}$$

The rate of strain s_{ij} is defined by:

$$s_{ij}=\frac{1}{2}\left(\frac{\partial u_i}{\partial x_j}+\frac{\partial u_j}{\partial x_i}\right) \tag{1.4}$$

If the differential equations of motion 1.1 is simplified by the continuity equation 1.2 and the rate of strain definition 1.4, the Navier-Stokes equations are obtained:

$$\frac{\partial u_i}{\partial t} + u_j \frac{\partial u_i}{\partial x_j} = -\frac{1}{\rho}\frac{\partial p}{\partial x_i} + \nu \frac{\partial^2 u_i}{\partial x_j^2} \quad 1.5$$

However, at high Reynolds numbers, it is virtually impossible to obtain an exact prediction of the flow, because there is an enormous range of length scales to be resolved at each time instant. Frequently, in engineering and natural sciences, the export of all these flow details is considered redundant and the average behavior of the flow emerges as the economic important issue. Consequently, statistical methods provide fruitful results in the efforts to predict turbulent flow parameters. Following **Reynolds decomposition**, equations, governing mean quantities such as the mean velocity are developed. Each velocity quantity u_i is decomposed into a mean component U_i and a fluctuation $u_i^{'}$, which represents the deviation from the mean, such that:

$$u_i = U_i + u_i^{'} \quad 1.6$$

We interpret U_i as time average, defined by:

$$U_i = \lim_{T\to\infty} \frac{1}{T} \int_{t_0}^{t_0+T} u_i dt \quad 1.7$$

Using an overbar notation, time averages (mean values) of fluctuations and of their derivatives, products, and other combinations are symbolized. By definition, the mean value of a fluctuating quantity is zero:

$$\overline{u_i^{'}} = \lim_{T\to\infty} \frac{1}{T} \int_{t_0}^{t_0+T} (u_i - U_i) dt \equiv 0 \quad 1.8$$

The use of time averages is suitable when measurements are taken at fixed locations in a statistically steady, but frequently inhomogeneous, flow field, such as in laboratory facility. In an inhomogeneous flow, a flow-field variable and its corresponding time average is a function of position and for such purposes, the use of spatial averages is considered inappropriate. For a time average to make sense, the integrals in equations 1.7, 1.8 have to be independent of t_0. This condition implies that the mean flow remains steady:

$$\frac{\partial U_i}{\partial t} = 0 \quad 1.9$$

The mean value of a spatial derivative of a variable is equal to the corresponding spatial derivative of the mean value of that variable, for example:

$$\overline{\frac{\partial u_i}{\partial x_j}} = \frac{\partial U_i}{\partial x_j} \tag{1.10}$$

$$\overline{\frac{\partial u_i^{'}}{\partial x_j}} = \frac{\partial \overline{u_i^{'}}}{\partial x_j} = 0 \tag{1.11}$$

Averages of products are computed by the following relation:

$$u_i u_j = U_i U_j + \overline{u_i^{'} u_j^{'}} \tag{1.12}$$

Correspondingly, after Reynolds decomposition we have the following relations for pressure, stress and strain tensor:

$$p = P + p^{'}, \overline{p^{'}} \equiv 0 \tag{1.13}$$

$$\sigma_{ij} = \Sigma_{ij} + \sigma_{ij}^{'}, \sigma_{ij} \equiv 0 \tag{1.14}$$

$$S_{ij} = \frac{1}{2}\left(\frac{\partial U_i}{\partial x_j} + \frac{\partial U_j}{\partial x_i} \right), s_{ij}^{'} = \frac{1}{2}\left(\frac{\partial u_i^{'}}{\partial x_j} + \frac{\partial u_j^{'}}{\partial x_i} \right) \tag{1.15}$$

$$\Sigma_{ij} = -P\delta_{ij} + 2\mu S_{ij} \tag{1.16}$$

$$\sigma_{ij}^{'} = -p^{'}\delta_{ij} + 2\mu s_{ij}^{'} \tag{1.17}$$

If we apply the decomposition rule and take the average of the equations of motion and continuity in the case of an incompressible and stationary in time turbulent flow, we reach the equation for the mean flow or the so-called “Reynolds momentum equation”:

$$U_j \frac{\partial U_i}{\partial x_j} = \frac{1}{\rho} \frac{\partial}{\partial x_j} \left(\Sigma_{ij} - \overline{\rho u_i^{'} u_j^{'}} \right) \tag{1.18}$$

The mean stress tensor T_{ij} in a turbulent flow can be written:

$$T_{ij} = \Sigma_{ij} - \overline{\rho u_i^{'} u_j^{'}} = -P\delta_{ij} + 2\mu S_{ij} - \overline{\rho u_i^{'} u_j^{'}} \tag{1.19}$$

The contribution of the turbulent motion to the mean stress tensor is designated by the symbol τ_{ij} and is called Reynolds stress tensor in honor of its original developer:

$$\tau_{ij} \equiv -\overline{\rho u_i^{'} u_j^{'}} \tag{1.20}$$

The Reynolds stress tensor is symmetric:$\tau_{ij} = \tau_{ji}$. The diagonal components $\rho\overline{u_i'^2}$ are normal stresses. In many flows, these stresses contribute little to the mean momentum transport. The off-diagonal components τ_{ij}, which are called shear stresses occupy the predominant role in the theory of mean momentum transfer in a turbulent environment.

The isolation of the effects that the fluctuations impose on the mean flow stands out as the major benefit of the Reynolds decomposition. However, the equations of mean flow contain six new unknowns which are carried by the Reynolds stress tensor τ_{ij} and are highlighted as the closure problem of turbulence.

2.1.2 Turbulent Energy Cascade

The equation governing the dynamics of the mean-flow energy $\frac{1}{2}U_i^2$ is obtained by multiplying equation 1.18 by U_i. The energy-balance or energy-budget equation becomes:

$$\rho U_j \frac{\partial}{\partial x_j}\left(\frac{1}{2}U_i^2\right) = \frac{\partial}{\partial x_j}\left(T_{ij}U_i\right) - T_{ij}S_{ij} \qquad 1.21$$

The product $T_{ij}S_{ij}$ is called deformation work and for an incompressible flow is calculated as:

$$T_{ij}S_{ij} = 2\mu S_{ij}S_{ij} - \rho\overline{u_i'u_j'}S_{ij} \qquad 1.22$$

The first component represents the direct viscous dissipation of mean kinetic energy via its conversion into heat. The second component usually represents a mean-flow kinetic energy loss to the fluctuating velocity field.

The product $T_{ij}U_i$represents transport of mean kinetic energy by pressure, viscous stresses, and Reynolds stresses, since it is calculated as:

$$T_{ij}U_i = \left(-PU_j + 2\mu U_i S_{ij} - \rho\overline{u_i'u_j'}S_{ij}\right) \qquad 1.23$$

If the product $T_{ij}U_i$is taken to be zero on a control surface, these terms can only redistribute energy inside the control volume surrounded by the surface.

The total energy budget of the mean flow presented by equation 1.21 can be rewritten now including all the transport and production-dissipation terms analytically:

$$U_j \frac{\partial KE}{\partial x_j} = \frac{\partial}{\partial x_j}\left(-\frac{1}{\rho}PU_j + 2\nu U_i S_{ij} - \overline{u_i'u_j'}S_{ij}\right) - 2\nu S_{ij}S_{ij} + \overline{u_i'u_j'}S_{ij} \qquad 1.24$$

Similarly, the final turbulent kinetic energy $k_t = \frac{1}{2}\overline{u_i^2}$ budget equation is obtained:

$$U_j \frac{\partial k_t}{\partial x_j} = \frac{\partial}{\partial x_j}\left(-\frac{1}{\rho}\overline{p' u_j'} + 2\nu \overline{u_i' s_{ij}'} - \frac{1}{2}\overline{u_i'^2 u_j'} \right) - 2\nu \overline{s_{ij}' s_{ij}'} - \overline{u_i' u_j'} S_{ij} \quad 1.25$$

The first three terms of the right hand of equation 1.25 have the same effect as in the budget of the kinetic energy of the mean-flow 1.24. The fourth term is thought of as the viscous dissipation of turbulent kinetic energy, and it is not proper to be neglected in the turbulent kinetic energy budget. Instead, the analogous term in the mean-flow kinetic energy budget is assumed negligible. The fifth term referred as the shear-production term, represents the rate at which the turbulent fluctuations extract kinetic energy by the mean flow. This energy exchange concept justifies the appearance of this term in the mean-flow kinetic energy budget with the opposite sign.

In steady, homogeneous, pure shear flow (in which all mean field variables except U_i are spatially invariant and as a matter of fact S_{ij} is constant, the energy budget equation reduces to:

$$-\overline{u_i' u_j'} S_{ij} = 2\nu \overline{s_{ij}' s_{ij}'} \quad 1.26$$

This means that the rate of production of turbulent energy by Reynolds stresses equals the viscous dissipation rate. In order this conclusion to be valid for large Reynolds numbers, after some dimensional analysis, we obtain that:

$$\overline{s_{ij}' s_{ij}'} \gg S_{ij} S_{ij} \quad 1.27$$

This implies that S_{ij} and s_{ij}' do not interact strongly. Therefore, the small-scale structures of turbulence appear to be uninfluenced by the direction characteristics of the mean shear flow. As result, a state of local isotropy corresponds to the small-scale motions. It is proven that the dissipation rate in isotropic turbulence is given by the following relation:

$$\varepsilon = 15\nu \overline{\left(\frac{\partial u_1'}{\partial x_1} \right)^2} \quad 1.28$$

The deduction of small interaction between the large eddies that are associated with the mean flow characteristics and the small eddies involved in the estimation of fluctuating strain rate, creates a need for an appropriate length scale describing the latter. This length scale was provided by G.I. Taylor and is called Taylor microscale λ. Using a scale approximation, the equation for the dissipation rate can be transformed:

$$\varepsilon = 15\nu \frac{\overline{u_1'^2}}{\lambda^2} \quad 1.29$$

The Reynolds number based on the Taylor microscale is valuable parameter for the characterization of turbulent flows:

$$\mathrm{Re}_{\lambda} \equiv \frac{u'\lambda}{\nu} \tag{1.30}$$

According to Dimotakis [8], a fully developed turbulent flow requires $Re_{\lambda} \geq 10^2$ to be sustained.

However, the group of eddy sizes where strong viscous dissipation occurs is not represented by the Taylor microscale. Instead, in 1941, Kolmogorov introduced a more appropriate group of microscales. His theory suggested the local homogeneity and isotropy of the smallest dissipating eddies, and that their size depends on two relevant parameters. The first parameter is ε, the rate at which kinetic energy is supplied to the smallest eddies, and the second one ν, the kinematic viscosity that annihilates the velocity gradients of the smallest motions. With these two parameters, length, time, and velocity scales are formed as follows:

$$\eta_{KOL} \equiv (\nu^3 / \varepsilon)^{1/4} \tag{1.31}$$

$$\tau_{KOL} \equiv (\nu / \varepsilon)^{1/2} \tag{1.32}$$

$$\upsilon_{KOL} \equiv (\nu\varepsilon)^{1/4} \tag{1.33}$$

the Reynolds number determined from them is:

$$\frac{\upsilon_{KOL} \cdot \eta_{KOL}}{\nu} = \frac{\upsilon_{KOL} \equiv (\nu\varepsilon)^{1/4} \cdot \eta_{KOL} \equiv (\nu^3 / \varepsilon)^{1/4}}{\nu} = 1, \tag{1.34}$$

which appropriately suggests a balance of inertial and viscous effects for Kolmogorov-scale eddies. From a phenomenology perspective, we can expect that the size of the small eddies not directly influenced by the large-scale turbulent structures but being nearly isotorpic, range from the Taylor microscale λ down to the Kolmogorov microscale η_{KOL}.

The energy exchange between the mean flow and the turbulence is governed by the dynamics of the large eddies. These large eddies, described by size of the integral length scale l, contribute most to the turbulent production, and dictate the transfer rate of energy and thus the dissipation rate ε to scales comparable to the Kolmogorov microscale. At this point the turbulent kinetic energy is dissipated into heat due to viscous effects.

Some useful approximations concerning the integral, Taylor and Kolmogorov length scales are:

$$\lambda \sim \mathrm{Re}^{-1/2} \cdot l \tag{1.35}$$

$$\eta_{KOL} \sim \mathrm{Re}^{-3/4} \cdot l \qquad 1.36$$

Figure 2-1 provides with evidence that an increase in Re causes a decrease in the size of the small eddies described by Taylor and Kolmogorov. This can be initiated either by increasing the input velocity or decreasing v that induce larger shear rates.

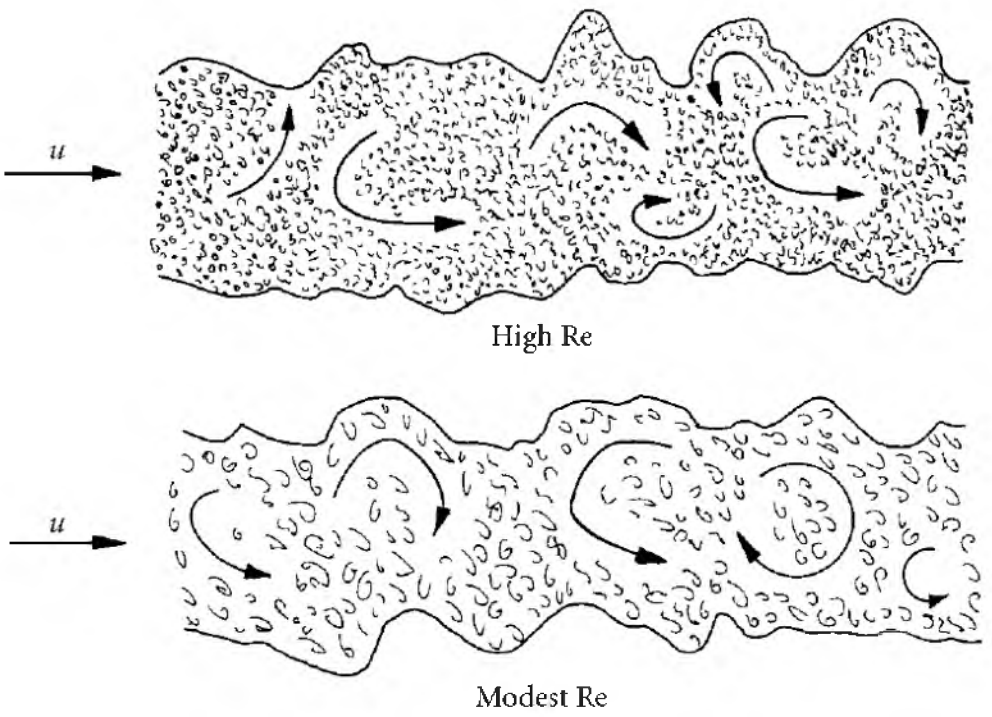

Figure 2-1 The influence of Re on the smallest scales in a turbulent wake. Davidson [9]

2.1.3 Statistical properties and spectral dynamics

The properties and spectral dynamics which will be presented in this subsection are based on one-dimensional analysis. Thich means that we examine the temporal and spatial variation of a parameter and more precisely the velocity fluctuation component u_i' only in the dimension i. This is done for reasons of simplicity and easier clarification of the phenomena but also because it is sufficient for the description of a homogeneous turbulent flow.

The mean square deviation σ^2 from the mean value is called variance. For a velocity component, the variance is calculated as:

$$\sigma^2 \equiv \overline{u_i'^2} = \lim_{T\to\infty} \frac{1}{T} \int_{t_0}^{t_0+T} (u_i - U_i)^2 \, dt = \lim_{T\to\infty} \frac{1}{T} \int_{t_0}^{t_0+T} u_i'^2 \, dt \qquad 1.37$$

The square root of variance is the familiar standard deviation (second moment) or the root mean square amplitude (rms) and is obtained by:

$$\sigma = \left(\overline{u_i^{'2}}\right)^{1/2} = u_{i,rms} \tag{1.38}$$

These quantities are of fundamental importance for the turbulent flows, since they represent an average estimation for the magnitude of the velocity fluctuations and thus the turbulent intensity. If we aim at deeper understanding of the temporal behavior of a fluctuating velocity, it is necessary to know how the values of fluctuations at different times are related. The answer is given by calculating the autocorrelation function of $u_i^{'}$ between two different times $t, t + \Delta t$:

$$R_{ii}(\Delta t) = \overline{u_i^{'}(t) u_i^{'}(t + \Delta t)} \tag{1.39}$$

It is also convenient to define the autocorrelation coefficient $r_{ii}(\Delta t)$:

$$r_{ii}(\Delta t) = \frac{R_{ii}(\Delta t)}{\overline{u_i^{'2}}}, \left|r_{ii}(\Delta t)\right| \le 1 \tag{1.40}$$

The integral time scale is characteristic of the large-scale motions in turbulence and represents the turnover time of a large eddy. It is calculated through the temporal autocorrelation coefficient:

$$T = \int_0^{\infty} r_{ii}(\Delta t) d\Delta t \tag{1.41}$$

As a generic approach it could be claimed that the integral time scale is a measure by which the memory of the turbulence is represented. It defines the time interval beyond which the self-correlation of a turbulent fluctuation is obliterated.

In order $R_{ii}(\Delta t)$ to be obtained, a temporally stationary variable needs to be sampled at different time spots without any variation in the position of the measurement. An analogous spatial autocorrelation coefficient is produced by sampling a variable at different positions at the same time:

$$R_{ii}(\Delta x) = \overline{u_i^{'}(x) u_i^{'}(x + \Delta x)} \tag{1.42}$$

$$r_{ii}(\Delta x) = \frac{R_{ii}(\Delta t)}{\left\langle u_i^{'2} \right\rangle}, \left|r_{ii}(\Delta x)\right| \le 1 \tag{1.43}$$

Notation $\left\langle u_i^{'2} \right\rangle$ is adopted for the spatial average of the fluctuations in order to be distinguished from the temporal $\overline{u_i^{'2}}$. In correspondence with the equivalent time scale, the integral length scale provides

a representative measure of the extent in space over which velocities are appreciably correlated. Therefore, through this measure, the size of the large eddies is identified:

$$l = \int_0^{\infty} r_{ii}(\Delta x) d\Delta x \qquad 1.44$$

A complementary means of gaining more insight in the characteristics of turbulent fluctuations, besides the information provided by the statistical properties described previously, is through the energy spectrum $S(\omega)$ defined as the Fourier transform of the autocorrelation function $R_{ii}(t)$.

$$S_{ii}(\omega) \equiv \frac{1}{2\pi} \int_{-\infty}^{+\infty} R_{ii}(t) e^{-i\omega t} dt \qquad 1.45$$

The energy spectrum provides with information on the distribution of turbulent kinetic energy of the various scales and its corresponding frequencies $\omega/2\pi$ that occur.

In analogy with $S(\omega)$ that is based on the time scale of the fluctuations, we can derive the $S(k)$, which is defined as the Fourier transform of the autocorrelation function $R_{ii}(x)$.

$$S_{ii}(k) \equiv \frac{1}{2\pi} \int_{-\infty}^{+\infty} R_{ii}(x) e^{-ikx} dx \qquad 1.46$$

The $S_{ii}(k)$ associates the energy distribution with the length scales of the eddies in terms of the wave number $k \sim 2\pi / length$. Eddies with small wave numbers expose a non-universal energy spectrum, since they correspond to the large-scale motions. The evolution of these motions is under the direct influence of the broader geometrical characteristics of a particular turbulent flow. On the other hand, regarding the group of smaller eddies, down on the lower level in the energy cascade local isotropy is approached. In this case the mean shear rate imposed by the external boundary conditions has negligible effects. As a result of these fluctuations $S(k)$ emerges as dependent on the kinetic energy cascade rate ε, the fluid's kinematic viscosity ν, and the wave number k. Using equation 1.46, the units of S are obtained to be $\mathrm{m}^3/\mathrm{s}^2$; consequently dimensional analysis using S_{ii}, ε, ν, and k requires:

$$\frac{S_{ii}(k)}{\nu^{5/4}\varepsilon^{1/4}} = \Phi\left(\frac{k\nu^{3/4}}{\varepsilon^{1/4}}\right), \frac{S_{ii}(k)}{\upsilon^2 \eta} = \Phi(\kappa\eta), k \gg 2\pi / l \qquad 1.47$$

For the remaining eddy sizes between l and η pertaining to the intermediate range referred as inertial subrange, the spectrum must be independent of both the mean shear and the kinematic viscosity. Losses due to viscosity are small during the turbulent kinetic transfer at this range of scales and they are not taken into account. Thus, the form of the spectrum in the inertial sub-range is obtained from dimensional analysis using only S_{ii}, ε, and k:

$$S_{ii}(k) = const \cdot \varepsilon^{-2/3} \cdot k^{5/3}, 2\pi / l \ll k \ll 2\pi / \eta \qquad 1.48$$

Equation 1.48 is often referred as the Kolmogorov's law $k^{5/3}$and it is one of the cornerstones of turbulence theory. For large Reynolds numbers a broad inertial sub-range is observed. This is attributed to the large deviation in size between the large energy containing eddies and the small dissipating Kolmogorov eddies. Figure 2-2 shows a plot of experimental spectral measurements of $2S_{ii}(k)$ from several different types of turbulent flows and the range of the Kolmogorov's law $k^{5/3}$.

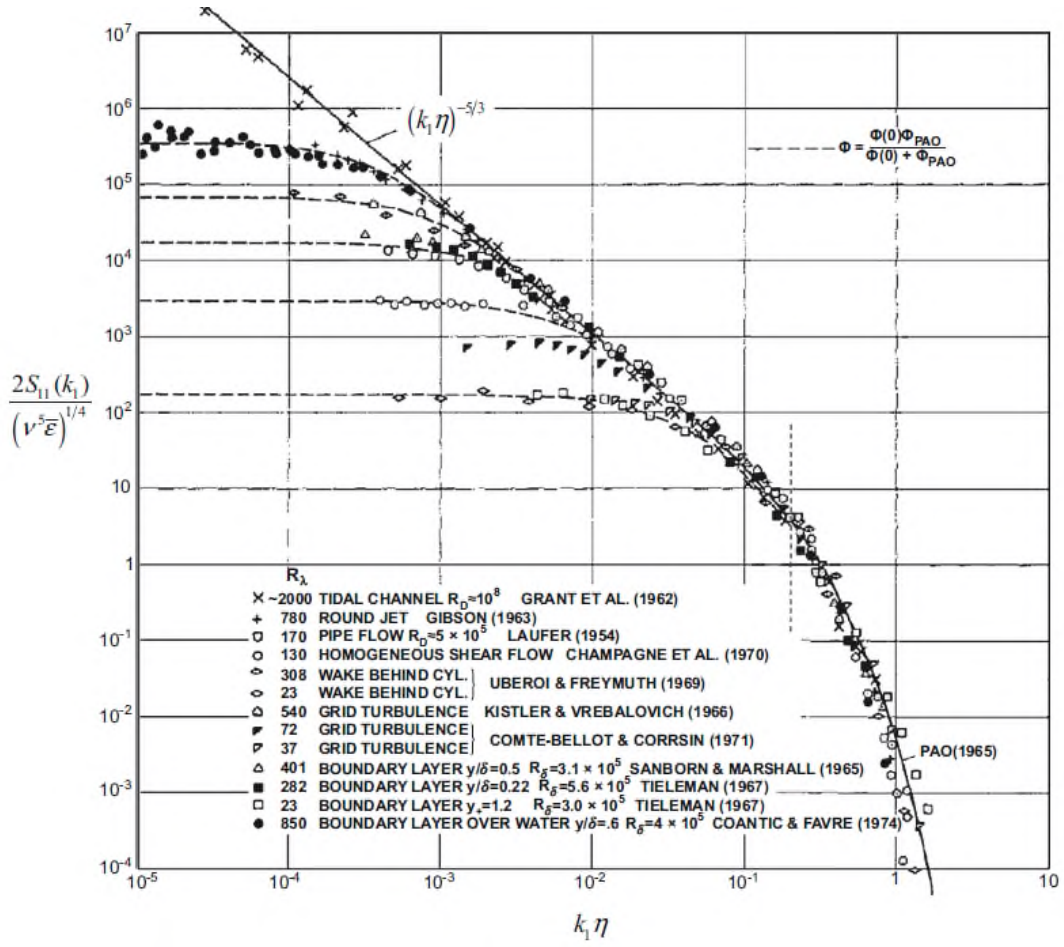

Figure 2-2 One-dimensional energy spectra from a variety of turbulent flows plotted in Kolmogorov normalized form, reproduced from Chapman (1979), Kundu et al. [10]

2.1.4 Homogeneous and isotropic turbulence (HIT)

It is well accepted that the Navier-Stokes equations are notably difficult to solve, due to their nonlinearity at high Reynolds numbers, when transition to turbulence and velocity fluctuations occur.

The existence of the closure problem prevents us from the direct solution (even numerically) of the RANS equations even with the imposition of convenient boundary conditions. In addition, having in mind that in a chaotic turbulent velocity field solutions are apparently chaotic, the statistical properties of turbulence arise with greater value compared to a detailed solution, at least from a more

practical point of view. Nevertheless, the approximation of turbulence as being homogeneous (or spatially stationary) and isotropic allows some considerable simplifications. Such assumptions enable us to reach out to as close as possible accurate predictions of the turbulent properties. As a result, homogenous-isotropic turbulence (HIT) has been studied extensively in theory, numerical simulation, and experiment.

At one and the same time with homogeneity and isotropy, it is useful to clarify the term of stationarity. Stationarity exists when the statistical properties are independent of time. It is worth noting that since the flow variables are fluctuating, stationary flows are not considered steady in the generic sense. However, since mean flow is steady, the first step is to apply time averaging to the category of stationary flows.

If the turbulence is homogeneous, then there are no spatial variations in the flow's statistics and all directions are equivalent. In terms of velocity fluctuations, this is formulated as:

$$\frac{\partial}{\partial x_i}(\overline{u_i' u_j'}) = 0, \frac{\partial}{\partial x_j}(u_{i,rms}) = 0 \tag{1.49}$$

Furthermore, the spatial variation of mean flow velocity must be constant for stationary in time turbulence:

$$\frac{\partial U_i}{\partial x_j} = cons\tan t \tag{1.50}$$

The characterization of turbulent fluctuations as completely isotropic implies the absence of directional preference. The normal Reynolds stresses are of equal magnitude and the Reynolds shear stresses are zero [11].

$$\overline{u_1'^2} = \overline{u_2'^2} = \overline{u_3'^2} = \overline{u'^2} \Leftrightarrow u_{1,rms} = u_{2,rms} = u_{3,rms} = u_{rms} \tag{1.51}$$

$$\overline{u_1' u_2'} = \overline{u_1' u_3'} = \overline{u_2' u_3'} = 0 \tag{1.52}$$

Moreover, for homogeneous and isotropic turbulence we have:

$$\overline{\left(\frac{\partial u_1'}{\partial x_1}\right)^n} = \overline{\left(\frac{\partial u_2'}{\partial x_2}\right)^n} = \overline{\left(\frac{\partial u_3'}{\partial x_3}\right)^n} \tag{1.53}$$

$$\overline{\left(\frac{\partial u_1'}{\partial x_2}\right)^n} = \overline{\left(\frac{\partial u_1'}{\partial x_3}\right)^n} = \overline{\left(\frac{\partial u_2'}{\partial x_1}\right)^n} = \overline{\left(\frac{\partial u_2'}{\partial x_3}\right)^n} = \overline{\left(\frac{\partial u_3'}{\partial x_1}\right)^n} = \overline{\left(\frac{\partial u_3'}{\partial x_2}\right)^n} \tag{1.54}$$

Using the above relationship for n =2 and some symmetry properties, the definition of dissipation rate for HIT can be reduced to the equation 1.28.

From equation that the total turbulent kinetic energy is obtained by:

$$k_t = \frac{1}{2}\left(\overline{u_1'^2} + \overline{u_2'^2} + \overline{u_3'^2}\right) = \frac{3}{2}\overline{u^{i2}} = \frac{3}{2}u_{rms}^2 \qquad 1.55$$

The simple framework provided by homogeneous and isotropic turbulence has proved very useful in the development of statistical theories of turbulence such as the case of local isotropy that describes the state of small eddies and was analyzed in par. 2.1.2. Many researchers still use it as a powerful model to elucidate the basic mechanisms underlying more complex turbulent phenomena and confront these situations successfully either by experimental or numerical means.

The rapid progress in computational power made the arithmetic simulations of homogeneous and isotropic turbulence very popular. However, despite the increase in computational sources, the number of time steps that can be accomplished is still limited. Consequently, experimental methods of approach are still very popular.

The main approach in creating isotropic turbulence is by use of a grid in a wind or water tunnel Uberoi and Wallis[12], Compte-Bellot and Corssin.[11], Britter et. al. [14]. This method produces nearly isotropic turbulence with an intensity characterized by free stream velocity U_{mean} and the geometrical characteristics of the grid. Despite its success in certain applications, the conventional static grid turbulence presents certain restrictions that are difficult to overcome. Firstly, it is difficult for high Re numbers to be accomplished, due to limitations in the increase of velocity and secondly, the decay of turbulent energy downstream imposes longitudinal non-homogeneity. In order for the level of turbulence to be increased, active oscillating grids instead of passive are employed, however at the cost of loss of isotropy Goepfert et. al. [15]. Such applications are described in works such as Thompson and Turner[16], Hopfinger and Toly [17] . Nevertheless, the decay of turbulence kinetic energy in the streamwise direction is inevitable. This energy decay can be “rectified” by the placement of one identical grid alongside the first one, Villermaux et. al.[18], Shy et. al.[19], [20], De Silva and Fernando [21], [22], Li et al. [23]. Such an arrangement is presented in Figure 2-3. Although increase in turbulent intensity is achieved in the region between the grids and the flow is homogeneous in planes parallel to the grids, the flow is not fully isotropic.

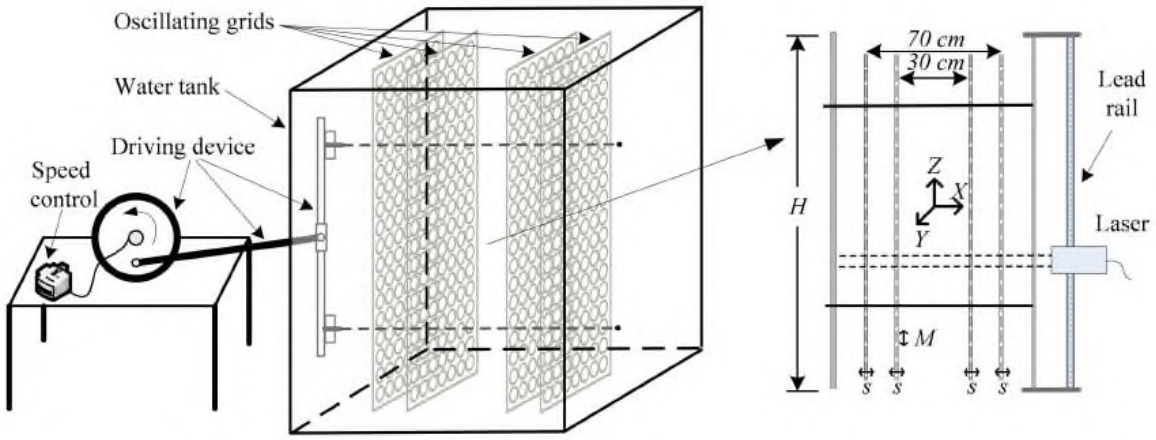

Figure 2-3 Scetch of the experimental system employed by Li et. al. [23] for the production of homogeneous and isotropic turbulence using symmetrically placed oscillating grids in a water tank.

Flow facilities with space distributed actuators (fans, synthetic jets) are the main option in order to overcome the deficits of grid turbulence. A configuration which produces turbulence in a water tank via a randomly actuated synthetic jet array (RASJA) is presented by Variano et. al. [24]. Compared to grid stirred tanks (GSTs), such a system offers smaller mean flows in terms of the ratio U/u_{rms} at equivalent Reynolds number. An extended version of the previous one (64 vs 9 synthetic) jets, was employed by Variano and Cohen [25], in order this time to create turbulence in a water-air interface. This kind of configuration is beneficial for examining turbulence at boundaries because turbulence with excellent two-dimensional homogeneity and isotropy is produced. However, when a RASJA forces a tank from only one direction, three-dimensional large-scale isotropy is unattainable due to turbulence decay. In order to overcome this deficit, symmetric forcing concepts (SF) are adopted. Experimental arrangements which are based on planar symmetric forcing (PSF) are described in the works of Krawczynski et. al.[26] and Bellani and Variano [27]. These arrangements include a configuration with two opposed jet arrays which interact and produce three-dimensional homogeneous and isotropic turbulence in the center region around the stagnation plane of the jets, Figure 2-4. In the first case [26], arrays of 16 conventional jets are used, attaining Re_λ 350, while in the second [27] arrays of RASJ are used attaining Re_λ 334. The high Re_λ and the large dimensions of the center HIT region (compared with the integral length scale of the turbulent flow) are the two benefits of these facilities.

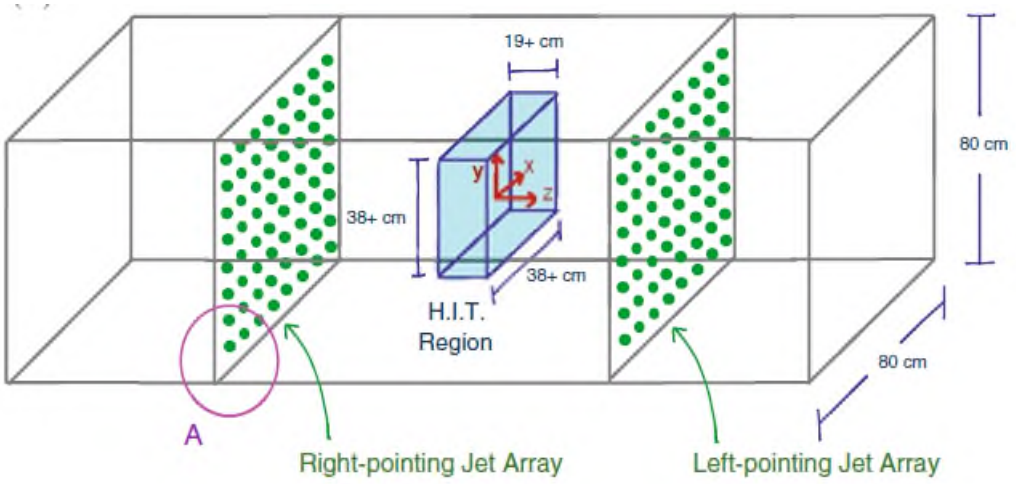

Figure 2-4 Production of homogeneous and isotropic turbulence using two opposed synthetic jet arrays in a water tank Bellani and Variano [27].

Spherically symmetric forcing (SSF) concepts usually include the placement of the actuators (jets or fans) at the corners of a cubic chamber. This type of arrangements commonly referred as “box of turbulence” and its evolution are analytically described in subsection 2.1.6. However, it is considered necessary to dedicate a portion of this section to analyze the formation and evolution of the synthetic jets, since their mechanisms and dynamics are not as straightforward and widely known as in the case of fans.

2.1.5 Synthetic Jets

The synthetic jet or zero-net-mass-flux (ZNMF) jet, was originally employed as a flow control method in the laboratory, in the 1990’s. Since then, it has attracted much attention due its broad range of applications in fluid mechanics such as controlling vortex shedding over bluff bodies [28] or the airflow over an airfoil [29], integration of synthetic jets in the flight control system of aircrafts or UAVs [30], heat transfer [31] and finally production of HIT [32], [33], [15]. which is the case with this thesis. Compact actuators arrangement with no need for external air supply and complex piping, constitute attractive features that make such arrangements a popular research area in fluid mechanics.

A full review of the vast variety of studies and applications of the synthetic jets is out of the scope of this thesis and one can find several examples in the paper of Zhang et. al. [34]. However, the basic principles of its formation and evolution will be given. The basic characteristic is that fluids can be periodically ejected and sucked from the orifice by the periodic motion of the device (piston, membrane, diaphragm) inside the cavity, Figure 2-5. Two separate phases of the motion can be distinguished, the blowing cycle and the suction cycle.

Blowing cycle: When the diaphragm or piston moves forward, the fluid is ejected from the orifice, forming the shear layer around the orifice due to flow separation. The shear layer grows and develops into vortical structures. The generation mechanism for the vortical structures depends on the condition of the boundary layer at the jet exit, Toyoda and Hiramoto [35] . For case of a laminar boundary layer, it separates from the orifice edge and rolls up forming vortical structures due to the presence of the Kelvin–Helmholtz instability. Instead, when the boundary layer is turbulent, large-scale vortices are produced and the vorticity in the shear layer is observed to be concentrated in the form of clusters. The self-induced velocity transports the vortical structures further downstream in space.

Suction cycle: During the backward motion of the diaphragm or piston (the suction cycle), the fluid outside the orifice is sucked into the cavity; at the same time, the vortex structures formed during the previous blowing cycles have moved further downstream and are little influenced by the suction process. Hence, the entrainment of the vortex ring or pair back into the cavity will be avoided. Consecutively formed vortex pairs coalesce and produce a momentum jet propagating away owing to its self-induced velocity.

Thus, a series of vortical structures is formed periodically during the blowing and suction process. For a narrow slot orifice, a vortex pair is generated, while a vortex ring forms from a circular orifice. The net flow flux of the synthetic jet during one period is zero. Thus, it is named the zero-net-mass-flux jet. Accordingly, there is no need for an external air supply for the application of the synthetic jet. However, the net momentum flux during one period is not zero.

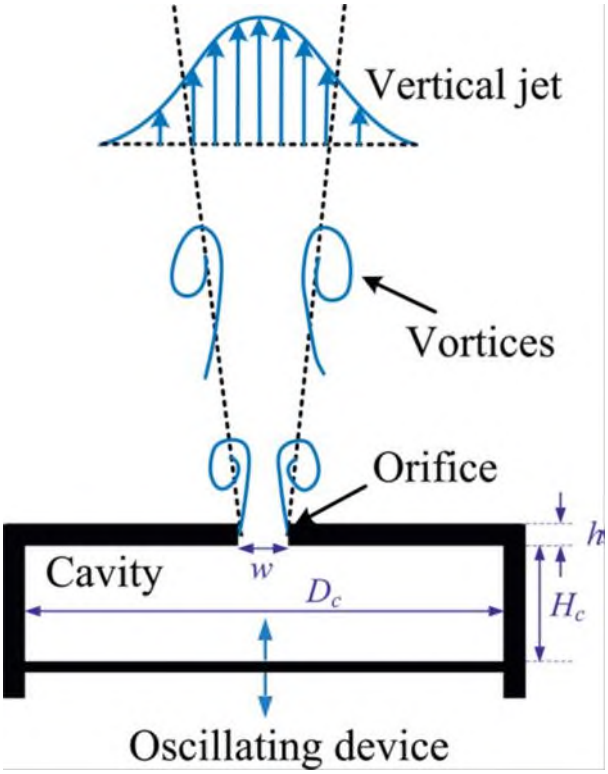

Figure 2-5 Formation and evolution of synthetic jets, Wang and Feng [36]

In order to simplify several operating, geometrical and fluid parameters that shape the main features of the synthetic jet, Glezer [37], Smith and Glezer [38] proposed two independent dimensionless parameters, the stroke length ratio and the Reynolds number based on the blowing stroke. Adopting the simple 'slug' model for vortex ring formation of Glezer [37], the stroke length represents the length of a fluid column containing the fluid that is forced out of the orifice during the blowing cycle:

$$L_0 = U_0 T, \tag{1.56}$$

where T is the period of actuator excitation and U_0 is the time-averaged blowing velocity over this period:

$$U_0 = \frac{1}{T}\int_0^{T/2} \overline{u_0}(t)dt \tag{1.57}$$

with $\overline{u_0}(t)$ denoting the instant stream-wise space averaged velocity over the orifice cross section. The Reynolds number is defined based on the actuator orifice diameter D_0 and the time-averaged blowing velocity over the entire period U_0:

$$\mathrm{Re}_{U_0} = \frac{U_0 D_0}{\nu} \tag{1.58}$$

The stroke length ratio $L_S = L_0/D_0$ is used as a generic representation of the geometry characteristics of the actuator. Thus, for an actuator-orifice configuration with constant L_S, the transition to turbulence can be assessed based on the Reynolds number.

Smith and Glezer [38] examined the formation and evolution of an air planar jet issuing from a rectangular slit under the influence of the periodic motion of a metallic diaphragm bonded on a piezoceramic disk. The Reynolds number varied between 104 and 489 and Schlieren imaging for the visualization of the flow in conjunction with hot-wire anemometry for the velocity measurements were employed. For streamwise sections z/h<80, h representing the slot width, distributions of the time-averaged streamwise and cross stream velocity components (U,V) accompanied with the corresponding velocity fluctuations $u_{rms,}$ v_{rms} exhibit self-similarity when plotted using common similarity coordinates , resembling conventional 2D jets. These cross-stream distributions of u_{rms}, v_{rms} exhibit peaks $0.25U_{cl}$ vs $0.2\ U_{cl}$, $0.3\ U_{cl}$ for the case of a continuous jet. The streamwise decrease of the mean centerline velocity of the synthetic jet is somewhat higher ($x^{-0.58}$) compared to conventional two dimensional (2D) jets ($x^{-0.5}$).

Smith and Swift [39] extended the above study on 2D synthetic jets for an increased Reynolds number ≈2200, suitable for aeronautical applications. They pointed out that in the well-developed region, synthetic jets behave very much like continuous jets, concerning the almost identical self-similar velocity profiles. Although in the near field, vortex pairs dominate the evolution of the synthetic jets and entrain more fluid than in comparison with continuous jet columns, further downstream, it appears that the time-averaged features of the jets exhibit little correlation with the initial generation process. In addition, they identified wider cross-section profiles for the case of a synthetic jet development in agreement with the observations of Bera et. al. [40]. In this latter paper increased peaks for the dimensionless cross-stream distributions of u_{rms}, v_{rms} (0.4, 0.35) are mentioned, thus resulting in higher turbulence intensity in comparison to the continuous jet. Similar observations, concerning the above increased downstream rms values are reported by Cater and Soria [41] for a round synthetic jet.

Muller et. al. [42] presented the flow structure and formation of axisymmetric synthetic jets for Reynolds numbers in the range [200, 2200] using PIV measurements. These authors reported that, dissimilarly to 2D jets [38], [39], where the entrainment rate was found larger for the synthetic jets, a round synthetic jet exhibits comparable entrainment levels with a conventional axisymmetric turbulent jet.

Mallinson et al. [43] examined the flow produced by a synthetic jet actuator with a round orifice both experimentally and numerically. Experimental data and LES predictions of centerline and cross-stream

velocity distributions were in good agreement with each other and with the theory for a continuous turbulent jet. Especially, mean centerline velocity decayed in the form $1/z$ as in conventional round jets. Statistical similarities with the conventional jet were also brought out by LES simulation realized by Lardeau and Leschziner [44], while studying the interaction of round synthetic jets with a turbulent boundary in a cross flow.

Based on the above aggregate of research studies it is considered safe and allowable to treat a round axisymmetric synthetic jet as a conventional one, especially in the far field of the developed flow.

2.1.6 Box of Turbulence

The assumption of steady, nominally homogeneous and isotropic turbulence (HIT) is considered advantageous for the investigation of a multitude of turbulent flows related with turbulence modulation[32], [45], thermal/species diffusion[46],[47], combustion and flame[48], [49],[50], droplet vaporization[51], inertial particle clustering[33], [52], [53], mixing in stratified layers[21] and interaction of plankton with turbulent water motions[54]. Oscillating grids and space distributed actuators (fans, synthetic jets) are regarded as the most usual means to produce HIT flow with zero-mean velocity in the laboratory. The case of actuators provides several advantages in comparison with traditional wind tunnels that rely on passive or active grids to produce turbulence. The most obvious among them are the small size and the avoidance of bulky, mechanically moving parts. The production of stationary (time invariant) turbulence statistics without excessive seeding requirements for LDA or PIV are additional favorable features of the actuators facility, whereas the oscillating grids present also the disadvantage of accomplishing homogeneity and isotropy on planes only parallel to them.

The available literature contains a relatively small number of studies including “box of turbulence” applications in comparison with the vast research material on grid generated turbulence. However, in the last two and a half decades, there have been several such experimental facilities, either using fans or synthetic jets. These configurations form the basis for the implementation of the current experimental setup and are worthy of a short description. The main properties of the implemented flows are presented in Table 2-1.

Early attempts to realize turbulent flow fields using fans as actuators are met in the works of Semenov [55], Andrews and et. al. [56]. In both studies, four fans were placed symmetrically in 90^{o} intervals to produce isotropic gaseous turbulence in closed vessels. Although these works have sparked the idea of producing isotropic turbulence avoiding using grids, they do not provide the characteristics of homogeneity and zero mean velocity of the flow. Moreover, the lack of LDV, PIV or other advanced image processing techniques did not permit reliable estimations of the flow properties.

Birouk et al. [51], [57] attempted to realize HIT in a cubic closed chamber, where the air inside was stirred with eight electrical fans that were placed in the corners of the cube. The external dimensions were $400\text{x}400\text{x}400\ \text{mm}^3$ and the corners were designed in a way to approach a nearly spherical internal volume of $40\ \text{mm}$ diameter, which was seeded by silicon oil droplets. The cubic chamber was built from aluminum but has been made optically accessible via four clear acrylic resin circular windows mounted on the four lateral sides. The turbulence kinetic energy or intensity was controlled by the fans speed. Single and two-point LDV measurements were taken in two directions in order to characterize the flow. The latter permitted the estimation of the integral length scale through calculation of the spatial autocorrelation coefficient. Measurements in the third direction were considered unnecessary due to the geometrical symmetry of the flow. The homogeneity and isotropy of the turbulent flow field have been verified within a spherical volume of $20\ \text{mm}$ radius around the chamber's center. In this volume, the mean velocities U and V were found quasi-zero and invariant with respect to the fans speed. In addition, the fans' speed showed no effect on the integral length scale. This particular flow facility was exploited for the investigation of turbulent effects on droplet vaporization [51], a phenomenon closely related to fuel atomization and combustion processes. The results showed that the vaporization process was boosted by the presence of turbulent velocity fluctuations in comparison with a stagnant environment.

A similar cubic chamber ($300\text{x}300\text{x}300\text{mm}^3$) using eight fans was employed by Fallon and Rogers [52] aiming to assess the turbulence induced preferential concentration of solid particles based on their Stokes number in microgravity conditions such as that exist in planet Mars. To extract the distribution of the particles, image processing techniques were used. Firstly, the properties of the turbulence flow field were estimated after a series of LDV measurements that took place on the ground (normal gravity conditions). This configuration created a turbulence of the same nature with Birouk et al. [51], [57] but was inherently of lower intensity and also had a nonnegligible one directional mean flow. The subsequent experiments concerning the visualization of particles behavior were performed by conducting a free-floating experiment aboard NASA's reduced gravity aircraft. The experimental results agreed with direct numerical simulations in the same field of research.

De Jong et. al. [58] employed an eight-fan-driven cubic turbulence ''box'' based on a chamber described by Birouk et al., in order to estimate the turbulent kinetic energy dissipation rate in zero-mean isotropic turbulence. The use of PIV afforded the calculation of spatial derivatives of rms velocities, necessary for the determination of dissipation rate. A two-velocity component LDA system was also used to validate the data collected by PIV. Six flow conditions, controlled by the fans rotation rate were examined giving Re_λ in the range [104, 184]. Five different methods for estimating the dissipation rate were assessed with the second-order structure function being found the most reliable.

The summarized results for this method show that the dissipation rate increases with the raise in turbulent intensity, whereas large eddy, Kolmogorov and Taylor microscales decrease, an observation that agrees well with theory. Instead, the large eddy length scale exhibits a relation of independence with turbulence levels, something that agrees well with the results of the other experiments carried out in similar flow facilities. Salazar et. al [59] employed the above facility in order to investigate the inertial particle clustering in isotropic turbulence and compare it with DNS, observing good agreement between the methods.

Webster et al. [60] achieved to realize nearly homogeneous and isotropic turbulence in a closed cubic chamber 400x400x400mm^3 , filled with salty water, in order to study the response of plankton to physically-realistic fluid motions. The chamber was built from plexiglass and the eight aqueous actuators were placed in each corner. The function of the actuators followed the design philosophy of the synthetic jet actuators of Smith and Glezer for a gaseous phase [38]. For the calculation of flow statistics over the center region ($4\text{cm}\text{x}4\text{cm}$), DPIV velocity measurements were conducted in two orthogonal planes for four turbulent intensity levels that were produced by varying the frequency and amplitude of the actuator excitation. The largest anisotropy was found 0.28 and the average length scale 2 cm, related to the large-scale geometry of the apparatus and independent of the turbulent intensity level.

Hwang and Eaton [32] extended the study of Fallon and Rogers [52] by replacing the fans by synthetic jets produced by propylene cone woofers pushing the air out of plenums through 19 mm diameter round orifices. The absence of moving parts made the apparatus more reliable mechanically, especially in the presence of particles (Figure 2-6). The velocity field in a 40 x 40 mm^2 region at the center of the chamber was captured by two-dimensional digital particle image velocimetry (PIV). An optimized synthetic jets momentum flux was accomplished at an excitation frequency of approximately 100 Hz, and the Re_λ was found 218. An isotropy ratio having a range of [0.88, 1.24] and a spatial average of 1.03 demonstrated a high level of isotropy throughout the region of interest. The normalized rms velocity spatial maps $u_{i,rms}/\overline{u_{i,rms}}$ was within 0.9–1.1, proving that the flow was also nearly homogeneous within the same region.

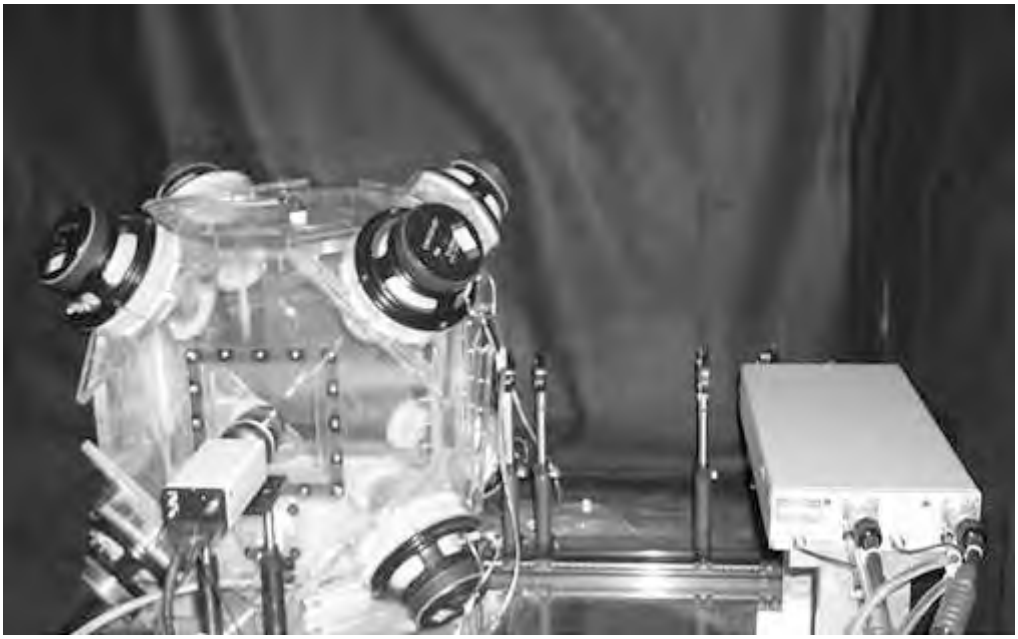

Figure 2-6 The experimental apparatus used by Hwang and Eaton [32] including a closed "Box of Turbulence" with eight loudspeakers in the corners and a PIV system

Goepfert et. al. [15] influenced by the concept of Hwang and Eaton [32], built a facility for generating HIT, having as objective the study of droplets evaporations into a turbulent air environment. The configuration adopted, consisted of an open turbulence chamber with no presence of fixed walls, Figure 2-7. This characteristic facilitated the introduction of droplets into the domain and made the optical methods more effective since there was no possible formation of liquid film. A set-up of six loudspeakers placed on each side of the domain was used instead of eight in the corners. The combined PIV and LDA two-point measurement techniques provided the means for a full characterization of the flow for a case of Re_{λ}=240. Homogeneity and isotropy with a small mean flow was achieved within a domain in the center of an average size of 50x50 x50 mm^3. Stationary turbulence statistics and scales showed fair agreement with the results of the relevant works in the field.

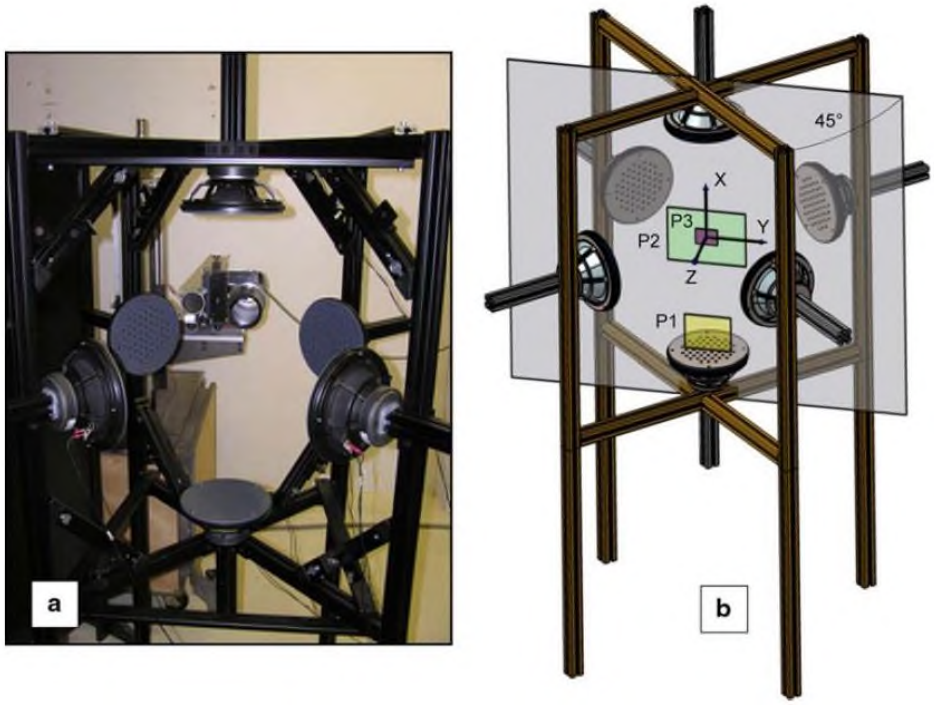

Figure 2-7 The open "Box of Turbulence" producing zero mean flow HIT using six loudspeakers symmetrically placed Goepfert et. al. [15]

The preferential concentration of poly-dispersed droplets in stationary isotropic turbulence was investigated in the work of Lian et. al. [33]. Eight loudspeakers were mounted on specially designed aluminum plates placed at the eight corners of a cubic box, all pointing at the center of it. The vibrations of the membranes of the speakers produced synthetic momentum fluxes. These fluxes were further transformed into arrays of jets due to the installation of perforated PVC plates (designed with 6mm round holes forming a triangular pattern) in front of each loudspeaker. Homogeneous and isotropic turbulence with four different intensities represented by turbulent Re_λ, and zero mean velocity was generated within a central domain of 40 mm^3. The instant velocity maps of the turbulent air flow were captured by PIV, enabling the calculations of spatial correlation coefficients. Using air-assisted atomization, droplets of different size distribution and Sauter mean diameters were generated and introduced into the 'box of turbulence'. Whereas DNS results of other authors had exposed a dependence of droplet preferential concentration on turbulent Reynolds number; keeping the Stokes number constant, this observation was not verified by the current experiment.

The largest until now Re_λ in "box of turbulence" facilities are presented for the synthetic jets chamber that is employed in the papers of Bertens et. al. [61] and Evans et. al. [62], [63]. In the first case, the validity of large eddy estimation of the dissipation rate ε using PIV is addressed, while in the other two, the dispersion of glowing droplets is studied. The chamber follows both the concept and the dimensions of the Hwang and Eaton [32] facility, nevertheless larger loudspeakers allow the

realization of larger Re_λ=490. In this way, the inertial subrange is widened producing the largest integral length scales and smaller Kolmogorov microscales.

A further implementation of the box of turbulence concept was materialized by Chang et al [64] and Bewley et al [65]. In their implementation of homogenous and isotropic turbulence, the number of synthetic jets was increased to 32. The spatial arrangement of flow actuators was realized by placing loudspeakers on each of the 20 hexagonal faces and 12 truncated vertices of an icosahedral structure, which served as an approximation of a sphere thus increasing the symmetry of the actuated air streams that merged to generate homogenous and isotropic turbulence. Conical nozzles with an opening angle of 30° and an orifice diameter of 5 cm were coupled to the loudspeakers to facilitate the production of synthetic jets.

Lu et al [66] attempted to assess the performance of a single camera holographic method for particle tracking in turbulent flow. For this purpose, they employed an HIT chamber with eight loudspeakers inspired by Hwang and Eaton [32]. The study demonstrated the efficacy of their method in reconstructing the 3D particle trajectories, minimizing the cost and complexity needed otherwise by using a multiple camera system.

Dou et al [67] also used the icosahedral structure concept for the construction of a facility for the generation of homogenous and isotropic turbulence which was purposed for the investigation of particle dynamics under homogenous and isotropic turbulence. Instead of synthetic jets as in Chang et al. [64] they utilized fans as flow actuators on each of the 20 hexagonal faces of the truncated icosahedron. They argued that fans are better suited than synthetic jets for particles in turbulence investigations as they minimize gravitational settling of particles and they avoid resonance effects that are possible by loud speakers in enclosed environments. Also, they opted not to install actuators on the pentagonal faces of the truncated vertices since they are at a different distance from the center of the icosahedron than the hexagonal faces. Due to the high number of fans that supplied energy to the flow, Taylor Reynolds numbers up to Re_λ=384 were achieved.

Webster et al [68] adapted the apparatus of Hwang and Eaton changing however the fluid medium from air to saltwater. Purpose of the study was to simulate experimentally the ocean fluid environment of small-scale isotropic turbulence. Such an experimental facility would be used subsequently for studies concerning the concentration of zooplankton in small scale oceanic turbulence. They used DPIV for capturing the flow field, and altering the turbulence intensity via variation of frequency and loudspeaker amplitude, they managed to produce finer Kolmogorov scale turbulence with increased dissipation rate for the higher intensity case.

A similar study to Webster et al. [60] concerning the response of microorganisms to small scale oceaning turbulence comes from Warnaars et al. [69]. In order to expand the HIT turbulence outside the central region of an HIT chamber, the researchers adopted an alternative approach to the Box of Turbulence. They placed two loudspeakers at each side of a rectangular reactor in conjunction with a grid in front of each loudspeaker. The grids aimed at the production of small-scale turbulence inside the domain and at low levels of dissipation rate.

In Table 2-1 , the turbulent flow parameters for each case of zero mean velocity HIT, using air as a fluid medium in a "Box of Turbulence" are summarized.

Table 2-1 Turbulent flow parameters for "Box of Turbulence" facilities (values in italics are not reported in the original works and were assessed from the other reported values)

		Birouk et al. [57]	Fallon & Rogers [52]	Hwang & Eaton[32]	De Jong et. al. [58]	Goepfert et. al. . [15]	Lian et. al. [33]	Evans et. al. [63]	Dou et al. [67]	Lu et al. [66]	Chang et al. [64]	Webster et al.[60]
Dissipation rate, ε	W/kg	82	$8.21\cdot 10^{-3}$	11.3	38.7	6.7	2.38	54	38	1.4	6.7	$2.51\cdot 10^{-5}$
Turbulent kinetic energy, k_t	J/kg	1.45	$1.35\cdot 10^{-3}$	1.1	1.72	1.11	0.42	5.5	3.65	0.54	1.82	$7.35\cdot 10^{-3}$
Integral Length Scale, L	mm	8.6	150	56	58.3	36	42.9	65	50	77	99	15
Integral Time Scale, T	ms	10	550	98	54	137	180	68	32	129	90	1620
Taylor microscale, λ	mm	1.7	0.24	3.83	2.58	4.5	5.29	3.9	3.8	7.6	6.4	7.3
Re_λ		110	50	220	184	237	185	490	384	260	481	68
Kolmogorov length scale, η_{KOL}	μm	80	800	132	97	150	190	89	100	220	155	450
Region of interest	mm	40	16	40	19	40	40	50	48		50	40

2.2 Axisymmetric round jets

Turbulent jets are one of the most common groups of flows that include a vast variety of both natural phenomena and projects attributed to engineering activity. The scales of these processes range from millimeters to kilometers. In nature, for example, the situation occurs in an estuary, where a river meets the ocean, or occasionally when a wind blows through an orographic gap. Industrial applications include wastewater discharges or gaseous emissions through vehicle exhausts of factory chimneys, thrust generators in ramjet, turbofan, rocket propulsion systems, turbulent jet ignition in IC engines, forced jets for heating or cooling and water jets for cleaning objects, vehicles, or buildings.

A round free jet is considered as a shear flow that emanates from a relatively narrow conduit in a larger body of fluid. Whenever this moving fluid enters the quiescent body of an ambient fluid, a velocity shear is created, causing turbulence and mixing. As the jet progresses, it eventually entrains the receiving fluid and spreads in the radial direction with downstream distance, with a reduction of the axial velocity. Eventually, the initial momentum and energy is neutralized by viscous dissipation, the jet ceases to exist, and the flow field is homogenized.

Figure 2-8 A water jet emanating from a nozzle round orifice into an undisturbed tank of water, Benoit Cushman-Roisin [70]

2.2.1 The theory of turbulent jets

Turbulent jets belong in the category of turbulent shear flows. By shear flows we refer to flows in which the mean velocity is predominantly one-dimensional in nature, such as wakes, boundary layers, submerged jets, and pipe flow. These flows are further categorized in two basic groups: wall-bounded shear flows and free shear flows. Wall-bounded flows include flows bounded by a rigid or at any rate nearly immovable walls such as pressure flow against pipes or flow of a liquid down a wide-open channel. On the other hand, free turbulent flows are bounded on at least one side by ambient fluid of nearly the same density which is not turbulent and is usually in irrotational flow. Turbulent jets, wakes and mixing layers rest on this category. Analytical details on the theory, structure and mathematical treatment of each flow can be found in the scripts of Townsend [71] and Abramovich [72].

The most basic type of turbulent jets is one developing through a medium at rest, and we call it a submerged jet. If the velocity distribution at the nozzle exit cross section is uniform, the central portion of the fluid enters the environment maintaining its initial mean velocity. At the same time, the annular boundary layer (case of round jet) formed on the solid surfaces evolves into a mixing layer with high vorticity generated on the fluid-solid interface of the nozzle. This axisymmetric mixing layer spills out into the bulk flow where it is swept downstream, forming two diverging surfaces. On the outside, the mixing layer encounters the fluid at rest, and the vortical motion is divided from the fluid in irrotational motion forming a highly convoluted interface between the two regions. This surface shows alternating periods of turbulent and non-turbulent fluctuations, thus producing an intermittently turbulent signal which characterizes the outer boundaries of the jet throughout its downstream evolution. Within the intermittent surface, the turbulence is roughly homogeneous in scale and turbulent intensity. Moreover, according to Dimotakis [8], above $Re \sim 10^4$, the turbulence appears to be fully developed, with a pronounced fine-scale structure. At the inner part, the surfaces of the mixing layer are separated by the core of the irrotational flow characterized by the initial uniform exit velocity. We refer to this portion of the jet as the potential core. Some distance after the nozzle exit, the inner surfaces of annulus mixing layer merge and the jet becomes a fully developed, self-preserving turbulent flow. The above description is depicted graphically in Figure 2-9. As a free flow, the jet spreads into the surrounding fluid and it is necessarily inhomogeneous in the streamwise direction as well as in a cross-stream direction.

The mathematical formulation of turbulent shear flows and jets subsequently, are described in detail in several textbooks Townsend [71], Abramovich[72], Tennekes and Lumley [73]. However, each description differs in extent, notation and the various scales employed to make the flow dependent properties dimensionless. Hence, the effort to extract the most basic principles of the turbulent jets

may evolve into a laborious and confusing process. For this reason, the most essential properties of the round jet will be presented in the following paragraphs, based on the needs and the scope of the thesis, guided by the textbook of Davidson [9].

Using polar coordinates (r, θ, z), the axisymmetric jet is characterized by $U_z \gg U_r$, and $\partial / \partial z \ll \partial / \partial r$. Of course, U_z falls off with axial distance while δ, the time-averaged diameter of the jet, increases with streamwise spreading. However, it is observed that, after ~30 diameters downstream of the source, the time-averaged velocity profile is based only on radial position, r, the local jet width, δ, and the local centerline velocity. It is then a dimensional necessity that U_z (r, z) adopts the self-similar form.

$$\frac{U_z(r,z)}{U_{cl}(z)} = f(r/\delta(z), \;\; U_{cl} = U_z(0,z) \tag{1.59}$$

Similarly to a planar jet, entrainment of the ambient fluid takes place as the convoluted outer edge engulfs irrotational fluid. As a result, an increase of the jet mass flux occurs with z. The governing equations for a round jet may be simplified for three reasons:

a) Axial gradients in the Reynolds stresses are much weaker than radial gradients.
b) Laminar stresses are negligible.
c) Radial components of the mean inertial force are negligible.

Under these conditions and taking into account that the pressure in the jet is considered invariable and equal to the surrounding fluid pressure (as shown by experiment), the end equation of motion takes the following form:

$$\rho \vec{U} \cdot \nabla U_z = \frac{1}{r}\frac{\partial}{\partial r}[r\rho U_r U_z] + \frac{\partial}{\partial z}[\rho U_z^2] = \frac{1}{r}\frac{\partial}{\partial r}[r\tau_{rz}^{'}] \tag{1.60}$$

from which we see that the momentum flux is conserved:

$$M = \int_0^\infty [\rho U_z^2] 2\pi r dr = 0 \tag{1.61}$$

Two different models have been developed, in order to obtain the velocity field and the geometrical characteristics of an established self-similar jet. The first one, which is based on a mixing length hypothesis and follows an entrainment approach is attributed to Tollmien (1926) and the second one, which follows a constant eddy viscosity assumption was calculated by Schlichting (1961). Both lead to the same conclusions regarding the evolution of the round jet.

$$\frac{U_{cl}}{U_e} = cons\tan t\left(\frac{d_e}{z}\right) \quad 1.62$$

$$\frac{d\delta}{dz} = a = cons\tan t \quad 1.63$$

Tennekes and Lumley [73] provides the value 6.4 for the constant included in equation 1.62, whereas the constant α takes the value ≈ 0.43. Using the latter value for the streamwise evolution of the local diameter, it is deduced that the jet spreads downstream with an angle of approximately 12^o. (The magnitude is a bit increased since in the entrainment approach theory, δ is defined as the width where $U_z \approx 0.1 \cdot U_{cl}$.)

2.2.2 Axial regions in a round free jet

The study of the evolution of an axisymmetric jet can be approached at first by defining three separate regions in the axial (streamwise) direction. Initially, within $0 \leq z/d_e \leq 6$, Wygnanski & Fiedler [1] we refer to the near-field region, which includes the potential core. The potential core is the portion of the flow just after the nozzle exit and around the centerline, where the axial velocity is considered uniform and identical to the exit velocity profile.

The far-field region, reached at about $z/d_e \geq 30$[1], is the fully-developed or self-similar portion of the flow and its characteristics will be analyzed furthermore later in this chapter. The intermediate-field region acts as the transition passage between the near- and far-fields of the jet. The near-and intermediate-fields (NIF) constitute the development portion of the jet, also called Zone of Flow Establishment (ZFE). Heat, mass, and momentum transfer in engineering processes are greatly influenced by the characteristics of the NIF and the exit flow conditions. Therefore, the ability to control the flow development in this region would have a vital impact on many of those engineering applications mentioned above Fellouah et. al. [74].

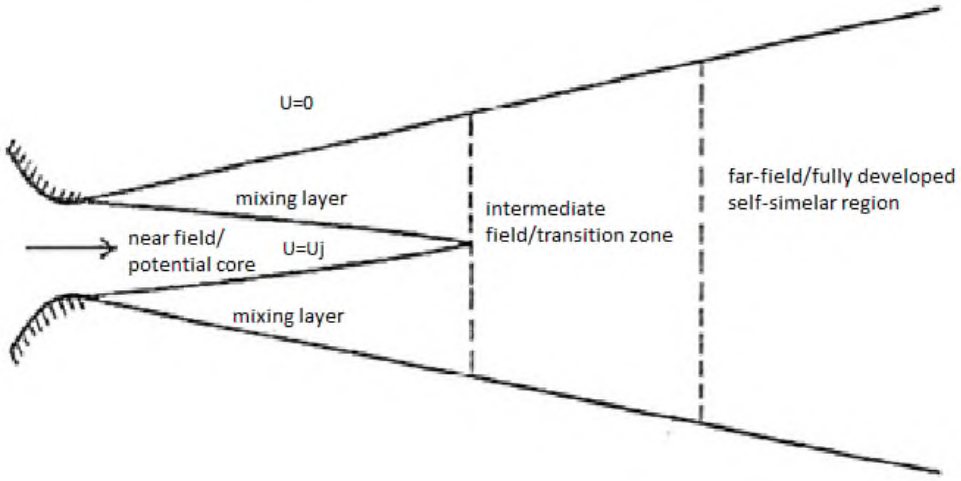

Figure 2-9 Axial regions in a round free jet

2.2.3 Radial layers of a round jet flow

As in the case of the axial direction, three also regions are readily identified in the radial (cross-stream) direction: the centerline region, the shear layer and the outer layer Fellouah et. al. [74]. The centerline region is where the axial mean velocity is maximum and coincides with the area around the longitudinal axis. In this central radial region and through the near and intermediate axial fields, the turbulence evolves to eventually reach equilibrium as the flow reaches the far-field. A significant observation regarding the radial direction concerns the large velocity gradients that occur. Because of this condition, a shear layer containing large vortex cores is formed. In the sequence, the initial vortices evolve and comprise broader structures described as large eddies. Subsequently however, these large-scale eddies break down into smaller turbulent time and length scales, according to the turbulence energy cascade concept. The velocities in the outer layer are typically ~10% of U_{cl} and normally fall to the free stream value as $r \to \infty$.

2.2.4 Mean Velocity Profiles

A characteristic feature of a turbulent jet, as described by theory and verified by a multitude of experiments, is the small ratio of the radial velocity divided by the axial component in any streamwise section of the flow. Moreover, as exposed by Figure 2-10, a continuous lowering and widening of the axial velocity profile takes place in each downstream distance from the exit.

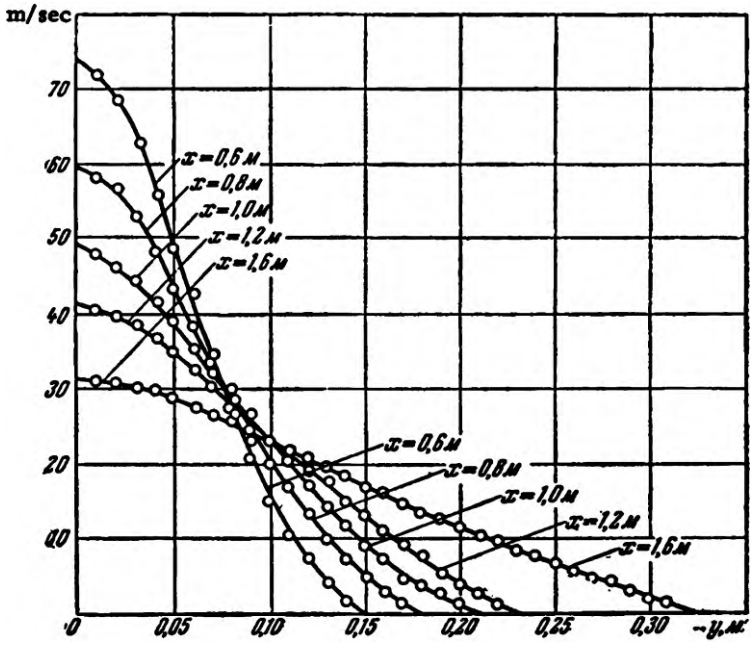

Figure 2-10: Velocity profiles in different sections of an axially symmetric submerged jet from Trupel' s experimental data (1915), the axial coordinate is denoted by x and the radial one by y , adapted by Abramovich[72].

Figure 2-11 presents the mean axial velocity profiles normalized by the centerline velocity U_{cl} plotted against the normalized distance r/d_e, for various normalized axial positions z/d_e. The broadening of the profile with increasing the axial distance from the source is again obvious as well as the symmetry and the Gaussian behavior that are repeated in each axial distance.

Figure 2-12 presents the mean radial velocity profiles normalized by the centerline velocity U_{cl} plotted against the normalized distance r/d_e and provides us with two noteworthy remarks. Firstly, the peak value of the radial profile is an order of magnitude smaller than the axial profile, verifying the introductory note of this paragraph. Secondly, the entrainment process is noticed, since the flow near the centerline expands symmetrically laterally outward, while the surrounding fluid moves inward (revealed by the negative sign at the outer portions).

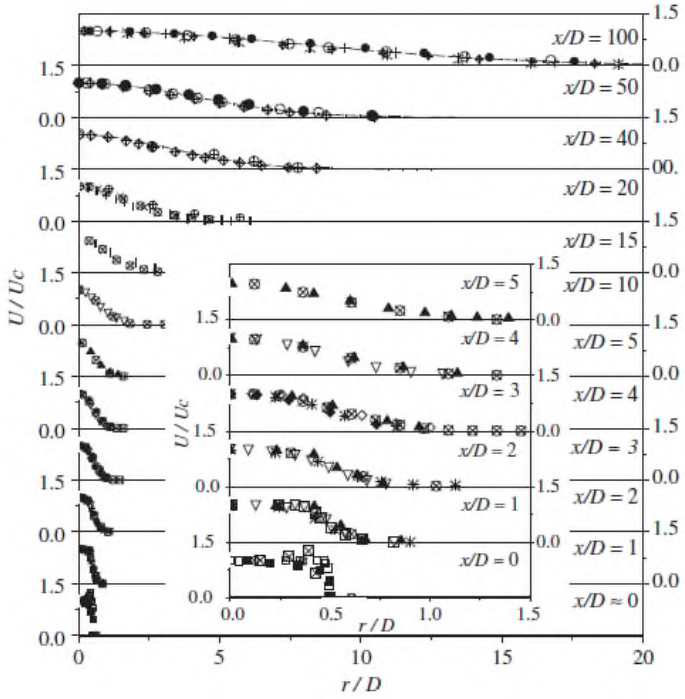

Figure 2-11 Normalized streamwise mean velocity profiles at different axial positions adapted from several experimental data Ball et. al. [75]**.**

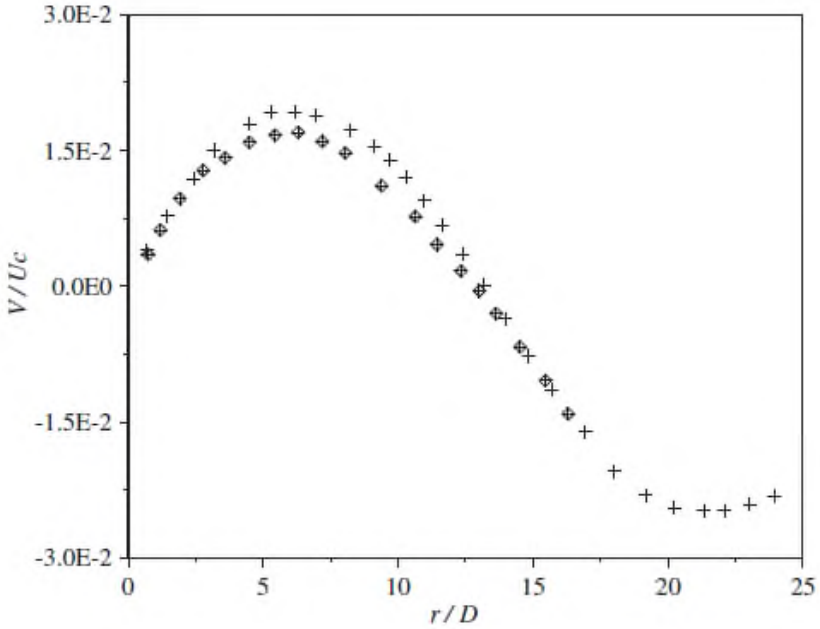

Figure 2-12 Normalized radial mean velocity profiles at different axial positions adapted from the experiments of Wygnanski & Fiedler [1] and Panchapakesan & Lumley [2], adapted by Ball et. al. [75]

2.2.5 Self similar fully developed jet in the Zone of Established Flow (ZEF)

A turbulent jet issues from the injection nozzle and forms throughout its first “infant” steps the potential core of nearly irrotational and uniform velocity fluid. This potential core is surrounded by the penetration of the annular mixing layer, until the latter merges and the former ceases to exist. At the same time, the turbulent flow enlarges and spreads radially outwards. The portion of the flow described until this point is commonly referred as the near to intermediate field or establishment/development phase. After this transitional zone, the far field, or Zone of Established Flow (ZEF) is reached and maintained until the death of the jet flow. This “mature” life portion of the jet is otherwise denoted as the self-similar flow portion due to the streamwise preservation of a similar mean velocity profile throughout this evolution phase.

A concise but at the same time thorough definition of self-similarity is given by Pope [76]: The spatial distribution of an axisymmetric flow property, say $q(z,r)$, is self-similar if it can be normalized with the streamwise variations of a scale for the property itself and of a scale for a transverse co-ordinate; and if it can be represented by a radial profile, having shape invariance with respect to the streamwise position.

In axisymmetric momentum jets, the centerline axial velocity U_{cl} decreases in the streamwise direction inversely with the streamwise distance z. The decay law is written as:

$$\frac{U_e}{U_{cl}} = \frac{1}{B}\left(\frac{z - z_o}{d_e}\right) \qquad 1.64$$

This decay law is in symphony with the theoretical prediction of equation 1.62. The virtual origin z_o is defined as the position on the longitudinal axis from which the jet would initiate if the exit was a source point of momentum. Figure 2-13 presents in a graph form an ensemble of experimental data that follow the decay law of equation 1.64.

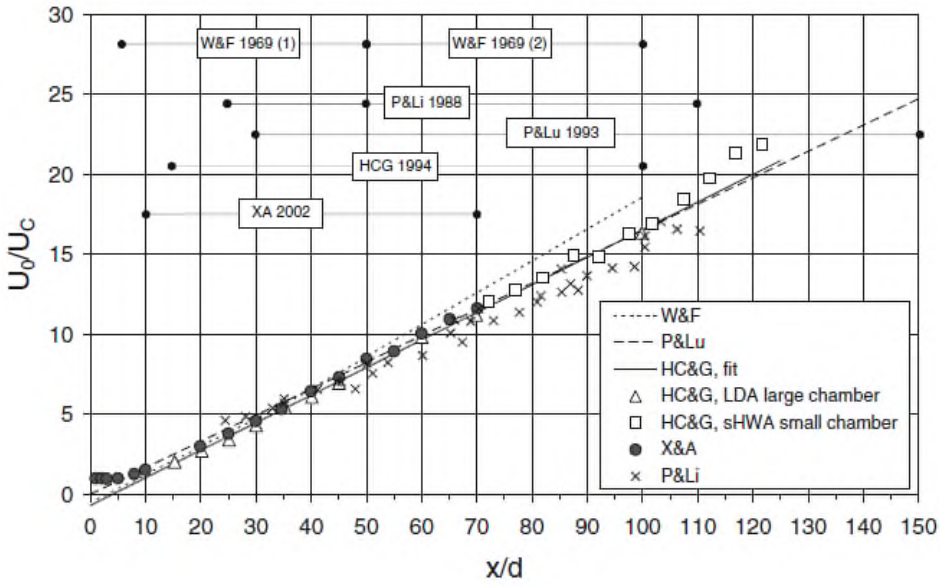

Figure 2-13 Centreline decay of axial mean velocity, aggregate of experimental data adapted by Lipary & Stansby [77]**.**

Figure 2-14 shows the streamwise evolution of the normalized normal axial and radial normal stresses (u', v') gathered by an ensemble of experimental data. As anticipated, the turbulent fluctuations decay following the same law z^{-1} as the centerline axial velocity U_{cl}, since in the far-field the normalized values of the turbulent intensities reach a nearly constant value. The axial intensity reaches a value of ≈ 0.28, whereas the radial a value of ≈ 0.20, producing an anisotropy ratio of ≈ 1.4.

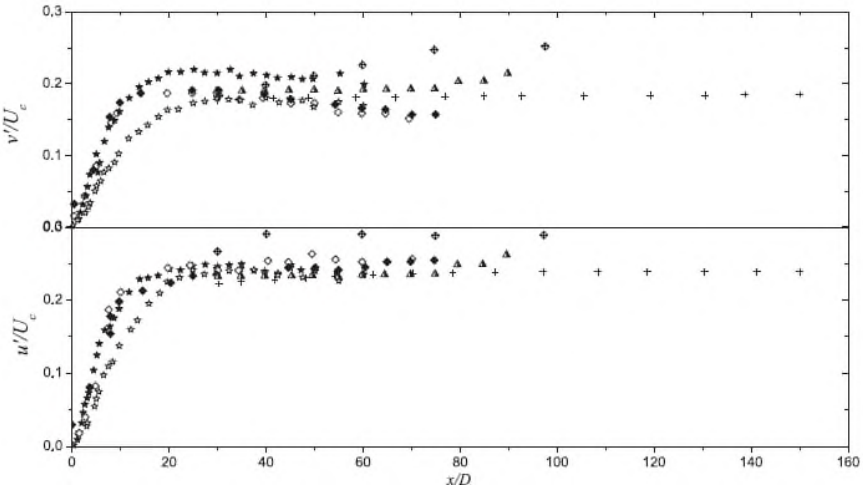

Figure 2-14 Turbulent intensities/normalized stresses axial evolution, aggregate of experimental data adapted by Ball et. all [75]

Before proceeding with the presentation of the radial profile of the mean and turbulent quantities in the self-similar region, it is considered noteworthy to make a citation to the jet half-width $r_{1/2}$, also

referred as half velocity width. Squire and Trouncer [78] proposed that the jet half-width should be a suitable indicator for the jet width, since the outer boundary is often hard to be identified experimentally and is in fact wider than estimations based on theoretical calculations by Ball et.al [75]. Similarly to the local diameter, equation 1.63, the mean spread rate of $r_{1/2}$,beyond the potential core, increases linearly with distance:

$$\frac{r_{1/2}}{d_e} = A\frac{z}{d_e} + cons\tan t \qquad 1.65$$

Values for the constant A about ≈ 0.097 are obtained from experimental data in Abramovich[72] and Ball et. al. [75].

In order to plot the radial profiles of a flow quantity $q(r,z)$ and to examine the self-similar behavior, it is necessary to employ an appropriate scale for the normalization of the transverse co-ordinate. The literature review uncovers two separate trends in the choice of this scale and imposes difficulties in a straightforward comparison among the several studies on the self-similar behavior of the round jet. The first one chooses the jet half-width $r_{1/2}$, as the appropriate scale and the second one the axial distance z. However, since these two scales are related with a linear law; equation 1.65, either choice proves equivalent in the determination of a self-similar zone. The most notable experimental studies however, which are presented in the review of Lipary [77], follow the normalization with the z scale, starting with Wygnanski & Fiedler [1]. In this particular paper, an explanation is given for not choosing $r_{1/2}$, "the use of this definition does not show any changes in the location of the hypothetical origin of the flow, which are sometimes significant (e.g. in the small deficit wake, Townsend [71]); and deviations from similarity are less visible". Consequently, the current thesis adopts the axial distance z as the suitable length scale to normalize the r coordinate: $\eta=r/z$, in order to access its results more effectively and compare it easily with the selected studies.

All the experimentally measured profiles of the axial velocity U normalized by the centerline velocity U_{cl} lead to a nearly identical profile within the streamwise extent. The radial shape of the axial velocity profile (Figure 2-15), is typically bell shaped, following a Gaussian profile, with typical values of K_U ranging between 75 to 95.

$$\frac{U}{U_{cl}} = \exp\left(-K_U\eta^2\right) \qquad 1.66$$

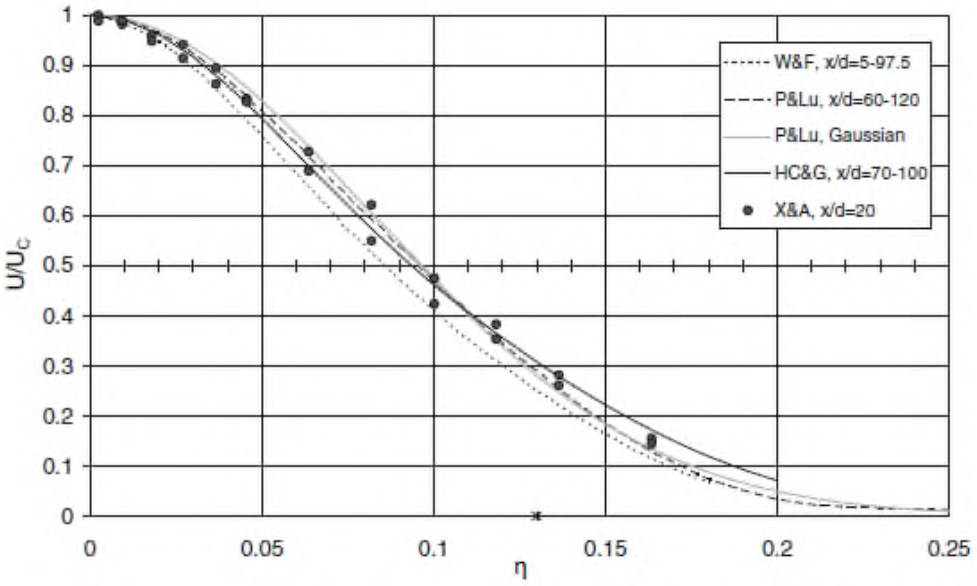

Figure 2-15 Radial profiles of the normalized axial velocity U from the experimental data of Wygnanski & Fiedler (W&F) [1], Panchapakesan & Lumley (P&Lu) [2], Hussein et. al. (HC&G)[79], Xu & Antonia (X&A) [80] as adapted by Lipari [77].

Figure 2-16 shows a typical radial profile of the radial velocity V in the self-similar zone. The η location, where the radial velocity takes zero value, marks the separation between the spreading and entraining portions of the flow. The largest outward velocity is on average ≈ $0.2U_{cl}$, while the inward ≈ $0.25U_{cl}$.

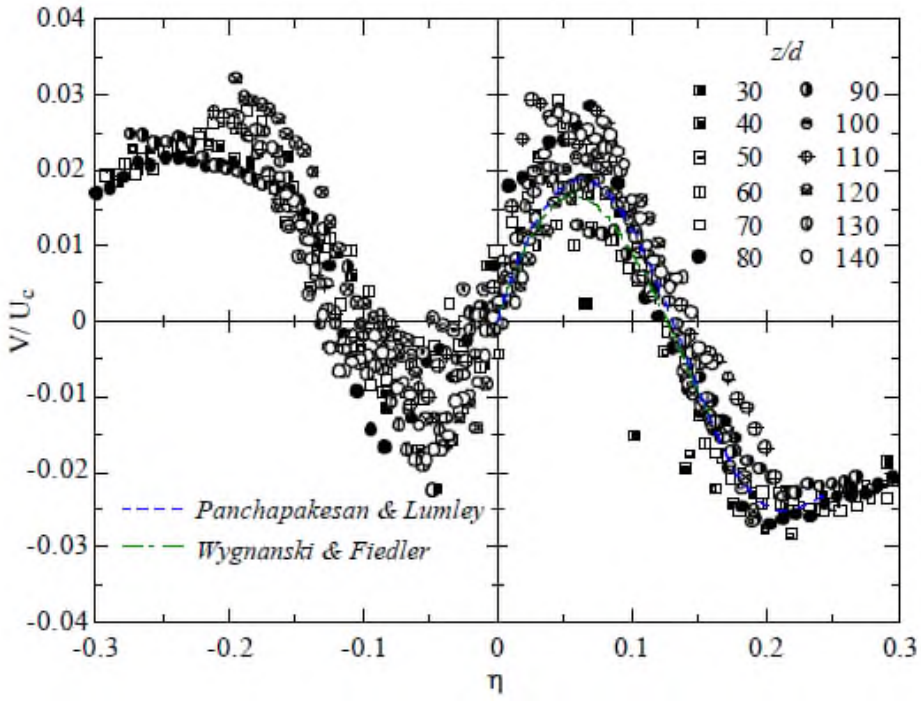

Figure 2-16 Radial profiles of the normalized radial velocity V from the experiments of Wygnanski & Fiedler (W&F) [1], Panchapakesan & Lumley (P&Lu) [2], Fukushima et. al. [81]

Figure 2-17 shows the radial profiles of the Reynolds normal stresses u', v'. The anisotropy ratio of the centerline peak values ≈1.4 which mentioned before in Figure 2-14 is repeated here. The off-axis peak results are attributed to the intense production of turbulent kinetic energy at the mixing layer, resulting in non-Gaussian type distributions.

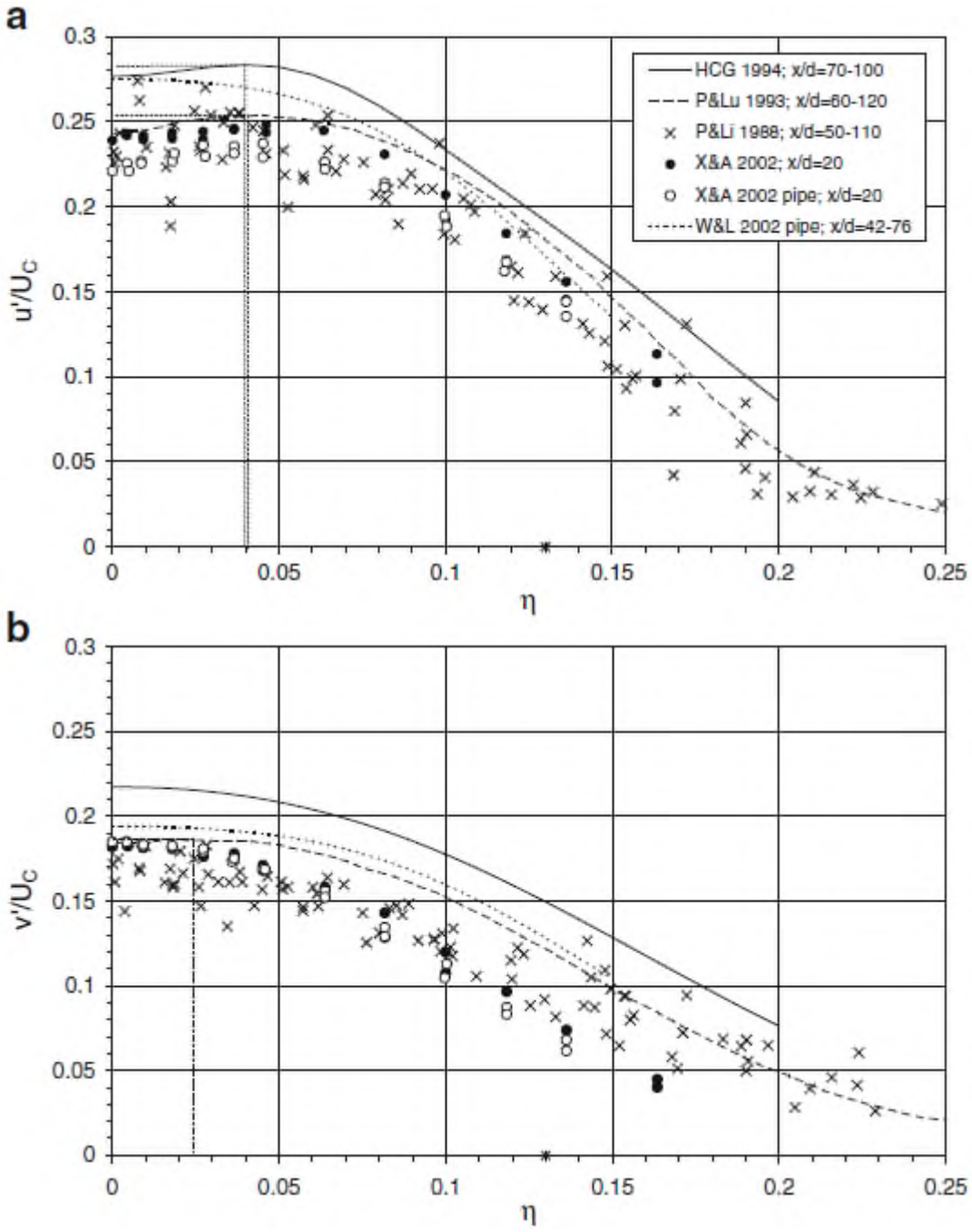

Figure 2-17 Radial profiles of the normalized Reynolds normal stresses from the experimental data of Wygnanski & Fiedler (W&F) [1], Panchapakesan & Lumley (P&Lu) [2], Hussein et. al. (HC&G)[79], Xu & Antonia (X&A) [80] as adapted by Lipari [77].

Figure 2-18 shows the radial profiles of the normalized Reynolds shear stresses $\overline{u'v'}$. The Reynolds shear stress is asymmetric about the central axis. It results positive for negative mean shear values, and negative where the mean shear is positive. The sign of the shear stress corresponds to the transport of high momentum away from the centerline.

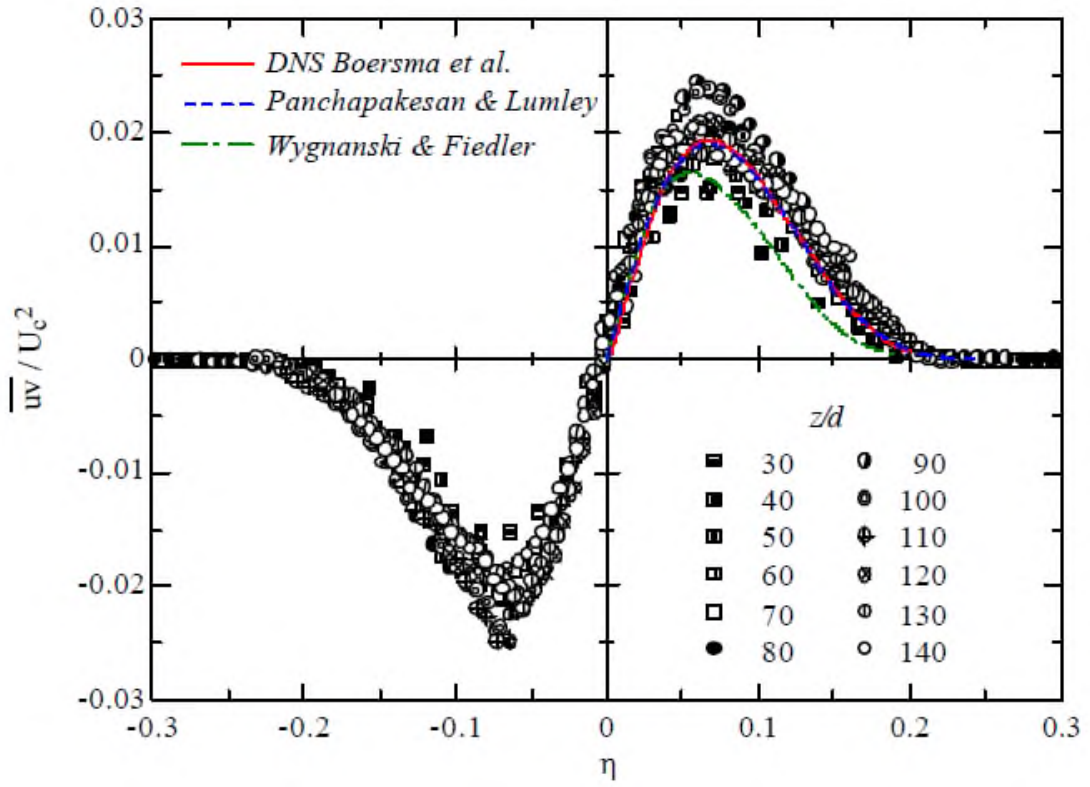

Figure 2-18 Radial profiles of the normalized Reynolds stresses from the experimental data of Wygnanski & Fiedler (W&F) [1], Panchapakesan & Lumley (P&Lu) [2], Fukushima et. al. [81]

Figure 2-19 shows the radial variation of the several contributions to the turbulent kinetic energy equation 1.25. This particular plot is rather qualitative and based on the analytical experimental results of Panchapakesan and Lumley [2] and Hussein et. al. (HC&G) [79]. The dissipation is approximately uniform near the centerline, falling off as we move to the edge, while the production term is small near the center where the mean rate of strain is weak. It peaks around $r=0.3\cdot\delta/2$ and then tends to zero as we move towards the edge. The transport of turbulent kinetic energy by pressure fluctuations and the triple correlations, is negative in the core of the jet and positive near the boundary.

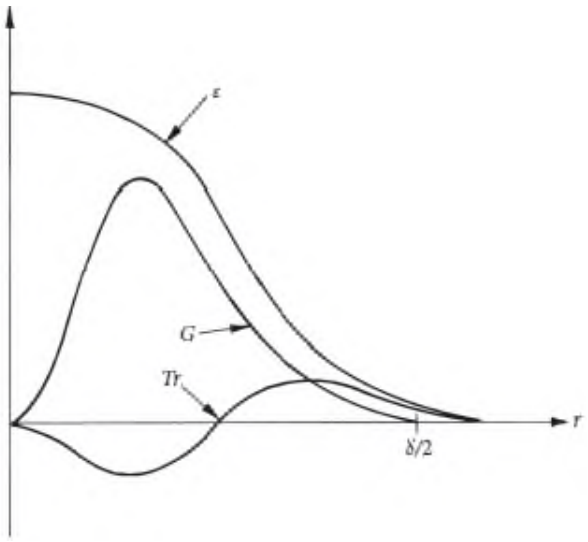

Figure 2-19 Radial profile of the budget mechanisms (energy, generation, transport) of turbulent kinetic energy, Davidson [9]

2.2.5.1 Review of key experimental studies

The first traces of research into the round jet coincide in time with the emergence of jet propulsion in aviation and the development of the first jet engines in the 1920s and 1930s. A summarized review of the early progress in the field is given by Ball et. al. [75], while more analytical descriptions of both theoretical models and experiments of this era are compiled in the "Theory of Turbulent Jets", by Abramovich [72]. However, experimental investigations and description of the flows up to 1960s were not well-comprehensive, since the technology required has been developing in parallel with the comprehension of jet flows and researchers attempted to develop physical and analytical interpretations, without often occupying the ensemble of the manifested jet flow features. During the early studies, the self-preservation of the Reynolds stresses was not yet evident. This scientific void in the field sparked the motivation for subsequent researchers to conduct more analytical measurements using more advanced experimental techniques such as linearized hot-wires and Laser Doppler anemometry.

Wygnanski & Fiedler (W&F) [1] paper is regarded a cornerstone in the round jet research and initiated the realization of more comprehensive and specific studies. An investigation of an air jet exiting a nozzle diameter d_e = 1.04 inch with exit velocities U_e :51 m/s, 72 m/s, corresponding to Re ~ 10^5 was carried out with linearized constant-temperature static hot-wire anemometers (SHWA). When the measurements were concluded for $z/d_e \leq 50$, the mean axial velocity decay constant B was found 5.7 and the position of the virtual origin z_o=3de, whereas taking into account measurements for $z/d_e \geq 50$, C=5 and $z_o=7d_e$ were obtained. This deviation was later explained by Hussein et. al. (HC&G) [79],

addressing the fact that the onset of recirculation in a small chamber caused some forward momentum loss in the jet. Judging from the plot of the axial velocity decay, the writers estimated that the mean velocity would appear self-similar already starting from a distance z/d_e =20. The radial profiles, starting from axial positions z/d_e=40 showed that the mean axial velocity U was already self-preserving at that region. On the other hand, the radial profiles of the turbulent intensities attained self-similar behavior after z/d_e=70. Based on that observation, the writers considered the jet truly self-preserving beyond this axial distance. Furthermore, by calculating the longitudinal and lateral spatial autocorrelation coefficients at different axial positions, the corresponding integral length scales were estimated in the jet's centerline as: $l_z = 0.0385z, l_r$=0.0157z. Moving away from the centerline, similar relations were derived with larger coefficients indicating an increase in the large eddy size. Finally, the study was further extended to include the behavior of third-order velocity moments (or correlations) and the kinetic energy budget.

Hussein, Capp and George (HC&G) [79], published measurements of the turbulent velocity field of an axisymmetric jet with nearly identical initial conditions with W&F, d_e = 1.04 inch, U_e :56 m/s, Re ~ 10^5. However, three different measurement techniques were used; static hot-wire (SHW), flying hot-wire (FHW) and Laser Doppler anemometry (LDA). A larger enclosure for the flow, at least twice the chamber of W&F was used. The centerline decay constant B and the virtual origin z_o obtained by measurements of SHW in the whole streamwise direction are in symphony with the values found for the distances $z/d_e \leq 50$ by W&F. Moreover, LDA measurements in a smaller enclosure exhibited a failure to stabilize to constant values of B, z_o as in the case of W&F. These two observations permitted the writers to assume that a relatively small chamber causes recirculation of the flow, leading to forward momentum loss in the jet in the far-field. Another key element of the study is the differences observed between FHW-LDA and SHW measurements. The deviations were becoming more intense while increasing the statistical orders of the measured quantities and departing from the centerline, where the turbulent intensity is minimum. This effect was attributed to cross flow and rectification errors of SHW in areas with high turbulent intensity.

A concurrent study with (HC&G) was carried out by Panchapakesan and Lumley (P&Lu) [2], the former being initiated as an assignment by the U.S. Air Force and the latter under the US Office of Naval Research. Although, HC&G published later their report, their experimental data were available to (P&Lu) and are included in their report, which contains a systematic comparison between the two. P&Lu's aim was to carefully measure velocity fluctuations up to fourth order, using FHW and evaluate models for triple moments produced by the Reynolds stresses equations. The Reynolds number for their experiments based on d_e = 6.1 mm, U_e :27 m/s, was $1.1 \cdot 10^4$; one order of magnitude smaller that (W&F) and (H&G). The decay constant B was found 6.06, larger than the cases of W&F (5.7) and HC&G

(5.8), while they managed to fit the records of the axial velocity decay with a line through the plot's origin; the virtual origin lying exactly at the nozzle exit. The larger constant B might be explained by the lower Re and turbulence intensity at the efflux point, leading to a slower far-field centerline decay because of the weaker turbulence downstream. The large chamber size and the advanced technique of FHW eliminated recirculation effects, leading to similar spreading rates of the jet with HC&G. The spreading rate is defined by the axial derivative of the normalized jet half width $r_{1/2}/d_e$. (P&Lu) found 0.096, HC&G 0.094, while (W&F) 0.086. Moreover, P&Lu identified off-axis peaks in the radial profile of the turbulent intensities' distributions, similarly with (HC&G), in antithesis with W&F. However, on the jet axis, the intensities of both the axial and the radial velocity components were found significantly lower in comparison with (W&F) and (HC&G), without a definite or comprehensive explanation to be given.

Fukushima et. al. (FA&We) [81] studied the behavior of turbulent round water jet with $Re=2\cdot10^3$, using Particle Image Velocimetry (PIV). Although, the Re was one or two orders of magnitude lower, the results for the velocity field exhibited fair agreement with the previous studies. Specifically, the profiles for the mean velocity collapsed into self-similarity beyond $z/d_e=30$ and for the higher moments for $z/d_e=60$. Moreover, the spreading rate was found 0.097; very close to P&L, HC&G and radial profile of the turbulent intensities exposed the symmetrical off-axis peaks. Although the centerline velocity U_{cl} exhibited linear decay, the decay constant B was not provided in this report.

The paper of Xu and Antonia (X&A) [80] presents an investigation into the effects on the development of a round free jet, characterized by different initial conditions imposed by a contraction nozzle and a long pipe. The Reynolds number for each flow was the same; $8.6\cdot10^4$. In the axial distance range [$20d_e$, $75d_e$], the contraction jet decayed more rapidly presenting a decay constant B=5.6, rather than the pipe jet with B=6.5. Moreover, for the contraction jet, the u' turbulent intensity attained the self-similar value 0.25 at $z/d_e=20$, earlier than the pipe jet, where the self-similar value 0.24 was attained at $z/d_e=40$. The spreading rate of the contraction jet was also larger than the pipe jet. The spreading rate of the former exhibited a value of 0.095, showing good agreement with (HC&G), while the pipe jet gave a value of 0.086 similar with W&F; despite the fact that W&F employed a contraction nozzle, the smaller spreading rate was attributed to the loss of axial momentum due to recirculation effects of the small chamber. While the radial distributions of the normalized mean velocity, normal and shear stresses showed differences between the jets in the near field, $z/d_e=3$, the intensity of such differences decreased further downstream, $z/d_e=20$. The distributions of all quantities were slightly wider for the contraction jet. The same phenomenon was also observed for the spatial axial and radial autocorrelation coefficients that were nearly similar in the far-field for both flows.

A similar study was carried out by Quinn [82], this time comparing a contraction round jet with a jet flow exiting from a round sharp-edged orifice, both with the same $Re=1.84\cdot10^5$. Although upstream nozzle configuration seemed to affect the jet's establishment zone, exposing higher mixing rates for the case of the sharp-edged orifice, further downstream, the various statistical quantities of the velocity field collapsed into self-similar profiles with nearly the same characteristics for both jets. It is noteworthy that the decay constant B was found nearly the same for both cases, i.e. contraction: 6.01, sharp edged: 5.99. Similarly, the spreading rates were nearly identical, i.e., contraction:0.096, sharp-edged:0.098.

The study of Vouros and Panidis (V&Pa)[83] contains LDA measurements for a pipe flow emitted air jet of $Re=5.5\cdot10^3$. A centerline velocity decay constant B=5.7 was estimated in symphony with the previous experiments, starting from a virtual origin $10d_e$, indicating a preserving core region larger than the rest experiments described above. The mean velocity attained self-similarity after $15d_e$, while the Reynolds normal and shear stresses did so after $40d_e$. The spreading rate though was found smaller, exhibiting a value of 0.078. It is worth noting that the pipe jet of X&A [80] also showed smaller spreading rates in comparison with jets emanating from contraction nozzles.

As a conclusion, it is deduced that the experimental investigations show that the mean flow properties and the turbulent quantities of an axisymmetric jet collapse into a self-similar profile in the established zone, at least for $z/d_e\geq70$, for $Re>\sim10^3$. Possible differentiations in the initial shape of the jet (contraction, pipe, sharp edged orifice) affect mainly the near-field region, leaving the spreading rate of the pipe jets as the only deviation from the norm. The values of the key flow parameters of the above studies are summarized in Table 2-2.

Table 2-2 Summary of turbulent round jet's properties

	W&F	HC&G	P&Lu	FA&We	X&A	Quinn	V&Pa
Distance from exit/d_e	10-70	20-120	30-160	20-140	0-75	18-55	2-60
Reynolds Number	10^5	10^5	10^4	$2\cdot10^3$	$8.6\cdot10^4$	$1.84\cdot10^5$	$5.5\cdot10^3$
Nozzle type	Contr.	Contr	Contr	-	Contr./Pipe	Contr./Sh.edg	Pipe
Measurement technique	SHW	FWH/LDA	FHW	PIV	FHW	SHW	LDA
Decay constant B	5.7	5.8	6.06	-	5.6/6.5	6.1/5.99	5.7
Virtual origin z_o/d_e	3	4	0	6.75	3.7/2.6	3.65/2.15	10
u' intensity peak value/U_{cl}	0.28	0.28	0.24	0.25	0.25/0.24	-	0.22
u'/v'	1.35	1.27	1.35	1.25	1.49	1.33	1.19
Spreading rate	0.086	0.094	0.096	0.097	0.095/0.086	0.096/0.098	0.078

2.2.6 Near to Intermediate Field-Zone of Flow Establishment (ZFE)

The analysis of the previous section has provided a thorough description of the flow in the region where a turbulent round jet attains an established state. This state is revealed by the self-similar behavior and asymptotic values of the flow properties and the basic statistical quantities. The treatment of this region as universally self-similar provided the means to obtain more simplified theoretical models that would enhance the solution for closure problems regarding the jet flow. This notion was supported by the theory of Hinze [84] accompanied by the extensive literature in the 70's to 90's, where the focus rested on the determination of the self-similar characteristics in the far- field region of the jet.

However, spread in the results among researchers regarding the above far-field asymptotic values in conjunction with practical engineering applications that are affected mainly by near field region sparked the interest on the influence of initial conditions on the jet's development. Starting with the theoretical analysis by George [85] numerous investigations since 90's have put into question the universality of self-similarity behavior ,i.e. the fact that a turbulent jet flow forgets its initial conditions as it develops further downstream.

Independently of the motivation of each study, several basic topics arise that help us to gain better insight in the development of a round jet flow, although the conclusions are not always straightforward and decisive. Nevertheless, useful background for the implementation of practical applications can be reached, when we seek answers to the following questions:

1) What is included in the term initial conditions?
2) Is there an appropriate Reynolds number value which characterizes the jet flow as turbulent?
3) Is there a distinctive limit based on certain flow characteristics between the near to intermediate field and the self-similar far field? How such a transition area can be described?
4) What is the influence of the exit conditions on the jet's basic properties such as the spreading rate, the U_{cl} decay rate and the final self-similar profile of the mean and turbulent quantities?

The review article of Abdel-Rahman [3] can be used as a first-step guide in the quest for more information regarding the above issues since it covers concisely and comprehensively the main factors affecting the flow as investigated by the available literature.

The term initial conditions of a jet include the exit Re number, the shape of the exit velocity profiles (both mean and turbulent), and the geometry of nozzle configuration. Moreover, the properties of the surrounding fluid domain where a jet issues; the existence of a co-flow or background turbulence for example, may influence the jet' growth.

Although observations and data from free shear flows led Dimotakis [8] to a deduction that " a fully turbulent flow to be sustained, a minimum Re of 10^4 is required", available literature and experience support the notion that "above Re=$2 \cdot 10^3$ the flow is considered turbulent" as cited by Xia and Lam [86]. The "legacy studies" of W&F, HC&G, P&Lu examining the asymptotic state in the far-field described in section 2.2.5.1 have assured a fully turbulent flow by keeping Re above 10^4. On the other hand, if values around Re=$2 \cdot 10^3$ are used, a more thorough examination of the transition from laminar to turbulent state and the effect of Re on the flow establishment is deemed necessary. Abdel-Rahman [3], assisted by the PIV images taken by Kwon and Seo [87], Figure 2-20, classifies the flow based on exit Re number as follow:

- Re≤30, the jet flow is laminar, and the jet is referred as the "dissipated laminar jet"
- Re≥500, there is a significant streamwise distance where the flow is laminar, and after which bursts into turbulence
- Re≥2000, the initial laminar-like region is shortened significantly after which a fully turbulent flow with constant spreading rate is attained.

Although there is a gap regarding the range between 30 and 500, the image for Re =177 suggests that there is a strong possibility for the flow to remain laminar in this range, especially in the ZFE depending on a particular flow configuration.

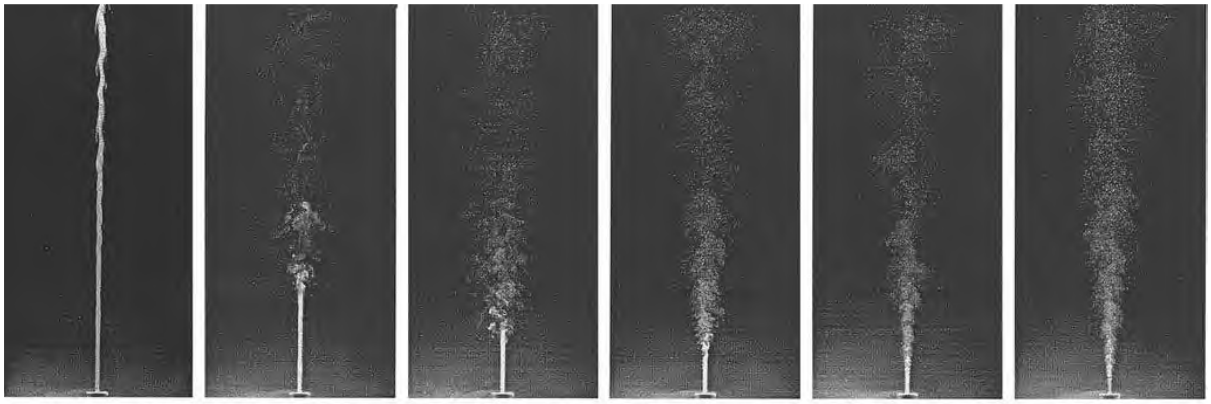

Figure 2-20: PIV images of an incompressible axisymmetric round jet for various Re numbers, Kwon and Seo [87]

Apart from the engagement with large Re numbers, most of the studies in the far-field have considered a jet exit flow emanating from a smooth contraction or otherwise contoured nozzle. This case corresponds to a condition where the mean exit velocity is characterized by a nearly uniform mean velocity or so called "top-hat" profile. Such a situation leads to the formation of a distinctive potential core with constant velocity for small distances in the vicinity of the nozzle, accompanied with

the pair up of the large vortical structures of the annual mixing layer further downstream, producing eventually the fully developed turbulent jet as described in sections 2.2.2 and 2.2.3. However, differentiation of the nozzle exit configurations is possible to alter the flow properties and subsequent jet growth. More contemporary studies investigate the characteristics of round jets issuing from long pipes or sharp-edged orifices, Figure 2-21.

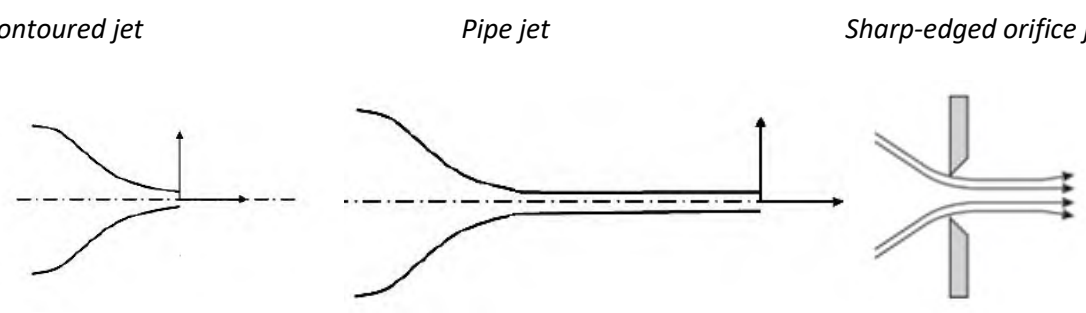

Figure 2-21: Nozzle exit configurations for the formation of a round axisymmetric jet

Each of the above geometrical configuration's results in a different shape concerning the radial or transverse profile of the mean and rms velocity at the nozzle exit plane. Such a profile is usually captured by measurements as near as possible to the exit plane, depending on the available experimental techniques of each study. Such profiles normalized by the U_{cl} are presented in Figure 2-22.

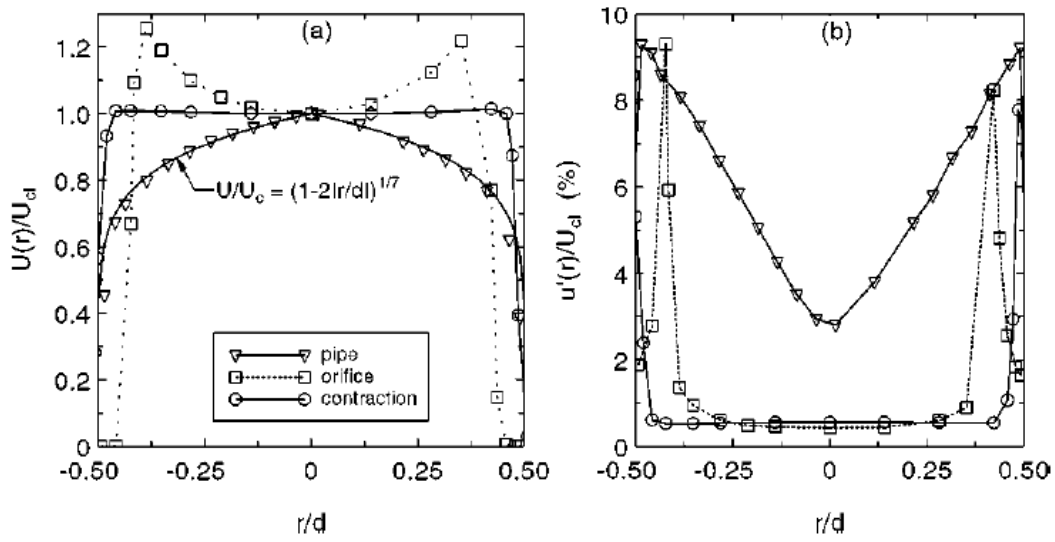

Figure 2-22: Normalized axial mean and rms velocity very close to the exit plane for contoured, a pipe, a sharp-edged orifice jet**,** Mi et al. [88]

The following observations can be made regarding the U_{mean} profile:

- Contoured jet: the exit flow follows a nearly uniform "top-hat" profile, with nearly zero value very close to the solid boundaries of the nozzle.
- Pipe jet: the exit flow carries the shape of a well-established pipe flow formed upstream of the exit, where the boundary layer is already turbulent. Such a flow is described by a power law given by:

$$U / U_{cl} = \left[(1 - 2(r / d_e)\right]^{(1/7)} \quad 1.67$$

- Sharp-edged orifice jet: There is a narrowing of the profile in comparison with the contoured case in conjunction with higher peaks than the unity value towards the edges of the jet. It should be noted also that the absolute U_{cl} value just after the exit is usually higher than in the exact position of the exit plane, as noted by Quinn [82]. These phenomena are attributed to the "vena contracta" effect that occurs in such a configuration.

The turbulence intensity as expressed by the normalized u_{rms} profile exposes similar characteristics between the contoured and the orifice jet. Increased values that are observed in the outer region of the thin shear layer collapse in the central portion of the jet. On the other hand, the pipe jet exhibits a more gradual decrease of turbulence intensity towards the center without the almost total collapse noted for the two former cases. This is a feature of the preceding fully developed turbulent pipe flow.

Before the examination of substantial features such as the velocity decay, the spreading and entrainment rate of a jet, it is fundamental to quantify the potential core region in the ZFE. In this effort, a transformation of equation 1.64 proposed by Fischer et al. [89] , emerges as a very usable tool:

$$\frac{U_e}{U_{cl}} = \frac{1}{B}\left(\frac{z - z_o}{d_e}\right) = \frac{z - z_o}{L_p - z_o} \quad 1.68$$

L_p is defined as the length of the potential core and the virtual origin z_o can take either positive or negative values according to the linear function fitted to the velocity decay. In the first case, the origin is virtually located downstream, whereas in the second one upstream of the exit plane. Subsequently, the length of the potential core can be calculated as:

$$L_p = B \cdot d_e + z_o \quad 1.69$$

Since the intermediate region between the potential core and the starting point of the self-similar region is considered as a transition phase, difficulties emerge in the exact identification of its boundaries. In addition, there is a variety between the exact locations of the initiation of the self-

similar behavior, depending on the flow property (it is found that the turbulent shear stresses become self-similar later than the mean flow). Furthermore, since the decay constant seems to obtain its value just after the potential core (when the flow starts to decay), to overcome possible uncertainties, the length of the potential core is often used to represent the ZFE. In many cases, the literature provides values of the virtual origin up to $5d_e$. As a result, it is not appropriate to neglect the term z_o in the equation 1.69.

Lam et al. [90] estimated the decay constant and length of the potential core of a jet of $Re=4000$, under the influence of ambient co-flow and counter-flow using PIV measurements. Under the presence of increasing co-flow, the decay constants B also increased, indicating a reduction in the decay rate as expected due to reduced shear between the jet and the ambient flow. At the same time, the length of the potential core remained almost invariant, except for the case of very strong co-flow, where a small reduction was noticed. On the other hand, the presence of counter-flow increased the decay rate of the jet, leaving however the length of the potential core nearly unaltered. The authors expanded their study to the investigation of the concentration field of rhodamine as an effluent, using Laser Induce Fluorescence. For the case of a scalar field, equation 1.68 can be transformed as:

$$\frac{C_e}{C_{cl}} = \frac{1}{B_C}\left(\frac{z-z_o}{d_e}\right) = \frac{z-z_o}{L_p - z_o} \qquad 1.70$$

The results showed that the presence of co-flow did not bring a noteworthy change in the decay rate of the concentration field, whereas a counter-flow presence imposed a faster decay rate. In both cases, the potential core of nearly steady concentration was shortened in a rather small degree under both cases of external flow.

The entrainment rate of the surrounding fluid is another representative property of the flow growth of the jet flow and its mixing efficiency. This rate can be estimated indirectly, if the spatial rate of change or the mass flow rate $\dot{m} = dm/dt$ is calculated in the axial direction. Ricou end Spalding (1961) [91] proposed that for a fully developed jet, starting from $z/d_e=15$, the entrainment rate attains a constant value governed by the equation:

$$\frac{d_e}{\dot{m}_e}\left(\frac{\rho_J}{\rho_S}\right)^{1/2}\frac{d\dot{m}}{dz} = C_m \qquad 1.71$$

The proposed value for C_m by the above authors is 0.32 and the properties $\dot{m}_e$, ρ_J, ρ_s, correspond to the initial mass flow rate at the jet exit, the density of the jet fluid and the density of the surrounding fluid. However, the several viewpoints about the behavior of the entrainment rate in the ZFE had been

controversial. Hill [92] demonstrated experimentally for a jet of $Re \geq 6 \cdot 10^4$, the entrainment rate increased non-linearly in an initial region until $z/d_e=13$, where the value close to 0.32 was obtained.

On the other hand, Boguslawski and Popiel [93] found a constant value 0.183 in the initial region of the jet up to $z/d_e=12$. It is noteworthy that the latter authors calculated indirectly the entrainment rate as mentioned before by integrating the velocity field in each axial distance.

$$\dot{m} = 2\pi \int_0^{\infty} \rho \bar{u} r dr \qquad 1.72$$

and used a pipe jet, while the Hill [92]measured the entrainment rate using a direct method and a short nozzle. Among the rest results of the study of Boguslawski and Popiel [93], we may include the fact that the largest levels of tke based on the shear stresses occurred at an axial distance of $6d_e$, while in the radial direction at $r/(d_e/2)=0.7,0.8$. These are the regions with the higher velocity gradients due to the mixing layer presence.

In an effort to draw some conclusions about the mixing process and heat convection in more practical configurations Obot et al. [94] studied the velocity field in the ZFE for two squared exit nozzle jets, with different L_t/d_e ratio 1 and 12, where L_t the tube length. The Re numbers employed were $13 \cdot 10^3$ and $12 \cdot 10^3$. The exit velocity profile of the ratio 1 jet approximated the contoured jet, while the ratio 12 the pipe jet. The U_{cl} velocity functions with axial distance exposed a faster decay (C=5.26) for the ratio 1 jet in comparison with the ratio 12 jet (C=5.88). Moreover, a decay constant value was established at $z/d_e=4$ for the former jet, while $z/d_e=8$ for the latter one. This was an indication of a smaller potential core for ratio 1 jet and a subsequent faster spreading process which was also verified by the larger $r_{1/2}$ spreading constant (0.088 vs 0.078). Furthermore, the investigators found that for the ratio L_p/d_e =1, the jet attained a constant entrainment rate from a very early-stage $z/d_e=1$, while the L_p/d_e =12 reached such a value much later at $z/d_e=10$. At closer distances, the latter jet exhibited smaller values of entrainment.

Mi et al [88] evaluated the mixing behavior of three different jet types (contoured, sharp-edged orifice, long pipes) based on the evolution scalar property of temperature. The jets were initially heated (T_o) and the centerline temperature T_{cl} and the temperature fluctuations θ' were measured as the jets evolved downstream. The normalized axial distribution of T_{cl} followed a similar linear decay law with velocity and concentration fields (equations 1.64, 1.70). Based on such distributions the decay rates B followed the descending order sharp-edged orifice<contoured<long pipe. Moreover, the linear spreading rates A for $r_{1/2}$ based on the radial positions, where $T=T_{cl}/2$ exposed an ascending order sharp-edged orifice>contoured>long pipe. Based on the two above observations the faster mixing and spreading occurs for the orifice jet, while the slower for the pipe jet. A root-cause for this trend can

be traced in the flow structures in the shear layer after the nozzle exit. The turbulence spectrum provides the means to identify such structures, since it reveals distinctive peaks in the energy which correspond to the certain coherent structures and frequencies dominating the shear layer for the case of contoured and orifice jets. On the other hand, the pipe jet collapses in a uniform fashion in the whole range of frequencies, indicating a fully developed turbulent flow from the beginning.

A preliminary reference to the study of Xu and Antonia [80] was made in section 2.2.5.1, where the differences between a contoured jet and a pipe jet in the ZEF were identified. The contoured jet exhibited sooner establishment of a self-similar behavior accompanied by larger decay and spreading rates. Similarly to Mi et al. [88] , the authors searched out for an explanation for the different behavior among the two jets at the near field structures. Instead of the longitudinal velocity spectra of u', used by Mi et al., the current authors used the transverse v' spectra at the locations of maximum shear. Both spectra presented peaks, but at different frequency levels. The pipe jet peaked at lower frequencies, meaning larger wavelengths. This fact implies that the vortex structures emerging in this jet type pair up further downstream, delaying the development and spreading of the jet flow. The spatial autocorrelation coefficients enabled the authors to compare the longitudinal l_u and transverse l_v length scales of the two flows in the ZFE. The pipe jet is characterized by larger l_u and smaller l_v, meaning larger displacement of the fluid large scales further downstream and smaller inward fluid movement and thus entrainment.

As mentioned before and depicted in Figure 2-22, the discrepancies in the mean velocity and turbulence intensity exit profile between an orifice jet and a contoured jet are not as pronounced as in the above case between a contoured and a pipe jet. The higher by only a small fraction decay and spreading rates found by Quinn [82] agree with the expectation of higher mixing of an orifice jet due to higher initial turbulent intensity and shear in the mixing layer. This notion is also corroborated by the shorter potential core that the authors found for the orifice jet. From time autocorrelation coefficients and energy spectra on the centerline, an isolation of a certain frequency with dominant energy peaks was possible for both cases, indicating the presence of large coherent structures in axial distances before the end of the potential core. Still, it is noteworthy that higher energy peaks of the orifice jet were present, strengthening the conclusion of more increased mixing efficiency in this case. This behavior ceased to exist at distances larger than $10d_e$, exposing a broadband signal which is characteristic of a fully turbulent flow for both jets.

Xia and Lam [86] added some more measurements of velocity and concentration in the literature, concerning the near to intermediate field of an axisymmetric jet flow, taking also into account the presence of a co-flow. The Re used was in a range [1000, 5000], to assess the behavior of a jet as a transition from laminar to turbulent conditions occurs. 2D LDA velocity measurements were taken in

conjunction with LIF for the assessment of the concentration field for a jet emanating from a contoured nozzle that produced a top hat exit velocity. The first noteworthy observation was that as the jet flow changed from laminar to turbulent, the length of the potential core was shortened, in agreement with Kwon and Seo [87]. However, the U_{cl} decayed more rapidly in the opposite trend (turbulent to laminar), in contradiction to Kwon and Seo. The observations came from both the velocity and concentration fields. At the same time, an intriguing fact emerged when the co-flow was imposed; the length of the potential core was shortened, which is opposite with the expectation of a longer potential core due to reduced shear between the jet and ambient flow. A solid justification of the phenomenon was not possible to be given. Generally, the presence of co-flow did not affect the establishment of self-similar profiles of flow quantities in the ZEF. However, it seemed to increase the turbulence intensity in the ZEF for the laminar and transitional Re, whereas this happened for the turbulent case in the ZFE. Regarding the concentration statistics, the presence of co-flow exposed an increase in the fluctuations level mostly for the laminar case and less for the turbulent jet.

In the effort to gather the main findings in the literature concerning near to intermediate field region of an axisymmetric turbulent jet, it was made clear that safe conclusions can be made only for a few aspects of the flow. The flow establishment is complex and gradual, and the isolation of the effects imposed by the various combinations of initial conditions from the experimental uncertainties do not permit the production of strict laws.

First, an exact Re number for the characterization of a jet as truly turbulent has not been established yet. It depends on the rest of the initial conditions and the transition to turbulence shall be validated in each experimental survey. However, to minimize such a labor, a general approach classifying the jets as turbulent at Re>2000 can be used. Apart from shortening the potential core, the variation or Re do not bring a unanimous influence on the decay, spreading and mixing rates and subsequent characteristics in the far-field.

Although the length of the potential core is considered to reach about (5-6)d_e, the results from the several studies exposed a wider range from (2-10)d_e. Some researchers use this length as synonym to the ZFE, without the inclusion of the intermediate field until the self-similar region. This is explained by the fact that the onset self-similar characteristics among the several flow statistics do not coincide. Furthermore, constants such as the decay and spreading rate obtain their established value early on, just after the potential core. Thus, the determination of the overall near to intermediate field is not a straightforward process.

The only safe conclusion is possible for the effect of the nozzle geometry on the jet growth as exported from measurements based both on velocity and scalar properties. A jet decays and spreads and entrains surrounding fluid more rapidly in the order: sharp-edged orifice, contraction, pipe jet.

This is attributed to the well-defined large coherent vortical structures produced by high shear in the mixing layer around the potential core in the first two cases. This process referred as engulfment leads to increasing mixing rates. In the case of the pipe jet, the turbulent boundary layer that emanates from the exit is thicker with a broadband signal, attenuating or allocating engulfment further downstream. This results to an elongation of the potential core of pipe jets.

As a general remark, the studies of an axisymmetric round jet in the ZEF and its consequences on the ZFE provides controversial results in many aspects, especially for the lower Re numbers. Nevertheless, these systematic studies provide the guidelines and shed light on the basic parameters that shall be included in investigations related to the near field of round jets.

2.3 Jets in background turbulence

The preceding extensive literature review has already revealed that jet flows are considered among the most substantial flows both in nature and engineering applications. As a result, a large quantity of data exists describing the jet behavior from its birth near the exit until several distances downstream. It has already been stated that in the far-field region, a round axisymmetric jet attains a self-similar behavior. At the same time, it would not be totally misleading to consider such a self-similar behavior independent of the initial conditions near the jet and especially the Reynolds number, mainly when the latter is considered large enough. The effects of the exit conditions have been analytically discussed in section 2.2.6 and it was deduced that they impose significant variations in the near to intermediate field.

Apart from the effects of the initial conditions, it has already been seen in section 2.2.6 that the nature of the ambient surrounding fluid is of relevant importance for many authors and studies on the impact of co-flow or counterflow has already been presented. Another key factor in the real world is the presence of turbulence in the surrounding environment and its interaction with the jet original characteristics.

Khorsandi et al. [95] considered such conditions of significant importance for the dilution and subsequent mixing process of a jet stream with the surrounding fluid and attempted a realization of such a model experimental facility. As a first step to form a baseline study, it was considered fundamental to isolate the background turbulence intensity from the mean flow, such as conditions of mean co-flow, counterflow or cross flow do not exist. The aim was to produce a homogeneous and isotropic turbulent (HIT) environment of zero mean flow with constant characteristics imposed on the whole evolution range of an emanating jet flow. In order for such a background turbulence to be implemented, a Random Jet Array (RJA) was used. The benefit of such a configuration is that although both a decaying mean flow and tke exist along the stream direction from the RJA's exits, several distances downstream the inhomogeneity is significantly attenuated. Moreover, in such a location and in a plane perpendicular to the streamwise direction of the RJA, the flow is expected to be fully HIT having negligible mean flow. Thus, such a plane was considered suitable for measurements concerning the evolution of a separate jet flow. For this reason, an axisymmetric round jet was released in a direction perpendicular to the direction of the RJA mean flow, Figure 2-23.

Such a configuration overcame the limitations of the experimental facility used by Guo et al. [96],[97], where the jet was released in a direction parallel and opposite to the direction of decaying grid

turbulence. In these experiments the breakup location of the jet was identified using flow visualization and PIV as the point where a sharp axial velocity decrease and a sharp radial velocity and jet spreading angle increase were observed. In such a breakup location, the background ambient rms velocity was found to be related to the round jet velocities as $0.44u_{rms}$ or $0.125U_{cl}$. The first drawback of these experiments rest on the fact that in the breakup location, there is increased ambient turbulence intensity due to its proximity with the grid and thus the influence of background turbulence in the overall jet structure is inhomogeneous. Secondly, the grid proximity can bias the results concerning the spreading and entrainment rates due to mass accumulation in that region.

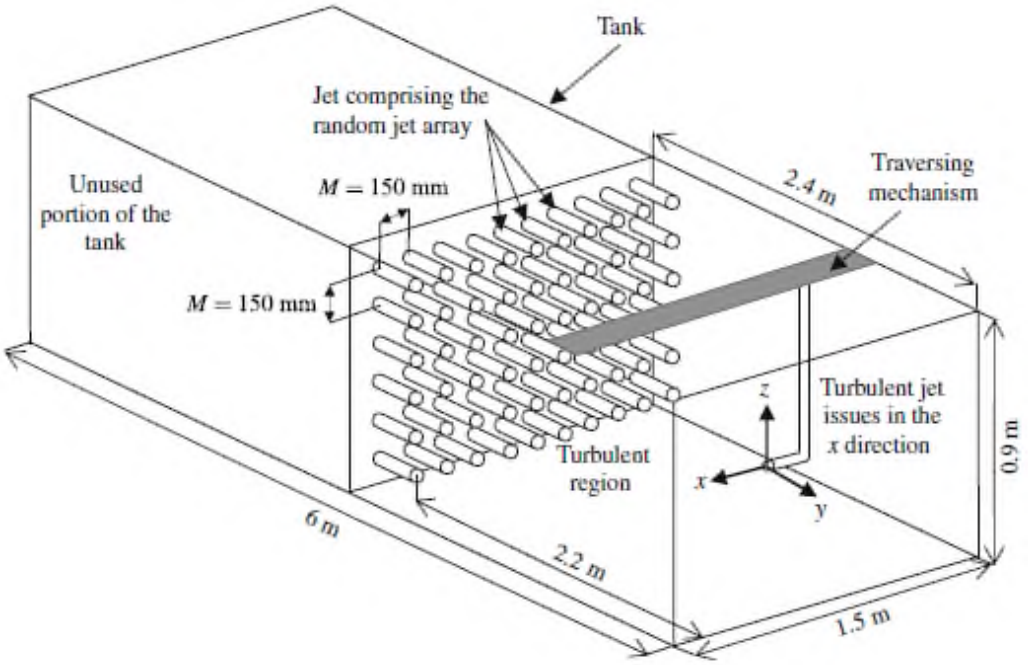

Figure 2-23: Axisymmetric round jet issuing in HIT background turbulence formed by RJA, Khorsandi et al. [95]

Going back to the study of Khorsandi et. al., the investigation included the study on the effects of two different levels of tke ($4.44\cdot10^{-4}m^2/s^2$, $9.33\cdot10^{-4}m^2/s^2$) on three different jet Reynolds numbers (5300, 5800, 10600). Firstly, the behavior of a turbulent round jet in a quiescent environment and the HIT plane were validated based on the available measurement techniques of Acoustic Doppler Velocimetry (ADV) and Flying Hot Wire Velocimetry (FHWV), where appropriate. Subsequently, the study of the jet in the turbulent background revealed the following elements, concerning the impact of surrounding turbulence:

- The jet centerline axial velocity U_{cl} decays faster and a power law instead of a linear law decay fits better the measured data.
- The Gaussian profile of the jet is being distorted with downstream distance.

- The radial profile of the radial velocity V gets wider, and this velocity component is found increased and occasionally positive towards the edges the jet, signifying a decrease in fluid entrainment.
- The jet half width growth is increased following a power law instead of a linear.
- The entrainment rate remains linear but is reduced to values 0.19 and 0.16 depending on background turbulence levels, instead of 0.34 for the jet in quiescent surroundings. This is in contradiction to the theoretical hypothesis of Wright [98] that there will be an additive term to the mixing rate due to ambient turbulence. However, this latter prediction was made by the author for a special case of a co-flow and was not generalized for other cases such as cross-flow, counter-flow or zero mean ambient flow.
- There is an overall increase in the measured u_{rms} of the jet and especially near the nozzle exit. However, lower background turbulence results in higher u_{rms} in the far-field.
- The far field self-similarity of the jet is being distorted.
- The breakup locations of the jet, where U_{cl} ceases to exist is a decreasing function of the ratio Re_{RJA}/Re_{jet}.
- For large axial distances, a deep penetration of the external turbulence towards the core of the jet takes place. Moreover, the mechanism of nibbling that describes better the entrainment in the ZEF of a jet seems to be substituted by turbulent diffusion that best describes flows characterized as shear-less mixing layers.

The above increase in centerline decay and jet half-width accompanied by reduced entrainment were also reported for a passive scalar field in a sequel article Sahebjam et. al. [99] for the above experimental facility. It was also shown that in the regions where the ratio of ambient turbulence intensity to jet intensity reached a value of 0.5 and above, the jet's structure and self-similar characteristics were distorted.

The above findings have shown that a simplified approach of superposition of jet-driven entrainment and ambient turbulent diffusion possibly is not valid. On the other hand, convergent reports verify that the existence of ambient turbulence causes an increase in the axial decay and radial spreading of the jet. Nevertheless, the information extracted from the existing literature remains limited and leaves plenty of space for potential studies on the behavior of a jet flow in background turbulence.

2.4 Opposed jets

Turbulent opposed jets configurations are met in several engineering fields, particularly in chemical engineering and combustion technologies. However, this type of flow configuration is found to be relatively restricted to specialized applications both in industry and in engineering research. This fact in conjunction with the complexity of the flow field which in most cases includes two phases, fluid-particle, has led to slow advances in the related technologies. An extensive literature review on chemical engineering impinging jets applications is provided by Tamir and Kitron [100]. Systematic research on the topic has been carried out since the 90's, but the majority of the publications date from 00's until the present day.

Commonly, such an arrangement consists of a combination of two jets that produce flows with opposite directions to each other. In some cases, however, the two opposed flows can emanate from opposed arrays of jets, instead of single opposed jets. Subsequently, the fluid jets, planar or round that are formed, interact producing an impinging zone, also referred as the stagnation plane. In this particular area of the flow, the chemical reaction or mixing process takes place and its efficiency and turbulence characteristics are under investigation.

In the region around the stagnation plane, a sharp axial velocity gradient develops leading to the minimization of the velocity at the stagnation point. At the same time a resulting pressure gradient elevates the static pressure of the flow. While the axial jet flow is minimized, the mass conservation principle imposes the channeling of the flow into the radial direction, creating two free radial jets. The evolution of the phenomenon as described above is presented in Figure 2-24. In Figure 2-25 the sharp linear velocity decay and the pressure elevation at the stagnation plane are noted by the appropriate graphs.

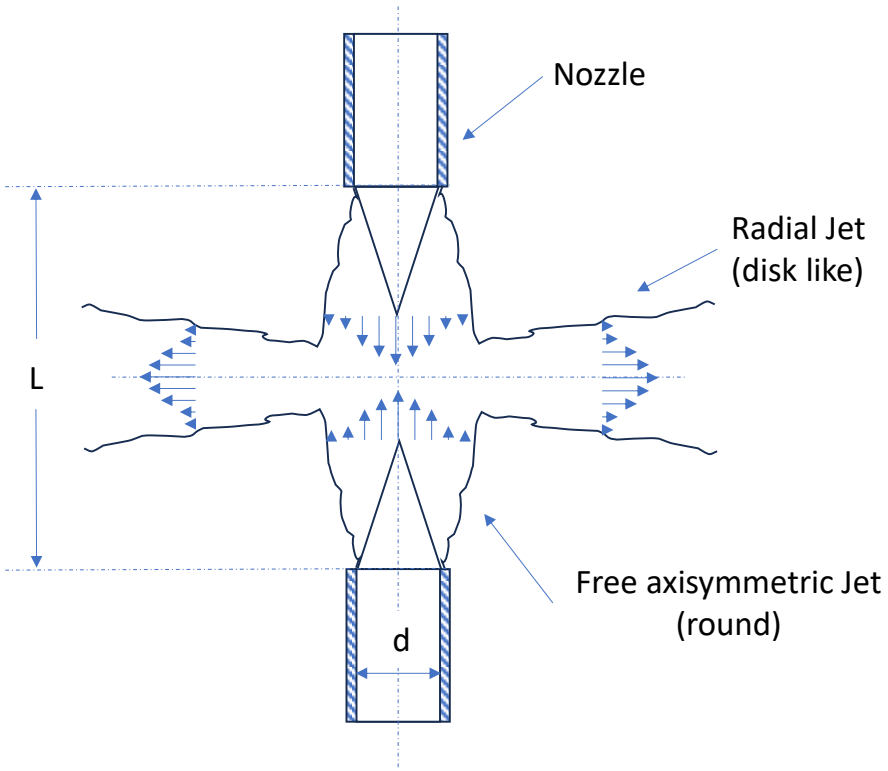

Figure 2-24 The flow evolution in an opposed streams configuration and the formation of radial jets

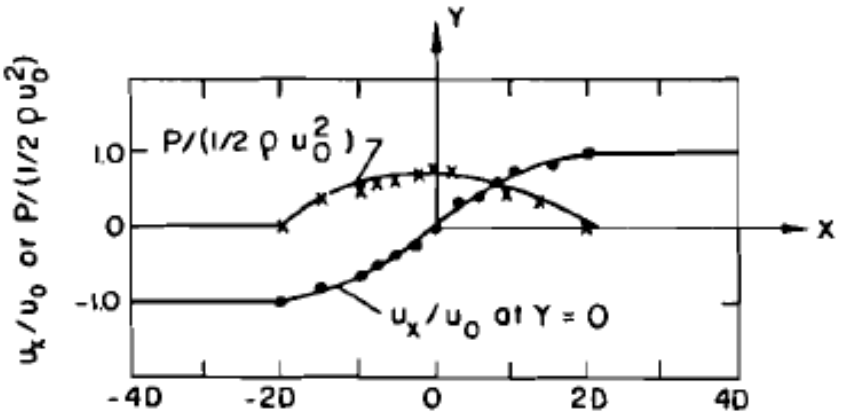

Figure 2-25 The variation of axial velocity and pressure along the jets axis normalized by the exit velocity Tamir and Kitron [100]

The main industrial applications of opposed jets configurations can be categorized as follows:

1) Closely spaced Turbulent Opposed Jets (CSTOJs): the configuration includes a combustion method, where a fuel jet impinges on a counterflowing oxidizer stream or two premixed oxidizer-fuel streams.
2) Opposed Multiple Burners (OMB): mainly used in pulverized coal furnaces and gasifiers.

3) Confined Impinging Jets Reactors (CIJR): these micro-mixer devices carry out processes to produce particles of the desired size and morphology in the pharmacology and biology domains.
4) Reaction Injection Molding (RIM): a manufacturing technology to produce plastic parts, where two or more liquids are combined in a high-pressure impingement zone, where the polymerization and the formation of molded parts occurs.

Although the aforementioned engineering fields are mainly preoccupied with CSTOJs flows, the first paper in literature comes from the natural sciences and more specifically form the Former USSR academia. Denshchikov and Kondrat'ev [101] described the natural phenomenon of local hurricanes (boras) as an interaction between two opposing air currents. For their investigation, they carried out an experiment, which included a two-dimensional opposed flow of two submerged water jets. The jets were also colored with ink, to satisfy the purposes of flow visualization, and were characterized by a Re of 10^3, based on jet exit velocity U_e and diameter d_e. By taking photographs of the visualized flow, the authors observed that the stagnation plane position and shape exposed an oscillatory behavior. They also determined the oscillation period T, in terms of the distance between the jet exit nozzles L and the value u of the single jet velocity at the position L/2. They concluded that the oscillations are determined by the system itself, based on the above parameters, neglecting the external perturbations that had no influence on the phenomenon. Finally, they attained the formula $T=6L/u$ for the oscillation period.

Stan and Johnson [102] paper is considered a distinguished study on the hydrodynamics of opposed jets. This view leans on the fact that their investigation is not driven from a particular set of applications but aims in the investigation of a simpler flow configuration where mass transfer and chemical reaction mechanisms are absent. Such additional effects make the comprehension of the flow properties more complex from a fluid dynamics standpoint. Furthermore, the experiments are carried out in an arrangement of opposed jets that is placed in a large tank, such as an unconfined case is simulated, avoiding wall effects, perturbations, and recirculation zones. The high Re of $11 \cdot 10^3$ and an ultimate large L/d_e ratio=20 make this study even more interesting, since it deviates from the common closed spaced opposed jets applications and also provides analysis for the formation and behavior of radial jets at the stagnation region.

The verification of the free radial jet concept was one of the basic purposes of the study. The flow visualization revealed the formation of two symmetrical streams with opposite directions perpendicular to the main axis in the collision region of the primary axial jets. Each stream spread out radially creating a three-dimensional free radial jet. LDA and PIV measurements along with k-ε CFD simulations exposed the Gaussian shape of the velocities verifying the existence of the free radial jet.

While the mean flow was symmetrical and the stagnation plane coincided with the L/2 distance from the nozzles exit based on LDA, PIV and CFD, the instantaneous PIV and flow visualization images elucidated the unsteadiness of that region and low frequency oscillations [1-20 Hz]. Nevertheless, the LDA measurements did not reveal any dominant frequency, implying a chaotic nature of the flow. This is also observed in the RIM mixers for Re number beyond a critical transitional value as will be described later in section 2.4.4.. The axial jets presented mean velocity self-similar behavior for $z/d_e=8$, before reaching the impingement region. This normalized axial distance was smaller in comparison to the value ≈30 (Wygnanski & Fiedler) [1], that was reported in 2.2.5. However, the turbulence quantities were unable to reach self-similarity for these axial distances. In respect to the radial jet, although the CFD predictions estimated self-similarity for $r/d_e>2$, this was not verified totally by the experimental data. Moreover, the normalized turbulent intensity in the radial direction reached a level of 60%, two times the turbulence intensity levels for a free turbulent round jet. This fact highlights the elevated turbulence values resulting in the stagnation region between two opposed jets.

Pawlowski et al. [103] focused on the stability of the stagnation plane of two opposed jets either planar of axisymmetric. By numerical methods, the different oscillatory regimes of the stagnation plane were identified in terms of the variation of Reynolds number and separation ratio L/d_e. The construction of two parameter maps presenting the transition among the different modes along with the application of these diagrams in the wide range of opposed jets configurations was the ultimate aim of the report. The four basic flow modes that occur in the stagnation plane of the jets are:

a) Steady symmetric state without movement of the stagnation plane.
b) Pitchfork bifurcation: This mode is further divided into three states. The first two are described as the stagnation plane offset; the mean axial velocity is zero in locations symmetrically in either side of the half-way distance. In the third state, the mean position of the stagnation plane is located half-way as in mode a) but oscillates periodically between symmetrical positions.
c) Hopf bifurcation: this is an unstable state, where each jet is deflected in the opposite direction, switching directions periodically causing the flapping of the stagnation plane, Figure 2-26. This flow state corresponds to the periodic motion that Denshchikov and Kondrat'ev [101] identified, Figure 2-27.
d) Hopf bifurcation (vortex shedding): in higher Re number the periodic oscillations become more chaotic and irregular and are described as the vortex shedding regime.

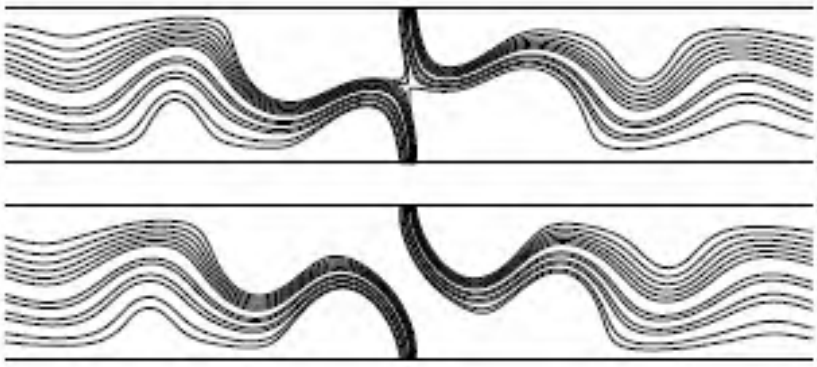

Figure 2-26 Hopf bifurcation representation by Pawlowski et al. [103]

Figure 2-27 Hopf bifurcation, deflecting jets and flapping Denshchikov and Kondrat'ev [101]

Before commenting on the two parameter maps of Figure 2-28 and Figure 2-29, in order to avoid confusion, we should clarify that the aspect ratio in these diagrams represents the inverse of L/d_e ratio, namely d_e/L. For the case of planar jets (Figure 2-28), it was noticed that as the separation L/d_e increased, the transition from the symmetrical steady state to the other modes occurred for lower Re numbers. For the larger L/d_e ratios the Hopf bifurcation occurred, while for lower the pitchfork bifurcation dominated. However, as the Re was further increased, the vortex shedding chaotic Hopf bifurcation was the primary mode irrespectively of L/d_e.

On the other hand, for the axisymmetric jets case in Figure 2-29, only a transition from the steady symmetric state to the pitchfork bifurcation mode was observed. For $L/d_e>2$, this happened for $Re>60$, while for smaller separations, larger Reynolds were needed in order for the transition to take place.

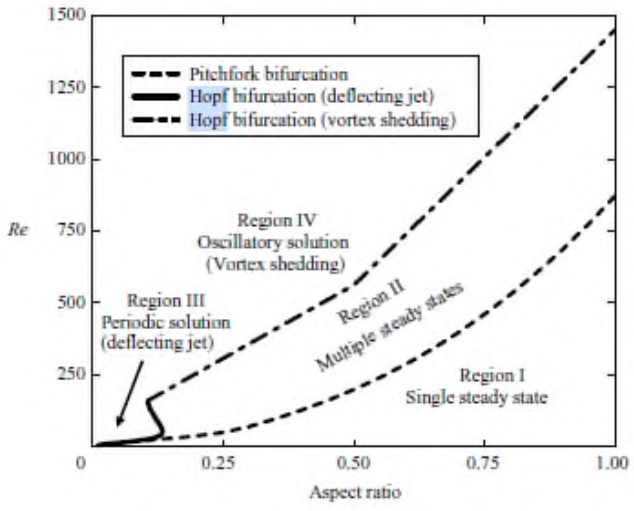

Figure 2-28 Two parameter map representing the transition between the four flow regimes occurring in planar jets, Pawlowski et al. [103]

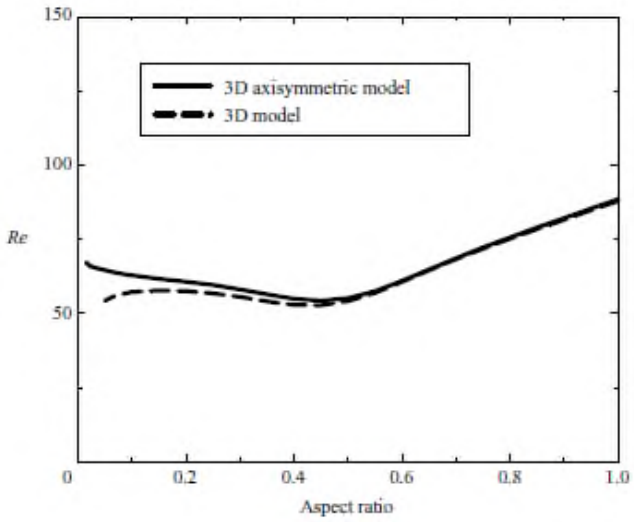

Figure 2-29 Two parameter map representing the transition between the two flow regimes occurring in axisymmetric jets, Pawlowski et al. [103]

2.4.1 Closely spaced turbulent opposed jets (CSTOJs)

The research of closely separated opposed jets, where the separation to nozzle diameter ratio L/d_e is in the order of unity, have gained particular attention due to its application in turbulent combustion Figure 2-30 . The flapping of the stagnation plane for large separations and high velocities constitutes a limiting factor in studies which focus on quantifying the phenomenon of the extinction of flame. The establishment of a robust and analytical background for this scientific area demands firstly the deployment of models that emphasize the comprehension of the fundamental fluid mechanical

properties of such configurations. Since the flame occurs right upstream of the stagnation region of the counterflow, its development and sustainment are directly associated with the flow properties at that region. Thus, normally before proceeding to the investigation of the combustion phenomena, investigators dedicate a substantial portion of their studies in the description of similar non-reactant cases.

In such a stagnating case, a compressive straining occurs in the axial direction, while the flow is extended radially in order the mass conservation to be satisfied. As a result, in the subsequent combustion phenomena, the flame is stretched radially, and the flame front propagates in that direction. Consequently, the strain rate emerges as one of the primary properties that determine the shape and behavior of the flame. The bulk strain rate, S_b, as defined in equation 1.73 represents the extensional straining of a fluid element and constitutes a premier property that is identified and examined.

$$S_b = \frac{\partial U}{\partial z} = -2 \cdot \frac{\partial V}{\partial r} =, \; u = 0 \qquad 1.73$$

The bulk strain rate calculated at the axial distance of the stagnation plane where the mean axial velocity U is zero and coincides usually with the point of origin in the relevant studies. Theoretical predictions for the S_b have been made, dealing with the stagnating flow as potential flow. The model of Champion and Libby proposes:

$$S_b = \frac{2U_e}{L} \qquad 1.74$$

, where U_e is the jet exit velocity and L the separation distance between the nozzles exit plane. Thus, the bulk strain rate can be increased theoretically by increasing the jet exit velocity or reducing the axial distance.

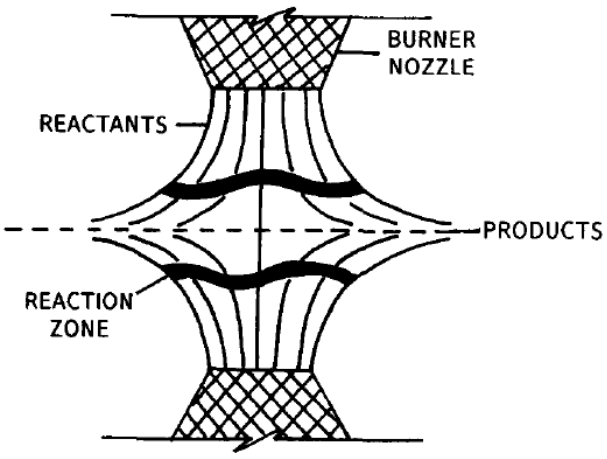

Figure 2-30 Combustion flowfield in a closely spaced opposed jet configuration Kostiuk et al. [104]

Although we emphasize on turbulent opposed jets, we will start the review of this entity by referring to the study of Rolon et al. [105] which investigated by LDA measurements the flow developed by two laminar jets with L/d_e in the range [0.6, 1.4]. A linear slope of the velocity gradients was observed concerning the axial evolution of U and radial evolution of V around the region of the stagnation plane, yielding strain rate values that deviated from the theoretical estimation of equation 1.74. However, this deviation was mitigated for L/d_e =1.4, leading to the assumption that the theoretical model would perform better for larger L/d_e values. Another notable observation from this study concerns the stagnation plane offset from the middle plane. Whereas the two jets exit momentum was kept equal, the stagnation plane axial position was in a certain steady axial distance in either side of the middle plane (pitchfork bifurcation). These observed locations were symmetrical about the middle plane.

Kostiuk et al. [106] conducted 2D LDA measurements focusing on a geometry with L/d_e =2. In contrast with Rolon et al. [105], the flow was characterized as turbulent due to the higher exit velocities employed and the introduction of turbulence in the jets by the placement of perforated plates upstream of the nozzles exit. An offset of the stagnation plane from the geometrical middle was observed due to the difficulties in regulating exactly equal flow rates in the two jets. Once again the linear axial and radial velocity gradients were identified and this time the theoretical prediction of equation 1.74 approximated the bulk strain rate sufficiently well. Both the axial and radial rms velocities exhibited a peak in an axial distance, which coincided with the stagnation point location, exposing a degree of correlation between the turbulence kinetic energy and the increase in strain rate. However, the Reynolds shear stresses $\overline{u'v'}$ were negligible in the jet's axis. Although this was considered valid for an axisymmetric flow, it signified that they did not constitute the basic mechanism to produce turbulent kinetic energy. The spectral analysis in the stagnation plane revealed that the energy contained by the larger scales was amplified and the smaller scales energy content was attenuated. This observation highlighted the vortex stretching due to high velocity gradients as a possible mechanism for the increase in turbulent kinetic energy. A bimodal pdf found in the stagnation region also implied that axial velocity oscillations also contributed to the above increase of turbulent intensity. While the previous study was carried out in a non-reacting flow, in a sequence study, Kostiuk et al. [104] marked the onset of extinction of the flame with larger stretch rates in a premixed oxidizer-fuel experiment. However, the heat release had little effect on the flow dynamics.

Korusoy and Whitelaw [4] examined a premixed methane-air turbulent opposed jet flow configuration (L/d_e =[0.2,3], Re=[1300,10.300]) using hot-wire probes and LDA measurements. HWA was used for the measurements near the nozzle exit plane, while LDA was employed for measurements in the stagnation region. The radial profile of the axial velocity at the exit plane revealed a region of reduced

magnitude near the jet's axis and peaks at a distance of $0.5d_e$. This occurred for L/d_e ratios <1 and was in agreement with the observations of Rolon et al [105] . At the same time for L/d_e >1, a more uniform distribution was attained in agreement with the observations of Kostiuk et al. [73], for larger L/d_e. However, the most significant remark of this work was the radial variation of the strain rate at the stagnation plane, which affects the stretch rate of the flame and its possible extinction. For small L/d_e ratios <0.8, the total strain rate which was defined as the sum of the radial and the axial strain rate, increased for a radial distance from $0.3d_e$ to $0.5d_e$, while for larger L/d_e separations, a uniform contribution was exhibited. These peaks in the strain rate were correlated with the peaks mentioned before for the mean velocity near the exit planes.

Movement of the stagnation plane for L/d_e >1 observed by the above authors led Lindstedt et al. [107] to carry out PIV measurements for L/d_e <1 and Re=5000 and Re=13.700. Once again flow imbalances caused asymmetries in the location of the stagnation plane, which were more pronounced for smaller L/d_e. Both the axial and radial normalized velocities near the exit plane reached its peaks for all cases at a distance about one jet radius from the jet axis. The same trend was followed for the radial velocity at the stagnation plane. The normal Reynolds stresses presented, peaked at the stagnation point along the jets axis and the comparison between radial and axial stresses revealed an increase in anisotropy at this area. The peak value observed for the axial component was 0.03 while for the radial 0.0075. For larger L/d_e >0.4, a constant radial velocity gradient was observed, whereas for L/d_e=0.4, an increase beyond $0.5r_e$ led to peaks in the radial velocity closer to the jet axis. These peaks for radial velocity corresponded to the maximum values for the Re stresses in the radial direction in the stagnation plane. The same nonuniformity was also remarked by the LDA measurements of Korusoy and Whitelaw [4] for smaller nozzles separations. The numerical simulations showed that the standard k-ε model agreed well enough with the PIV measurements concerning the mean strain rates, whereas overpredicted the turbulent kinetic energy at the stagnation plane by a factor of 5. This fact indicates that the k-ε model performs well in respect to the mean flow simulation but exhibits weakness in the calculation of turbulent properties in an anisotropic flow. On the other hand, the deviations of the RSM model were less than a factor of 2.

Overall, the studies on CSTOJs lead to the following basic conclusions:

a) The difficulties in the precise regulation of equal momentums of the two opposed jets result in a stagnation point offset from the middle plane.
b) The turbulence intensity peaks at the stagnation plane because of vortex shedding.
c) A constant linear velocity gradient characterizes the impingement region, which presents increased values and non-uniformities for small L/d_e ratios. These effects can cause extinction and instabilities of the flame in a combustor of such configurations.

d) Larger L/d_e can cause flapping and deflecting oscillations of the stagnation plane and are avoided for CTOJs combustion studies.
e) The turbulent properties for such an impingement flow exhibit anisotropy and a more suitable CFD model such as the RSM can deal better in simulating the flow field.

2.4.2 Coal combustion and gasification

The abundance and the stable price of coal around the world has established it among the primary natural sources for energy generation and carbon-based chemical products. Nevertheless, coal combustion industrial facilities are heavily related with the environmental pollution through CO_2, NO_x, ash emissions and the slag waste; created due to the melting of the carbon solid particles in elevated combustion temperatures. Therefore, the industry is compelled to develop and incorporate technologies that reduce or even eliminate this negative pollution imprint to comply with the clean energy social needs alongside with the governmental legislative requirements.

As a result, extensive research has been made in this direction by countries heavily related to coal combustion facilities during the last three decades. These efforts include the study, development and incorporation of devices that reduce the NO_x and carbon coke emissions by the achievement of more efficient combustion rates and more stable combustion processes. Moreover, the evolution of coal gasification technologies facilitates the fulfilment of clean processes targets. In contrast with the mere coal combustion, which is used to generate heat and subsequently electricity through the kinetic energy in a water steam turbine, coal gasification aims in the conversion of the combustible solids into combustible gases. The employment of coal gasification has a double prospect. Firstly, combustible gases have much larger burn rates, and a two-stage turbine can be used. One stage exploits directly the combustion gases and a second one functions by the produced steam. The second aspect of the advantages of coal gasification is that the mixture of the combustible gases, commonly referred as syngas (an intermediate to synthetic natural gas) contains CO and H_2 and CH_4. This composition makes syngas eligible for a variety of further uses, such as converting it to more clean and efficient fuels than carbon, as pure H_2, diesel or gasoline. Such an industrial configuration is depicted in Figure 2-31 and its operating principles are analyzed a couple of paragraphs below, in order a description of a chronological evolution of the applications and relevant studies to be satisfied.

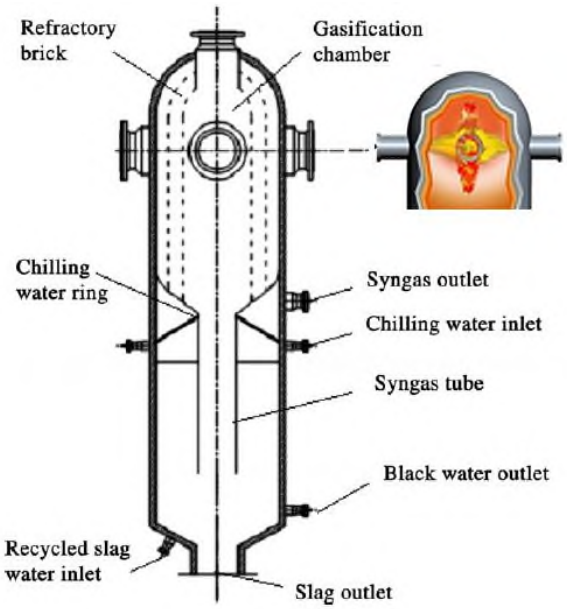

Figure 2-31 Opposed coal gasification layout [108]

Opposed jet burners are employed both in pulverized coal combustors and in coal gasifiers as well, as a means to meliorate the reaction process in each case. Among the countries with the heaviest coal industry, China has invested primarily in the research and development of OMB technologies, driven by the increased environmental concerns caused by the heavy air pollution observed in its cities and its heavy dependence on coal production energy. For this reason, the published studies originating in Chinese institutions make up the majority of those that will be referenced in this subsection.

A first attempt to develop and install an OMB is described by Zhao [5]. The purpose of the study was to develop a mechanism in order to achieve flame stabilization without bluff bodies and recirculation of the hot gases without swirlers. A pair of two concentric rings were placed opposite a main combustion chamber quarl where the main stream of fuel-oxidizer was introduced. In each ring, a number of holes was evenly distributed. Compressed air passed through the holes, forming jets of equal number opposing the main stream. Two separate cases were examined both experimentally and numerically. In the first one, described as the cold flow, combustion did not occur. In this case, the recirculation ability of the opposed ring jets was compared with the presence of a bluff disk (having the diameter of the outer ring instead). The results showed a very satisfactory recirculating zone. In the second case the primary air stream was fed with pulverized coal and a single opposed jet ring was employed. The pulverized coal ignited immediately in the recirculating zone formed by the presence of the opposed jets. The measurements taken showed the achievement of low levels of NO_x regardless of the carbon fuel enrichment and the level of maximum temperatures observed. These findings led

to the conclusion that such a configuration could be used as a retrofit of existing burners for a variety of coal compositions.

Since the above proposal, significant progress has been made in the field and a more complete configuration is described by Dai et. al. [108]. In this paper, the technical characteristics of an entrained flow coal gasifier were presented focusing primarily on the chemical dimensions of the process, and also on the effects of temperature and pressure on the chamber, giving smaller priority in a detailed study on the flow-field characteristics. Nevertheless, a clear idea about the operating principle of such an industrial facility was provided. Pulverized coal was carried by a gaseous medium of N_2 or CO_2 in elevated temperature into the chamber. These streams issued by four nozzles that were symmetrically placed at the same horizontal level, forming two pairs of opposed jets. In order for the gasification process to be realized and syngas (H_2 & CO) to be produced, superheated steam was introduced through a parallel channel with the main stream, located in each nozzle. A mixture of water-ash slag had to be extracted by the chamber through a separate outlet. The operating temperature range of the gasifier [1300 ^oC, 1360 ^oC] resulted as a compromise between the ash fusion point (necessary for molten deslagging) and the temperature which the refractory brick walls could resist. This type of gasifier enabled operation under pressure levels above the atmospheric. However, the variation of gasification pressure exhibited no effect on the composition of the syngas. The authors concluded that this model provided better coal conversion rates and high CO and H_2 quantities, in comparison with the existing water slurry methods. Furthermore, the use of CO_2 as a carrier increased the content of CO and H_2, since it acted also as a gasification agent in relation with the N_2.

In the sequel, a study on the gas-particle behaviour flow in the above facility was carried out by Ni et al. [109]. Numerical and experimental data of the flow were taken for four cases with ambient temperature and pressure, using air as a carrier and water droplets as particle tracers, providing similar results. The gas flow field was simulated using the realizable k-ε model, while a dual Particle Dynamics Analyzer (PDA) captured the velocity field. Significant findings concerning the characteristics of the phenomenon included the formation of a stagnation point in the center of the four opposed jets accompanied by the increased particle concentration in this area, four times larger than the concentration at the jet exits. Moreover, at the stagnation point, the turbulence level exhibited its peak. At the same time, two opposed streams emerged perpendicularly to the horizontal plane of the four opposed jets. The role of the upward stream emerges as a notable parameter in the design of the gasifier since it affects the deposition of slag/ash content in the walls of the upper dome of the chamber. Since the larger amount of carbon conversion is desirable, the small entrainment of particles in the residual slag content is an index of the efficiency of the gasifier. The numerical prediction for the real cases, with the presence of flame and increased pressure showed no differentiation in

comparison with the cold cases, regarding this factor. At the same time, visualization of the opposed jets suggested the same velocity distribution as predicted with both the “hot” and “cold” numerical simulations.

The dynamic behaviour of the stagnation plane is a crucial factor for the efficiency of opposed jets flow and use in industrial applications. Difficulties in the alignment of the nozzles and in balancing the exit velocities may result in offset of the stagnation plane from the mid plane between the exit nozzles or an unstable movement around it. These features have given motive to some researchers for analytical treatment and research on this subject. Among them, Li et al. [110] investigated both experimentally and numerically how the variation of axial spacing L/d_e (range [1, 20]) and unequal exit velocities (ratios range [1, 0.7]) affect the stagnation point offset of turbulent opposed axisymmetric jets. Due to the fact that the numerical simulation based on the RSM model, and the static HWA provided only steady state results, the authors relied also on flow visualization in order to observe the stagnation point position at different instances. The flow visualization revealed that when the two exit velocities were equal, the stagnation plane position varied in a region between two relatively stable positions (pitchfork bifurcation). On the other hand, when the velocities were unequal, the stagnation plane took a steady state position, shifting to the side of the lower momentum jet. A slight decrease in the velocity of the weaker stream (ratio=0.97) caused an offset up to $2.7d_e$ or 0.45L depending on the axial distance L/d_e. The effects of the axial distance L/d_e could be parted into two categories. For $2\leq L/d_e \leq 8$, the axial velocity gradient decreased with nozzle separation, and a sharp increase in the stagnation point offset with the decrease in the jet velocity ratios was observed. On the other hand, for $L/d_e <2$ & $L/d_e >8$, the velocity gradient remains nearly constant and the stagnation point offset increases linearly with the decrease in the velocity ratios, having also in total, smaller values in comparison with the first case.

This work was further extended by Li et al. [111] in order to investigate more thoroughly the factors that cause the stagnation point offset. The flow visualization indicated that the offset between the two semi stable positions that was described in the above paragraph, when the velocity ratio equaled unity, took place only for $L/d_e =4$. This observation was also corroborated by the fact that with a slight decrease of 3% in the velocity ratio, an offset peak value of $1.33d_e$ was observed for this particular L/d_e value. Furthermore, simulations carried out for very slight differences of velocities between the two jets (5 ‰) predicted also the $1.33d_e$ offset. Therefore, the conclusion that the stagnation point position was very sensitive to very small flux imbalances could be deduced. A comparison between HWA measurements, which corresponded to top-hat exit velocities and numerical simulations, where uniform exit velocities were imposed, showed that the offset was larger for top-hat exit case. However, the more noteworthy element of this study was that using a nozzle that provided increased

turbulence intensity, stabilized the position of the stagnation point near the middle. This was attributed to the smaller scale vortices in the jets boundary layers, whose interaction resulted in lower-level instabilities in the flow.

Li et al. [112] studied the dynamic behaviour of both planar and axisymmetric opposed jets, using flow visualization techniques. The nozzle's characteristic dimension was 10 mm diameter (d_e) for the axisymmetric jet and 10 mm height (H) for the slit in the planar jet case. The Reynolds number varied between 786, 6288. The purpose of the study was to produce a map that could capture the transition between the various flow field regimes as these varied with the alteration of the two basic parameters, i.e. Re and the L/d_e distance ratio between the jet nozzles. For the case of the round jets, three flow patterns were observed. The first one, was characterized by a quasi-periodic oscillation of the stagnation plane around the middle of the distance, with a dominant frequency about 10 Hz. This behavior occurred for $L/d_e \leq 2$. By increasing the distance L/d_e, a transition to a stable stagnation plane offset from the middle took place. For larger $L/d_e \geq 8$, a symmetry condition was attained, with the stagnation plane located stably in the middle. The Re number had an effect on the transition; at smaller Re, the transition occurred for $L/d_e \geq 12$. The explanation given described this phenomenon because of helical instabilities of low Re jets, which delayed the occurrence of a symmetry stable condition. Contrary to the three regimes described above for the axisymmetric jets, the planar jets exhibited two behavioral patterns: one horizontal instability similar to the first regime of the round jets, and a second one described as deflecting which had the same shape with Denshikov and Kondrat'ev [101]. The transition L/H ratio between the two regimes was found 5 and the Re had little effect on this value.

Since an opposed jet flow includes regimes of quasi periodic oscillations of the stagnation plane, a key element of the flow is the frequencies of such a motion and their origin. The low frequency oscillations observed in an unrestricted axisymmetric TOJ configuration are mainly attributed to external disturbances of the flow in contrast to self-sustaining oscillations observed in confined TOJ configurations such as in RIM. In order to approximate such a disturbance Li et al. [113] introduced a modulation in the inflow of each jet aiming to investigate how the imposed excitation frequency and amplitude affected the stagnation plane motion. The resulting flow field was captured by flow visualization techniques and the motion was analyzed by image processing. HWA was also employed for near nozzle exit velocity and turbulence measurements. The $2 \leq L/d_e \leq 8$ range, which was described as the stagnation plane offset regime in the previous articles, was identified as the case of the largest oscillations. In this case, the stagnation plane is carried by the momentum imbalance of the jets, since at this point the flow is located inside the potential core of its jet, where the velocity difference equals the excitation amplitude, as a peak. In general, the frequency of the stagnation plane oscillation

followed the excitation frequency, and the velocity amplitude of the stagnation plane followed the modulated inflow velocity amplitude. The displacement amplitude of the stagnation plane was found to vary proportionally with the excitation amplitude and inversely proportionally with the excitation frequency. The introduction of turbulence by perforated plates before the nozzle exits resulted in a decrease in the oscillations and, similarly to Li et al. [125] Once again, this observation was interpreted as the result of the breakup of the large vortex rings of the axial region of the jets, into smaller structures under the influence of increased turbulence intensity.

Li et al.[114] investigated experimentally the influence of particle presence on the opposed jets flow-field, by PIV for L/d_e=12 and Re=14500. The particles were simulated by glass beads of 100 μm average diameter, leading to a mass loading ratio of 0.04. For the measurement of the gas velocity, smoke tracers of average diameter of 5 μm were also introduced into the flow. For the case of the gas-solid particle flow measurements, the raw images were filtered to separate the velocity flow-field of the gas phase resulting from the tracers, from the velocity field of the solid particles. It should be noted that for this mass loading, the inter-collisions of solid particles could be neglected, a fact that could be verified by the absence of strong radial motions of the particles in the impinging region. On the contrary, the particles inter-penetrated the opposite streams respectively. The first significant observation of the experiment was the smaller overall velocities of the solid phase, which led also to the reduction of the gas-phase velocities in the two-phase flow case. Concerning the turbulence intensity and the dissipation rate, while for the single phase, these two properties exhibited their peaks in the stagnation region and in the axial jets boundaries, for the two-phase case the peaks were observed in the jet axis. This fact signified that the presence of particles may downgrade the transfer rate in the impinging region. Furthermore, apart from the increase in turbulence intensity in the jet axis, the existence of particles led also to increased integral length scales in this region. This means that the penetration of particles in the opposed stream axis leads to higher gas-particle relative velocities and as a result elongated vortex coherent structure there. In contrast, for the single phase, the largest structures were found in the radial jets produced by the impingement of the opposed jets, strengthening the notion that the mixing rates due to turbulence are more profound there.

Wu et al. [115] tried to identify the characteristics of the stagnation plane formed by two TOJs with Re=4050 and L/d_e=12, numerically. In their efforts, they used two separate methods. The first one was Proper Orthogonal Decomposition (POD), to reconstruct the Eulerian stagnation plane (ESP) from the different modes of oscillations that occur in a such a flow. Following such an approach, it was necessary to extract the different modes-structures from data given either by non-steady numerical solutions such as DNS/LES or PIV results. In their study, they implemented a high-order finite difference DNS, to form their flow database. The second method included the location of a Lagrangian

Stagnation Plane (LSP), by identifying the large coherent structures occurring in the flow. A finite-time Lyapunov exponent technique was needed for this purpose. The POD analysis demonstrated the contribution of the different modes to the generated turbulence intensity. The first dominant mode related with the large-scale axial oscillation of the stagnation plane contributed up to 90% of axial velocity fluctuations. On the contrary, to reach 90% of the radial fluctuations, at least the first 100 modes where needed, which meant that the turbulent kinetic energy in the radial direction was produced by the smaller scale flow structures. Three groups of large-scale structures were identified by the second method: LSC 1, which corresponded to the vortices produced by shear in the boundary layer of the axial jets, LSC 2 located in the border line which was formed by the impingement of the opposite streams and LSC3, which contained the convoluted region of vortices produced in the radial direction in the impingement location.

As a continuation of the above study Wu et al. [116] investigated the influence of the particle presence in a TOJ flow under the same L/d_e =12 and similar Re=13500 with the study of Li et al. [114]. The main differences with the above paper were that the current study used a LES instead of PIV measurements and also took into account the inter-collisions of the intruded particles. Among the most significant observations of this study, the following conclusions stand out:

- Particles of increased inertia as described by elevated Stokes number penetrated deeper in the opposite stream. This penetration resulted in an increase in the axial particle rms velocity in this maximum penetration region.
- Aggregation of particles near the stagnation plane was attained either by small inertia particles that followed better the gas phase, or by larger particle volume fractions that resulted in higher inter-collision probabilities at that area.
- Increased level of interparticle collisions resulted in increased radial mean and rms velocities of the particles, whereas increased particle inertia led to the opposite results.
- A good correlation between the particle and the gas phase was found for the small inertia particles and for the case of the increased collisions in the stagnation plane as well.
- The presence of particles in general decreased the axial velocity of the gaseous jets and the decay/strain rate near the stagnation plane consequently.
- Whereas with the absence of particles the location of the stagnation plane presented a bimodal offset from the middle point, the presence of particles attenuated this trend and stabilized the position of the stagnation plane near the middle. As a result, the turbulent kinetic energy of the gas phase related to the instability of the stagnation plane was absorbed by the particle phase.

After the presentation of the above studies, it is useful to make some remarks on the basic observations emanating from the analysis of the results.

a) The increase in the tke in the stagnation plane results from the axial large-scale oscillations and the production of smaller scale structures in the radial direction
b) The presence of solid particles in such flow decelerates the velocities of the jets gas phase and leads to the attenuation of the instabilities of the stagnation plane and reduction of the strain rates.
c) Elevation of the turbulence levels in its jet using suitable nozzle configuration stabilize the position of the stagnation plane.
d) Two parameter (Re, L/d_e) maps show that for $L/d_e<8$, a transition from a steady symmetric stagnation plane condition to a pitchfork bifurcation mode occurs for turbulent round jets. This was not observed by Pawlowski et al. [103], who stated that for increased Re only the mode of pitchfork bifurcation exists. However, a similarity between the two cases rests on the absence of Hopf bifurcation mode (deflecting oscillations) for the axisymmetric jets. In both cases, the deflecting oscillations take place in a planar opposed jets configuration for larger L/d_e ratios>6-8.

2.4.3 Confined Impinging Jets Reactors (CJIR)

Confined Impinging Jets Reactors (CJIR) are a special category of microreactors that are often used in chemical processes or micro and nanoparticles for a variety of products such as pharmaceuticals, dyes, pesticides etc. Rapid mixing under controlled conditions necessitates the development of such kinds of micromixers with the objective to form a region of high turbulence dissipation. In the case of the CJIR, this zone coincides with the stagnation plane formed by the opposed jets. Apart from the characteristics of such a flow-field, research in this field aims at the assessment and further development of more precise and effective methods of measurement and simulation of such devices.

There is extensive literature on CJIR, mainly driven by chemical engineering applications, focusing on mixing and reaction performance of such devices. Johnson and Prud'homme [6] provide an informative summary on the relation of the mixing length scales (macro, meso, micro) and the turbulent length scales (large convective length scales, inertial subrange eddies, Kolmogorov microscales). This relation between mixing and turbulence is better illustrated in Figure 2-32. The effectiveness of the homogenization process is dependent on the formation of a mesomixing volume of high energy dissipation, such as all the fluid passing from that region. Such a mesomixing volume is created by the collision of the two opposed fluid streams in their stagnation plane. The confinement of the process ensures the passage of the discharged fluids through this high turbulent volume. The

writers developed a scaling theory based on experimental data. The key result of the article was the correlation of the characteristic mixing time with jets velocity, inter-nozzle distance and momentum diffusivity.

$$\tau_m \sim \frac{v^{1/2}(L/d_e)^{3/2} d_e^{1/2}}{u_e^{3/2}} \qquad 1.75$$

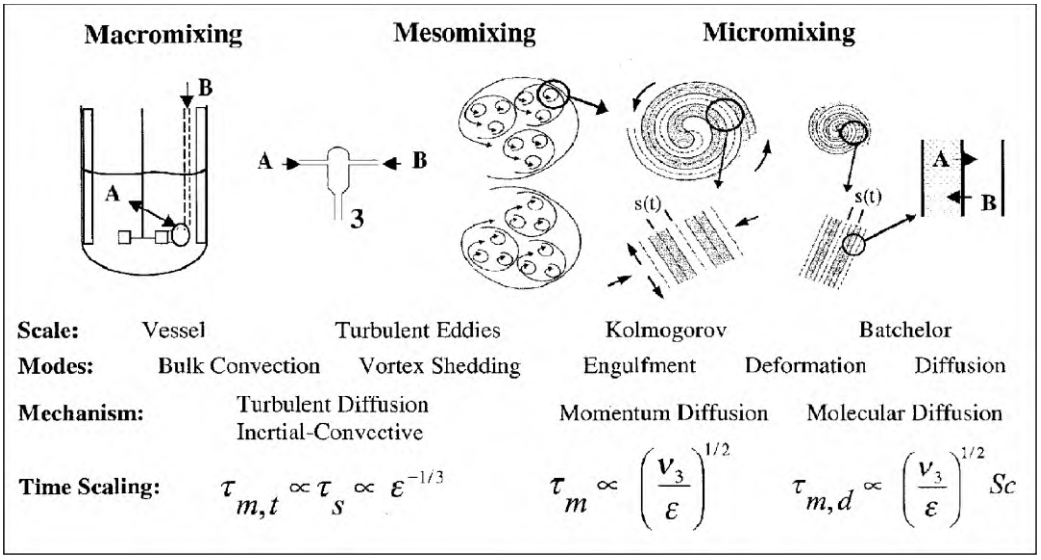

Figure 2-32 The correspondence between mixing processes scales and the turbulent length and time scales, Johnson and Prud'homme [6]

Normally, in CJIR the flow based on jets exit Re is laminar and a transition to turbulence occurs as a result of the impingement. This was the reason why the CFD predictions made by Liu et al. [117], [118] showed deviations from PIV measurements and experimental data from Johnson and Prud'homme [6] for L/d_e=4.76. The standard k-ε model with enhanced wall treatment that they used overpredicted the turbulent kinetic energy for lower Re, since it is a turbulent model, and the turbulence was restricted in the chamber. On the other hand, for higher Re, the k-ε model underpredicted the turbulent kinetic energy because it was unable to capture the unsteady flapping motion of the stagnation plane observed by the PIV, since it is a Reynolds Averaged Navier-Stokes (RANS) model.

Gavi et al. [119] made further progress based on the configuration Johnson and Prud'homme [6] in the assessment of more than one RANS model. They tested the standard k-ε and RSM model both with Enhanced Wall Treatment (EWT) and Standard Wall Function (SWF). The comparison with experimental data and a LES solution exposed the superiority of the RSM model with EWT, with the standard k-ε model being very close. However, significant deviations from the experimental data and

the LES were found, highlighting the necessity for a suitable near wall treatment for a case of a confined wall configuration, especially where the inter-nozzle separation is small as in this case. The increase in Re number signified an improvement in the output of the RANS models, since a larger portion of the flow in the chamber was turbulent. Moreover, for increased Re the stagnation region became thinner and with larger turbulent kinetic energy and dissipation rates.

While Johnson and Prud'homme [6] employed a competitive reaction scheme for their scaling, theory, Marchisio et. al.[120], used an alternative approach for the investigation of mixing performance in a CJIR with similar geometry by producing barium sulfate as the test reaction. The reactants were brought into the chamber as aqueous solutions. As in the case of the previous paragraph, Gavi et al. [121] implemented a CFD simulation by adopting the mixing process model of Marchisio et al. [120]this time. The validity of the k-ε with EWT solution was checked by comparison with micro PIV measurements and showed satisfactory agreement for the mean axial and radial velocities. However, the RANS model underestimated the tke, since it was unable to capture the turbulence created by the unsteady oscillatory movement of the stagnation plane. Moreover, this is the reason why the maximum actual dissipation rate measured by the PIV was distributed over a wider axial region around the middle, where the CFD model predicted a distinctive peak. A more general remark that applies to the ensemble of the CJIR, was provided by the authors based on the experimental observations. As Re increases, the radial stream upwards is intensified, hits the upper head wall of the reactor, and then is reflected downwards. As a result, this stream interacts with the jets breaking them into smaller structures intensifying the turbulence level and destabilizing the stagnation plane even more.

Icardi et al. [122] used micro PIV in conjunction with DNS to investigate the flow emanating from two opposed round jets in cylindrical CJIR with L/d_e=4.8. An aqueous solution of urea seeded with fluorescent particles was discharged into the chamber at laminar Re [62-600], nevertheless they resulted in turbulent flow due to impingement that took place. The PIV images showed that for all Re, the flow was unsteady, and the stagnation plane shifted from one direction to the other periodically. However, as the Re increased, together with the oscillations, the laminar flow broke up into turbulence. These smaller eddies that emerged led to instantaneous deterioration of a distinguishable stagnation plane form. Based on the mean and rms velocity plots (both streamwise and cross-stream), a significant discrepancy between the PIV and DNS predictions was observed. The narrow region of increased strain rate near the stagnation plane predicted by the DNS simulations was not verified by the PIV. Instead, when a harmonic oscillation was included in the inlet velocities boundary conditions, the DNS approximated very well the PIV captures, highlighting the importance of the proper selection of boundary conditions in the DNS simulations of such an unsteady flow.

2.4.4 Reaction Injection molding (RIM)

Another engineering field related to CIJR with directly opposed jets includes RIM techniques. The purpose of RIM technology resides on the fast reactions of two liquid monomers that lead to the production of polymer plastic parts. A sketch of such a configuration is provided in Figure 2-33. The diameter of a commercial RIM mixing chamber is 10-15 mm. Two opposed reactant jets emanate through a 1-3 mm holes at a Re of 100-500 and impinge in the chamber. A movable piston drives out the resulting mixture into a mold through the outlet of the chamber.

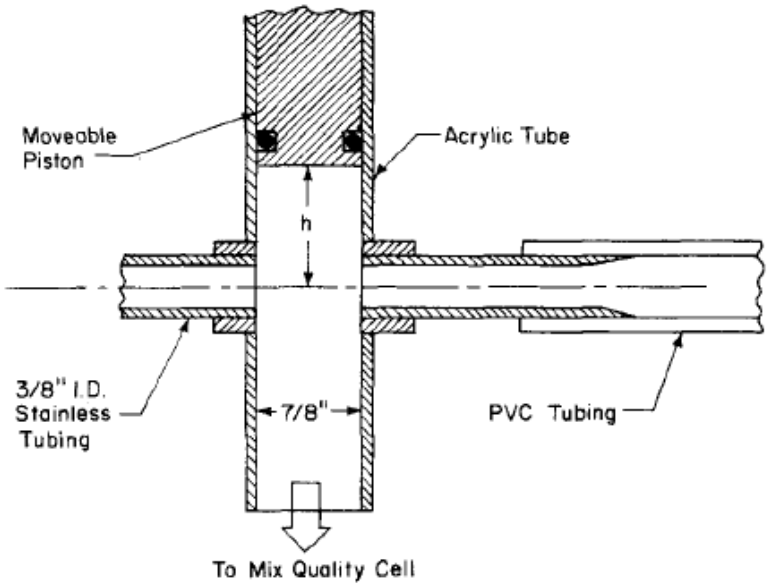

Figure 2-33 CJIR head used for Reaction Injection Molding (RIM), sketch of the scaled model used in the experiment of Tucker and Suh [7]

Very fast kinetics of the initial stages of polymerizing reactions demand a very fast mixing process accomplished by a high vorticity turbulent field. Although strong mechanical instabilities are observed around the stagnation point, completely developed turbulent flow is not attained due to the high viscosity of the reactants. The whole process in a RIM takes place under very high pressures, up to 10 MPa.

Tucker et Suh. [7] defined the operating regime of a RIM based on the opposed jets Re. Using flow visualization techniques, they concluded that effective mixing takes place for Re above 140, although these Re values do not correspond to turbulent flow for the jet flow emanating from the pipe nozzles. The segregation scale was directly related to the turbulence microscale, which for this type of flow decreased to the -3/4 power of Re. Moreover, they remarked that the transition to chaotic, turbulent like flow is aided by larger chamber to nozzle diameter ratios. In a second paper Tucker and Suh [123]

further reduced the optimum operating regime to Re=[100,150] by using a second impingement or a mechanical aftermixer as aids.

Wood et al. [124] observed the onset of instabilities of the stagnation point, using flow visualization and LDA for Re=90. This value is very near to Re=94, where Tucker et. Suh [7] noticed the emergence of large eddy motions in the mixing chamber. Moreover, they remarked the absence of a stable impingement point for Re above 150. Furthermore, they examined the role of viscosity and exit velocity on the resulting flow. By altering the jets exit velocity and fluid viscosity, but maintaining the same Re, they found oscillations frequencies giving the same Strouhal number. This fact suggested the existence of a dynamic similarity based on Re for a given geometry.

LDA measurements made by Johnson et al. [125] revealed the onset of unsteady three dimensional flow for Re >150. The authors also concluded that a small chamber to nozzle diameter ratio $D/d_e=5$ led to higher mixing efficiency as a result of unidirectional flow towards the outlet of the chamber that provided more uniform and even mixing.

Taking also into account the study of Johnson and Wood [126], we can describe the flow produced in the stagnation region of RIM mixer: A structure with the shape of a disc is formed, where the jets collide, which exhibits lateral self-oscillations with frequencies based on the jets Re number. The plane of the disc is parallel to the nozzle exit plane and the diameter is a bit larger than the jet's. There is a lower Re limit below which, no oscillations are observed and an upper limit above which, a dominant frequency is not observed, and the flow is irregular. For two cases with chamber to nozzle diameter $D/d_e=5$ and $D/d_e=10.67$, which correspond to commercial applications geometrical ratios, these limits were found Re=[120,217] and Re=[99,131] respectively, for the same dynamic viscosity≈0.025 Pa·s. In the range formed between the two limits the dominant frequencies increase with Re. Furthermore, higher fluid viscosities provide higher frequency values.

A more detailed and comprehensible set of studies on the hydrodynamics of RIM mixers has been conducted by a series of researchers in the Dep. of Chemical Engineering, University of Porto. LDA [127], PIV and numerical simulations [128] were made in order to investigate the flow characteristics of a commercial pilot RIM machine, in a Re range [50-600]. The chamber diameter was D=10 mm, while the nozzles diameter was 1.5 mm, leading to a $D/d_e=6.67$ ratio. The two glycerol aqueous solutions jet streams had equal momentum. Both the LDA and PIV measurements exposed the laminar segregated flow for lower Re, up to 100. The absence of oscillations was further verified by the unimodal velocity probability density function at the stagnation point. For larger Re, up to 200, a bimodal pdf was attained, revealing the oscillatory behavior with distinctive peak frequencies, obtained by spectral energy analysis. The Strouhal number increased with Re number at this regime,

until the upper limit was reached, beyond which it remained constant (a small negative slop was observed). Turbulent intensity and Reynolds stresses followed also the same ascending trend in this regime, while beyond the upper limit, the increase of these properties with Re was attenuated. A more detailed set of PIV measurements revealed that the sharp increase in turbulent intensity begins at Re 120. Variations in Froude numbers, while keeping the Re constant, revealed that smaller Froude imposed a dumping effect in the oscillatory behavior, thus downgrading the mixing effectiveness. This means that lower viscosity fluids are not proper for mixing studies and applications in RIM. The numerical model that was developed for the modelling of self-induced oscillations showed good agreement with the aforementioned observations concerning the resulting Strouhal number and the restrictions imposed by Froude number in the flow properties. In this particular model, the oscillations in the jet axis were simulated as a linear spring undamped system, where the spring coefficient was replaced by the pressure drop. The pressure fluctuations were estimated by a numerical simulation, using Fluent. Subsequently, the model was employed for the calculation of the oscillation frequencies.

The main conclusion that is deduced from the preceding analysis on RIM hydrodynamics is that the determination of the operation regimes in such devices rests on the Re which describes the transition from regular oscillations to a chaotic flow. The above studies showed that this transition occurs in a Re range [120-200]. Beyond this critical Re, the mixing efficiency remains invariant and increased flowrates and pressures are considered unnecessary.

2.4.5 Conclusions on Turbulent Opposed Jets literature review

The literature on the fundamentals of turbulent opposed jets is limited and sporadic. As a result, engineers and scientists cannot make use of a generalized and consolidated theory. The literature review until now, focuses on studies that emphasize on special aspects of the flow that influence the ultimate goals of specialized applications, i.e. relation between straining rates and flame extinction in combustors or relation between turbulence statistics and mixing efficiency in chemical processes. Furthermore, the total of the studies quoted in this chapter describe flow configurations for small L/d_e ratios<20. This means that the behavior of two well-developed self-similar opposed jets has not been investigated until now.

Although there is not a theory in a generalized form that can describe the flow-field of turbulent opposed jets, an investigation should include the examination of the following aspects towards a more comprehensive description of opposed jets.

1. The validation of the free radial jet concept in the stagnation plane and its related properties (mean velocity, turbulence statistics, self-similarity).

2. The effects of such a configuration on the development of the free axial jets (mean velocity, turbulence statistics, self-similarity).
3. The variation of the axial and radial strain rates in the stagnation plane region.
4. The oscillatory behavior of the stagnation plane (steady symmetrical, stagnation plane offset, deflecting oscillations)
5. The influence of Re and geometrical factors such as L/d_e on the variation of the above properties.

3. Materials and Methods

In this section the materials and methods that were used in this investigation are described in detail. For the experimental investigation two facilities are utilized. The first facility was used for the generation of homogenous and isotropic turbulence with near zero mean flow. This facility was originally build by Stapountzis et al. [47] and modified for the current experiments. The second facility was responsible for the production of single and opposed jets. At the later stage of the investigation, the two individual facilities were merged so that the development of single and opposed jets could be examined within homogenous and isotropic turbulence without mean flow. For the control and characterization of the flow, both conventional and optical instruments were used, which are also presented.

3.1 Experimental setup

3.1.1 Box of Turbulence

The facility that was used for the generation of homogenous and isotropic turbulence with little mean flow is commonly referred to as a "box of turbulence". The principles of operation of such facilities were presented in detail in section 2.1.6 along with the various implementations that have been used in the past by other researchers. In the implementation used here, the actuators used for the generation of turbulence were synthetic jets rather than fans. The basic schematic of the box of turbulence facility is shown in Figure 3-1. The location of the opposed jets is also included for reference. The synthetic jets were mounted at the 8 vertices of a cubic metal frame and aimed at the center of the cube. The volume of turbulence was generated at the cube center where the jets met, cancelling mean flow while producing turbulence in the region.

The cubic metal frame was constructed using four tubular steel columns of 60mm diameter. The columns were joined by eight horizontal steel beams to form a cubical frame with dimensions of 1.80 m × 1.80 m × 1.80 m. This frame arrangement left ample space for the placement of the synthetic jet actuators, the measurement instrumentation and for the installation of the single and opposed jets later on. The faces of the cube were left open, resulting in an "open type" turbulence chamber. This facilitated optimal physical and optical access to the center of the cube where the experiments are conducted. It also minimized the effect of confinement and, therefore, the re-circulation of ambient air resulting to large scale structures that might interfere with the flow in the region of interest at the center of the cube. Facilities of the "closed type" chamber where the faces of the frame are closed by walls and windows would be preferable if containment of the flow constituents such as

solid particles was required. However, since only smoke was used for the experiments, containment of was not an issue and the open type configuration was deemed preferable.

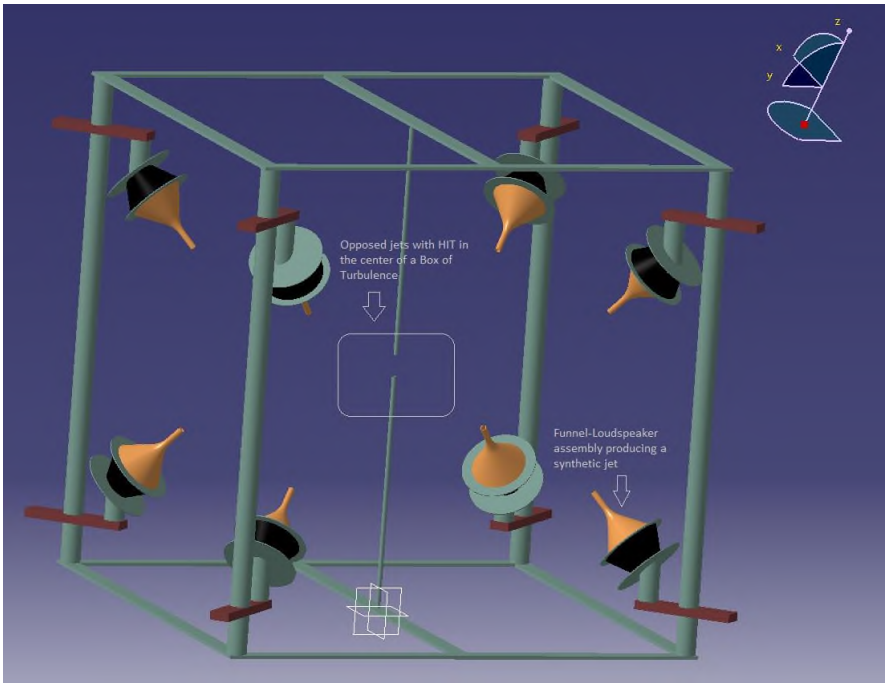

Figure 3-1: Schematic of the basic arrangement of the synthetic jets on the cubic frame.

Eight synthetic jet actuators were placed at the location of the vertices a cube in the metal frame to induce the turbulence at the center of the facility. The driver of each actuator was a loudspeaker made by Sphynx, model SP-W200-PP. The loudspeakers were of the cone type, where a conical diaphragm vibrates under the influence of a coil driven by an external source. The loudspeaker cones were made of polypropylene, the diameter of the cones was 200 mm, the loudspeaker coil impedance was 8 Ω, and the loudspeaker frequency response was in the 30 Hz-5 kHz range. In order to generate flow, each loudspeaker was capped with a plastic funnel with a nozzle exit diameter of 14 mm. By capping the loudspeaker with the funnel, a flow actuator was obtained. The vibrating diaphragm of the loudspeaker acted as a piston inducing periodically alternating inflow and outflow of air from the funnel nozzle exit. This caused entrainment of the surrounding air a synthetic jet was produced at the exit of the funnel in the direction of the funnel axis.

The flow actuators were directly mounted on ball and socked joints which allowed free adjustment of the orientation of the actuators. The ball and socket joints were then mounted on horizontally oriented jacks allowing adjustment of the horizontal distance of the actuator from the vertical column. In turn the jacks were mounted on the vertical frame columns by clamps so that the height was also adjustable. In this was it was possible to orient each actuator to be coincident with each diagonal of a

virtual cube of 0.60 m × 0.60 m × 0.60 m size. As a result, when the synthetic jets met at the center of the metal frame to produce a turbulent field the mean flow would cancel out. A detailed overview of the implementation of the 'Box of Turbulence' facility is presented Figure 3-2.

The loudspeakers of the flow actuators were driven by periodic excitation. The signal source was Hameg HM8030 function generator. Due to the absence of walls to the frame, acoustic resonances within the frame were minimized and random phasing of the driving signal to suppress the possibility of standing waves which could affect the flow was unnecessary. The frequency of the driving signal was 40Hz which was close to the resonant frequency of the loudspeakers, which is at 45Hz. As the power output of the function generator was too small to drive the loudspeakers, a Nedis AAMP16120KB power amplifier was used to amplify the original signal.

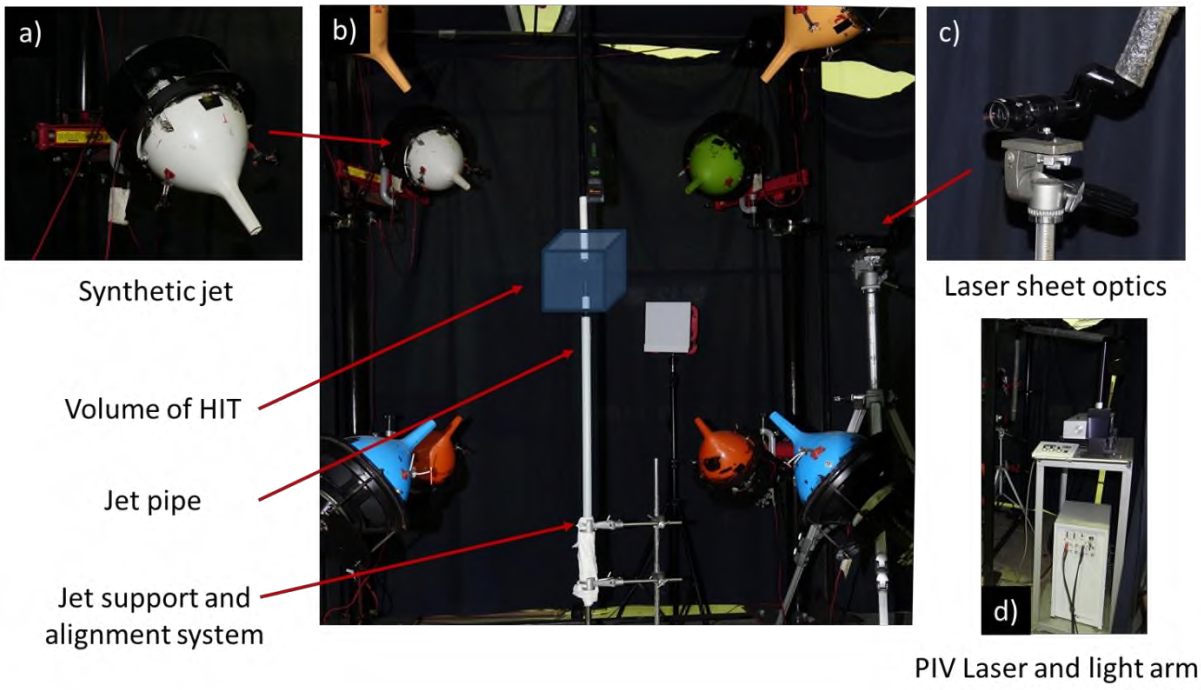

Figure 3-2: Overview of the experimental arrangement a) the synthetic actuator, b) the overall setup, c) the laser sheet optics and d) the Nd:YAG laser.

3.1.2 Flow characteristics within the box of turbulence

The characteristics of the flow within the region of interest were estimated from planar velocity measurements, conducted using Particle Image Velocimetry (PIV). Details of PIV will be described in Section 3.2. Measurements of single jets were conducted in an extended region of interest which was approximately 200mm x 200mm, equivalent to about $16d_e$.x $16d_e$. This is the extent of length that the development of a single jet in turbulence will be investigated. A summary of the flow characteristics

is shown in Figure 3-3 which includes the contours of the spatial distribution of U (Figure 3-3a), the contours of the spatial distribution of V (Figure 3-3b), the contours of the spatial distribution of homogeneity u'/< u'> (Figure 3-3c), the contours of the spatial distribution of homogeneity v'/< v'> (Figure 3-3d) and isotropy v'/u' (Figure 3-3e). The mean value of U was equal to 0.038 m/s and a mean value of V was equal to -0.031 m/s (with maximum values below about 0.2) and is always smaller than the fluctuating velocity which is about 0.3m/s for u' and v', while also there is no preferential direction within the domain. The spatial distribution of homogeneity is within about ±10% for both u' and v', while isotropy is within about 0.8-1.2.

For the case of opposed jets, the region of interest is narrower and covers an area of about 110mm x 110mm which is more than adequate for the investigation of the maximum opposed jet separation of $7.5d_e$ which translates to about 100mm. In this case the characteristics of the flow within the region of interest are presented in Figure 3-4). In the narrower region of interest, the mean value of U was equal to 0.045 m/s and a mean value of V was equal to -0.016 m/s (with maximum values below about 0.1m/s) and is always smaller than the fluctuating velocity which is about 0.3 m/s for u' and v' as in the expanded region of interest. The spatial distribution of homogeneity is within about ±10% for both u' and v', while isotropy is within about 0.8-1.2.

For the evaluation of the properties of turbulence the integral length scale l was estimated from the integration of the longitudinal two-point correlations following the suggestions of Goepfert et al [15] based on Bachelor [129]

$$R_{uux} = \overline{u'(x,y)u'(x+r,y)} \Big/ \sqrt{\overline{u'(x,y)^2}}\sqrt{\overline{u'(x+r,y)^2}} \quad 1.76$$

$$R_{vvy} = \overline{v'(x,y)v'(x,y+r)} \Big/ \sqrt{\overline{(x,y)^2}}\sqrt{\overline{v'(x,y+r)^2}} \quad 1.77$$

and the turbulent kinetic energy

$$k_t = \frac{3}{2}\left(\frac{u'^2 + v'^2}{2}\right) \quad 1.78$$

The dissipation rate is calculated as:

$$\varepsilon = C_\varepsilon \frac{(2k_t/3)^{3/2}}{l} \quad 1.79$$

where C_ε is a constant known as the normalized energy dissipation rate, which is taken to be equal to 0.5 [15]. From ε and k_t, all the turbulent quantities of interest can be determined which include the Taylor length scale, λ

$$\lambda = \left(\frac{10 \nu k_t}{\varepsilon} \right)^{1/2} \tag{1.80}$$

where ν is the kinematic viscosity of the medium, the Taylor scale based Reynolds number, Re_λ

$$\mathrm{Re}_\lambda = \frac{\lambda \left(2k_t/3 \right)^{1/2}}{\nu} \tag{1.81}$$

and the Kolmogorov length and time scales.

$$n = \left(\frac{\nu^3}{\varepsilon} \right)^{1/4} \tag{1.82}$$

$$\tau_k = \left(\frac{\nu}{\varepsilon} \right)^{1/2} \tag{1.83}$$

A summary of the flow characteristics in the region of interest is provided in Table 3-1

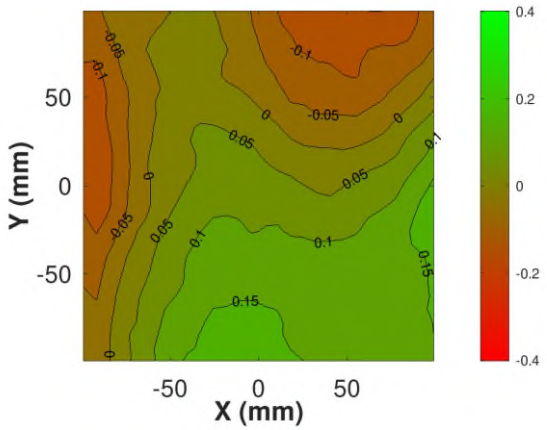

a) Spatial distribution of U

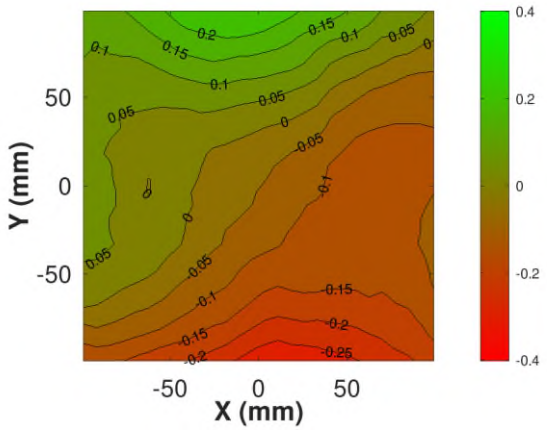

b) Spatial distribution of V

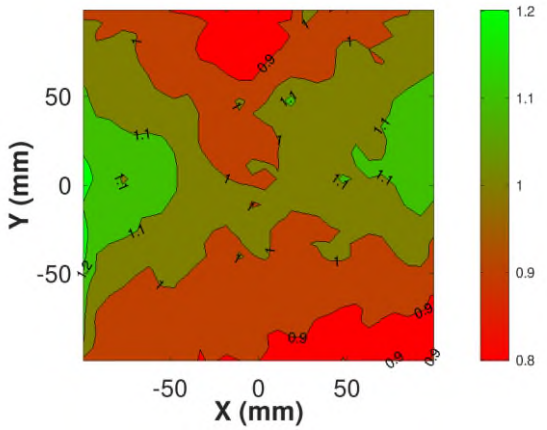

c) Spatial distribution of homogeneity u'/< u'>

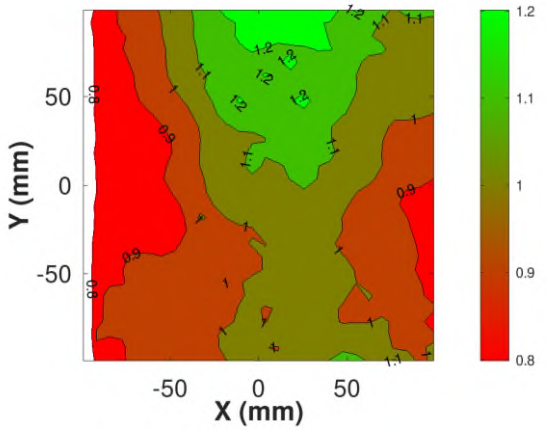

d) Spatial distribution of homogeneity v'/<v'>

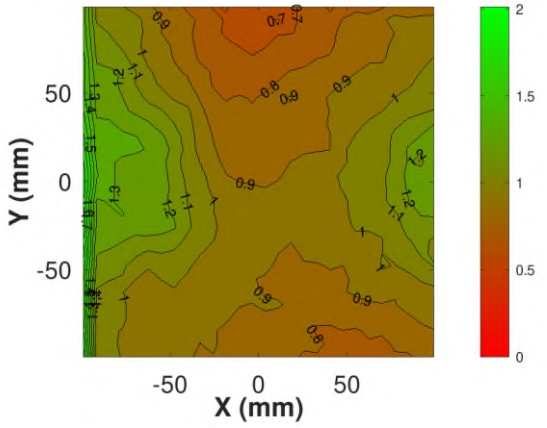

e) Spatial distribution of isotropy, v'/u'

Figure 3-3: Summary of the flow characteristics within the extended region of interest (200x200mm) in the box of turbulence.

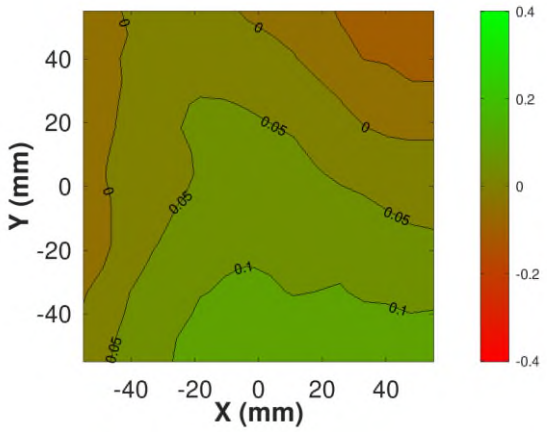

a) Spatial distribution of U

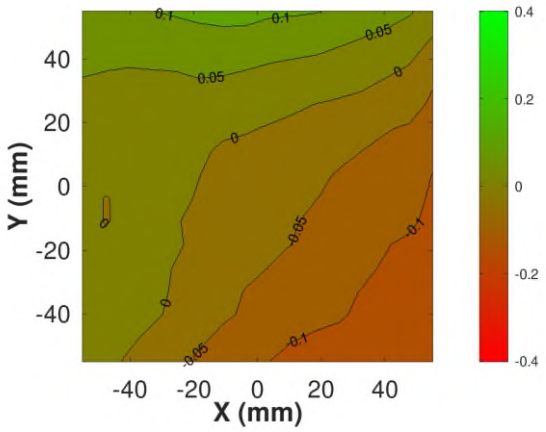

b) Spatial distribution of V

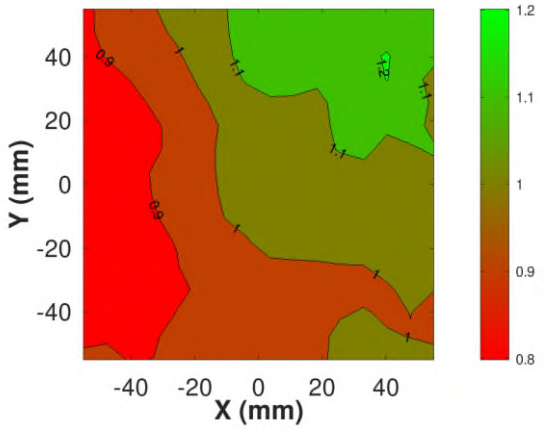

c) Spatial distribution of homogeneity u'/< u'>

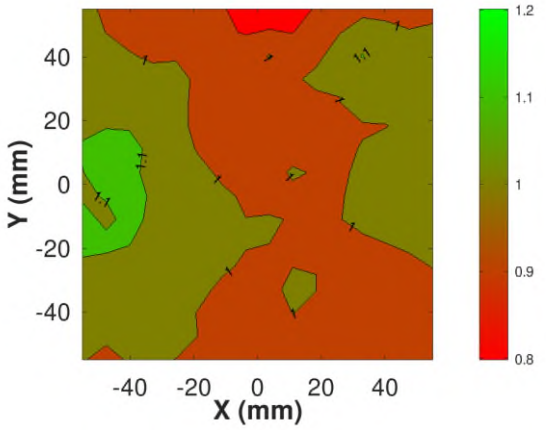

d) Spatial distribution of homogeneity v'/<v'>

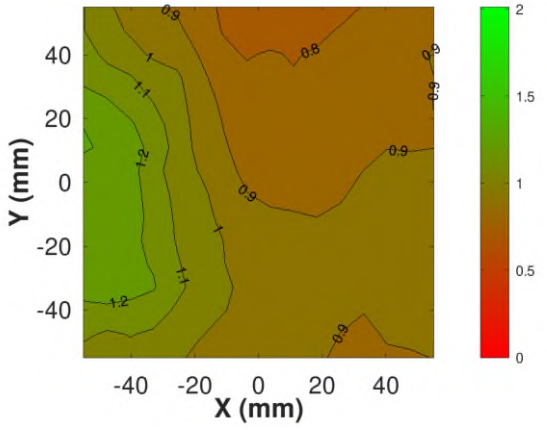

e) Spatial distribution of isotropy, v'/u'

Figure 3-4: Summary of the flow characteristics within the narrower region of interest (110x110mm) in the box of turbulence.

Table 3-1 Summary of turbulence characteristics within the box of turbulence within the extended and narrow regions of interest.

Characteristic	Magnitude (narrow-extended ROI range)	Units
Median u′	0.30 – 0.31	m/s
Median v′	0.29 – 0.29	m/s
Re_λ	181 - 184	
k_t (tke)	0.136 - 0.132	J/kg
Dissipation rate, ε	0.254 -0.228	W/kg
Large eddy scale, l	$5.41 \cdot 10^{-02}$ - $5.71 \cdot 10^{-02}$	m
Taylor length scale, λ	$8.98 \cdot 10^{-03}$ - $9.31 \cdot 10^{-03}$	m
Kolmogorov length scale, η	$3.39 \cdot 10^{-04}$ - $3.49 \cdot 10^{-04}$	m
Large eddy time scale, T	0.54 – 0.57	s
Kolmogorov time scale, τ	$7.67 \cdot 10^{-03}$ - $8.11 \cdot 10^{-03}$	s

3.1.3 Single and Opposed jet facility

The single and opposed jets that were examined in this investigation were produced from steel tubes with an internal diameter of $d_e = 12.8 \cdot 10^{-3}$ m. The tube length was over $L/d_e=60$. The working gas for the jets was air and no other gases were considered. The air to the jets was supplied from the central compressor of the Mechanical Engineering Department. Since the central compressor supply pressure can vary, an SMC EAW211 pressure regulator was used to set the pressure of the inflow to the laboratory to $3 \cdot 10^5$ Pa. Additionally a humidity trap was used to remove condensation. The compressed air was divided in two branches, one for each jet. Jet “A” was used for both single and opposed jet flow experiments and was seeded with smoke. Jet “B” was used only for opposed jet experiments and was not seeded.

The flow leading to the jet flow “A” was regulated by a needle valve and the flowrate monitored with a digital gas flowmeter Cole-Parmer P/N 32908-75 (Accuracy: ±0.8% of reading +0.2% full-scale, Repeatability: ±0.2%). After the flowmeter and before entering the tube, the flow passed through a chamber containing a Prosound P/N N41DZ smoke generator. The smoke generator seeded the air with micron sized particles of theatrical smoke which were used for the visualization of the jet and as tracer particles for PIV. A second chamber was serially connected to absorb any flow pulsations. The seeded flow was finally supplied to the tube that produced Jet “A”. The Jet “A” tube was oriented vertically and exhausted upwards. The tube was supported by two tree-prong extension steel clamps mounted on a retort stand. In this way the tube orientation and nozzle exit location could be easily adjusted. The retort stand in turn was mounted on a two-axis milling table so that the tube horizontal location could be finely adjusted in both dimensions. The tube exit was located at the center of the box of turbulence facility within the volume of homogenous and isotropic turbulence.

The flow leading to Jet “B” was also regulated by a needle valve. This flow was monitored by a Kytola rotameter model EK5-FR (Accuracy ± 5% F.S). A manometer was added to the rotameter to record the differential pressure between the air in the rotameter and the environment in order to correct the rotameter reading. However, as no pressure difference was measurable no corrections were required. Past the rotameter and before entering the pipe, a pressure chamber was introduced to absorb any possible flow pulsations. The air flow in this branch remained unseeded so that it allowed the stagnation plane of the opposed jets was easy to identify. The Jet “B” tube was supported by two three-prong extension steel clamps mounted on a retort stand. The retort stand was supported at the box of turbulence frame top face on a steel platform and the Jet “B” flow exited downwards. The tube exit was placed at the center of the metal frame within the region of homogenous and isotropic turbulence and the tube axis was aligned exactly with the axis of the opposed Jet “A”. The distance between the two nozzles was easily adjustable at the three-prong extension steel clamps while the exact alignment of the two opposed jets was checked by a low clearance fit external tube which was able to slide on both Jet “A” and Jet “B” tubes when they were correctly aligned. A summary of the flow conditions examined is given in Table 3-2.

Table 3-2: Summary of examined flow conditions

Background Environment	quiescent								
	Homogeneous isotropic Turbulence (HIT), $Re_\lambda \approx 183$								
separation L in case of opposed jets	5 d_e (exit diameters)								
	7.5 d_e (exit diameters)								
Flowrate Q (L/min), d_e=12.8 mm	10	20	30	40	50	60	70	80	90
Re	1100	2200	3300	4400	5500	6600	7700	8800	9900

3.2 Particle Image Velocimetry (PIV)

In order to describe and quantify the flow fields of the box of turbulence facility and the single and opposed jets, a 2D Particle Image Velocimetry (PIV) system was used. The system was able to capture the flow velocity field across full planes of the regions of interest. A succinct but also cohesive definition of the principle of the 2D PIV method is provided by Stamhuis [130]: “Mapping of average displacements of groups of tracer particles over a short time interval in a fluid flow by correlating sub-images of two successive images of one illuminated plane of that flow”.

Particle Image Velocimetry is preferable to the other two dominant velocity measurement methods, Hot Wire Anemometry (HWA) and Laser Doppler Velocimetry (LDV), because if measures the flow velocity across a whole flow plane while the other methods only offer point-wise measurements of the flow making the experimental measurement laborious and time consuming. HWA is also not well suited for measuring near zero flow velocities, such that are found in the box of turbulence, close to the edges of jets or near the stagnation plane of opposed jets. PIV (as well as LDV) is an optical method, which means that it is not intrusive and as a result the measurements are not affected by the presence of a physical probe as in the case of HWA which may cause some interference. Additionally, as PIV captures full planar velocity measurements, spatial velocity correlations are possible by PIV which is not the case for HWA and LDV. Finally, as PIV captures an image of the flow it also provides flow visualization, such as in this investigation the image of a seeded jet in an unseeded environment or the visualization of the stagnation plane when a seeded and an unseeded opposed jets meet.

A drawback of standard 2D PIV, is that it is not readily capable of time resolved measurements, unlike HWA and LDV which have natively high temporal resolution. For temporally resolved PIV measurements, a high-speed PIV system is required. Nevertheless, for the investigation of phenomena which are stationary in time, such as the flows investigated here, temporal resolution of the measurements is not essential. Other more evolved PIV systems permit the estimations of 3D velocity vectors or even the estimation of the flow field in a volume instead of a plane. However, since the opposed jets that we study are axisymmetric and the background turbulence is homogeneous and isotropic a 2D PIV system is considered sufficient.

The main components a 2D PIV system such as the system used for this investigation are:

- a laser source
- light transmitting optics and light-sheet forming optics
- an imaging camera and optics
- a control computer

- a synchronizer
- seeding

The experimental arrangement of a 2D PIV system is shown in Figure 3-5. A summary of the main components of the TSI 2D PIV system that was used for the experimental measurements here and their key characteristics is offered in Table 3-3.

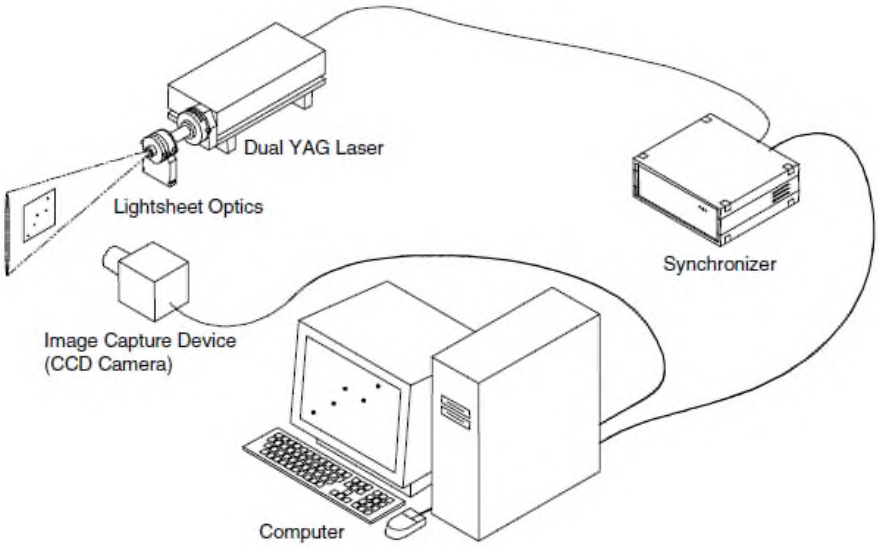

Figure 3-5: 2D PIV System Overview, PIV System Installation Manual P/N: 1990733F, TSI

Table 3-3 2D PIV Specifications

Laser source: Dual YAG Laser	Light transmitting	imaging camera and optics	Computer	Synchronizer
• Laser: Litron Nano L135-15 PIV • Pulse Energy: 135mJ @532nm • Pulse Duration: 9ns • Wavelengths: 1064nm (fundamental) and 532nm (emitted)	Laser sheet optics • 500mm positive spherical lens • -25mm negative cylindrical lens Laser beam steering • TSI LaserPulse Light Arm	• Model: TSI Powerview Plus 4MP CCD camera • Sensor: Progressive Scan Interline CCD w/microlens • Resolution:2048 x2048 pixels • Frame Rate: 16fps • Imaging lens: Sigma 70-200mm f/2.8 lens 532nm bandpass filter	• Processor: Intel Core i5 • RAM: 4GB • Windows 7 • TSI Insight 3G PIV	• 8 independent output channels • 2 input channels • 250 pico-second time resolution

3.2.1 Laser Source

For the illumination of the tracer particles of the examined flow, a powerful light source is required. A practical source is lasers, whose monochromatic characteristic also prevents aberration and diffusion phenomena. In order to obtain clear snapshots and avoid motion blurring of the tracer particles images, very short illumination duration is required. With the exemption of slow flows, this necessitates the use of pulsed rather than continuous lasers. The laser pulse duration is typically of the order of 5 ns which guarantees that the particle will not move during the illumination duration. For such purposes, a pulsed laser Nd:YAG laser is normally used. In an Nd:YAG ($Y_{2.97}Nd_{0.03}Al_5O_{12}$) solid state laser, the dopant neodymium ions replace about 1% of the host crystal yttrium ions $Y_3Al_5O_{14}$ providing the lasing activity. The first harmonic in Nd:YAG lasers is at 1064 nm, which is in the infra-red where the human eye and most cameras are not sensitive. For this reason, before the beam exits the laser head a frequency doubler is also utilized for converts two 1064 nm photons the one 532 nm photon. Light at 532 nm is much more practical as it can be observed by the human eye so that the laser illumination can be easily aligned to the region of interest of the flow, and digital cameras are highly sensitive to this wavelength.

The laser utilized for this investigation is a Litron Nano L135-15 PIV laser. The pulse duration is about 6-9 ns and the beam diameter at the laser exit is about 5 mm. The maximum energy of each pulse that the laser produces at 532nm is on the order of 120 mJ which translates to a power of about 30 MW. This laser is specifically produced for PIV and utilizes two distinct cavities integrated into a single unit for the generation of two separate laser pulses with precise inter-pulse time adjustment. Using the same cavity for both pulses is not practical as the time interval (order of 100 μs) between the two pulses usually is too short.

3.2.2 Light transmitting optics and light-sheet forming optics

The output of the laser is a thick round beam with a gaussian profile. The region of interest is a planar cross section of the flow. This necessitates the conversion of the thick round beam to a wide and thin light sheet, known as a laser-sheet. The laser sheet is created by transforming the round original laser beam by optical elements. The basic principle of such an optical arrangement is presented in Figure 3-6, with a combination of a spherical and a cylindrical lens. The originally round parallel beam is first passed through a positive long focal length spherical lens. This lens would focus the beam to a point at some distance f, equal to its focal length. However, a negative short focal length cylindrical lens is placed after the positive lens. This lens causes the beam to expand in only one direction. As a result, a triangular laser sheet is produced that focuses on a line at a distance of about f from the spherical lens and expands. The location of the measurement is at the focal distance where the

thickness of the laser sheet is narrowest and a thin cross section of the seeded flow is illuminated. Here a positive spherical lens of focal length of 500 mm in combination with a negative cylindrical lens of -25 mm focal length were used for the generation of the laser sheet.

Before the laser beam is converted to a laser sheet, it needs to be transmitted from the laser head and aligned with the plane of flow measurement. This is not generally possible by aligning the laser head directly. A more practical and safer approach is to use an articulated light arm, which receives the laser beam from the laser head and then by means of optical elements transmits the laser beam with minimal attenuation at the measurement location. The laser light arm used in this investigation was a TSI LaserPulse Light Arm 610015, shown in Figure 3-7.

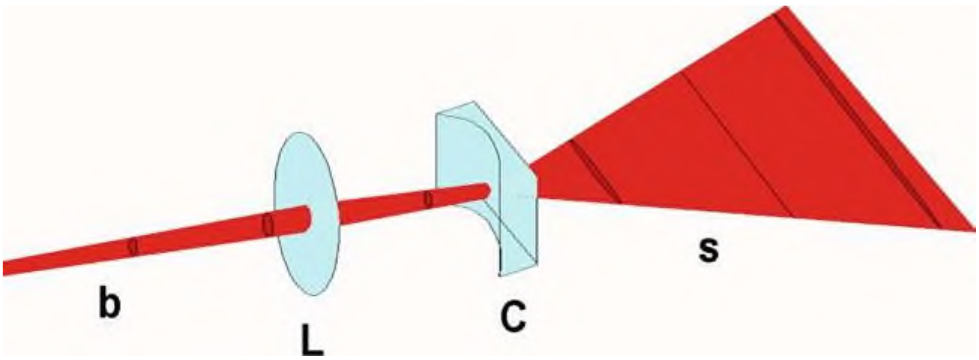

Figure 3-6: Laser sheet optics b (beam), L (spherical lens), C (cylindrical lens), S (sheet) (image source: Stamhuis [130])

Figure 3-7: TSI LaserPulse Light Arm 610015 used in this investigation. (Image from TSI web site)

3.2.3 Imaging Camera

An imaging device is required for imaging the illuminated particles on the measured flow plane. For this purpose, either CCD or CMOS cameras are commonly used. The imaging camera needs to capture

a pair of images in quick succession when the two laser pulses illuminate the particles of the seeded flow (Figure 3-8). The recording of a pair of sequential images is called frame straddling technique and for flow capturing and analysis the camera operates in the frame straddling mode. The exact interframe times, Δt, depends on the particulars of the measured flow, such as the magnitude of the flow velocities and the imaging magnification, and can be as small as a few microseconds to a few milliseconds.

The camera used in the current investigation was a TSI Powerview Plus 4MP CCD camera. The camera sensor was monochrome, as color is not required for capturing particle images, and had a resolution of 2048x2048 pixels with each pixel spanning an area of 7.4 × 7.4 μm. The dynamic range of the sensor was 12 bits meaning that it can record up to 4096 gray levels before saturation. The minimum time between successive image pairs for PIV images was 200 ns and it was able to capture up to 16 frames pairs per second.

For imaging the illuminated particles, a lens needs to be mounted to the camera. Here, a Sigma full frame imaging zoom lens with a focal length of 70-200 mm and an aperture of f/2.8 was used. In order to suppress background noise and isolate the seeding particles in the PIV images, the camera lens was fitted with a narrow bandpass filter centered on 532 nm. The filter allowed only light with a wavelength around 532 nm, such as the light of the laser sheet, to pass through and rejected all other visible light. In this way the particle images were free from light noise that originated from background sources and could interfere with the image processing software.

After the acquisition of a temporally correlated particle image pair, the acquired image pair was transferred from the camera to the control PC through a standard Camera Link cable. On the PC side the cable was connected to an X-Celera-CL PX4 frame grabber which was installed in an expansion bus slot in the computer.

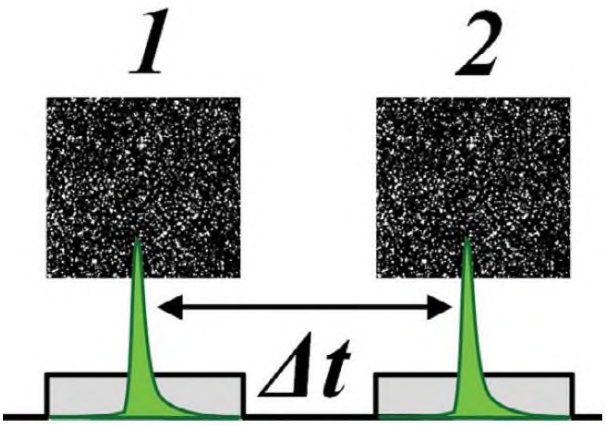

Figure 3-8: Frame straddling technique of capturing sequential images separated by Δt laser pulse time interval (Image from TSI web site)

3.2.4 Synchronizer

Coordinating the timing of the triggers of the laser was performed by a Model 610036 TSI LaserPulse Synchronizer. The synchronizer function was to control the timing of the TTL (Transistor–Transistor Logic) pulses that triggered the laser and the camera. It had 8 independent output channels and 2 input channels with 250 pico-second time resolution. By correctly timing the trigger pulses, each of the two laser light pulses was released in synch with the acquisition of each particle image by the PIV camera and at the desired time interval. (Figure 3-8)

3.2.5 PIV Image Processing

After a particle image pair has been captured, it is possible to estimate the flow field velocities by evaluating the displacement of the particles during the separation time Δt, between the images of each image pair. In PIV this is done by tracking the displacements of groups of particles rather than single particles. This is because when tracking groups of particles, the image can be divided into regular grids. Conversely, when tracking single particles, the particle locations are random. The first approach makes statistical processing of the velocities easy while in the later approach statistical processing is problematic. Additionally, tracking single particles can be problematic as single particles may have moved in or out of the imaging region between the two images. When tracking groups of particles, the addition or absence of one or two particles among many will not cause significant problems in identifying the particle pattern. Finally, it is relatively easy to match the pattern of a group of particles between two images while it is difficult to identify the displacement of individual particles as all single particles appear identical.

For processing purposes, the first image of the image pair is divided in a regular grid of small sub-image regions, typically of 16x16, 32x32 or 64x64 pixels, called interrogation windows each containing a group of particles that form a unique pattern. Subsequently, the location of this particle pattern is searched for in the second image of the image pair. The sub-region of the second image where the pattern of the particles of an interrogation window of the first image is searched, is called search window and it is as wider than the interrogation area as the maximum displacement of the particle pattern is expected to be.

Matching the particle patterns of the interrogation window of the first image within the search window in the second image is accomplished by correlating the light intensity pattern of the interrogation window with the light intensity pattern of sub-regions within the search window in the second image. The correlation coefficient between the intensities of the N × N pixel wide interrogation window and the intensities of each of the $(M-N+1)^2$, N × N pixel sub-regions of the M × M search area is calculated as:

$$\sigma(\Delta x,\Delta y)=\frac{\sum_{i=1}^{N}\sum_{j=1}^{N}\left[I(i,j)-\bar{I}\right]\cdot\left[I'\left(i+\Delta x+(M-N)/2,\ j+\Delta y+(M-N)/2\right)-\bar{I'}\right]}{\sum_{i=1}^{N}\sum_{j=1}^{N}\left[I(i,j)-\bar{I}\right]^2\cdot\sum_{i=1}^{N}\sum_{j=1}^{N}\left[I'\left(i+\Delta x+(M-N)/2,\ j+\Delta y+(M-N)/2\right)-\bar{I'}\right]^2}$$

where Δx and Δy are the horizontal and vertical pixel displacements of the interrogation area in the search area, I the intensity of the pixels of the interrogation area and I' the intensity of the pixels in the search area. An example is presented in Figure 3-9 showing the tracing of a 4px × 4px interrogation window within an 8px × 8px search area to produce a 5px × 5px correlation map.

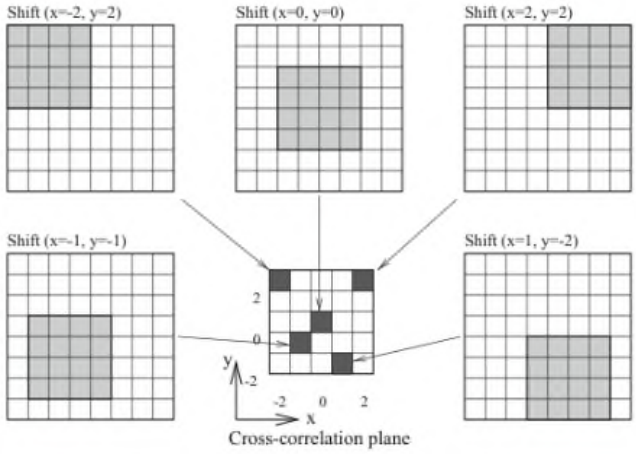

Figure 3-9: Tracing of a 4px × 4px interrogation area within an 8px × 8px search area to produce a 5px × 5px correlation map. The central matrix is the correlation map. (Image source [131])

The value of the correlation coefficient for each combination of horizontal and vertical displacement of the interrogation area in the search area is stored in the correlation coefficient map, whose size is M-N+1 × M-N+1. The pixel displacements which correspond to the greatest value of the correlation coefficient in the correlation coefficient map are considered to represent the best estimate of the particle displacement. This is demonstrated in Figure 3-10.

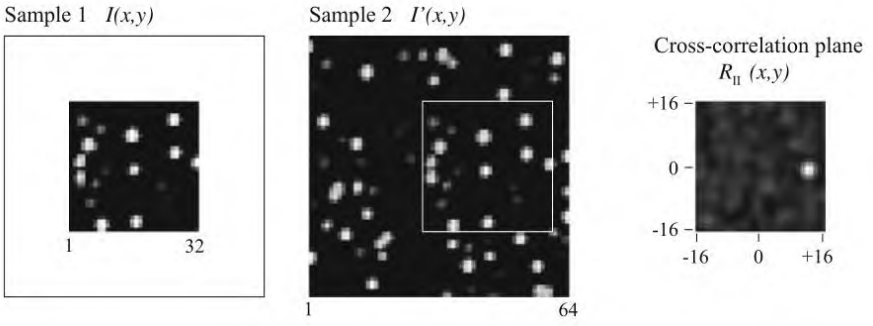

Figure 3-10: Finding the displacement of a group of particles of first image, in the second image. The correlation map of all possible displacements, identifies the displacement that best matches the particle pattern in both images (Image source [131])

Ultimately the velocity of particles in the interrogation window can then be estimated as

$$u = C\frac{\Delta x}{\Delta t}, \qquad v = C\frac{\Delta y}{\Delta t}$$

with C being a calibration constant with dimensions m/px and corresponds to the physical size of a pixel in the imaging plane.

A shortcoming of the evaluation of the flow velocities with PIV, is that the particle displacements that are determined is in integer pixels. Therefore, the velocities are evaluated in rather coarse step increments. In order to address this drawback, the correlation coefficient in the region of the correlation peak is fitted to a gaussian function as shown in Figure 3-11. In this way a smooth function of the correlation coefficient is obtained and an improved estimation of the particle displacement can be obtained from the peak of the gaussian function that includes sub-pixel displacements. This approach can increase the accuracy of the PIV velocity evaluation by an order of magnitude and resolve the aforementioned shortcoming.

The PIV images acquired during the measurements were processed by the PIV engine of the TSI Insight 3G software.

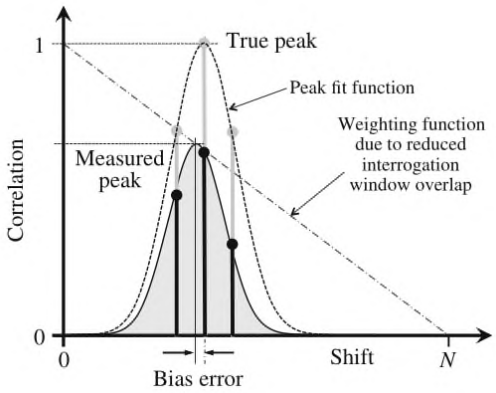

Figure 3-11: Improvement of the PIV velocity estimation by fitting the correlation coefficient to a gaussian function. (Image source [131])

3.2.6 Seeding

The PIV method uses tracer particles to seed the flow and measures the displacements of these particles in the flow. Therefore, the velocities obtained from PIV are actually those of the tracer particles rather than the velocities of the carrier fluid. If the particles are too large and heavy then the

particle inertia will be too great for the particles to follow the changes of the flow closely and the PIV measurements will be erroneous.

In order to assure that the measured particle velocities correspond to the carrier gas flow velocities, the tracer particles need to be very small. At the same time, there is a limitation to the lower value of their size since very small particles will be difficult to visualize as they do not scatter light well. This is because the scattering intensity from a particle is approximately proportional to the surface area ($\sim D^2$) of the particle. For gases, such as air, liquid particles are commonly used with sizes in the range of 0.5-2.0 μm [131].

The particles used in this investigation were produced by a Prosound N41DZ 400W smoke generator. The smoke generator used a water solution to produce liquid particles with diameters in the order of 1 μm which were deemed very suitable to follow the flow within the box of turbulence and of the jets closely.

3.3 Computational Fluid Dynamics

In the last decades, significant progress has been made in the field of Computational Fluid Dynamics (CFD). This progress has been boosted by the development of robust engineering and scientific models for the solution of the equations describing the mean and turbulence quantities of the flow in conjunction with the increase in computational resources. The implementation of computation techniques for simulating a particular flow can save a large amount of manpower, which otherwise would be directed to extensive experiments in the laboratory. Moreover, CFD can fill the gap where experimental shortcomings or uncertainties take place. In addition, CFD offers the possibility for both primary estimation and extensive parametric study of the flow, which can highlight the most important or complex characteristics of the phenomena, where the engineer shall investigate more analytically. Consequently, the investigator may focus the experimental efforts in these most crucial areas of his research that demand rigorous experimental proof and validation.

Having the above notions in mind, it was decided that a parallel CFD analysis of the phenomena examined by the current thesis would be appropriate. Cross-validation between CFD and experiment offers the possibility for improvements in the experimental setup and the exposure of inherent weaknesses of the CFD models. At the same time, observations from the available literature shall be present in this procedure to provide an overall assessment of the results.

In order for the above investigation to be as reliable as possible, a suitable CFD approach had to be chosen based on the characteristics of the flow, the scope of the analysis and the restrictions of available time and computational resources. The choice of the CFD methods in the current thesis will be analyzed in the next paragraphs.

3.3.1 DNS, LES, RANS Models

There is a variety of available choices in executing numerical simulations in fluid dynamics. The researcher may choose the appropriate method, based on the applicability of its method in calculating the quantities of the phenomena relatively reliably, and the demands in computational power that the method imposes. There are three main categories of CFD methods: Direct Numerical Simulation (DNS), Large Eddy Simulation (LES), Reynolds Averaged Navier-Stokes models.

3.3.1.1 DNS

DNS methods aim at computing the motion of every eddy in the flow from the largest to smallest at every time and space point, by integrating numerically the Navier-Stokes equations. These methods do not use the statistical description of turbulence in the form of Reynolds decomposition. As a result,

they attempt to provide every spatial and temporal detail of flow field, which seems to be the ultimate wish of the scientist.

Trying in a deterministic approach to reach solutions of the Navier-Stokes equations, which are characterized by their nonlinear behavior requires advanced numerical techniques and vast computational resources. The great advances in computer science of the last decades gave high hopes for the availability of computer power corresponding to the needs of DNS. However, the reality came to contradict such hopes for the widespread use of DNS in CFD. The main obstacles in the progress of DNS arise from the following observations:

- The typical number of grid points and computer time for executing a DNS are provided below:

$$N_x^3 \sim (\frac{L_{BOX}}{l}) \mathrm{Re}^{9/4} \quad 1.84$$

$$\text{computational time} = N_x^3 N_t \sim (\frac{T}{l/u})(\frac{L_{BOX}}{l})^3 \mathrm{Re}^3 \quad 1.85$$

, N_x representing the number of grid points in one direction, L_{BOX} the size of the computational domain in the same direction, l the corresponding integral length scale, N_t the minimum number of time steps, u an appropriate scale for the turbulent velocity u' and T the total duration of the simulated phenomenon. It is evident that increase in Re in the levels of practical engineering and applied physics lead to huge computational time.

- According to Moore's law, maximum computer speed doubles every 18 months. This permit doubling of maximum Re_λ every decade.

As a result, DNS remains mainly a scientific tool applied to very simple geometries, mainly involving homogeneous turbulence in the absence of solid boundaries, where the computational domain and the total duration do not include many length scales and eddy turnover times respectively.

3.3.1.2 LES

LES methods offer the possibility for numerical predictions by integrating the Navier-Stokes equations, but at a reduced computational cost in comparison with DNS. However, the reduced computational demands are accompanied by decreasing the range of information describing the flow quantities. In practice, an LES estimates the flow motion down to a certain scale. As a result, the methods are named after the "large eddies" of the flow that they can capture accurately, leaving the contribution of the smaller scales kinetic energy to be modeled by approximation. The potential of LES rests on the fact that from the engineer's point of view the large scales of the motion contain the largest portion of

energy (80% for a good LES) and are of practical importance. Nevertheless, there are cases where the behavior of smaller scales cannot be neglected at near boundaries. Furthermore, in cases where the range of the dynamically important scales is broad enough, the required computational power is increased dramatically, making LES cost ineffective. The implementation of LES is based on the idea of filtering out the small scales. The filtered velocity is denoted by u and the corresponding small scale residual components by u'. We shall underline the fact that $\bar{u}_i$ is not the mean motion as in the case of RANS but represents the mean motion including the large-scale fluctuations and as a result is time dependent. The overall set of filtered equations of motion has the general form below:

$$u = \bar{u}_i + u_i' \tag{1.86}$$

$$\frac{\partial \bar{u}_i}{\partial t} + \frac{\partial (\bar{u}_i \bar{u}_j)}{\partial x_j} = -\frac{1}{\rho}\frac{\partial \bar{p}}{x_i} + \frac{1}{\rho}\frac{\partial \tau_{ij}^R}{\partial x_j} + \nu \nabla^2 \bar{u}_i \tag{1.87}$$

$$\tau_{ij}^R = \rho[\bar{u}_i \bar{u}_j - \overline{u_i u_j}] \tag{1.88}$$

The residual tensor $\tau_{ij}^R$is modeled using an eddy viscosity model (see next paragraph details about eddy viscosity), transforming the above set of equations to their final form for the Smagorinsky model:

$$\tau_{ij}^R = 2\rho \nu_R \bar{S}_{ij} + \frac{1}{3}\delta_{ij}\tau_{kk}^R \tag{1.89}$$

$$\frac{\partial \bar{u}_i}{\partial t} + \frac{\partial (\bar{u}_i \bar{u}_j)}{\partial x_j} = -\frac{1}{\rho}\frac{\partial \overline{p^*}}{x_i} + 2\frac{\partial}{\partial x_j}[(\nu + \nu_R)\bar{S}_{ij}] \tag{1.90}$$

The eddy viscosity ν_R shall be estimated in the form:

$$\nu_R \sim l(v_L^2)^{1/2} \tag{1.91}$$

where v_L^2 represents the turbulent kinetic energy and l the size of the large eddies in the flow. In the case of the Smagorinsky model, the eddy viscosity is estimated as:

$$\nu_R = C_S^2 l^2 (2\bar{S}_{ij}\bar{S}_{ij})^{1/2} \tag{1.92}$$

3.3.1.3 RANS-Boussinesq-Prandtl Theory

In sections 2.1.1 and 2.1.2, the concept of Reynolds decomposition was introduced and aided in the statistical description of turbulence through the RANS equations. As a result, a statistical quantity $\tau_{ij} = -\rho\overline{u'_i u'_j}$, called the Reynolds stress tensor has emerged. The Reynolds stresses represent the influence of the turbulence in the mean transport of momentum. It was shown also through the kinetic

energy budget, how these stresses extract energy from the mean flow raising the turbulent kinetic energy of the eddies. Although a path has been opened towards the isolation of the effects that the turbulence imposes on the mean flow, there has been a catch, called the closure problem; the Reynolds stress tensor contains six new unknowns to the existing set of equations.

A response to the closure problem comes from the combined theory of Boussinesq and Prandtl, which in its general form is summarized in the two equations below:

$$\tau_{ij} = 2\rho\nu_t S_{ij} - (\rho/3)(\overline{u_k' u_k'})\delta_{ij} \quad 1.93$$

$$\nu_t = l_m V_T \quad 1.94$$

Equation 1.93 is attributed to Boussinesq, who relates the turbulent quantities to the mean strain tensor, by the introduction of a new term ν_t, called eddy viscosity. Eddy viscosity is based on the assumption that the momentum exchange through eddies resembles the microscopic momentum exchange through molecules. Equation 1.94 is attributed to Prandtl, who influenced by the kinetic theory of gases suggested an estimation of eddy viscosity analogous to the kinematic viscosity $\nu=1/3\cdot(lV)$, l being the mean free path of the molecules and V their rms velocity. Prandtl's approximation is known as mixing length theory after l_m, representing the probable eddy motion of a lump of fluid and V_T, a measure of the rms velocity u' or $k^{1/2}$. This means that the more energetic are the eddying motions leads to increased momentum transport through turbulence, an assumption that sounds reasonable. Furthermore, we can relate l_m with the integral length scale of the flow, since the large eddies are responsible for the largest portion of momentum exchange.

The Boussinesq-Prandtl theory led the path for the development of semi-empirical models for making the RANS equations a closed system of equations, since equation 1.94, needs some input data based on existing information for the integral length scale and the estimate of the turbulent kinetic energy of particular flows, when applied. Despite also the crude approximation between molecular transport and eddy momentum transport, the RANS closure models have exhibited quite success for CFD simulations from the engineer's point of view and needs for accuracy levels. Despite several weaknesses that will be discussed in the next paragraphs, the production of reliable results for the needs of engineer in computational time, orders of magnitude less than DNS and LES, have established RANS models the most popular choice for the simulation of flow problems.

3.3.2 k-ε model

Among the several RANS models, the k-ε model stands out as the most successful and widely used. It has been named after k and ε, which are the inputs for modeling the eddy diffusivity, since equation 1.94 can take the alternative form of:

$$\nu_t \sim \frac{k^2}{\varepsilon} \tag{1.95}$$

For the case of the standard k-ε model, the RANS is closed by adding equation 1.93 and the following set of equations:

$$\nu_t = c_\mu k^2 / \varepsilon \tag{1.96}$$

$$\frac{\partial k}{\partial t} + (U \cdot \nabla)k = \nabla \cdot \left[(\nu + \frac{\nu_t}{\sigma_k})\nabla k \right] + G - \varepsilon \tag{1.97}$$

$$\frac{\partial \varepsilon}{\partial t} + (U \cdot \nabla)\varepsilon = \nabla \cdot \left[(\nu + \frac{\nu_t}{\sigma_\varepsilon})\nabla \varepsilon \right] + c_1 \frac{G\varepsilon}{k} - c_2 \frac{\varepsilon^2}{k} \tag{1.98}$$

, $G = (\tau_{ij}/\rho)S_{ij}$ representing the production term in the turbulent kinetic energy budget. The values of the coefficients, which often suffice for the most simple shear flows are taken as: c_μ=0.09, σ_ε=1.3, σ_k=1, c_1=1.44, c_2=1.92.

Although the k-ε model has been proven a powerful and successful tool in the hands of engineers, as a product of the eddy diffusivity theory, it inherits its main deficiencies, which are summarized below:

- The assumption of a scalar eddy diffusivity is not valid in strong anisotropic turbulence.
- For one-dimensional shear flow, where S_{ij}=0, the normal Reynolds stresses are predicted to be equal, which is not always valid.
- The Reynolds stress tensor is exclusively related to the local mean strain rate, neglecting the history of turbulence straining. This gives disputed results, in cases where rapid straining of the flow occurs.

3.3.3 Realizable k-ε model

The realizable k-ε model is a more recent model that remedies some weaknesses of the standard k-ε, as experience has revealed. The realizable k-ε:

- Performs better for flows with large pressure gradient, strong separation, high swirl and large streamline curvature.
- addresses the inaccurate prediction of the spreading rate of round jets.

- In the case of stagnating flows does not predict excessive values of k.

The model is called realizable because the standard k-ε leads to negative values of $u_i^{'2}$, when there is large strain rate. For example, using the Boussinesq approximation, this happens when:

$$u'^2 = \frac{2}{3}k - 2\nu_t \frac{\partial U}{\partial x} < 0 \Leftrightarrow \frac{k}{\varepsilon}\frac{\partial U}{\partial x} > \frac{1}{3c_\mu} \quad 1.99$$

The realizable k-ε fixes this issue by making c_μ a variable. The other difference of the k-ε realizable is in equation 1.98, which is transformed as:

$$\frac{\partial \varepsilon}{\partial t} + (U \cdot \nabla)\varepsilon = \nabla \cdot \left[(\nu + \frac{\nu_t}{\sigma_\varepsilon})\nabla \varepsilon \right] + c_1 \cdot \varepsilon \cdot \sqrt{2S_{ij}S_{ij}} - c_2 \frac{\varepsilon^2}{k + \sqrt{\nu\varepsilon}} \quad 1.100$$

The constants for the model are c_2=1.9, σ_κ=1.0, σ_ε=1.2 and $c_1 = max[\,0.43, \frac{\eta}{\eta+5}], \eta = S\frac{k}{\varepsilon}, S = \sqrt{2S_{ij}S_{ij}}$.

As mentioned above, C_μ is not a constant, but a function of mean strain rate, rotation rates and angular velocity of the system rotation. Presenting the analytical expression of the equations producing C_μ, is out of the scope of this thesis, which focuses on the end results of the implementation of such a model, rather than the manipulation and analysis of CFD techniques. For more details on the function of C_μ, the reader can refer to Ansys Fluent Theory Guide. The presentation of equations 1.95 - 1.100 aim at giving a general background of how the closure problem is confronted by RANS k-ε models and therefore to show their usefulness and applicability.

3.3.4 k-ω model

The k-ω model has become a very popular RANS model in recent years, since it has exhibited superior performance for free shear flows and low Re number flows compared to the k-ε family models. It is often used when accurate resolution of the boundary layer is a necessity and has also provided satisfactory results for impingement studies. Thus, it is considered appropriate for the opposed jets case study in the current thesis. The k-ω model is an eddy diffusivity model, that instead of solving for ε, we solve for the quantity ω=ε/k, which is called either specific dissipation rate or inverse time scale. The equations for the standard k-ω model are given below:

$$\nu_t = ak/\omega \quad 1.101$$

$$\frac{\partial k}{\partial t} + (U \cdot \nabla)k = \nabla \cdot \left[(\nu + \frac{\nu_t}{\sigma_k})\nabla k \right] + G - \beta^* f_{\beta^*} k\omega \quad 1.102$$

$$\frac{\partial \omega}{\partial t} + (U \cdot \nabla)\omega = \nabla \cdot \left[(\nu + \frac{\nu_t}{\sigma_\omega})\nabla \omega \right] + \alpha \frac{\omega}{k} G - \beta f_\beta \omega^2 \quad 1.103$$

For the definition of α, σ_k, σ_ω, β, β^*, $f_\beta{}^*$, f_β, the reader is referred to Ansys Fluent Theory Guide [132]. In our case a variant of the above model will be used called the SST k-ω model. This model ameliorates the standard (Wilcox) model by in a sense that approaches the effectiveness of k-ε model for the free stream case of developed turbulence and adverse pressure gradients.

3.3.5 Reynolds Stress Model

Although the realizable k-ε and k-ω model solves some of the issues relating with the simpler form of the standard k-ε model, remedying the round jet anomaly and insufficiencies relating to large strain rates, turbulent quantities for anisotropic flows still cannot be treated. The solution to this problem comes from the Reynolds Stress Model (RSM), which can provide us with the detailed field of Reynolds stresses in an anisotropic flow. Although, it is the most sound and analytical of the RANS models, these characteristics make it the more difficult for implementation in terms of convergence of the solution. Nevertheless, still being a RANS model seems to have an advantage over LES, when it comes to limited computer resources and in cases where the simulation of the flow near boundaries is important for the investigator.

Summing up the features of CFD methodologies provided in the previous paragraphs, we can reach the following conclusions.

- DNS is the more analytical method, capturing the whole range of scales. However, it demands huge computational power, thus being restricted to modest to low Reynolds number for experimental flow geometries, which do not apply to industrial flows.
- LES solves the large scale eddies of the turbulence, which are important from an engineering perspective. As a result, it shows great potential when the computational source permits it.
- The RANS methods remain until today the preferred method for CFD simulations due to the low computational cost and their reliable predictions, when high levels of detail and accuracy are not the main scope. The k-ε model is the most prominent among them, with its realizable version addressing several weaknesses of the standard one, such as the spreading rate of the round jet. On the other hand, if the estimation of the anisotropic nature of the turbulent Reynolds stresses cannot be neglected, the more sophisticated RSM model finds a place in the simulation.

3.3.6 Implementation of CFD

In our case, computational resources were limited. As a result, implementing RANS simulations of the flow emerged as the only choice. Based on the characteristics of the models as described in this

paragraph, a hybrid approach combining the k-ε realizable model and the Reynolds stress model was chosen as the suitable one for the jets study. Initially the mean flow was obtained using the k-ε realizable model. Afterwards, maintaining the results for the mean flow, the turbulent properties were only calculated using the RSM model. In such a way, the solution both for the mean flow and the anisotropic turbulence properties of the jet converged in reasonable computing time. Furthermore, for the case of opposed jets deviations from the experimental results were observed using the above approach. Thus, some additional trials took place by replacing the k-ε realizable with the k-ω model. For the above implementation, the commercial software ANSYS Fluent was used. For the convergence of the solution in each case the criterion was the residual of each quantity to reach the value of 10^{-6}.

In order for the convergence of the solution to be successful a proper meshing of the geometry was necessary. The symmetry of the configuration permitted the construction of a well-structured mesh, using hexahedral elements, Figure 3-12. The assessment of the mesh quality was made based on the criteria for minimum orthogonal quality>0.1 and maximum skewness<0.95 [133]. The density of the mesh elements was adjusted using edge sizing (Figure 3-12) in the periphery of the jet exit orifice, where a velocity inlet boundary condition was imposed and in the outer periphery of the cylindrical domain. In its face of the domain a pressure outlet boundary condition was set, with a constant pressure value equal to the atmospheric. To further adjust the density of the elements in the streamwise direction a facing method size was used.

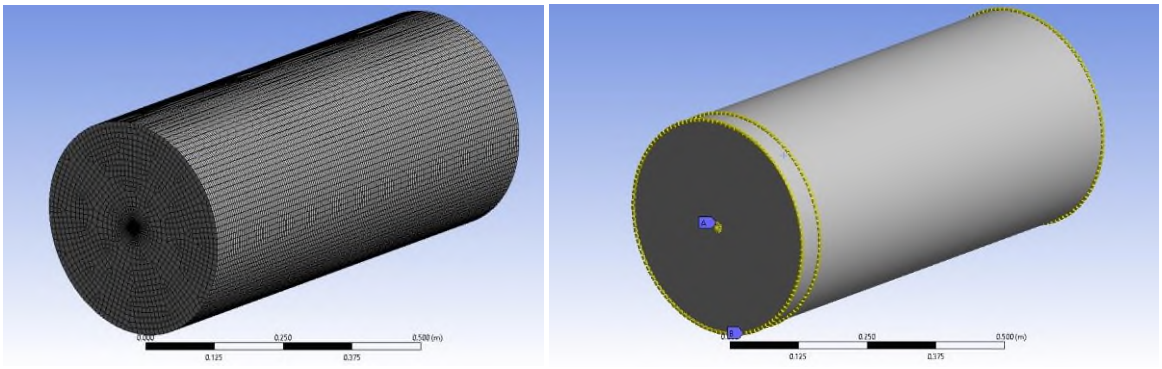

Figure 3-12: Meshed geometry for the case and impose edge sizing in the nozzle exit (velocity inlet boundary condition) in the case of the single jets case

In the case of the single jets, the results provided in Chapter 4, are based on a mesh consisting of 1676147 nodes and 409190 elements, having average orthogonal quality of 0.988, which is considered excellent and a minimum orthogonal quality 0.751, which is considered very qood according to Ozen [133]. Furthermore, the average skewness was 0.111, which is considered excellent and the maximum 0.678, which is considered good, according to the same author [133]. In order for the results to be considered mesh independent, two extra sets of simulations were run for Re 3300 and Re 9900, one with 1174493 nodes and 285790 elements and another with 6360911 nodes and 1563375 elements.

There was no variation among the results provided by the three mesh configurations. Consequently, the results chosen to be presented in Chapter 4, are considered mesh independent and was the best compromise in terms of spatial analysis and computational time.

In the case of the opposed jets, were the L/d_e ratio of the distance between the jets was set equal to 5, the results provided in Chapter 5, are based on a mesh consisting of 2268467 nodes and 522840 elements, having average orthogonal quality of 0.990, which is considered excellent and a minimum orthogonal quality 0.673, which is considered qood according to Ozen [133]. Furthermore, the average skewness was 0.008, which is considered excellent and the maximum 0.734, which is considered good, according to the same author [133]. As in the case of the single jets, in order for the results to be considered mesh independent, two extra sets of simulations were run for Re 3300 and Re 9900, one with 1164373 nodes and 326231 elements and another with 8527353 nodes and 1776560 elements, without showing significant variation.

In the case of the opposed jets, were the L/d_e ratio of the distance between the jets was set equal to 7.5, the results provided in Chapter 5, are based on a mesh consisting of 3104842 nodes and 759390 elements, having average orthogonal quality of 0.990, which is considered excellent and a minimum orthogonal quality 0.673, which is considered good according to Ozen [133]. Furthermore, the average skewness was 0.008, which is considered excellent and the maximum 0.734, which is considered good, according to the same author [133]. As in the case of the single jets, in order for the results to be considered mesh independent, two extra sets of simulations were run for Re 3300 and Re 9900, one with 140517 nodes and 450757 elements and another with 9819572 nodes and 2237426 elements, without showing significant variation.

4. Single axisymmetric jet

A study of the flow-field of a single axisymmetric pipe jet was deemed necessary at first before proceeding to the opposed flow configuration. Such an investigation provides a more thorough understanding of the flow characteristics of each jet in the range of interest of Re numbers. Thus, the validation of the experimental and computational methods employed for the study in opposed flow configuration is rendered more reliable. In addition, some of the underlying mechanisms that form the stagnation region characteristics in the opposed flow are exposed by this preliminary study of the single jet. Furthermore, it should be noted that the phenomena under investigation take place in the near to intermediate field of the jets [1-16]d_e. Consequently, as described in section 2.2.6, many uncertainties arise regarding the flow features (length of the potential core, initiation of self-similarity, effect of Re number and surrounding environment on the spreading and entrainment rate of a jet). Thus, to assume certain characteristics of the flow examined in this thesis for-granted based on a universal theory is not possible. A rigorous and analytical study of the parameters described in the preceding literature review in the case of specific flows established in this thesis is considered mandatory.

4.1 Preliminary assessment of single jet behavior without HIT

The graphic representation of the flow properties based on the contours of mean and turbulent velocities as visualized by PIV enables a preliminary assessment of the single jet behavior based on exit Re number. In this way we can differentiate the jets flow into range, laminar and turbulent. The first range includes the cases of Re 1100 and 2200, while the second range includes Re 3300 to 9900 (with Re 3300 and 4400 being not fully turbulent). This categorization facilitates the subsequent more thorough investigation of turbulent jets and their interaction with surrounding turbulence, which is the main objective of the thesis. From section 4.2 and on, the focus will be given to jets with Re>2200 in the turbulent range results, since literature (section 2.2) focuses on the axisymmetric turbulent jets. Furthermore, the CFD models tested are characterized as turbulent and are not applicable to laminar flows. However, the distinction between the two ranges has to be demonstrated by appropriate evidence. This evidence comes from the jet images of Figure 4-1. It is obvious that, above Re 3300, after a small distance near the exit, the jet spreads in the cross-stream direction in the same manner irrespectively of Re as a turbulent jet. However, for Re 1100 the jet boundaries coincide with the exit diameter for the whole distance captured, indicating a laminar behavior, whereas for Re 2200 the jet remains laminar until about $10d_e$ where it starts to spread in the ambient surroundings.

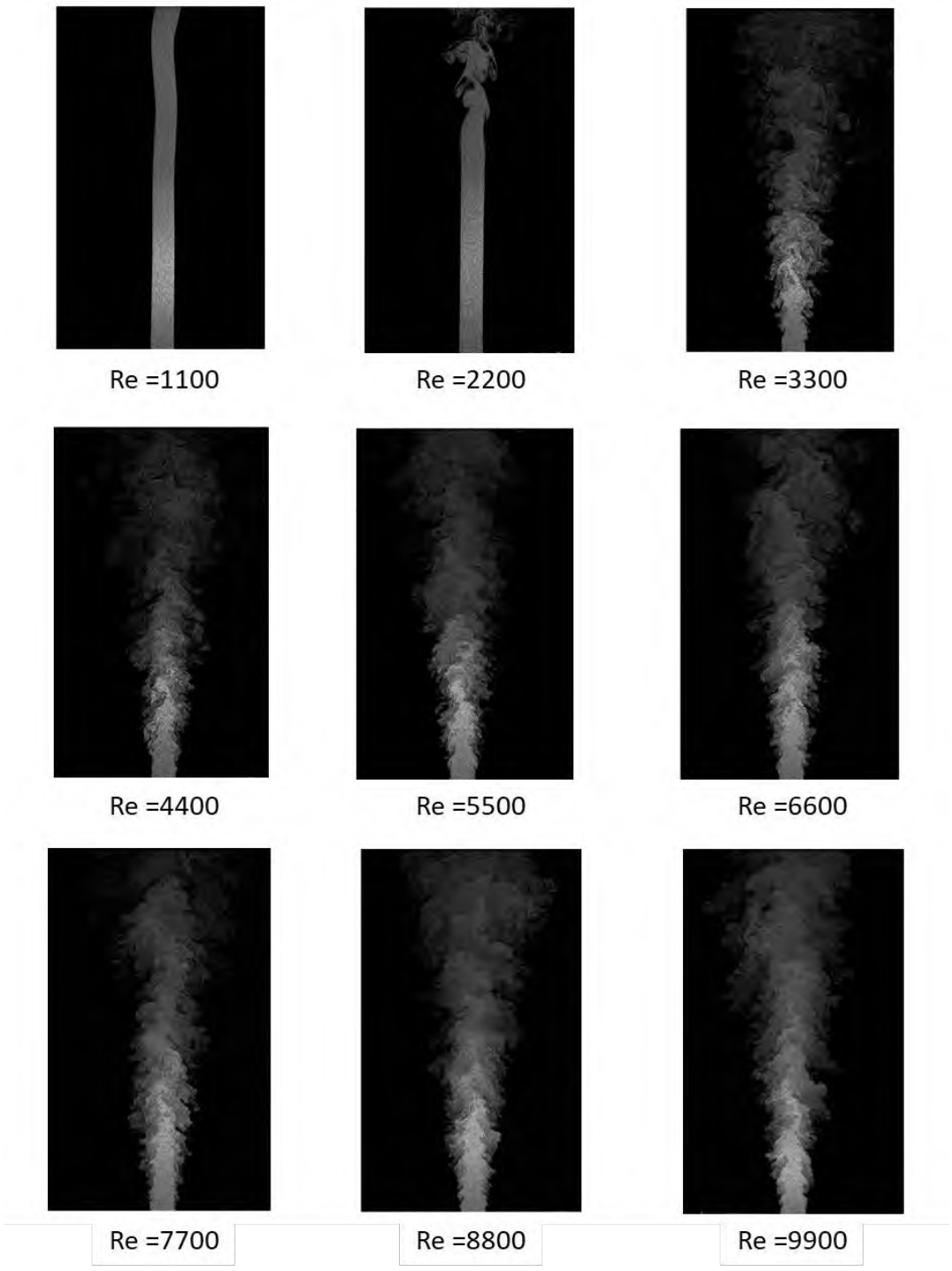

Figure 4-1: Jet images of a single jet for each Re number. The jet diameter at the nozzle exit is 12.8mm.

To further validate the differences between the lowest Re numbers 1100, 2200 and the rest of the cases, the mean velocity and rms velocity contours of the streamwise U and cross-stream V velocities are presented in Figure 4-2 through Figure 4-5. Similarly to the visualization of Figure 4-1, there is clear

differentiation between the laminar and a representative fully turbulent jet of Re 7700 jets shown in Figure 4-6 through Figure 4-9. The jet retains its initial laminar exit mean velocity profile until the end of the measured domain for Re 1100 and the rms values are very small, verifying the laminal behavior of the jet. In the case of Re 2200, there is a delayed breakup of the laminar flow at $10d_e$, which is accompanied by elevation of turbulence levels as expressed by the rms values.

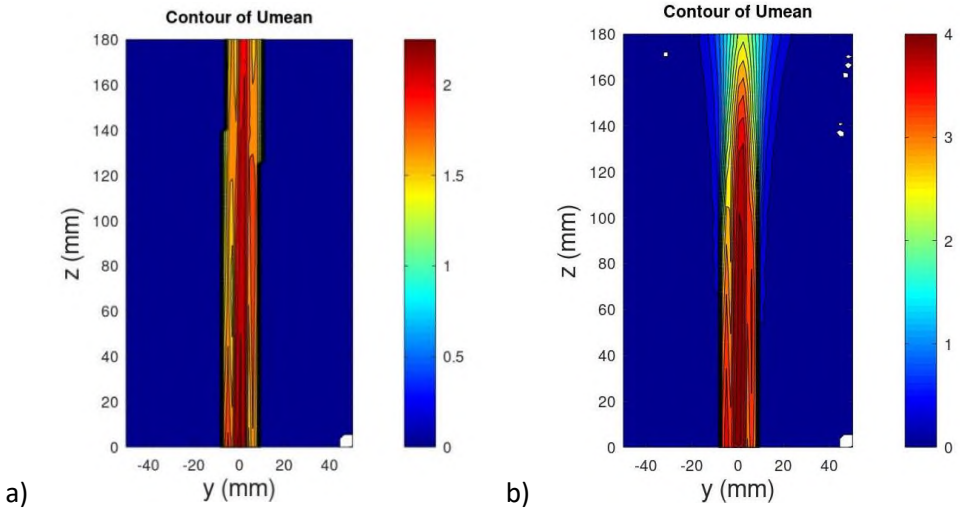

a) b)

Figure 4-2: Contour of mean streamwise velocity U, a) Re 1100 PIV, b) 2200 PIV

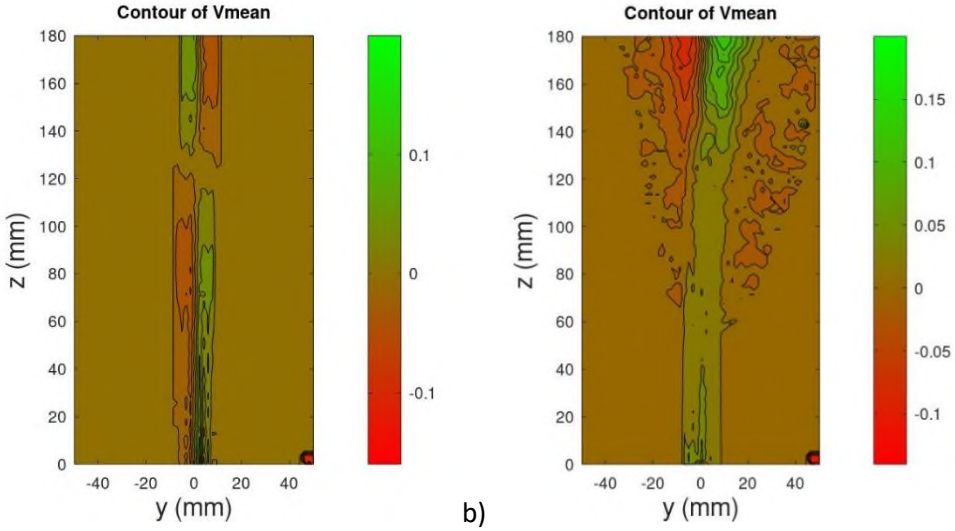

a) b)

Figure 4-3: Contour of mean cross-stream velocity V, a) Re 1100 PIV, b) 2200 PIV

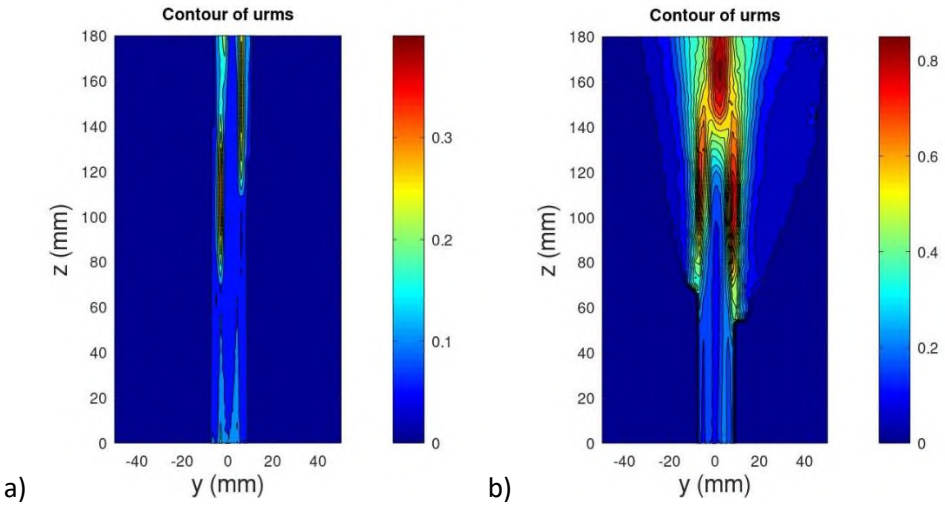

a) b)

Figure 4-4: Contour of turbulent streamwise velocity u_{rms}, a) Re 1100 PIV, b) 2200 PIV

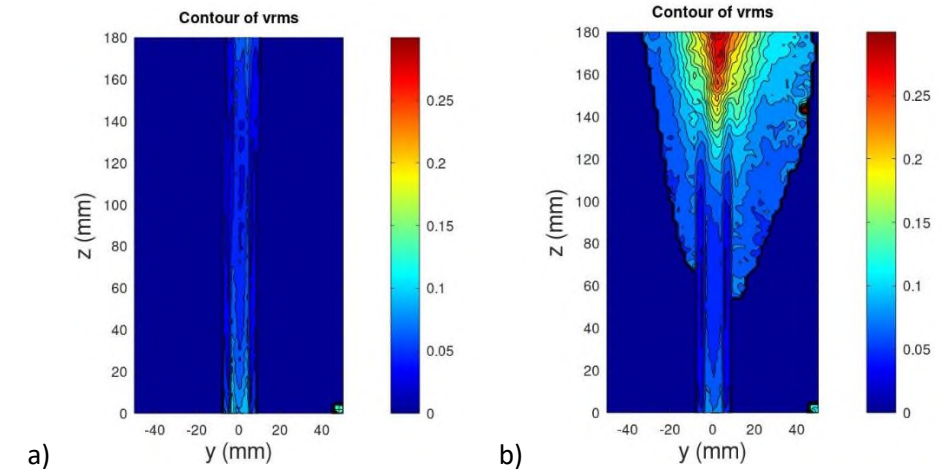

a) b)

Figure 4-5: Contour of turbulent cross-stream velocity v_{rms}, a) Re 1100 PIV, b) 2200 PIV

After the examination of the lower Re number jets, where laminar characteristics of the flow exist, we proceed in the examination of the higher Re number jets where turbulent flow is expected. A series of representative contours taken from the case Re 7700 provide a first glance on how the mean velocity and turbulent velocity fluctuations of an axisymmetric turbulent jet evolve. Figure 4-6 through Figure 4-9 provide the contours of mean and turbulent streamwise and cross-stream velocity U, u_{rms}, V and v_{rms}, from both PIV measurements and CFD simulation. In all contours there is qualitative agreement of the flow development between PIV and CFD.

From Figure 4-6, an initial region that extends to approximately $5d_e$, where the U component is nearly constant and equal to exit velocity U_e is distinguished. After that region, the U component decays and the jet spreads outwards.

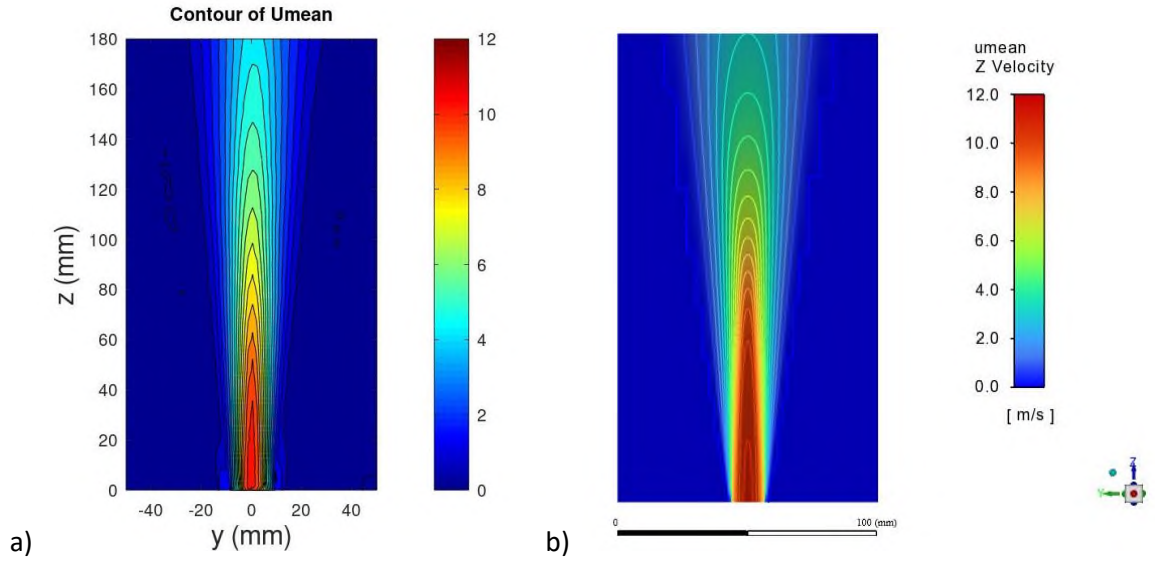

Figure 4-6: Contour of mean streamwise velocity U, Re 7700 a) PIV, b) CFD

As the jet spreads, an increase of the cross-stream component V (Figure 4-7) is observed in the radial direction. The magnitude of the V component increases symmetrically starting from the zero value on the centerline and then drops gradually again until the surrounding environment is reached.

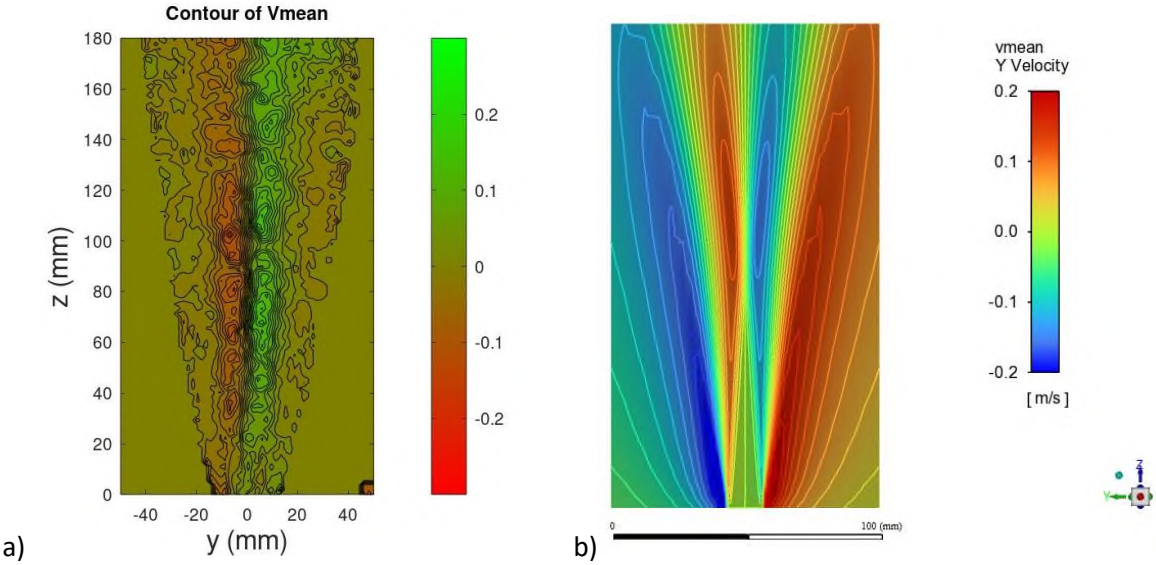

Figure 4-7: Contour of mean cross-stream velocity V, Re 7700 a) PIV, b) CFD

The fluctuating velocities u_{rms}, present off centerline symmetrical peaks (Figure 4-8), with large magnitude surrounding the potential core of the jet. This is the region of strong shear between the ambient fluid and the higher momentum jet flow. Subsequently, two symmetrical mixing layers merge and the spreading of a self-similar axisymmetric jet occurs.

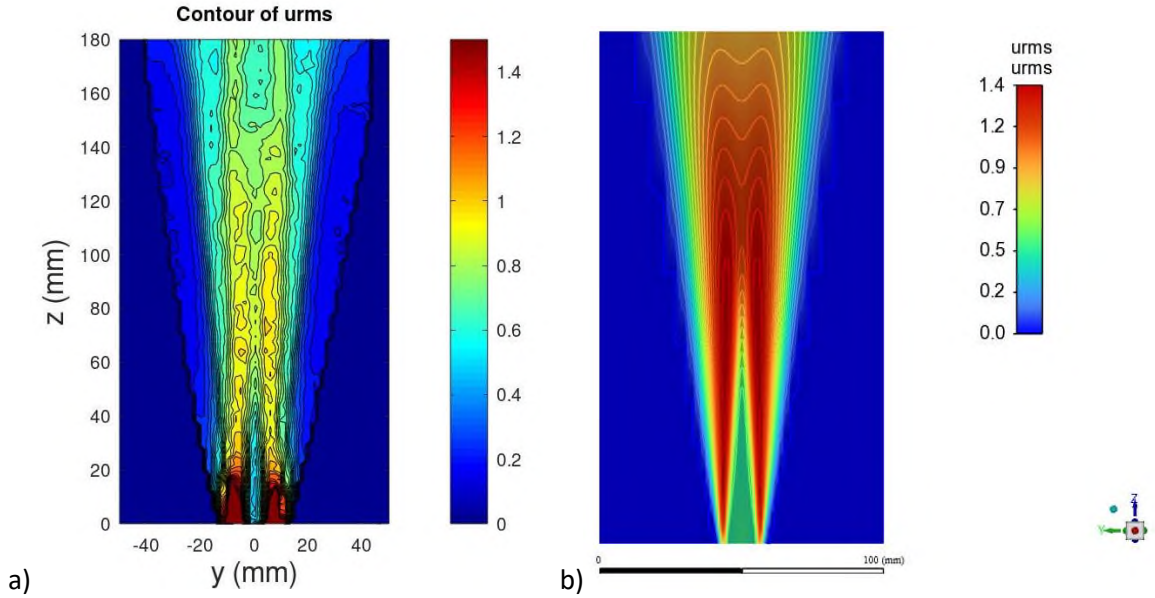

Figure 4-8: Contour of turbulent streamwise velocity u_{rms}, Re 7700 a) PIV, b) CFD

Figure 4-9 shows that v_{rms} follows the behavior of u_{rms}, in lesser degree however as presented by the PIV measurements. Furthermore, the magnitude of v_{rms} is smaller than u_{rms} exposing the anisotropic nature of the jet flow.

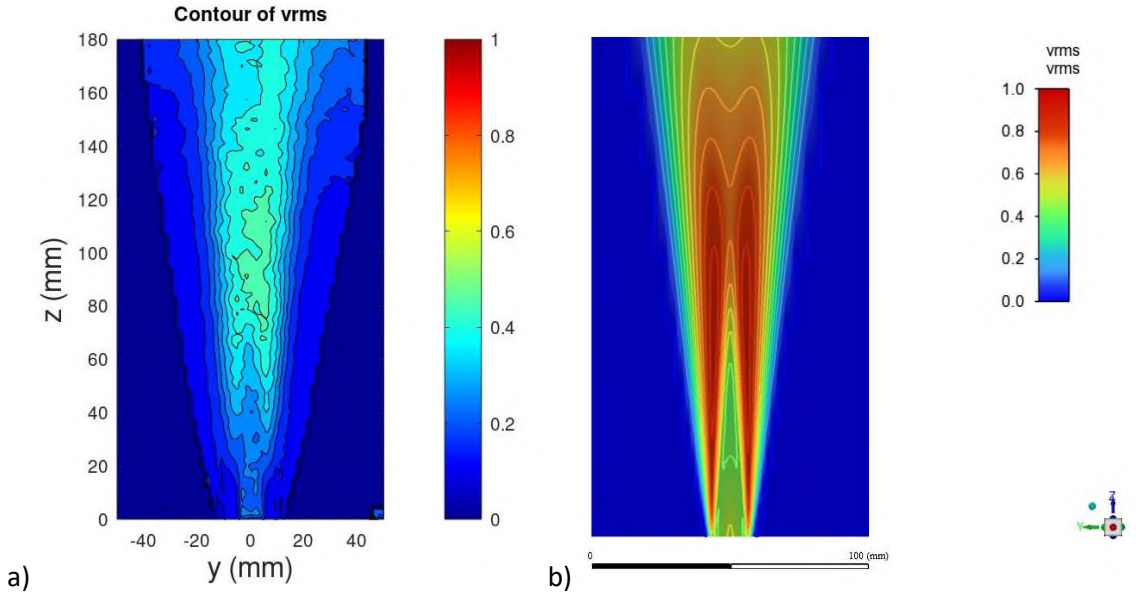

Figure 4-9: Contour of turbulent cross-stream velocity v_{rms}, Re 7700 a) PIV, b) CFD

From this introductory part, it is evident that the observations provided in the literature review in section 2.2 seem to be validated by the present results. Nevertheless, a rigorous study requires a more thorough investigation of the characteristics of our particular flows.

4.2 Streamwise mean centerline velocity decay of single jet without HIT

The decay of the mean centerline streamwise velocity U_{cl} as the distance from the exit is increased, is the first feature of a jet flow that is examined. This decay is quantified by constructing the diagrams of the evolution of U_e/U_{cl} vs z/d_e. The normalization of the centerline velocity with the exit velocity and the downstream distance with the nozzle diameter provides the means for presentation of the results in a universal form and enables the comparison with similar jet flows as described in the available literature. These plots are presented in Figure 4-10 for each jet Re number, including both the PIV and CFD results and accompanied with the experimental results of X&A [80]. Furthermore, Table 4-1 summarizes the estimated decay constants as extracted by a linear fit to each plot data.

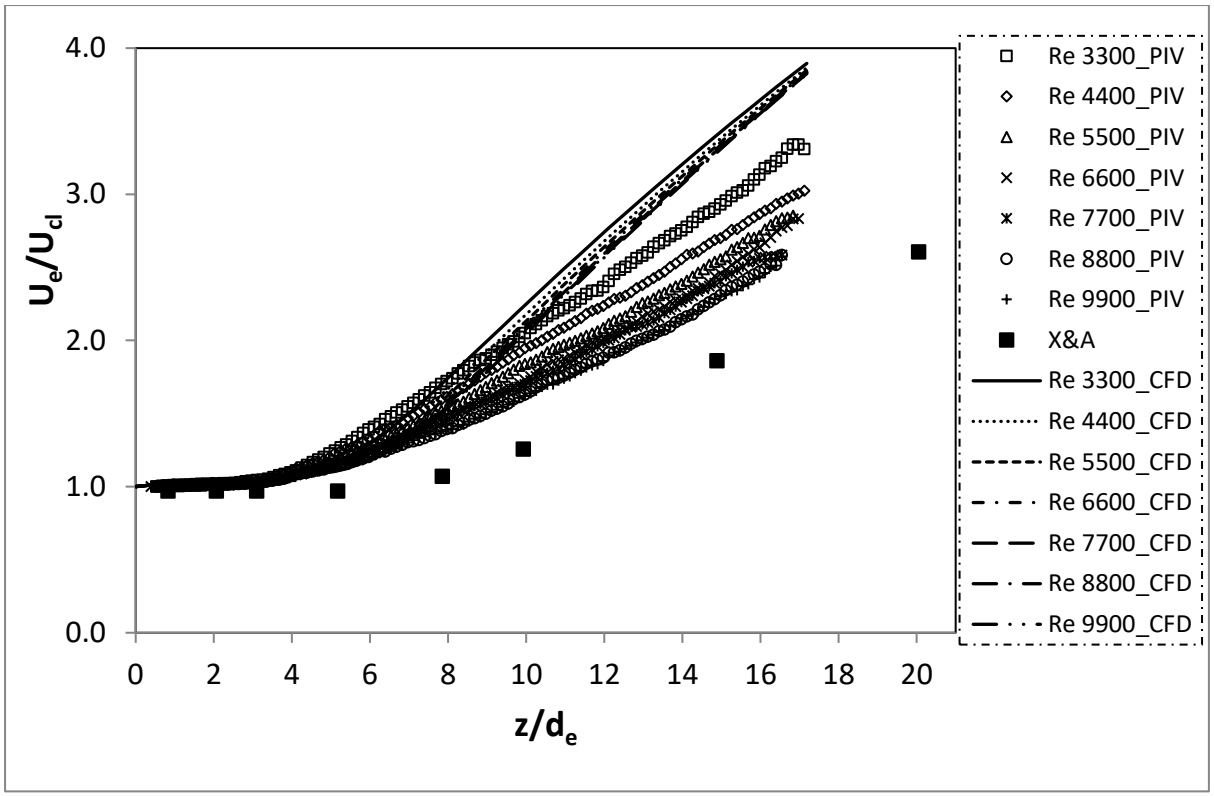

Figure 4-10: Normalized mean centerline streamwise velocity decay for all Re, PIV measurements and CFD simulations.

From the above plots and Table 4-1, the most significant observations that can be made are:

- There is an initial region, where the velocity is constant and approximately the same with the exit velocity. This region corresponds to the potential core of the jet. The length of the potential core is estimated to be about 4de by the PIV measurements and by the CFD simulations.

- Beyond the potential core, the velocity decays in inverse proportion to the distance from the nozzle. The decay constants **B**, (equation 1.64) are provided in Table 4-1.
- From the graphs and Table 4-1, it is observed that in the experimental results as the Re increases the decay constant **B** increases too. Since the decay rate is inversely proportional to the slope of the linear portion of the curves, according to equation 1.62, this means that the values obtained indicate faster decay of the jet for lower Re and slower decay for higher Re.
- There is a difference between the decay constant **B** values of Table 2-2, of the PIV and the CFD results. The PIV measurements give larger values of **B** except for the lowest Re. A range of **B** within 5.6-6.5 is reported by X&A [80]. Nevertheless, examining more carefully the data provided by X&A [80], a value of the decay rate of 7.88 can be estimated if only the measurements up to $22d_e$ are used instead for its evaluation rather than the range of up to $75d_e$. for which the decay rate was reported. This value rests well in the range of the measured PIV values of Table 4-1. As a result, the deviation of the PIV results from the existing literature can be attributed to the fact that the latter refers to the self-similar ZEF of the jet flow. On the other hand, the CFD model is more consistent with the experimental data of Table 2-2. Although in the near to intermediate field region the **B** decay constant is about 4.2, when the whole CFD dataset is plotted until at least 60de a value of 5.6 comes out regardless of Re.

Table 4-1: Decay constants for mean centerline streamwise velocity of a single jet

Re	3300	4400	5500	6600	7700	8800	9900
CFD	4.21	4.20	4.19	4.18	4.18	4.17	4.18
PIV	5.86	6.65	7.15	7.59	7.86	8.43	8.60

4.3 Fluctuating centerline velocity evolution of single jet without HIT

The second step towards the assessment of the flow behavior is to look at the streamwise evolution of the velocity fluctuations, u_{rms} and v_{rms}. In the same manner as in the previous paragraph, the measured quantities will be normalized by an appropriate scale, this time being the centerline velocity U_{cl} at each streamwise position, giving us the so called “turbulent intensities”. The main findings based on the relevant Figure 4-11 and Figure 4-12 include the following:

- Both PIV measurements and CFD modeling agree qualitatively with the shapes of Figure 2-14, which shows the axial evolution of the turbulent intensities reported in the review of Ball et. all

[75]**.** In all cases, there is an initial increase of the normalized rms velocities leading to a self-similar constant value. Self-similarity is more profound for higher Re cases.

- The CFD model approaches better the self-similar state values reported by X&A [80] and are summarized by the other authors in Table 2-2. These values are 0.23 for u_{rms}/U_{cl} and 0.14 for v_{rms}/U_{cl} at Re 3300, while are increased to 0.26 and 0.16 for Re 7700.
- The PIV results deviate from the above values leading to smaller levels of turbulent intensity on the jet axis. However, it seems also that V&Pa [83] also report similar values within the region of jet flow establishment, of up to 0.15 within the first $15d_e$. It is noteworthy that V&Pa [83] investigation is conducted for a Re number of 5500 which is more pertinent here because it is of the same order of magnitude as the Reynolds numbers considered in this investigation.
- Both PIV and CFD have captured the anisotropy between u_{rms} and v_{rms}, exposing larger levels of anisotropy in comparison with X&A [80], as the self-similar region is approached. The CFD predicts normalized u_{rms} about 0.25 and v_{rms} 0.18, thus anisotropy of 1.38, while the PIV gives u_{rms} 0.15 and v_{rms} 0.08, thus anisotropy of 1.87. X&A data give values of u_{rms}/v_{rms}=0.21/0.17=1.23. Furthermore, data for the v_{rms} are not provided by V&Pa [83]. The authors state that in their case, the initial increase of the v_{rms}/U_{cl} starts after $10d_e$ and self-similarity of this property is delayed. However, no further explanation for this deviation from the rest studies is provided.
- According to PIV measurements, as the Re number is increased the turbulent intensity at the centerline seems to be decreased. The normalized u_{rms} reaches levels starting from 0.2 for the lower Re ending to 0.13 for the higher Re, while the corresponding values for the v_{rms} are 0.10 for the higher Re and 0.7 for the lower Re. This reduction to "so called" asymptotic values is attributed mainly to the normalization by U_{cl}, since according to the findings section 4.2 the increase of Re led to smaller U_{cl} decay. It is also an indication that the flow becomes more stable as Re 10^3 is approached.

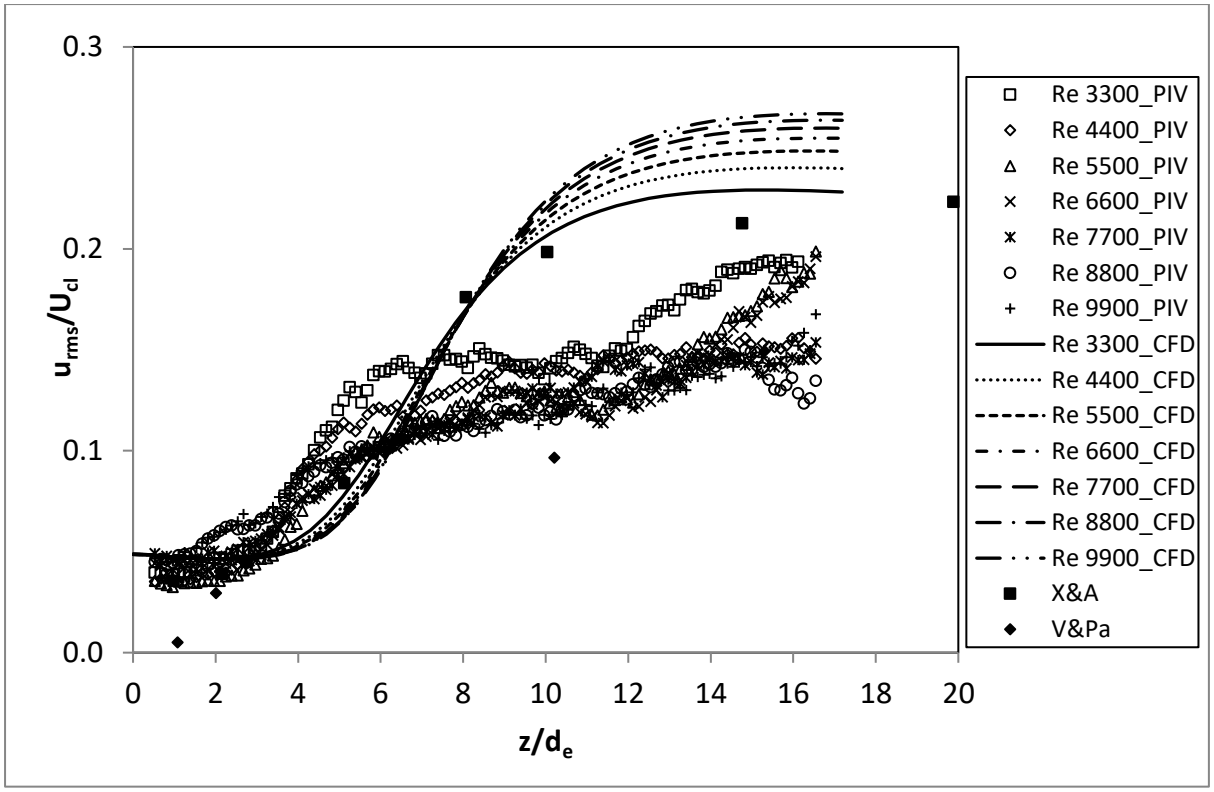

Figure 4-11: Normalized turbulent streamwise u_{rms} along the centerline of the jet for all Re numbers, PIV measurements and CFD simulations.

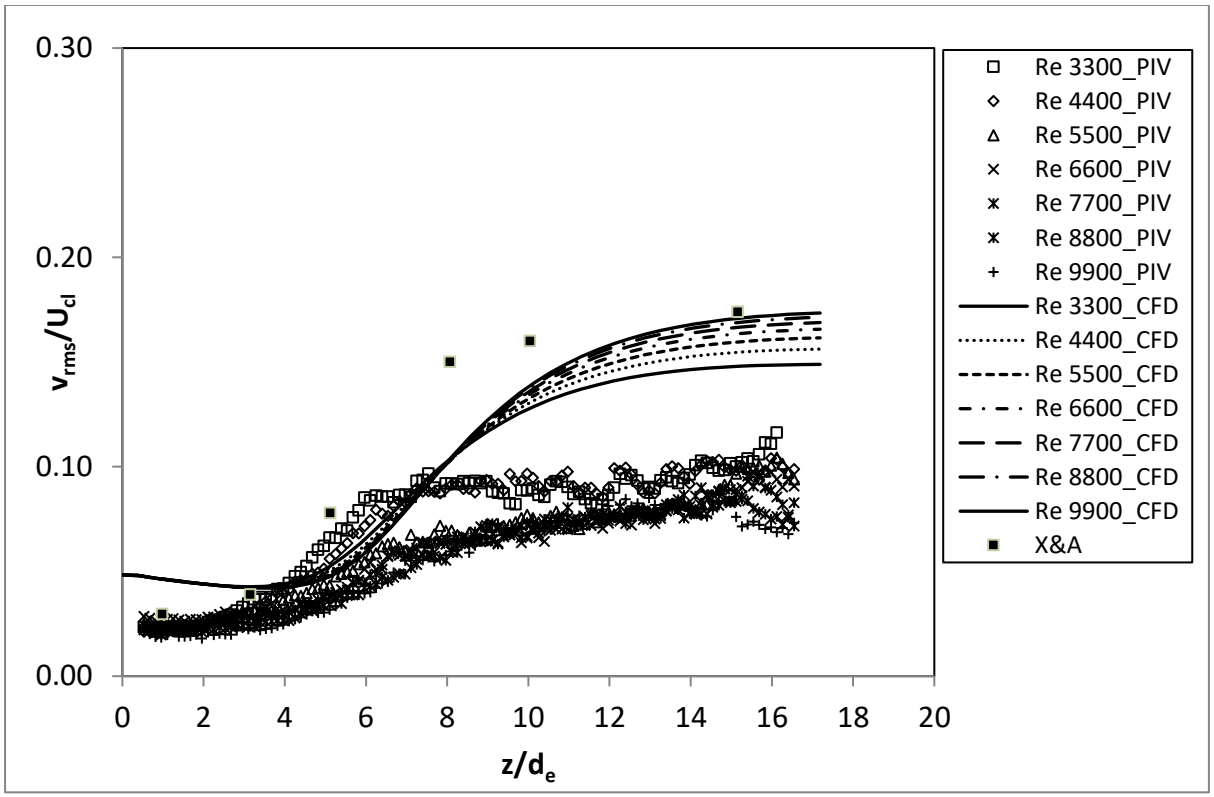

Figure 4-12: Normalized turbulent cross-stream v_{rms} along the centerline of the jet, all Re numbers PIV measurements and CFD simulations

4.4 Cross-stream mean and turbulent velocity- establishment of self-similarity of single jet without HIT

Until this point, the behavior of the mean and turbulent quantities was examined along the centerline axis of the jet. Some discrepancies were identified in relation to previous investigations W&F,[1], P&Lu[2], H&G[79]. These can be attributed to the investigation in the development of the jet in the near nozzle exit region and to the relatively small Re. To further characterize the turbulent axisymmetric jet, it is necessary to examine the profiles of the mean and turbulent quantities in the cross-stream direction, y. For this purpose, the cross-stream jet development was examined at four selected distances from the nozzle exit, namely at $2d_e$, $5d_e$, $10d_e$ and $15d_e$. The maximum distance of $15d_e$ that was considered here is beyond the maximum distance that the jets of this investigation will develop when opposed jets are examined in the next section. In order to facilitate direct comparison with the literature data of par.2.2.5, it should be noted that the examined quantities were normalized with the centerline velocity, U_{cl} and the axial distance from the nozzle, z.

Starting with the cross-stream profiles of the mean streamwise velocity, U_{mean}, it was noted that the behavior of the jet is similar regardless of the Re number. For reasons of brevity, the cases of Re 3300 and Re 7700 were chosen to present the behavior of U_{mean} while the rest of the cases are omitted on purpose.

Figure 4-13 and Figure 4-14 show the evolution of the streamwise velocity U of the jet in the cross-stream direction. The main observations that can be made based on the figures are:

- There is agreement between the PIV measurements and CFD results.
- There is a gradual narrowing of the velocity profiles as the distance from the nozzle exit increases, leading to a self-similar gaussian profile after $10d_e$. The flatter velocity profile for the distance $2d_e$ situated in the potential core, is explained by the fact that the jet has not yet developed sufficiently.
- The experimental data of X&A [80] for $3d_e$ rest between the current data of $2d_e$ and $5d_e$, while the experimental data of X&A [80]for $20d_e$ and V&Pa [83] for $15d_e$ are very close to the current data for distances above $10d_e$.

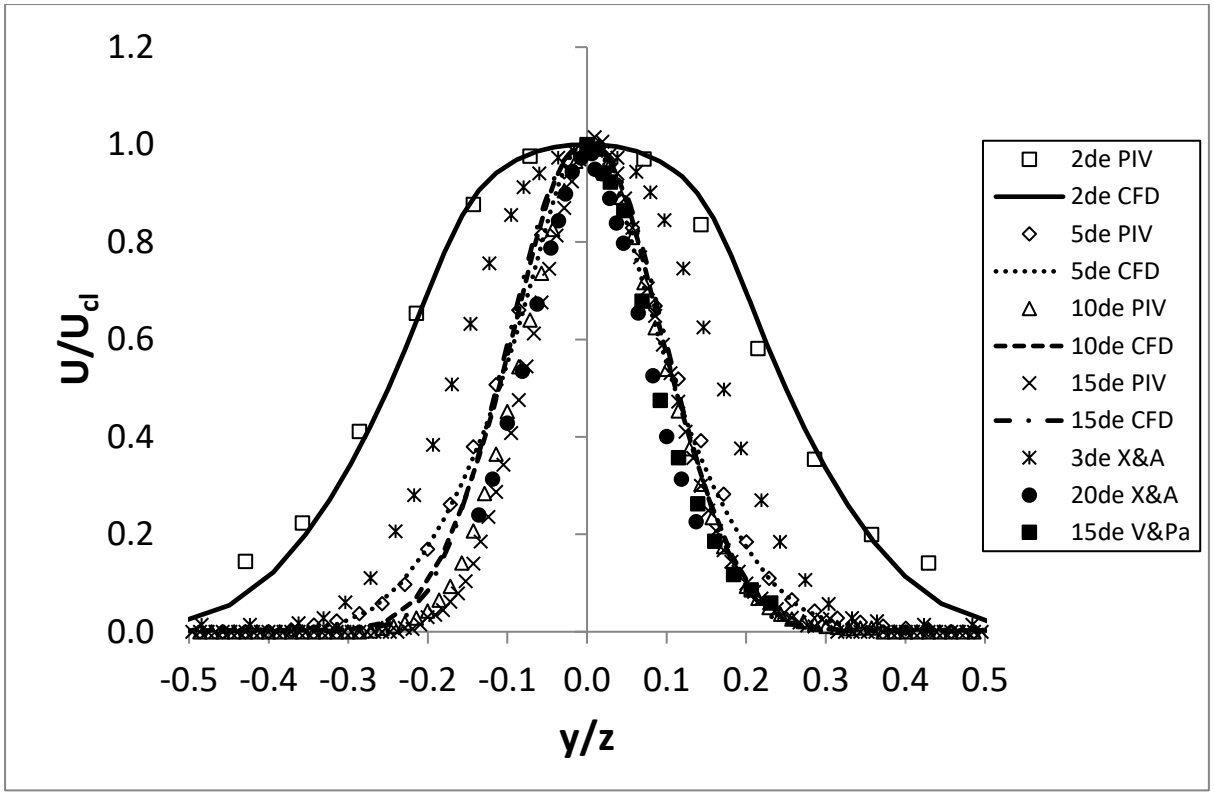

Figure 4-13: Normalized cross stream profiles of mean velocity U, Re 3300

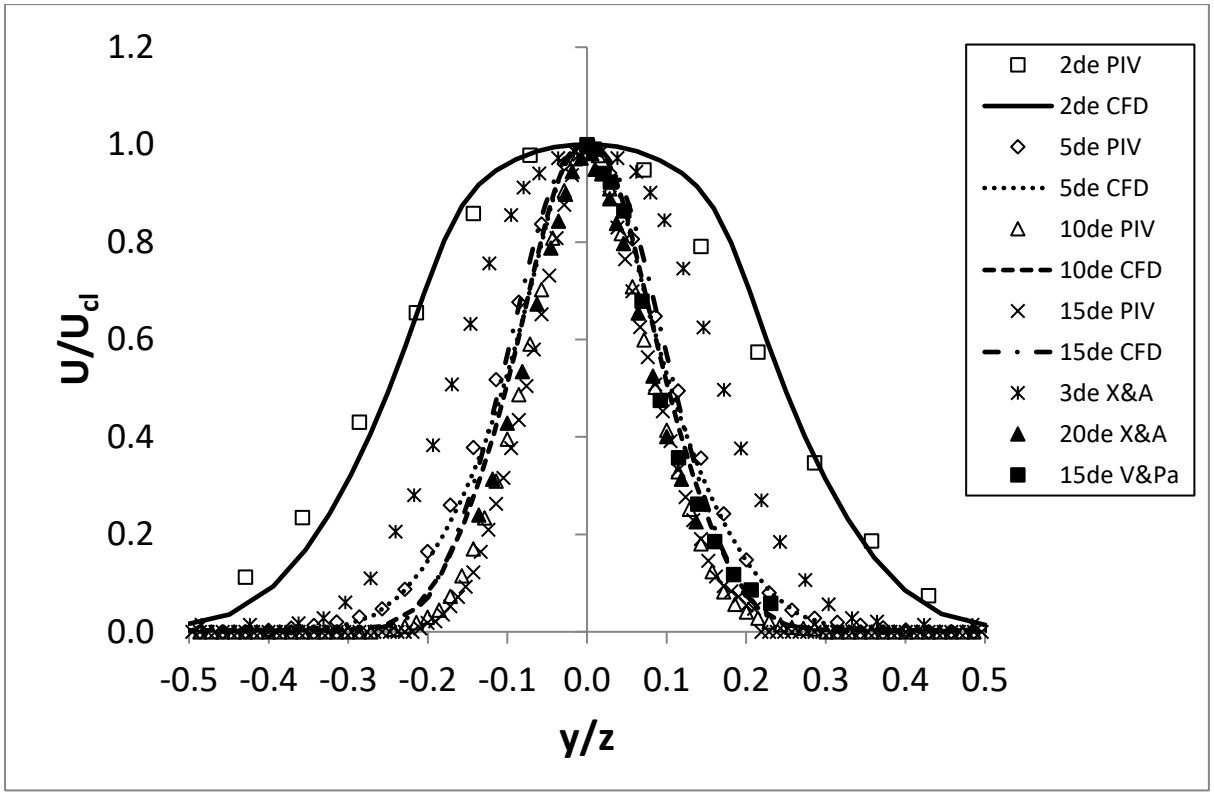

Figure 4-14: Normalized cross stream profiles of mean velocity U, Re 7700

Next, the evolution of the cross-stream velocity V of the jet along the cross-stream direction is presented in Figure 4-15 and Figure 4-16. Although small quantitative deviations are observed between PIV measurements, CFD results and literature data, it is obvious that the jet profile approaches a self-similar behavior after $10d_e$, exposing larger peaks as the distance from the exit increases. This indicates that after the potential core, the jet starts to spread radially in a uniform way.

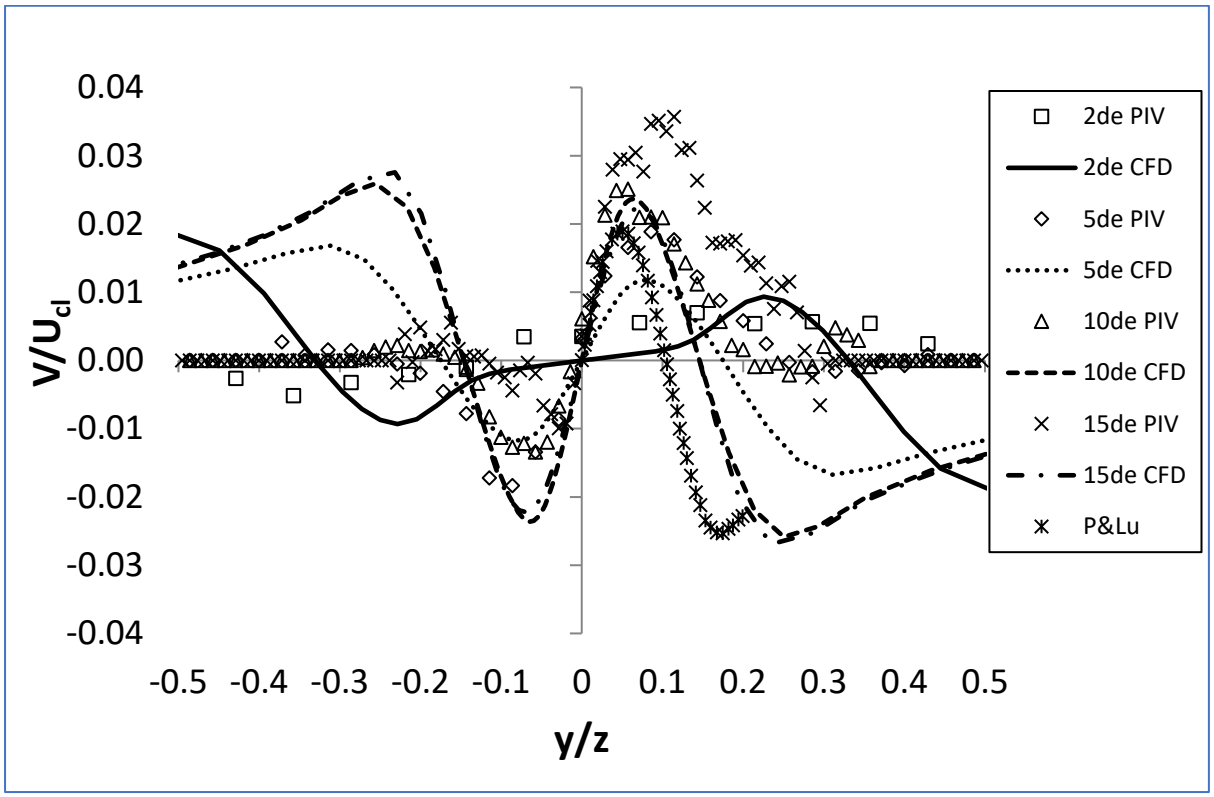

Figure 4-15: Normalized cross stream profiles of mean velocity V, Re 3300

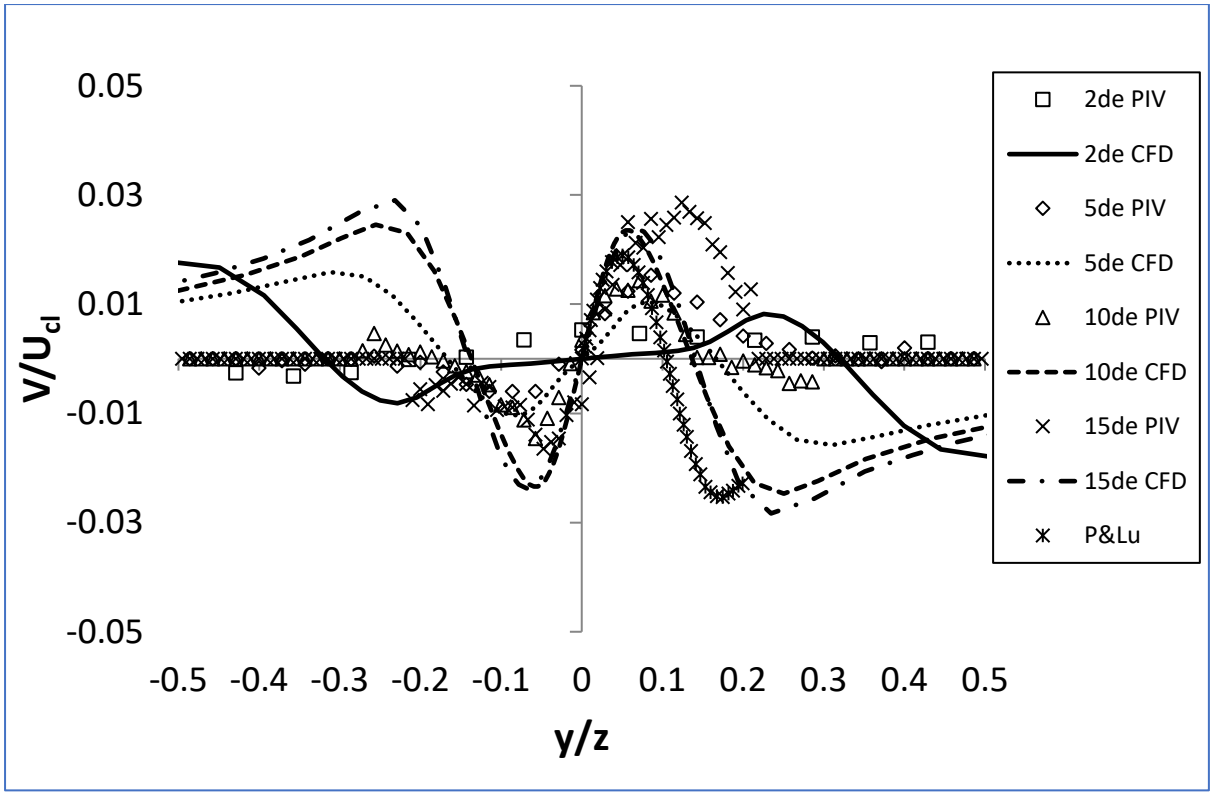

Figure 4-16: Normalized cross stream profiles of mean velocity V, Re 7700

The cross-stream profiles of the normalized u_{rms} are presented in Figure 4-17 and Figure 4-18. It is evident that PIV measurements agree qualitatively with section 2.2.5. Nevertheless, the maximum values at the self-similar region are smaller than those included in Table 2-2 and the CFD simulations. This fact is related to the observations made in section 4.3, where the smaller turbulent intensities were attributed to the smaller decay of U_{cl} rate measured by the PIV. However, close to the exit for $2d_e$, the PIV and CFD data are in better agreement, especially for the Re 7700 case. Moreover, the PIV results towards the self-similar region are in good agreement with the data of X&A and V&Pa [83]. What is also worth mentioning is the presence of off centerline symmetrical peaks. The location of the peaks is an indication of strong shear in the mixing layer between the surrounding fluid entrained by the jet and the radial motion of the injected fluid.

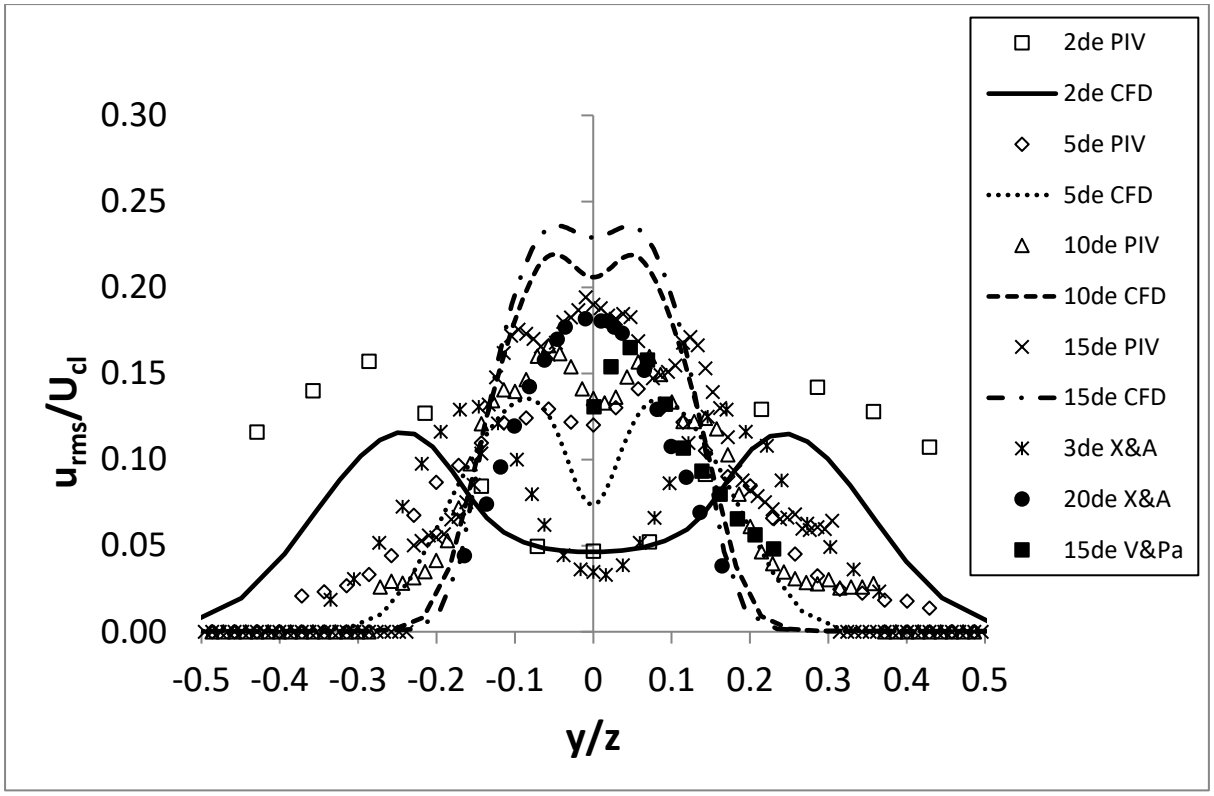

Figure 4-17: Normalized cross stream profiles of u_{rms}, Re 3300

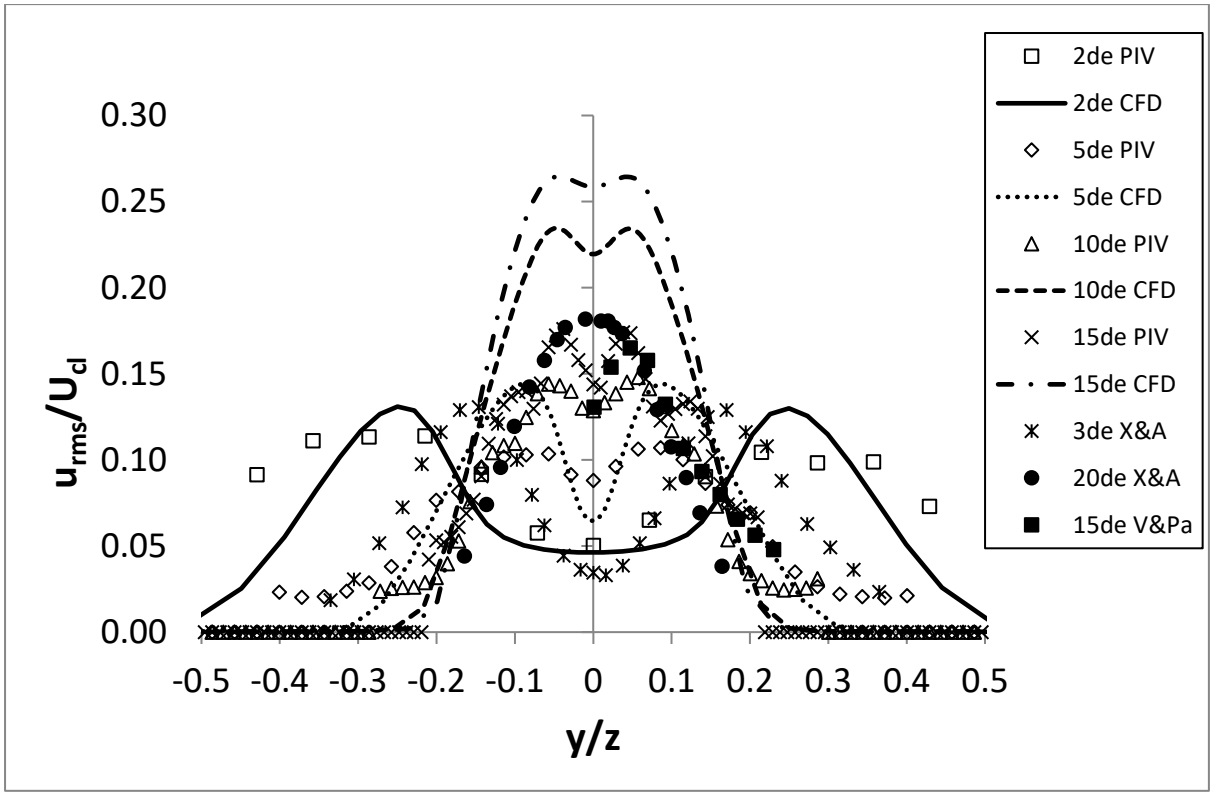

Figure 4-18: Normalized cross stream profiles of u_{rms}, Re 7700

The profile of the normalized v_{rms} as shown in Figure 4-19 and Figure 4-20 is similar to that of u_{rms}, but with smaller magnitude due to the anisotropy of the flow. The CFD results remain also higher than the measured values, as in the case of u_{rms}. The literature data provided by X&A [80] for $20d_e$ are examined with reservation since they are of the same magnitude when compared to the u_{rms}; u_{rms} should be larger since the flow is anisotropic (the axial component being stronger) as explained in section 2.2.5 and presented Table 2-2. It is assumed that it is due to an error in the symbols used in Figure 9 of the referenced paper. This conclusion is supported by the Figure 3 of the same paper, where the values of u_{rms} and v_{rms} at the same distance $20d_e$ on the centerline expose anisotropy of 0.23/0.17=1.35. The estranging small peak values (half of what is measured by the PIV in the current study) from the data provided by V&Pa [83] are explained by the authors statement that in their case, the initial increase of the v_{rms}/U_{cl} starts after $10d_e$ and self-similarity of this property is delayed, as mentioned before in section 4.3.

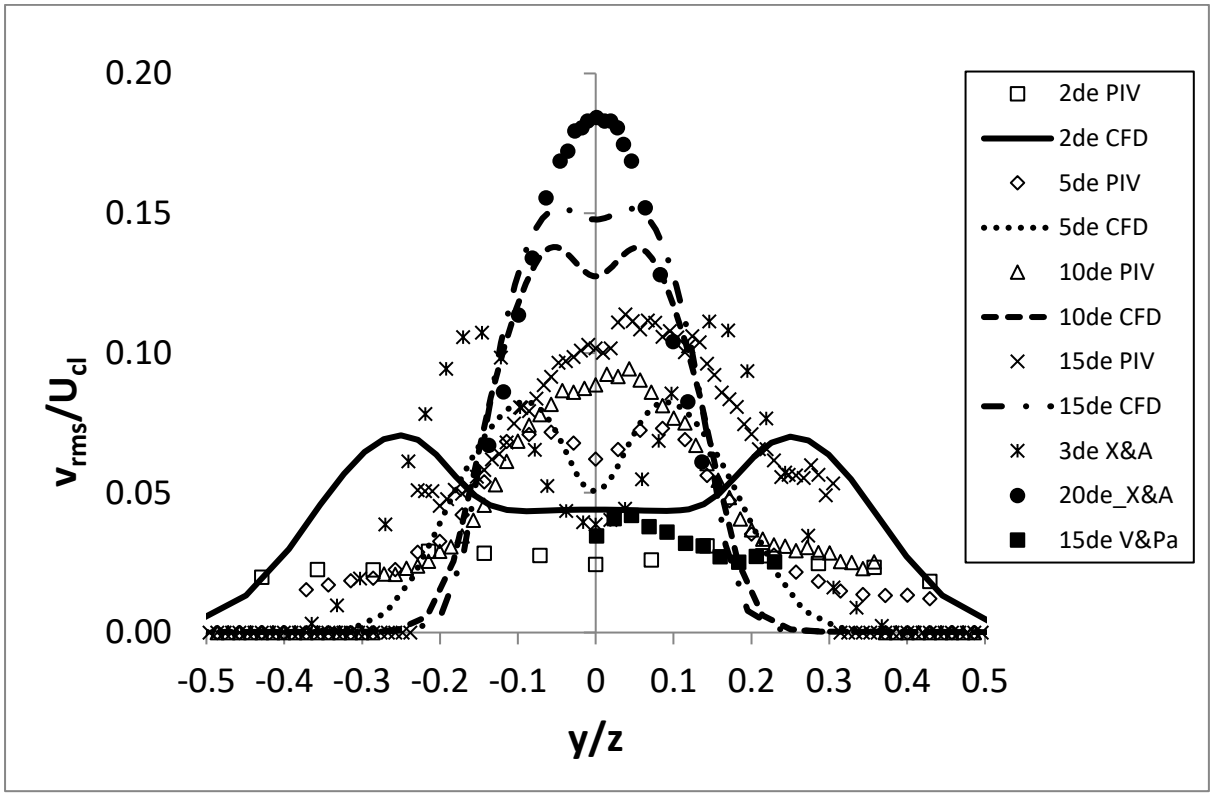

Figure 4-19: Normalized cross stream profiles of v_{rms}, Re 3300

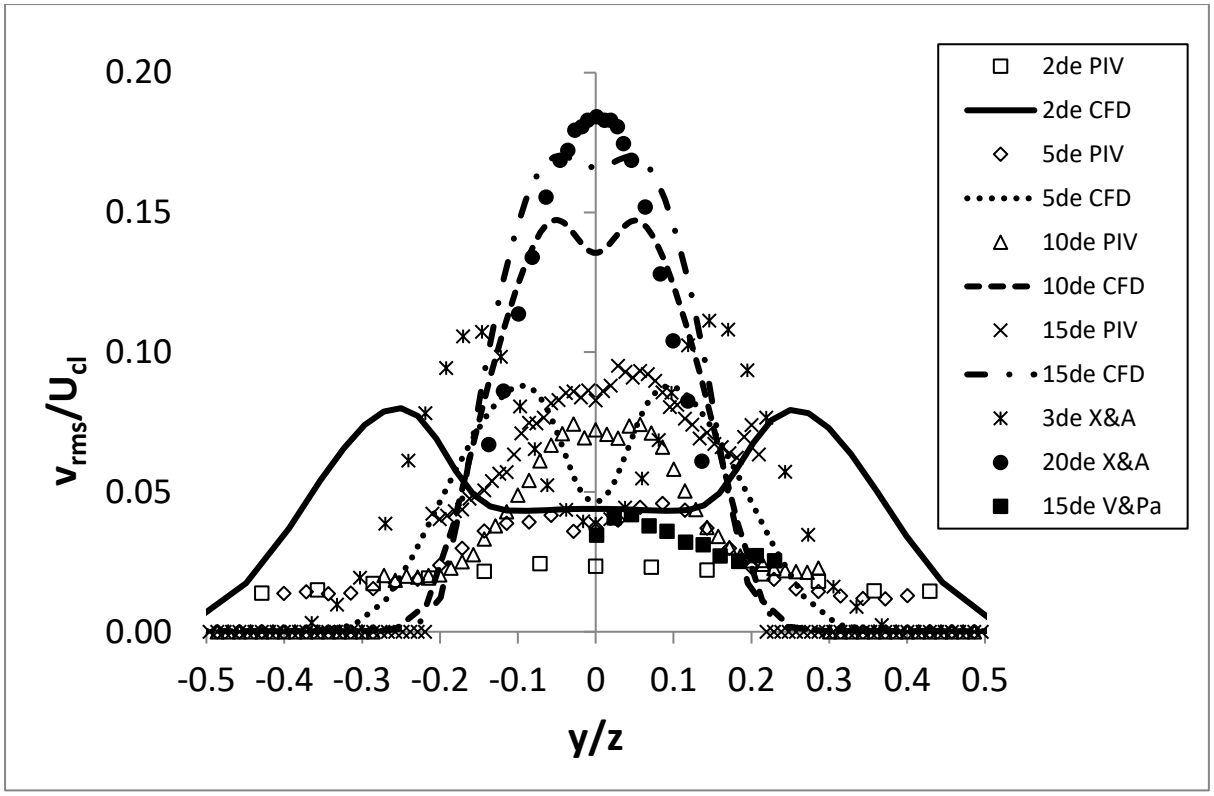

Figure 4-20: Normalized cross stream profiles of v_{rms}, Re 7700

4.5 Spreading rate and flow entrainment of single jet without HIT

The evolution of the jet half width $r_{1/2}$ (the cross-stream distance from the axis where the U_{mean} velocity is equal to $U_{cl}/2$) for all cases studied both with PIV and CFD, is presented in Figure 4-21. A linear behavior of the jet half width with the distance from the nozzle is verified by the plots in all cases, after the jet exits the potential core. According to Table 2-2, the spreading rate constant is equal to 0.086 for a pipe jet as in our case and 0.095 for a contraction jet X&A. V&Pa report the value of 0.078 for a Re~$5.5 \cdot 10^3$ which it is a closer match to our findings. The spreading rate constants attained by Figure 4-21 are summarized in Table 4-2. The spreading rate constant from the PIV data, ranges from 0.1037 to 0.0630, with the smaller values corresponding to larger Re numbers. Kwon & Seo [87] mention the reduction of the spreading rate constant with Re increase, for low Re~10^3. This agrees with the observations in the previous paragraphs, where it was noted that for larger Re, smaller velocity decay was observed, thus the jet seemed to spread more slowly. The value 0.078 of V&Pa at Re~$5.5 \cdot 10^3$, is between the limits of this range as it is close to the value of 0.0837 attained here for Re=5500. The same value 0.078 appears also in the paper of Obot et.al [94] for measurements in the near field and Re~$10.^4$ On the other hand, CFD predicts larger spreading rates, ranging from 0.1157 to

0.1123 which is even greater than the literature data taken from contoured nozzles at higher Re> 10^4, and agrees better with the larger velocity decay observed in the previous paragraphs for the CFD.

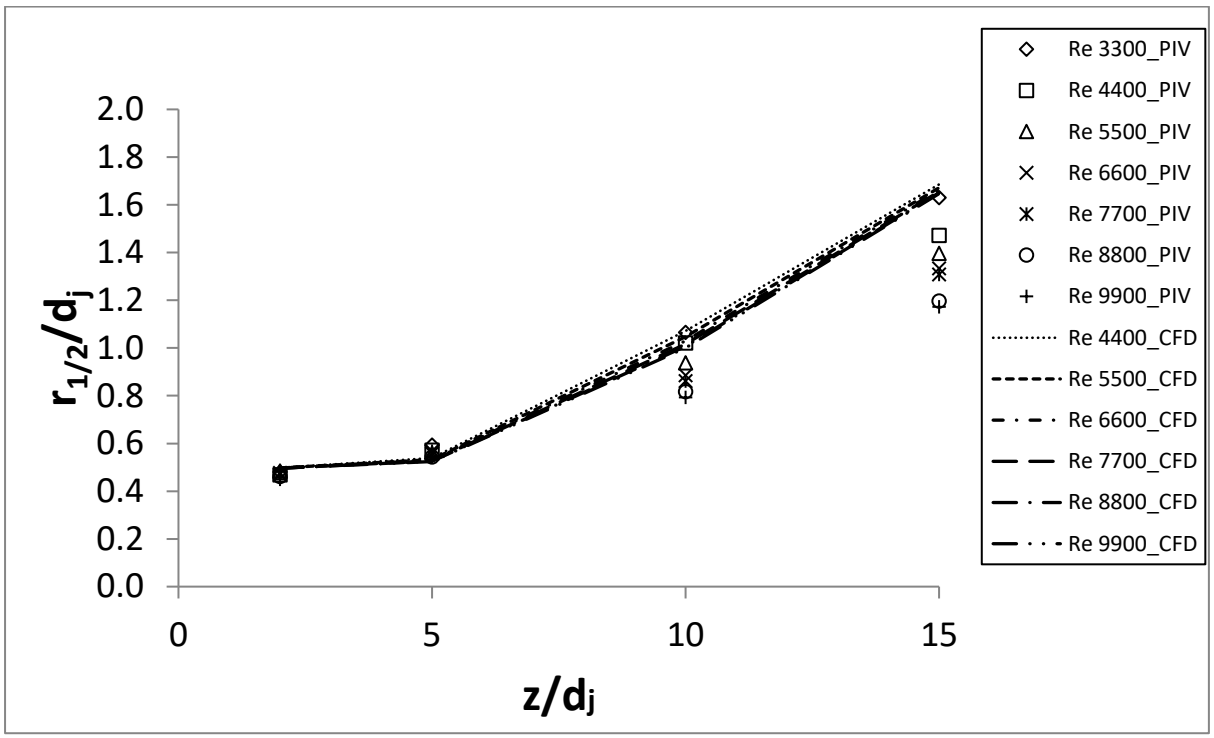

Figure 4-21: Jet half width $r_{1/2}$ as a function of distance from the jet exit.

Table 4-2: Spreading rate constants.

Re	3300	4400	5500	6600	7700	8800	9900
CFD	0.1157	0.1147	0.1139	0.1133	0.1128	0.1125	0.1123
PIV	0.1037	0.0901	0.0837	0.0775	0.0741	0.0653	0.0630

Examining the entrainment mechanisms of the jet flow, we can rewrite 1.71 as:

$$\frac{d(q/q_e)}{d(z/d_e)} = C_m \qquad 1.104$$

since the density of the jet fluid and the density of the environmental fluid are equal to that of air. As a result, it is possible to plot the rate of entrainment at distances $2d_e$, $5d_e$, $10d_e$, and $15d_e$ past the jet nozzle exit. The calculation of the flowrate at each downstream distance from the nozzle was made by implementing the trapezoidal rule for integrating the velocity data of U_{mean} over the y cross-stream coordinate. The plots for both PIV and CFD are shown in Figure 4-22 and the entrainment constants are presented in Table 4-3.

The plots show that the flowrate increases linearly with distance from the nozzle as in Ricou & Spalding[91] and Hill [92], verifying that the jet entrains ambient air at a constant rate as it progresses further downstream. While the CFD predicts an entrainment constant 0.23 that does not change with Re, the PIV results in constants in the range [0.387, 0.23] with 0.23 being the value obtained for the highest Re number considered. Ricou & Spalding [91] also noted the reduction of flowrate with Re, but the reference is made for a specific distance from the exit $13.7d_e$ and $25.6d_e$ for Re<25000. Beyond Re<25000 the entrainment was reported independent of Re. Boguslawski & Popiel [93] found an entrainment constant of 0.183 in the near region of a jet with Re~10^4, which is close to 0.23 for Re 9900 in our case. The decrease of the rate of entrainment with increasing Re number is in agreement with the observations in the previous section, where it was found from the experimental measurements that the spreading rate of the jet also decreases with increasing the Re. Furthermore, the value C_m= 0.32 noted in the literature review section 2.2.6 is within the range extracted from the PIV measurements.

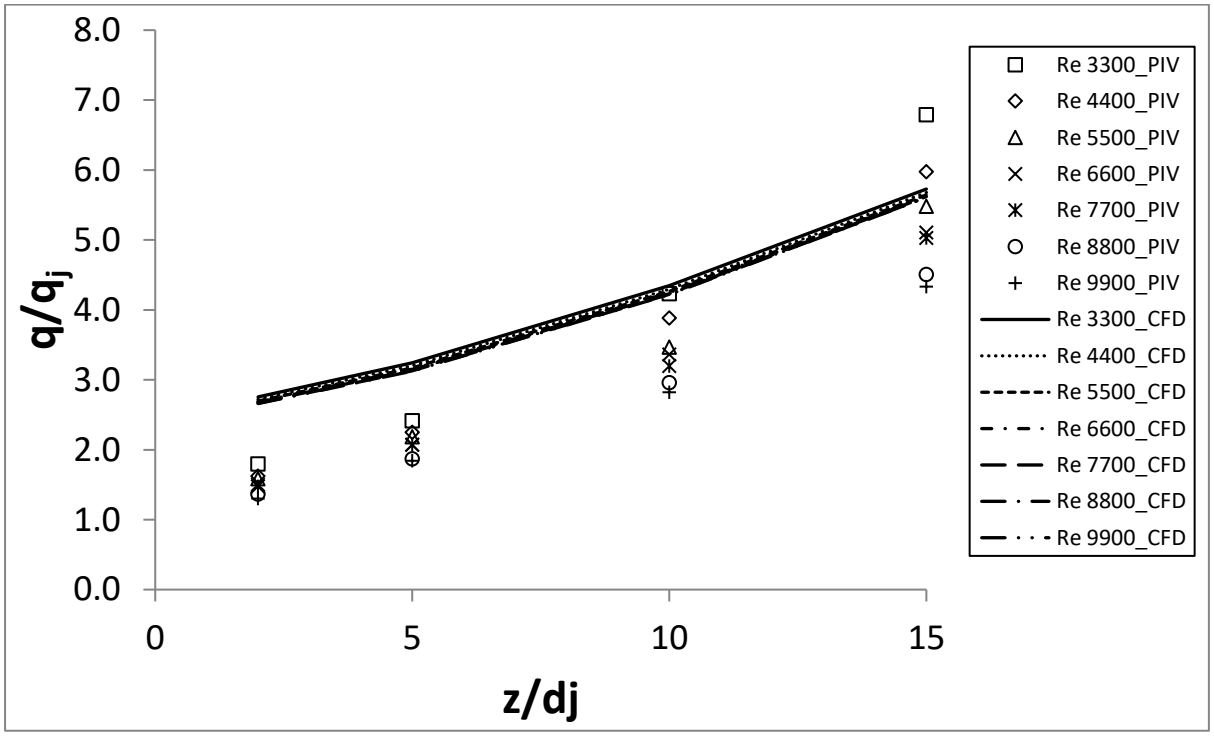

Figure 4-22: Flow entrainment rate of a single jet for various Re, PIV and CFD data

Table 4-3: Flow entrainment constants

Re	3300	4400	5500	6600	7700	8800	9900
CFD	0.229	0.229	0.228	0.228	0.228	0.228	0.228
PIV	0.387	0.339	0.298	0.278	0.271	0.241	0.230

4.6 Preliminary assessment of single jet in HIT

The analysis of the previous paragraphs assessed the flow field of a single axisymmetric jet in a quiescent environment by examining a number of characteristic flow field properties. The study focused on the near nozzle to intermediate flow field region and considered relatively low Re numbers <10000. This analysis will serve as a baseline for the examination of the influence of an environment of homogenous and isotropic turbulence (HIT) in the development of a single jet. In this case, the jet emanates in an HIT region, which extends until the jet's streamwise distance of interest. Thus, it can be said that the whole near to intermediate development of the jet is influenced by the HIT. In the case of single jet in HIT, no CFD results will be presented due to the complexity and subsequent uncertainty that such a reproduction implies.

Figure 4-23 presents example jet images for the reader to obtain a visualization of the jet flow with the presence of HIT. Similarly to section 4.1, an overall picture of how the HIT affects the jet with variation of Re number is given by the contours included in Figure 4-24. An initial assessment of the contours provides us with the following remarks:

- The lower Re (1100, 2200) jets which are laminar are deteriorated by the presence of HIT in the surrounding environment, since the jets have low momentum which is not sufficient to counteract the presence of environmental turbulence. As it can be seen by the contours, the streamwise velocity U_{mean} diminishes very early at small distances from the exit ($3d_e$ for Re 1100 and $5d_e$ for Re 2200). On the other hand, as shown in Figure 4-2, without the presence of HIT significant jet mean flow of about 2 m/s is maintained for both cases up to $14d_e$. Moreover, the laminar flow without HIT does not exhibit jet spreading, with the exit velocity profile maintained until the breakup of the jet. This laminar shape does not occur in the presence of HIT and spreading occurs even at the small distances reached by the flow. As the Re number increases beyond Re 3300, the jet momentum increases and as it can be seen in Figure 4-23 the jet is able to penetrate within the region of turbulence. As a result, the more detailed investigation that will follow in the next paragraphs will include once again the cases for Re>3300 where the jet is able to maintain some structure.
- Whereas in the case where external turbulence is absent, from the instantaneous images Figure 4-1 a symmetrical evolution of the jets takes place around the centerline, under turbulence fluctuations of the jet around the centerline can be observed in the instantaneous images of Figure 4-23. This is due to the fluctuations of the turbulence velocity field and take place mainly in the regions, where the jet mean velocity decays enough to be comparable with the turbulence

rms, which is found around 0.3 m/s. However, the temporally average velocity profile of the jet, Figure 4-24, is symmetric around the jet axis.

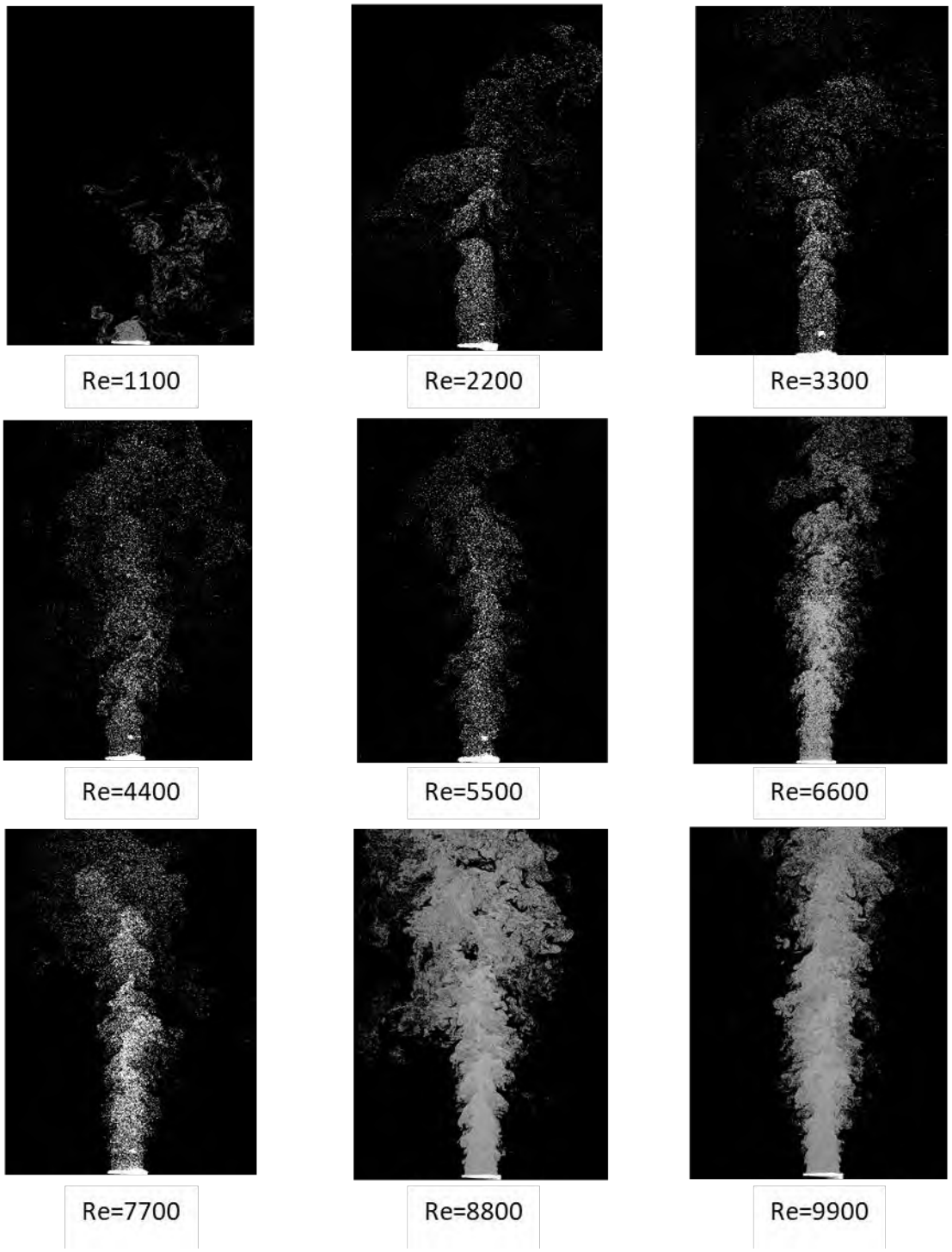

Figure 4-23: Jet images of a single jet under HIT for each Re number

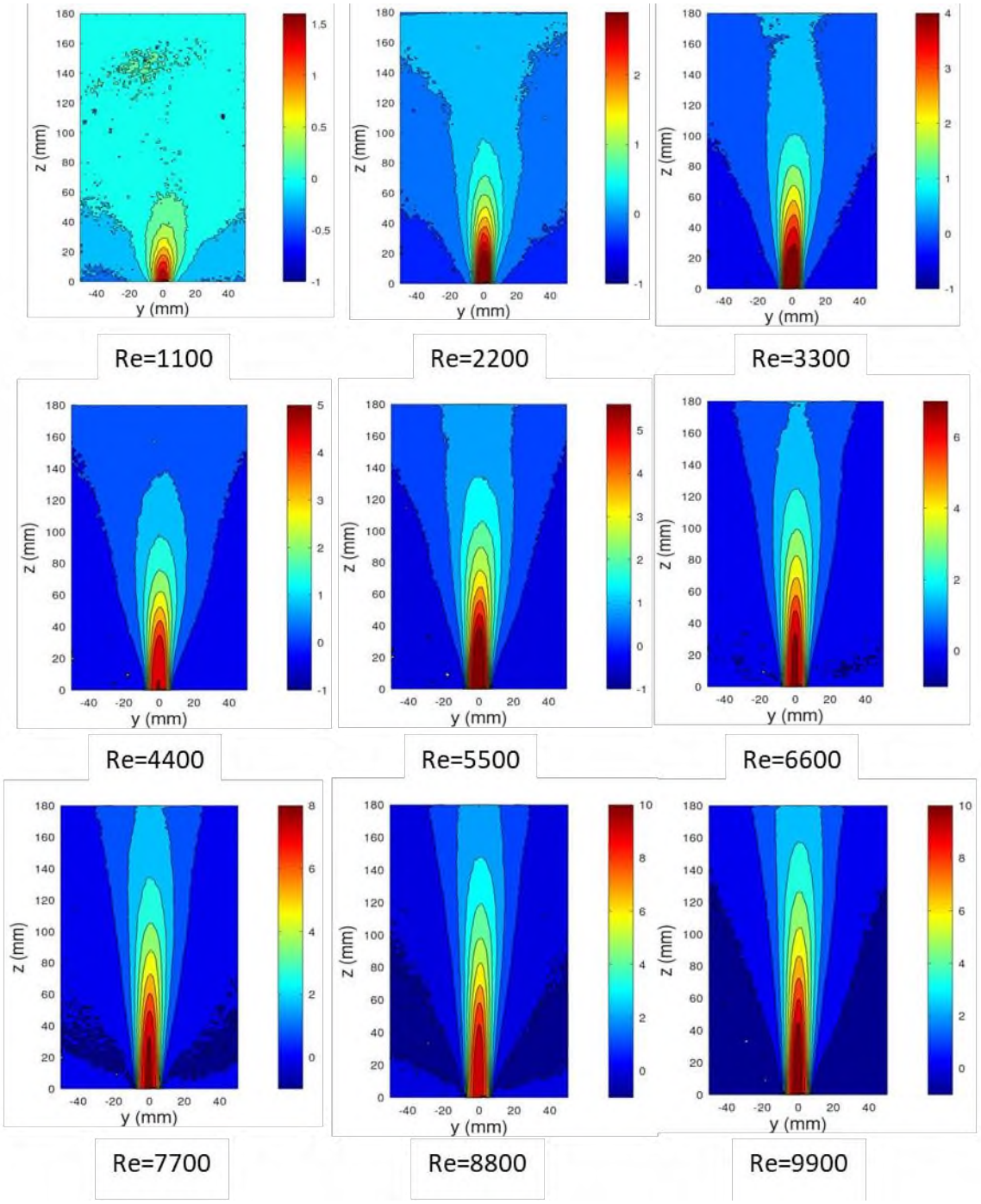

Figure 4-24: Contours of streamwise velocity U_{mean} for a single jet under HIT.

4.7 Streamwise mean centerline velocity decay of single axisymmetric jet under HIT

Similarly to section 4.2, the decay of the mean streamwise velocity U_{mean} along the jet's centerline is investigated this time under the influence of HIT. In this effort, we are aided by Figure 4-25, which

includes the normalized velocity and distance data and Table 4-4, which summarizes the estimated decay constants. Furthermore, in Figure 4-25, the data pertaining to the case of the strongest Re 9900 without HIT are added for reasons of comparison. The remarks that can be made based on observation of the data are:

- There is a significant decrease in the decay rate constant of the jets under HIT. The decrease is mitigated as the jet gains momentum when the Re number increases. It should be reminded that the decay rate constant has an inverse relationship with the jet's velocity decay rate; the smaller the decay constant the faster the jet decays, equation 1.64. However, even for the maximum considered Re number of 9900, the decay rate constant does not reach the value obtained in a quiescent environment showing that the effect of turbulence is significant in all considered cases.
- In the case of the lower Re number, the jet evolution deteriorates after about $12d_e$ as it is revealed by the collapse of the linear decay of velocity, mainly for the lower Re cases. However, until this distance the linear nature of the velocity decay is maintained, in contrast with Khorsandi et al. [95], who identified a power law decay for a jet in background turbulence.

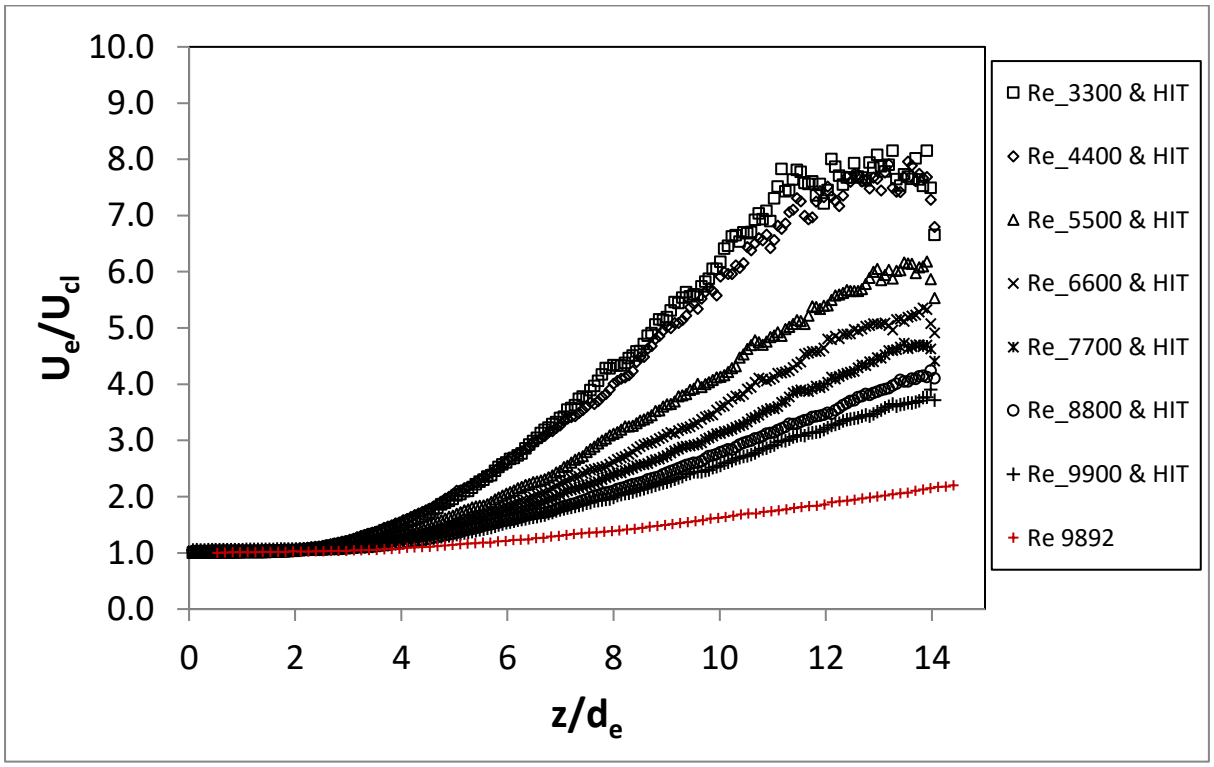

Figure 4-25: Normalized mean centerline streamwise velocity decay for all Re under HIT

Table 4-4: Decay constants for mean centerline streamwise velocity of a single jet in quiescent environment and in HIT

Re	3300	4400	5500	6600	7700	8800	9900
Quiescent	5.86	6.65	7.15	7.59	7.86	8.43	8.60
HIT	1.36	1.55	2.22	2.77	3.44	4.03	4.60

4.8 Fluctuating centerline velocity evolution of single axisymmetric jet under HIT

In this section, the influence of HIT on the evolution of the velocity fluctuations in the streamwise and cross-stream directions are examined along the jet centerline. In this effort, the same approach as in section 4.3 is followed. The evolution of the normalized turbulent streamwise velocity u_{rms} along the centerline of the jet is presented in Figure 4-26 while the evolution of the normalized turbulent cross-stream v_{rms} along the centerline of the jet is presented in Figure 4-27 for all Re. As in the previous section, the case of Re 9900 without HIT is included in the figures for reference. Based on the findings the main remarks that can be noted are:

- There is an increase of the turbulent intensities of both the streamwise and the cross-stream velocities, in comparison to jet injection in a quiescent environment shown in Figure 4-11 and Figure 4-12. The increase in turbulence intensity, Table 4-5, is more profound for the lower jet Re (about ten times greater than at the highest Re considered here) and is then mitigated gradually with increasing Re. This effect can be attributed to the higher turbulence intensity of the jet caused by the interaction with the HIT of the environment as well as the decay of the mean axial streamwise velocity (decrease in the denominator of intensities). Both of these effects are more prevalent at lower Re numbers where the momentum of the jet decreases and the influence of the environmental turbulence increases.
- There is a sharp increase of turbulent intensities towards the end of the potential core ($2d_e$-$4d_e$) which is mitigated afterwards. This characteristic comes from the nature of the single axisymmetric jet. Near the end of the potential core, the area where the shear layers formed by the surrounding fluid and the injected fluid merge. This is an area of high mixing and turbulence.
- The anisotropy ratio u_{rms}/v_{rms} observed in the case of jet injection in a quiescent environment (Figure 4-11, Figure 4-12) is maintained in the presence of HIT for all Re numbers.

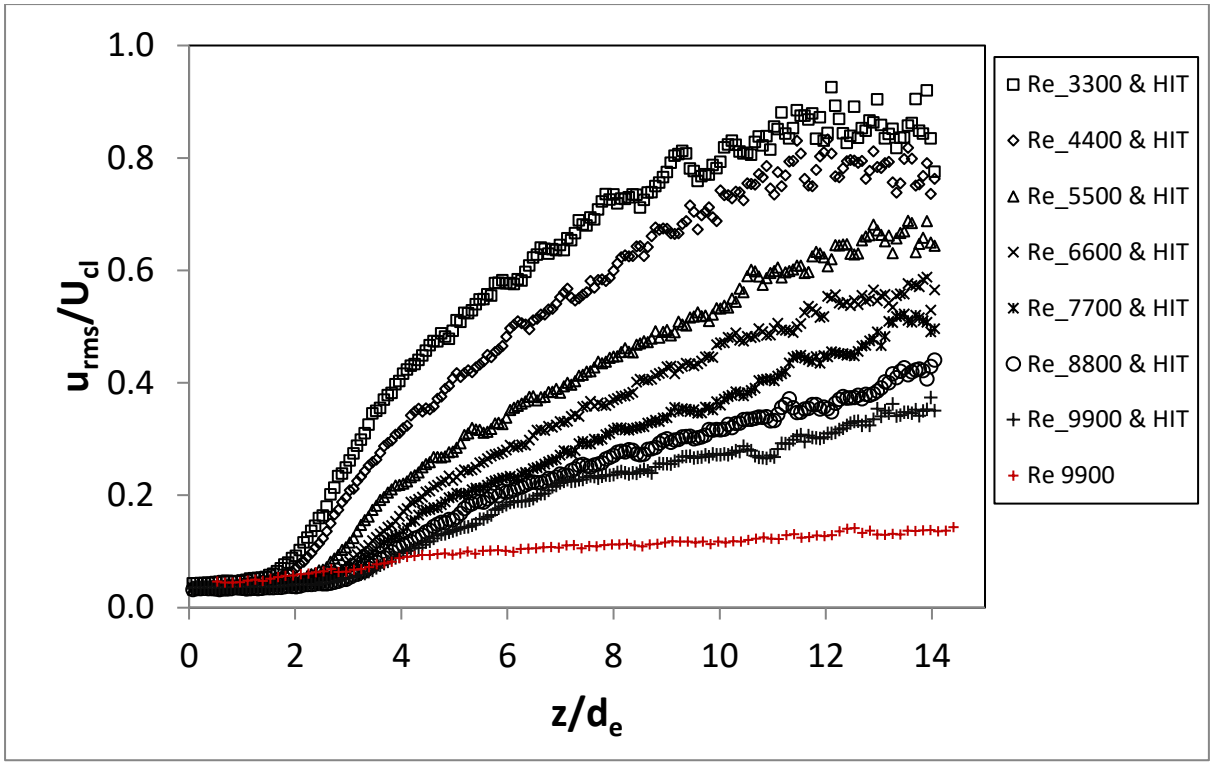

Figure 4-26: Normalized turbulent streamwise u_{rms} along the centerline of the jet for all Re under HIT

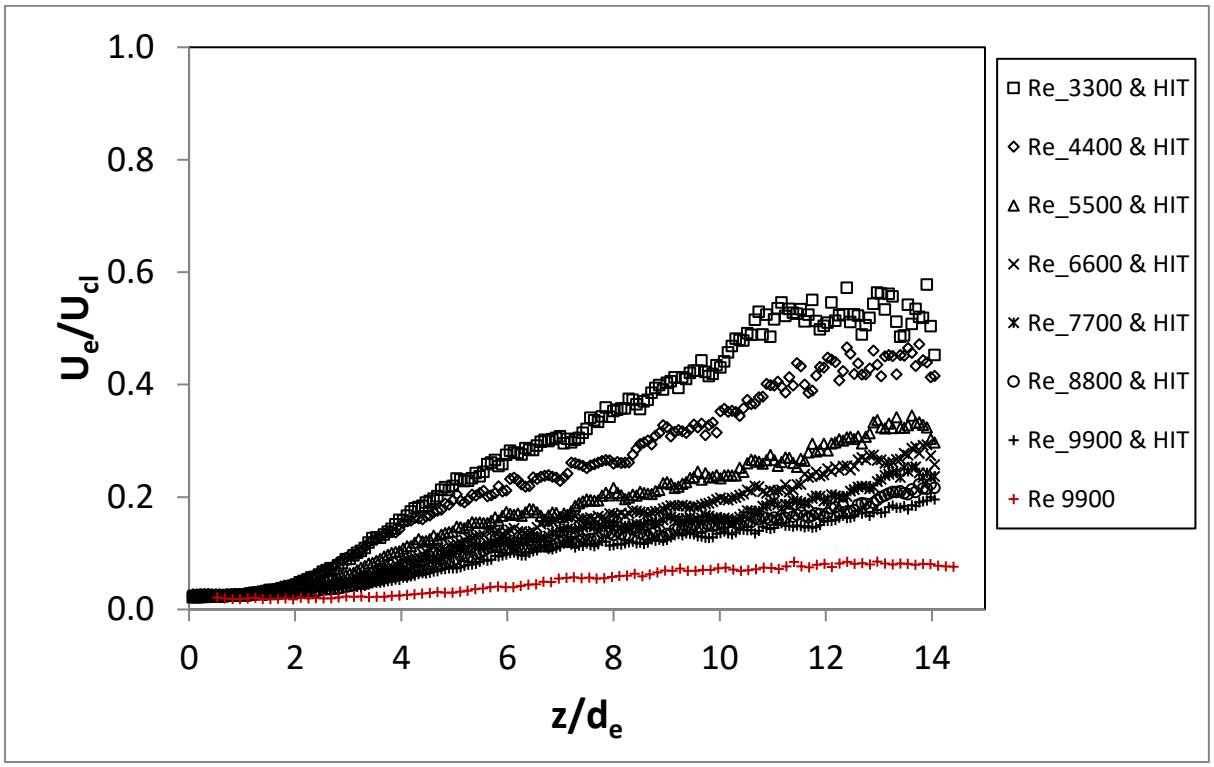

Figure 4-27: Normalized turbulent cross-stream v_{rms} along the centerline of the jet for all Re under HIT

Table 4-5: max u_{rms} increase due to HIT in comparison with jet injection in a quiescent environment.

Re		3300	4400	5500	6600	7700	8800	9900
$\Delta(u_{rms})$ m/s	HIT	0.65	0.49	0.46	0.40	0.32	0.31	0.30
$\Delta(v_{rms})$ m/s	HIT	0.19	0.13	0.19	0.20	0.16	0.20	0.13

4.9 Cross-stream mean and turbulent velocity- establishment of self-similarity of single jet under HIT

In order to attain a broader and more quantified interpretation of the influence of HIT in the single jet development, the development of the jet is examined in the cross-stream direction, using the approach of section 4.4.

The evolution of the streamwise mean velocity U of the jet in the cross-stream direction is presented in Figure 4-28 and Figure 4-29 for Re 3300 and 7700 respectively. The main observations that can be made based on the figures are:

- The gaussian shape of the velocity is maintained under the presence of HIT.
- For small streamwise distance $2d_e$ there is a minor effect, regardless of the amplitude of HIT and jet Re. Being in the potential core, the jet momentum overcomes the influence of HIT.
- For larger streamwise distances at $5d_e$, where the absolute mean velocity decays, the presence of HIT in the environment on the jet development is perceptible, since the gaussian shape is wider in comparison to that for jet injection in a quiescent environment shown in Figure 4-13 and Figure 4-14. This means that HIT spreads the jet radially. This is more profound in the case of lower jet Re 3300 where the jet momentum is lower.
- In the case of low Re 3300, the jet is unable to attain a self-similar behavior. This is because it is deteriorated by the environmental HIT before it develops sufficiently. Although, a narrowing of the curves takes place for $5d_e$, a rewidening takes place for $10d_e$.
- As the Re is increased to 7700, a return to self-similarity occurs, since the curves collapse into a nearly identical profile.

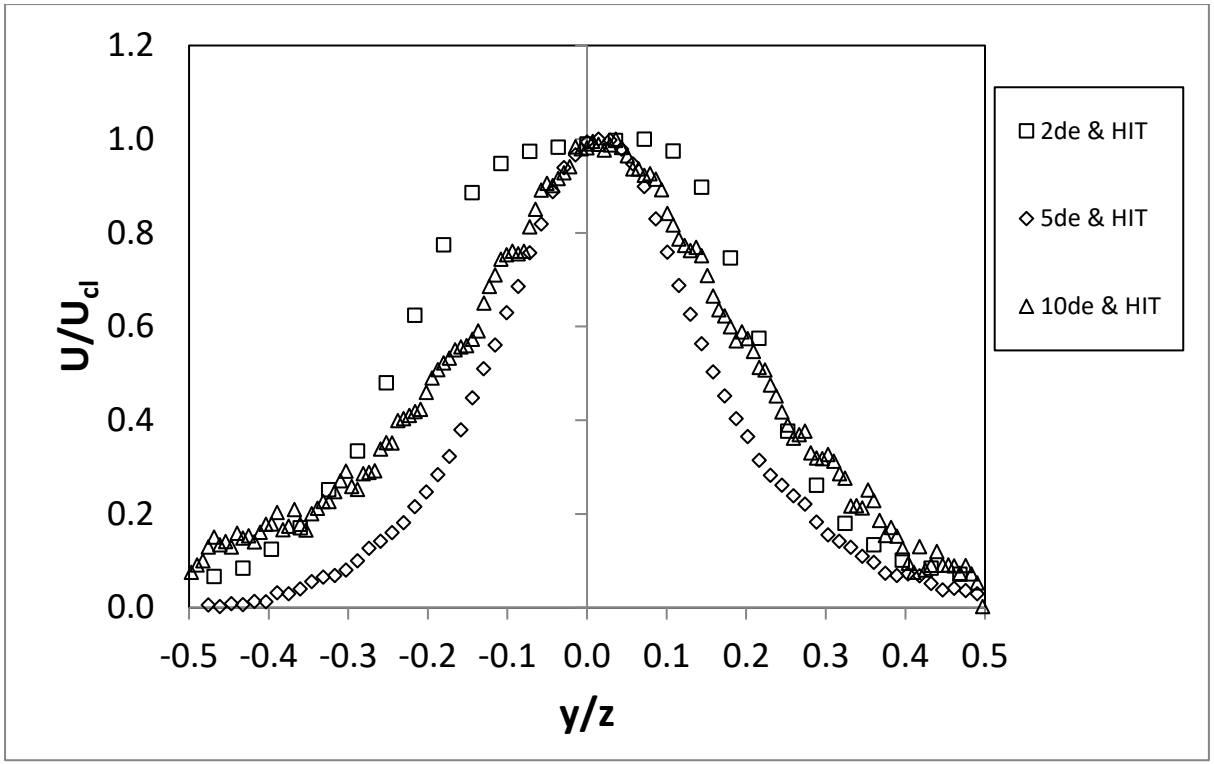

Figure 4-28: Normalized cross stream profiles of mean velocity U, Re 3300 under HIT

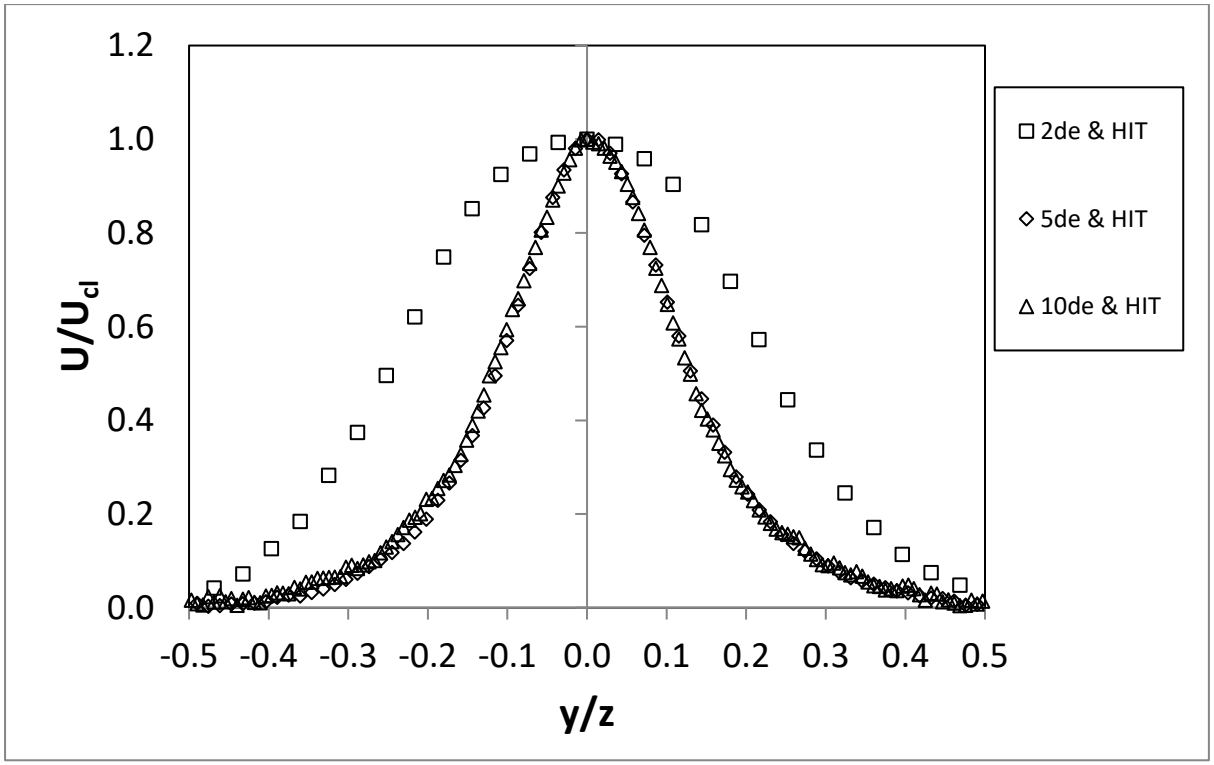

Figure 4-29: Normalized cross stream profiles of mean velocity U, Re 7700 under HIT

The evolution of the cross-stream velocity V of the jet in the cross-stream direction is shown in Figure 4-30 and Figure 4-31. In both Re cases, the HIT increases the maximum of V/U_{cl}. The maximum

for a turbulent jet in a quiescent environment according to literature and section 4.4 (Figure 4-15 and Figure 4-16) is expected to be about 0.02-0.03. If we focus on the intermediate distance of $5d_e$, it is noted that for Re 3300, it reaches levels of at least 0.1, while in the same distance for Re 7700 reaches values of 0.05. Khorsandi et al. [95] also stated the increase in the peak values of V component for a single jet under background turbulence. Furthermore, a qualitative change from the behavior in the quiescent environment is noticed in the presence of HIT. In the first case, for the cross-stream distances examined, the V component flow changes direction, signifying the transition from spreading to entrainment. On the other hand, in the second case, such a transition does not occur, for the cross-stream distance examined, especially in the case of the lower Re 3300, where the effect of HIT is more profound. This means, that the jet under turbulence remains under the spreading regime for larger cross-stream distances, creating a potential for larger spreading rates, as will be verified in the next section 4.10.

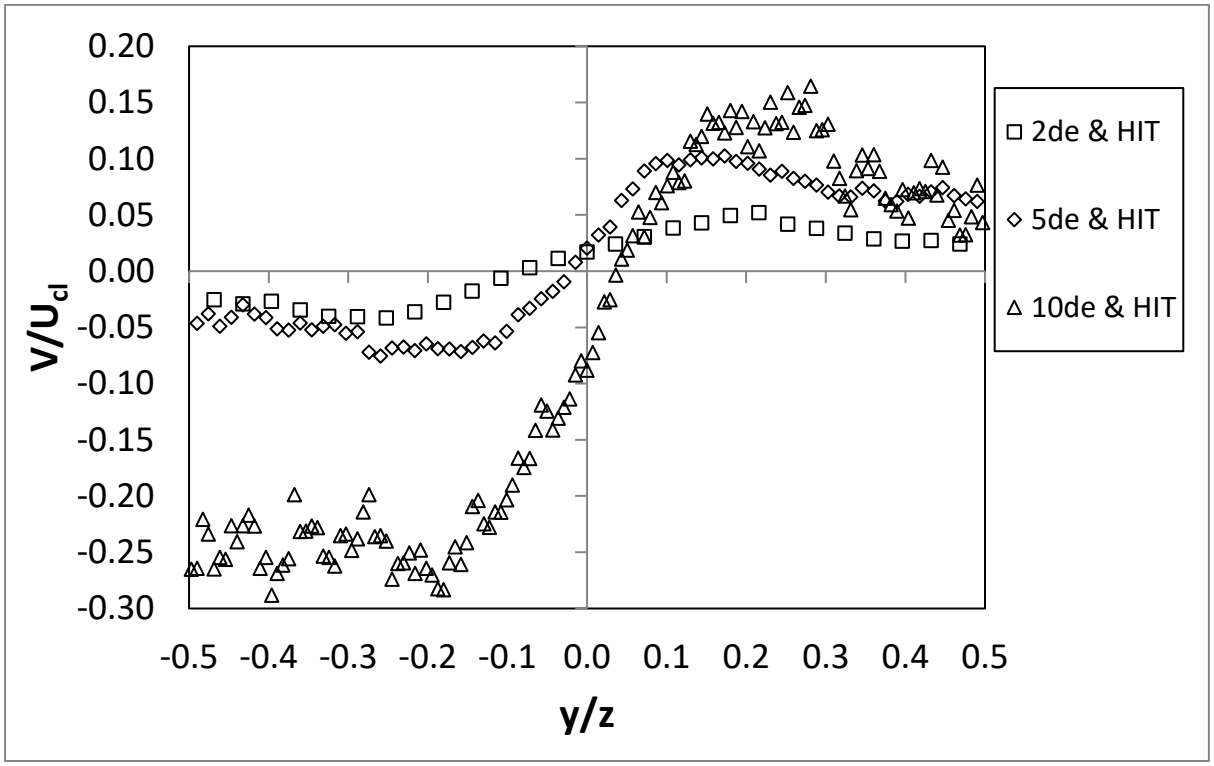

Figure 4-30: Normalized cross stream profiles of mean velocity V, Re 3300 under HIT

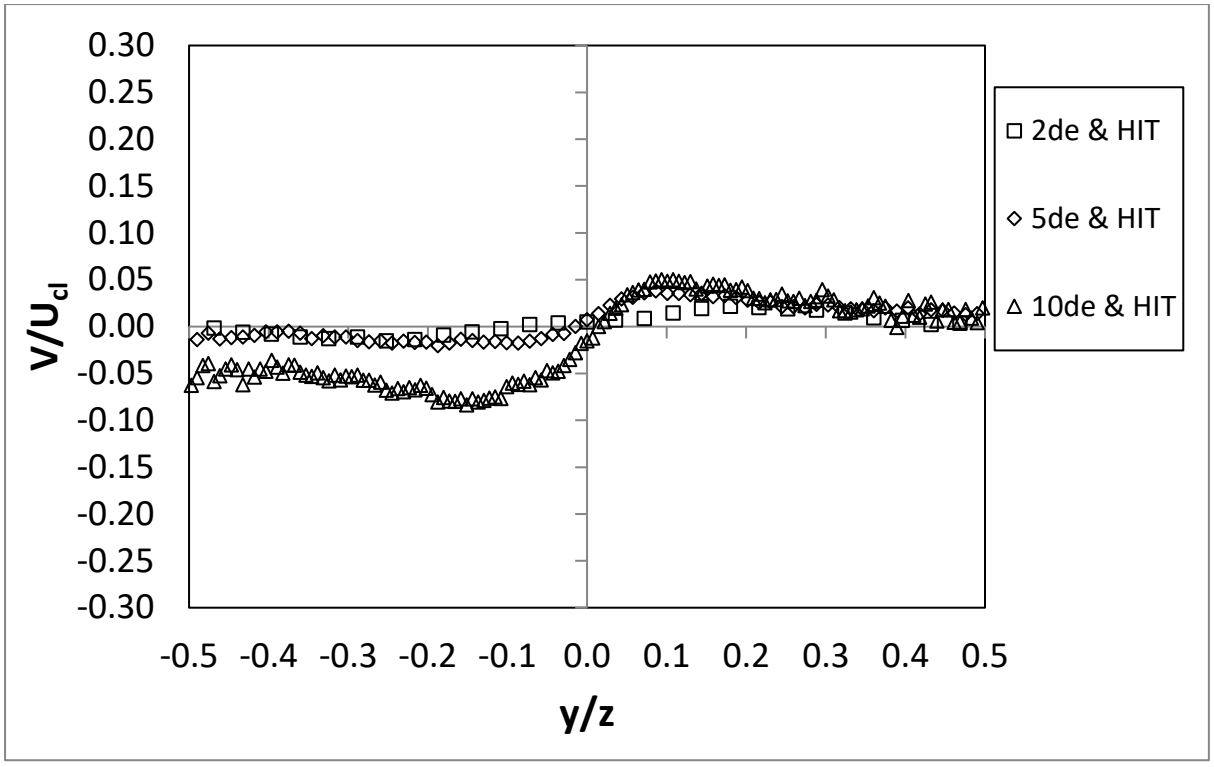

Figure 4-31: Normalized cross stream profiles of mean velocity V, Re 7700 under HIT

The profiles of the normalized u_{rms} are shown in Figure 4-32 and Figure 4-33 for the Re numbers of 3300 and 7700. By comparing the two cases, it is evident that the HIT of the environment results in a significant increase in turbulence intensity in the weaker jet. It should be reminded that the maximum values for a turbulent jet injected in a quiescent environment is about 0.2-0.3 according to theory and <0.2 according to the findings of section 4.4. Moreover, self-similarity was not attained, and the peak turbulence intensity appears at the jet boundaries only around the potential core, while downstream peak turbulence intensity appears along the centerline. The only location case that reminds us of the behavior without HIT is $5d_e$ for Re 7700. However, it is not maintained in the far-stream since subsequently external HIT dominates and disperses the jets turbulence intensity.

The results for v_{rms} presented in Figure 4-34 and Figure 4-35 agree with the above conclusions concerning the influence of HIT on u_{rms}. The anisotropy observed between u_{rms} and $v_{rms.}$ should also be noted. For example, for the case of Re 3300 and $5d_e$, around the jet axis the normalized u_{rms} value is ~0.5, while under the same conditions the normalized v_{rms} is 0.25, giving an anisotropy of 2. For Re 7700, the respective values are 0.2 and 0.1, leading to the same levels of anisotropy for this particular distance. Furthermore, the fluctuating velocity profiles become flatter, especially at larger distances, where the HIT prevails and homogenizes the jet turbulence (see Re 3300 -$10d_e$). This becomes more evident for the v_{rms}, since being weaker in comparison to the u_{rms}, is more prone to be influenced by

the HIT. The HIT has similar levels of u_{rms} and v_{rms} that are maintained in the whole region of interest due to homogeneity, meaning that the intensity is nearly invariable with distance.

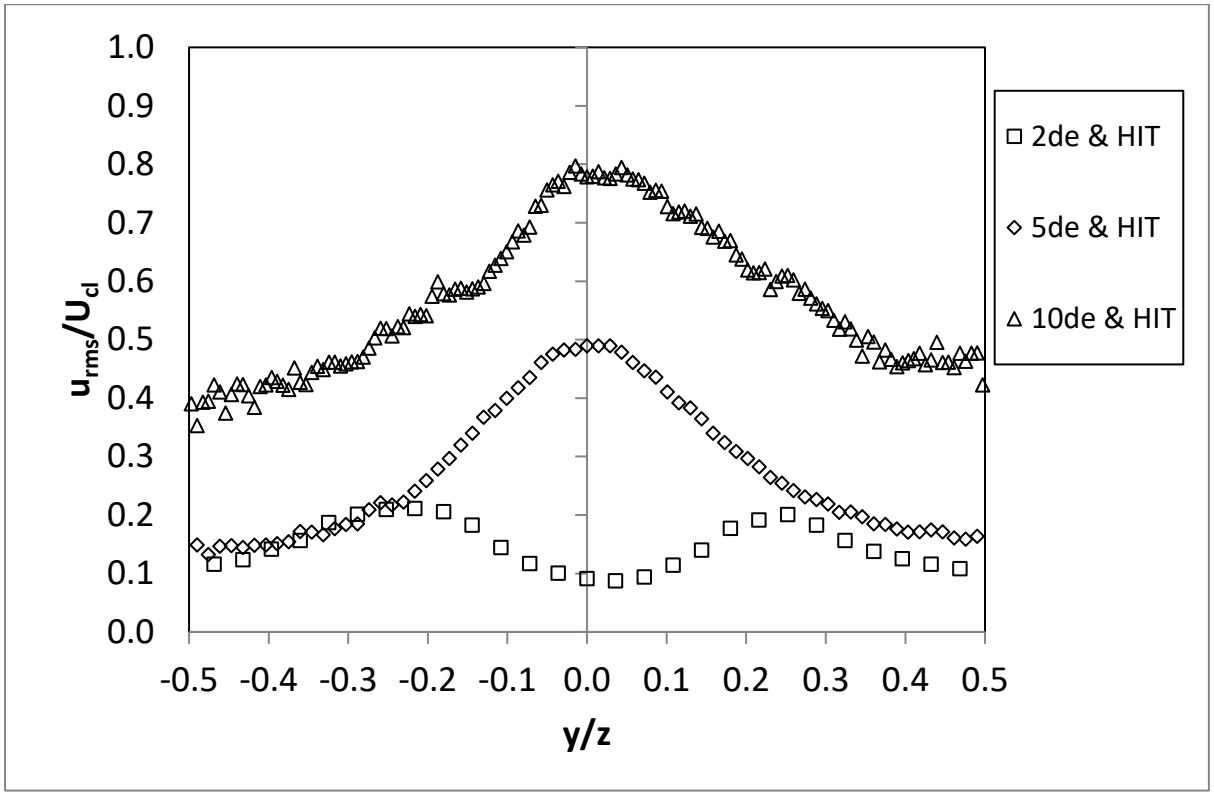

Figure 4-32: Normalized cross stream profiles of u_{rms}, Re 3300 under HIT

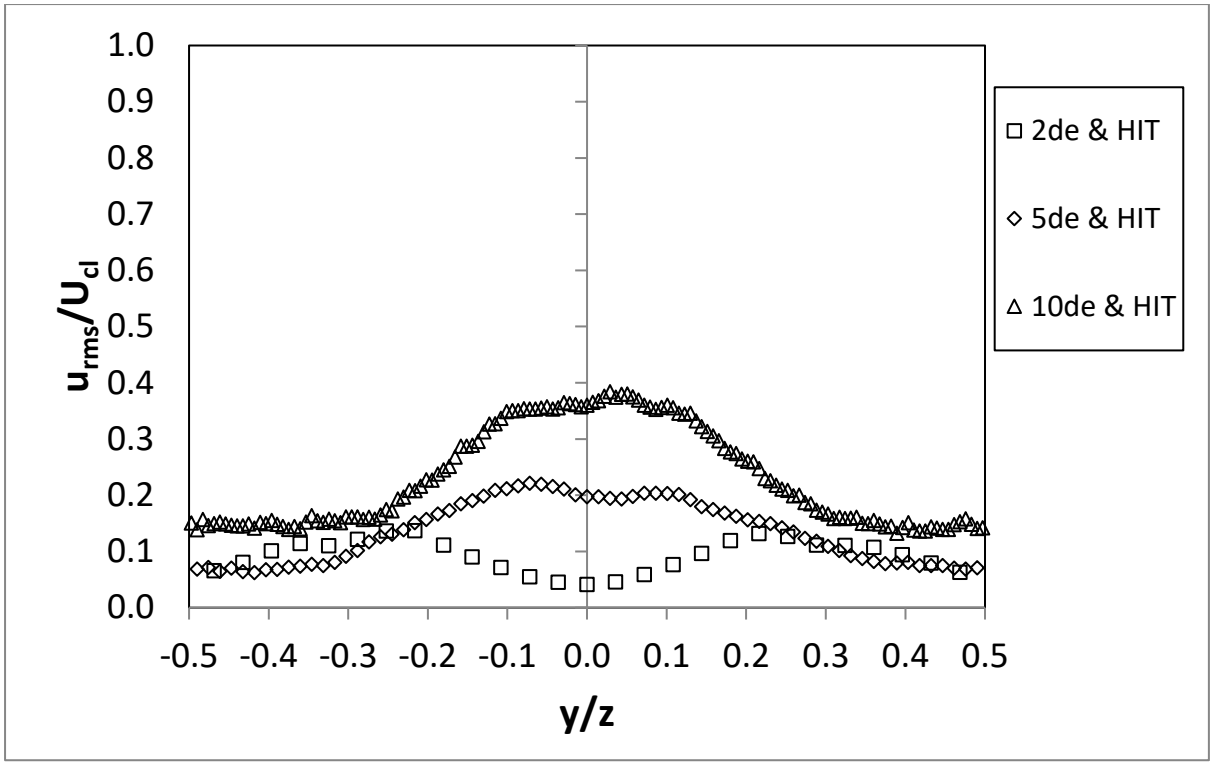

Figure 4-33: Normalized cross stream profiles of u_{rms}, Re 7700 under HIT

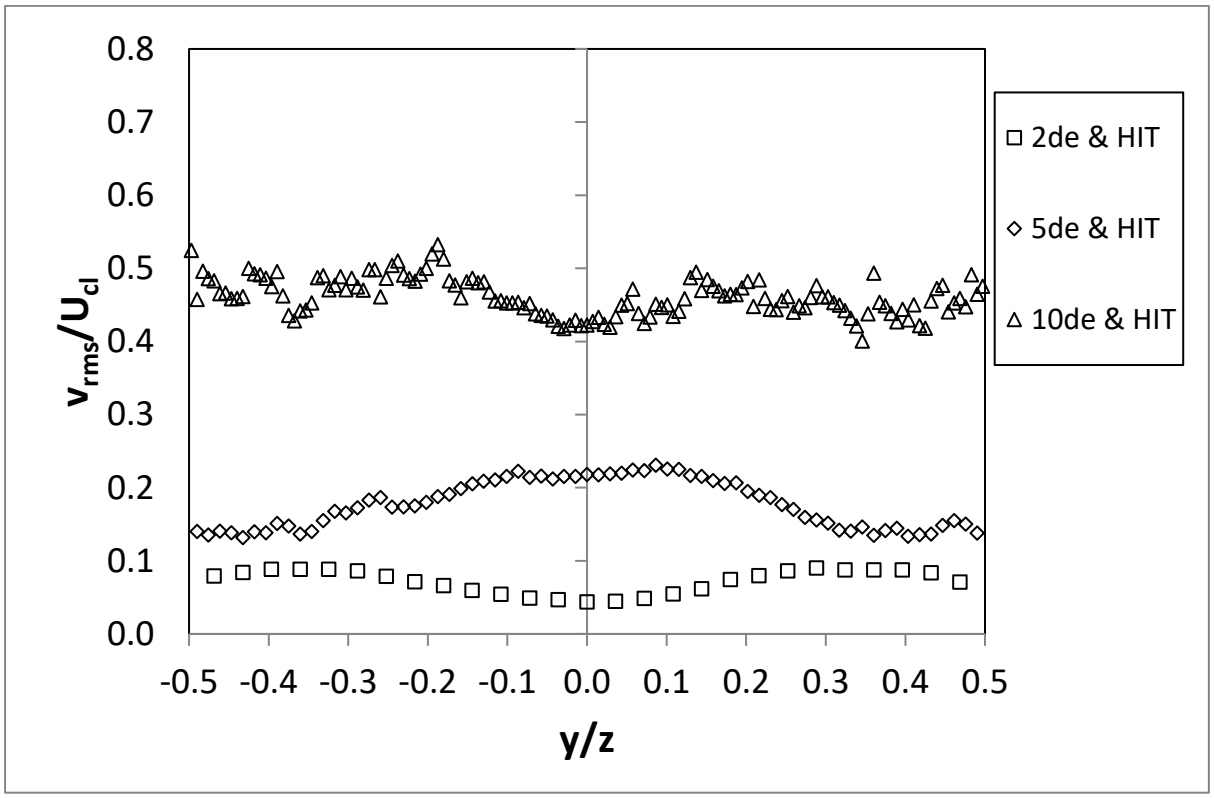

Figure 4-34: Normalized cross stream profiles of v_{rms}, Re 3300 under HIT

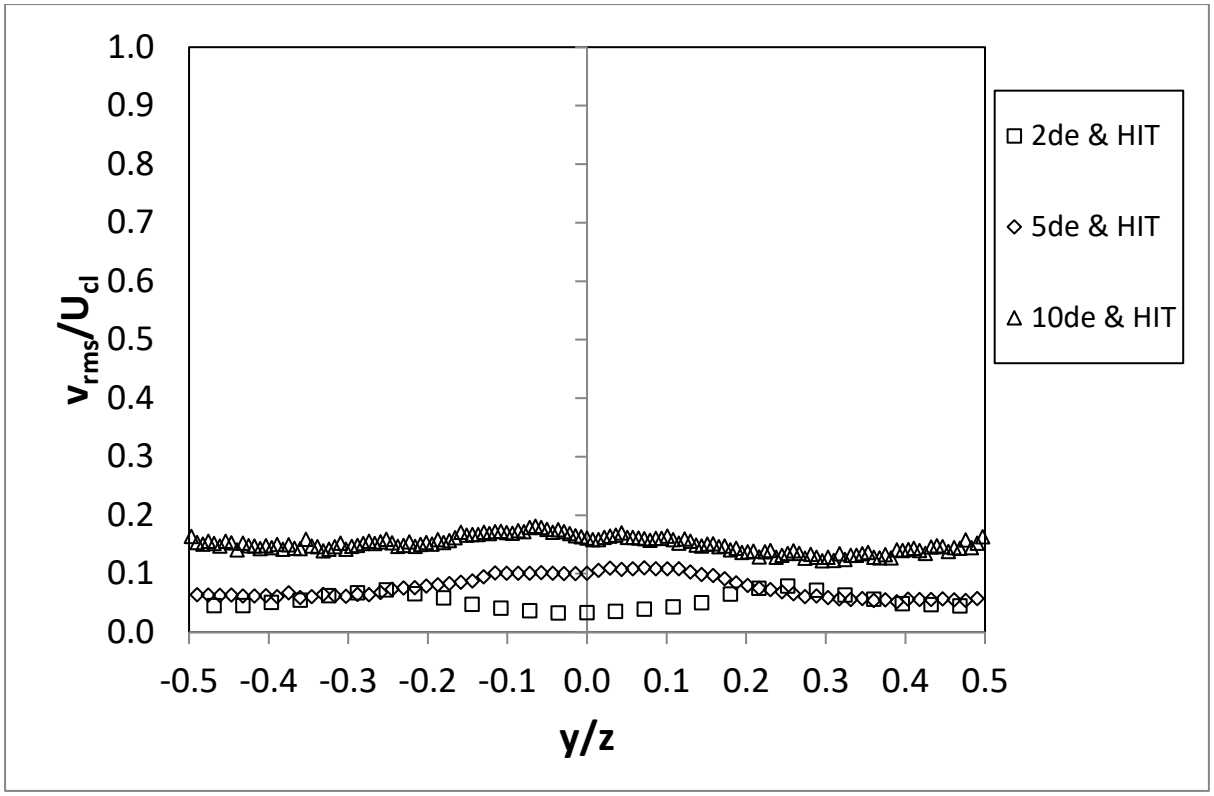

Figure 4-35: Normalized cross stream profiles of v_{rms}, Re 7700 under HIT

4.10 Spreading rate and flow entrainment of single jet under HIT

In section 4.5, it was shown that the measured PIV spreading rate follows a linear increase with distance as the theory of turbulent jets dictates. Nevertheless, in the near nozzle to intermediate field that was examined, the estimated spreading rate was smaller than what the literature review data report in the far-field. A similar effort was made to estimate the spreading rate based on the jet's half-width for the case of a jet in a HIT environment. The results are presented in Figure 4-36, with the reference case of a jet with Re=3300 injected in a quiescent environment for comparison. This particular Re was chosen because it exhibited the higher spreading rate in section 4.5.

It is observed that the presence of HIT increases the amount of jet spreading in comparison with the cases without environmental turbulence. This is also related to the faster jet decay that is observed in the presence of HIT, concerning the relationship between Re and decay rate; the lower the Re the higher the spreading rate and decay rate. However, the presence of HIT alters the behavior of the jet's spreading rate, which in this case is not constant with distance. In contrast to jet injection in a quiescent environment where the jet spreading rate was linear with downstream distance, the

exponential equation 1.105 offers a better description the jet half-width. However, as the Re increases it is obvious that the jet half-width approaches the case without HIT. The increase in spreading rate for a jet in background turbulence was also one of the findings in the paper of Khorsandi et al. [95].

The constants C_r and N_r are summarized in Table 4-6.

$$\frac{r_{1/2}}{d_e} = C_r e^{N_r \frac{z}{d_e}} \qquad 1.105$$

From the exponents N_r as presented in Table 4-6, it can be deduced that the larger spreading rate is achieved at low Re jets.

The main mechanisms of a jet entrainment is engulfment and nibbling according to Khorsandi et al. [95]. Engulfment is the mechanism where large volumes of surrounding fluid are entrained into the jet, whereas nibbling is the small-scale process that takes place at the thin (order of Kolmogorov scale) interface of the jet and its surroundings. Furthermore, since the jet half-width is considered an estimate for the jet's length scale [76], in Figure 4-36 the HIT integral length scale and Taylor microscale are added for comparison. The HIT integral length scale is larger than the jet's half width. This means that turbulent structures of that scale do not interact directly with the jet to result in ambient fluid entrainment. On the other hand, the Taylor microscale, which is an estimate of the majority of length scales of a turbulent flow (the intermediate scales from the integral to Kolmogorov), intersects the jet half width plots. It may be assumed that entrainment is caused by turbulent diffusion Khorsandi et al.[95], due to the interaction of the large scale eddies of the jet and the intermediate length scales of the HIT.

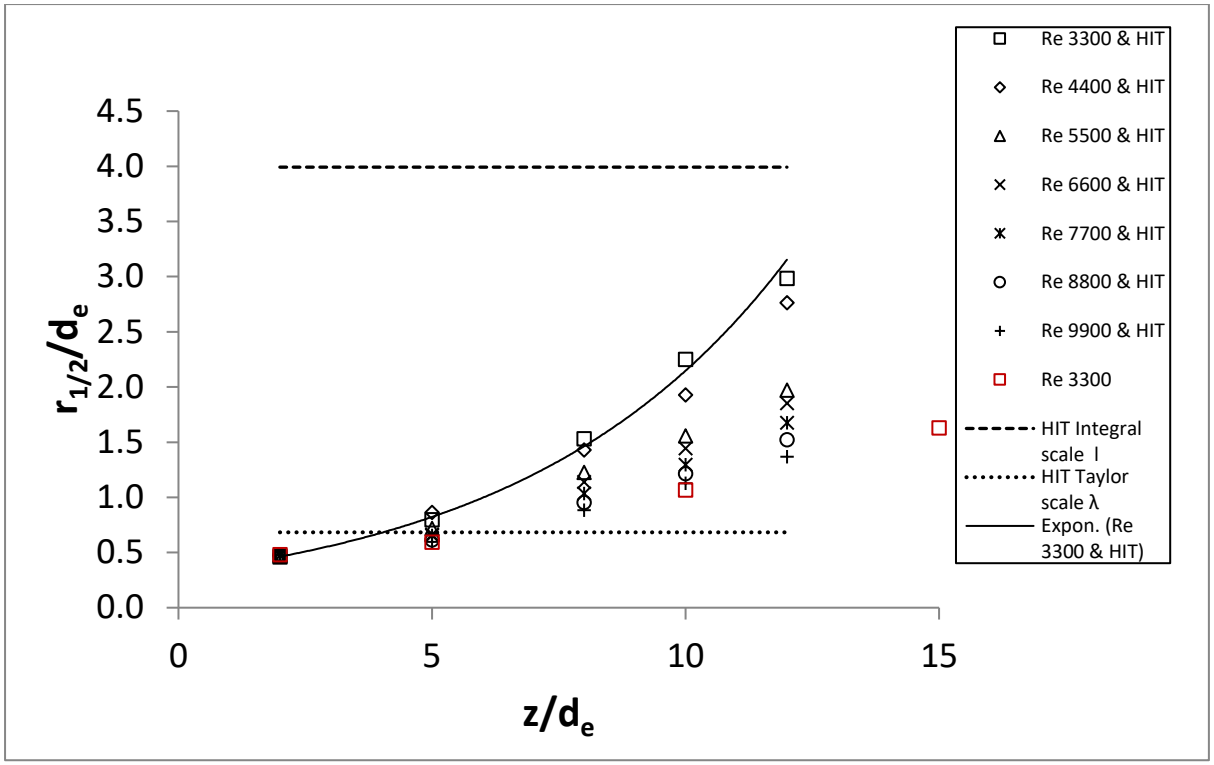

Figure 4-36: Jet half width $r_{1/2}$ as a function of distance from the jet exit, under HIT

Table 4-6: Spreading rate constants of exponential growth of jet half width in HIT

Re		3300	4400	5500	6600	7700	8800	9900
HIT	coefficient C_r	0.315	0.347	0.358	0.350	0.359	0.359	0.368
	exponent N_r	0.192	0.174	0.145	0.140	0.129	0.120	0.109

The elevated spreading of the jet due to turbulence is caused by the entrainment of more surrounding fluid. This is demonstrated by Figure 4-37, which depicts the normalized jet flowrates. However, contrary to the spreading rate, the entrainment rate is linear until $10d_e$. Beyond this axial distance, the jet deteriorates and the mixing due to external turbulence prevails. The flow entrainment constants are summarized in Table 4-7. The values of the entrainment rates are larger than what was estimated in Table 4-3, for the case without HIT. This observation is in contrast with the conclusions of Khorsandi et al. [95] for reduced flow entrainment as described in 2.3. On the other hand, the current observation comes in support to the theoretical prediction of Wright [98], who proposes that the ambient turbulence has an additive effect on the entrainment rate. Wright further emphasizes this conclusion for cases where the jet width is smaller than the ambient turbulence integral scale. This condition is valid in the current experiment as shown Figure 4-36, since the ratio of HIT l to the

maximum value of jet half width $r_{1/2}$ for the case of Re 3300 in a quiescent environment is approximately 2.67.

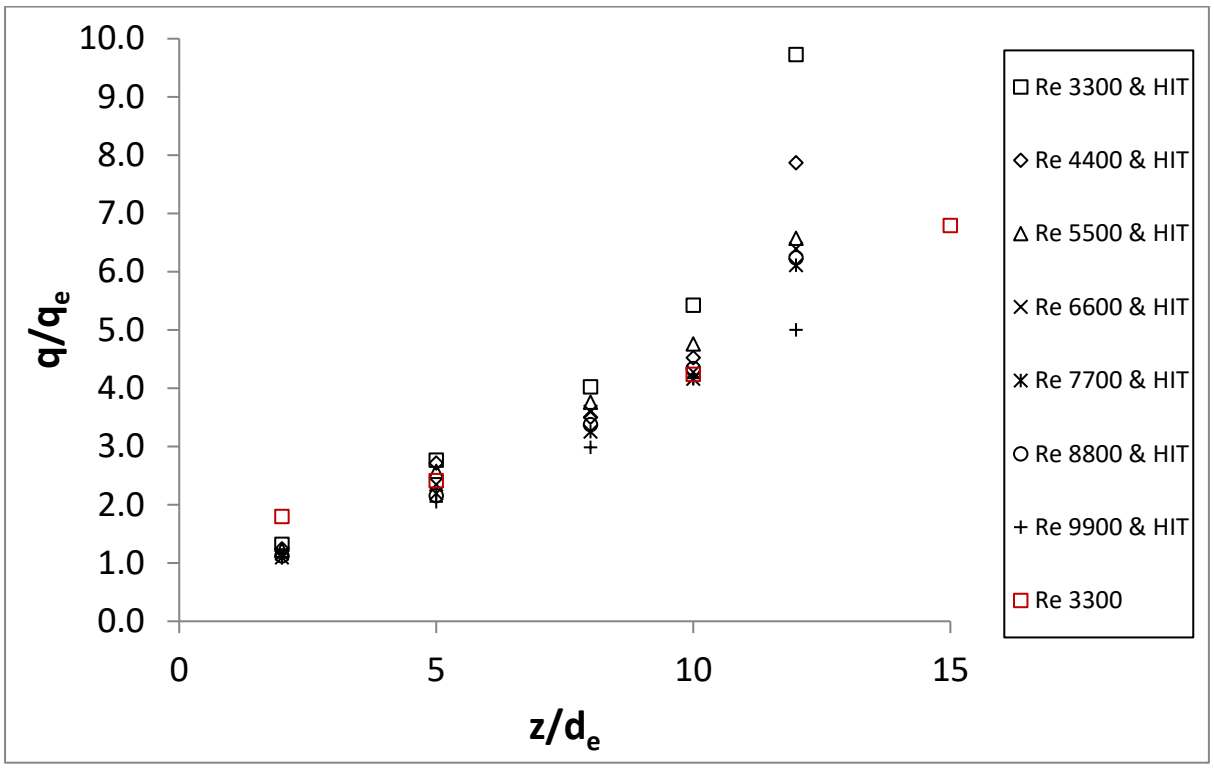

Figure 4-37: Flow entrainment rate of a single jet for various Re, under HIT

Table 4-7: Flow entrainment constants of a single jet in HIT

Re	3300	4400	5500	6600	7700	8800	9900
HIT	0.498	0.392	0.436	0.393	0.378	0.427	0.393

5. Opposed jets

Following the experimental and numerical investigation of the flow field of a single axisymmetric jet in a quiescent and a turbulent environment for the Reynolds range of our interest (3300-9900), the opposed jet configuration was the next step in the study. Two jet separation distances, L, were considered, L/d_e=5 and L/d_e=7.5. The choice of these two jets separation results from the dimensions of the HIT domain created by the box of turbulence. The maximum separation of the opposed jets was L/d_e=7.5 which corresponds to L=0.096 m. This distance is narrower than the distance that single jets were investigated. This is because narrower regions of interest have better conformity to HIT turbulence without mean flow, as discussed in section 3.1.2. In order to investigate the effect of jet separation, a separation of L/d_e=5 was also considered. The ratio of the two separations considered in this study is 1.5, which is deemed sufficient to detect its effect, if any, on the flow field, while allowing for sufficient jet development ahead of the stagnation plane. Closer jet separations were not considered as there would be minimal development of the jets ahead of the stagnation plane.

The mean velocity vector fields from the PIV measurements for all Re under investigation at L/d_e=5 are shown in Figure 5-1. The velocity fields are determined from the particle motion of the lower jet, since seeding is provided to this jet only. The stagnation plane is identified as the location where velocity vectors in the streamwise direction in the central region of the images and around the centerline of the jet attain near zero magnitude. Normally, in this area there is minimal penetration of particles beyond the stagnation plane. However, as the distance in y cross stream direction increases, due to mixing there is penetration of seeding particles which enables the study of the radial jet.

A coherent turbulent radial jet structure seems to emerge for Re≥5500, as is shown in Figure 5-2, when the opposed jets are turbulent. More specifically, for laminar jets of Re=1100 and 2200, an axisymmetric turbulent flow presenting radial spreading does not emerge at all. In these cases, a flow limited by a thin region in the cross-stream direction exists, which is laminar and breaks up forming vortices far from the opposed jets centerline as is shown in Figure 5-2, for Re 2200. From the same figure, it is noted that as the Re is increased the existence of vortices moves near the centerline, establishing a turbulent jet for Re 5500. Based on the existence and shape of the radial jet, the intermediate Re 3300 and 4400 can be characterized as a transition regime between laminar and turbulent behavior. Consequently, the focus of the analysis in the course of the chapter rests on the cases above Re 5500, where the flow is turbulent in the whole plane of investigation.

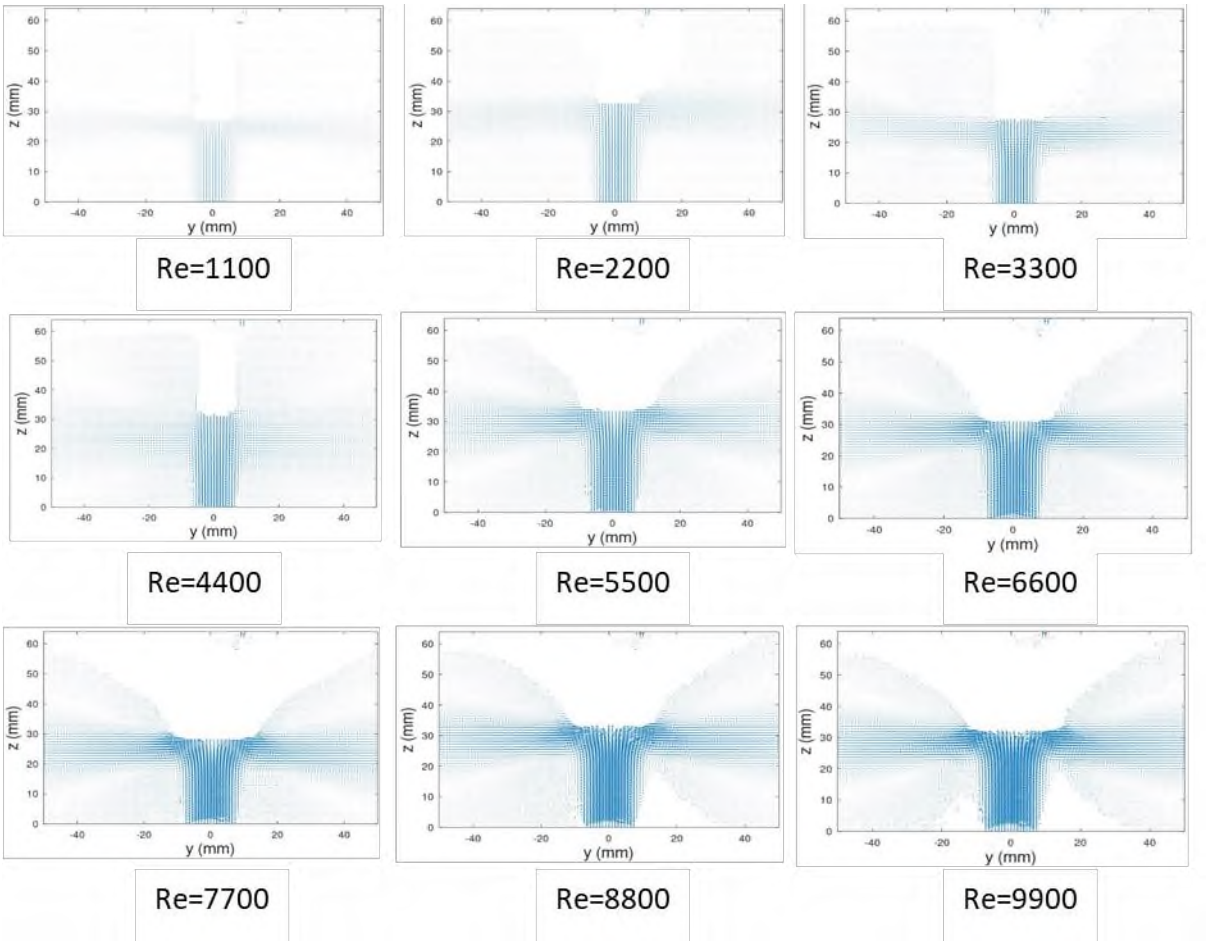

Figure 5-1: Mean velocity vector maps of opposed jets without HIT for each Re number, L/d_e=5

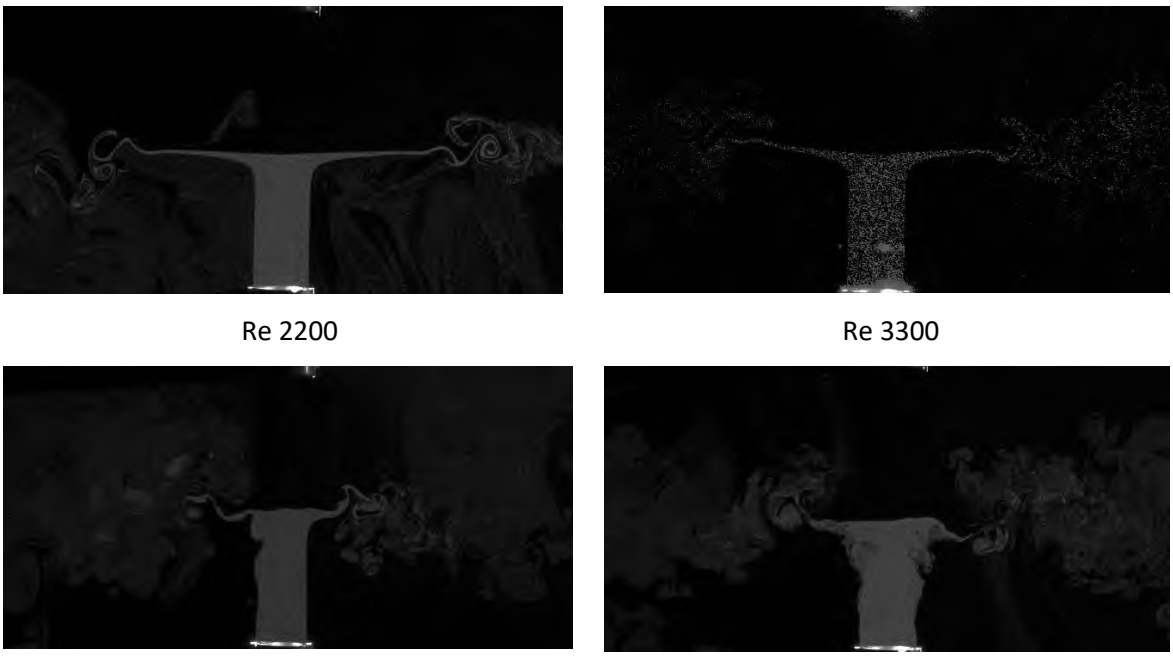

Re 2200 Re 3300

Re 4400 Re 5500

Figure 5-2: Instantaneous PIV images for L/d_e=5

In conjunction with the literature review of section 2.4, a strategy was drawn for identifying and examining the key features of the flow. In the following paragraphs of this chapter, the flow will be investigated as below:

- Evaluation of flow development along the jet centerline leading to the stagnation region, including U_{mean}, u_{rms}, v_{rms}, tke, and estimating the axial strain rate in the stagnation region.
- Examination of the flow in the radial direction of the stagnation plane along a "stagnation line" in the same manner as on the longitudinal centerline.
- Examination of the existence of the free radial jet developing in the stagnation region and its potential self-similar state.

Before proceeding to the above analysis, a few preliminary remarks that work as a guide and contribute to a more complete view of the phenomenon shall be included in this introductory section.

The verification that the jets emanating from the pipe are turbulent in nature comes from the shape of the velocity U_e at the exit plane. The profile of the PIV measured velocity as depicted in Figure 5-3, Figure 5-4 follows the power law of equation 1.67 with an exponent of n=1/7 that corresponds to a fully developed turbulent boundary layer flow. The CFD data are imposed as a boundary condition for the simulations and as a result the model used subsequently does not alter the outcome at the jet exit. The CFD velocity profile plot for Re=7700 is chosen as representative, and since for the other CFD cases the velocity profiles are identical they are omitted. There is good agreement between the experimental PIV measurements and CFD concerning the exit profile. Furthermore, considering the experimental data, it is noted that the opposed flow does not bring any alterations in each jet turbulent exit velocity profile, in contrast with the observations of Korusoy and Whitelaw [4] extracted however for smaller L/d_e ratios. In that case, for L/d_e=2 the exit profile maintained the top-hat velocity profile due to the use of contoured nozzles while as the L/d_e was reduced until L/d_e=0.2 the profile became "wake like", having a minimum on the centerline. The "wake like" profile is attributed to the strong counteraction of the jets and the stagnation produced due to the close proximity of the opposed exit nozzles.

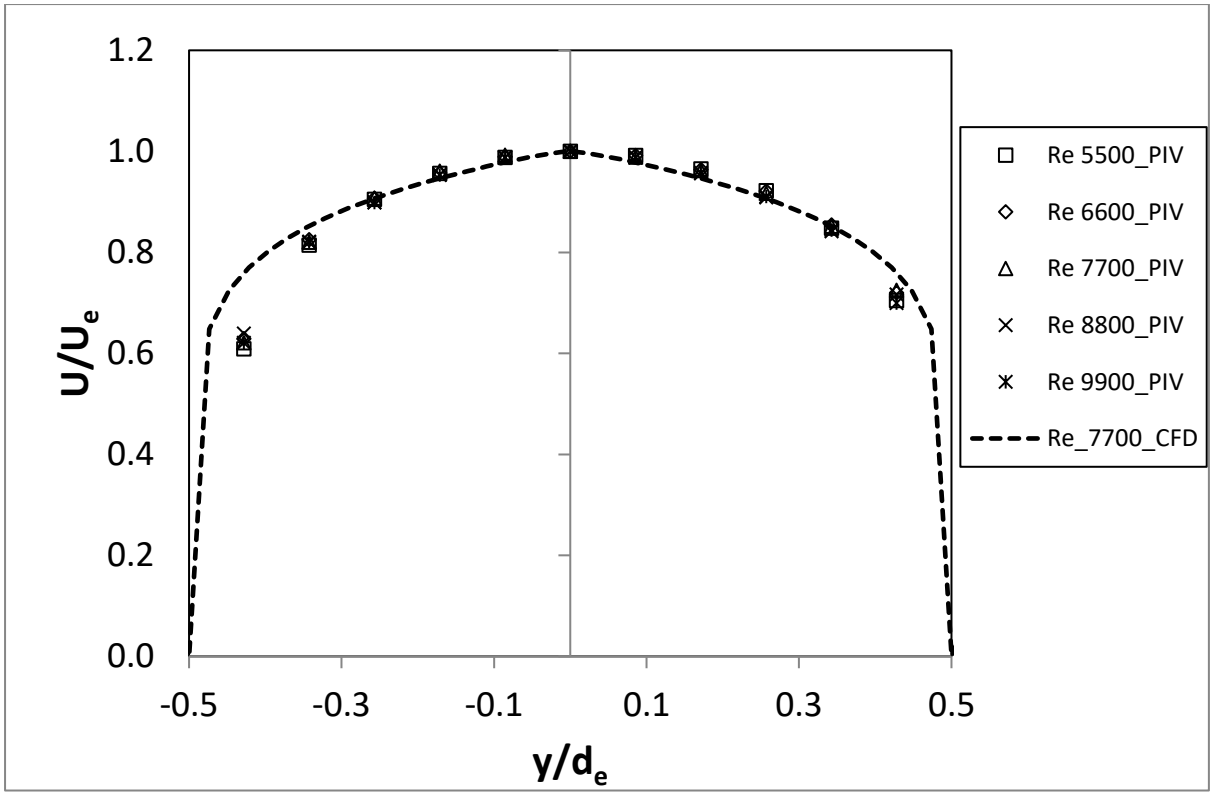

Figure 5-3: U_e velocity profile at the pipe exit, L/d_e=5, PIV & CFD Data

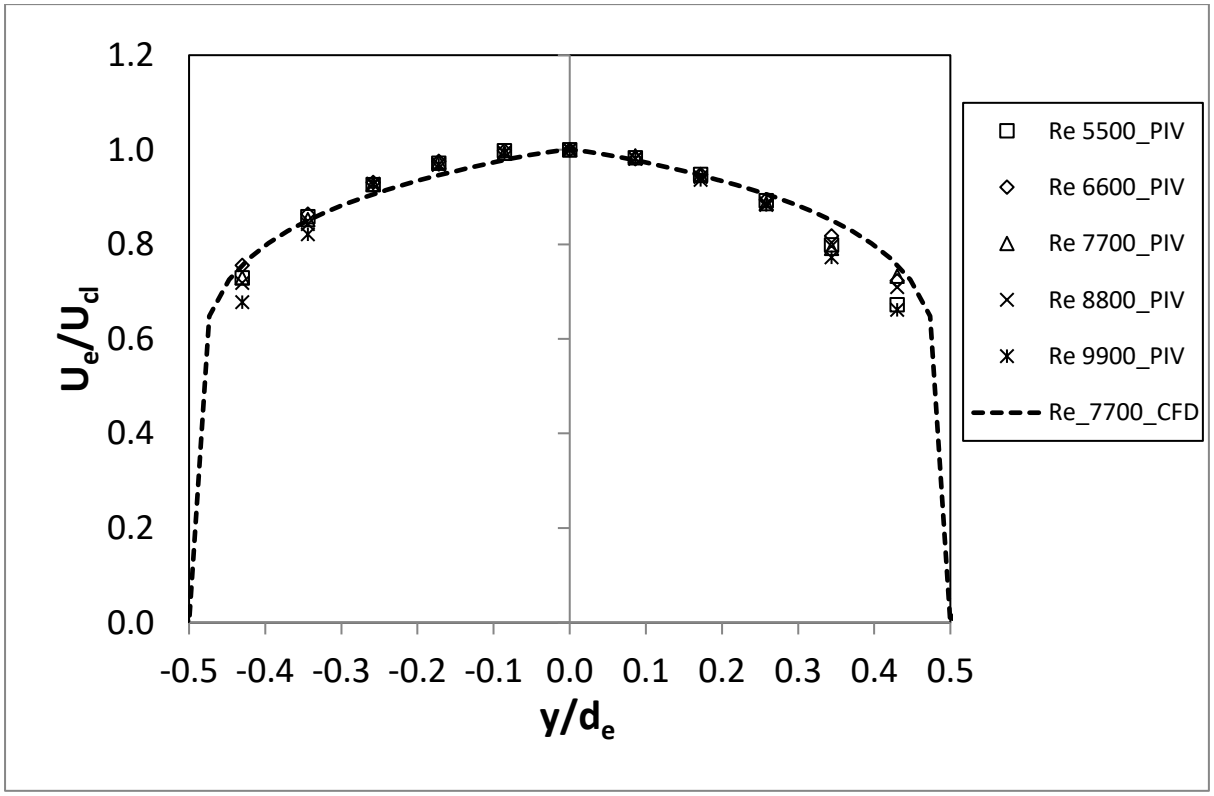

Figure 5-4: U_e velocity profile at the pipe, L/d_e=7.5, PIV & CFD Data

5.1 Opposed jets flow along their centerline without HIT

In this section, the behavior of the mean and turbulent quantities along the centerline axis of the opposed jets for Re>5500 are examined. Before proceeding to the presentation of the results, it should be noted that due to seeding of only one of the two jets, measurements of the flow velocity along the jet centerline were possible effectively from the exit of the seeded jet up to the stagnation plane. As a result, the graphs are plotted up to the stagnation plane, while the opposite half of the flow field is considered to have a similar behavior due to symmetry. Additionally, the stagnation plane forms before the jets can reach the ZEF and begin to spread. Consequently, the flow remains within the initial zone, or the potential core of the jets and an examination of the self-similar characteristics is omitted here.

The evolution of the streamwise component of the velocity for $L/d_e=5$ and $L/d_e=7.5$ is presented in Figure 5-5 and Figure 5-6 respectively. The coordinate system is placed on the exit of the bottom jet. The longitudinal distance z from the bottom nozzle is normalized as $(z-z_{st})/(L/2)$, as in Mastorakos's PhD thesis [134]. In this way the longitudinal distance is normalized in the range between -1 and 1 with the bottom jet located at -1 and the stagnation plane located at 0. Setting the stagnation plane at 0, was deemed more suitable for a symmetric configuration. As the jet exits the nozzle, the velocity does not change longitudinally, due to the existence of the potential core. However, as the stagnation plane is approached, the flow is slowing down in a linear fashion until the zero value is reached at stagnation. The location at which the slowing of the streamwise longitudinal velocity begins to decrease is at about $(z-z_{st})/(L/2)=0.4$ before the stagnation plane in the case of $L/d_e=5$, while in the case of greater jet separation of $L/d_e=7.5$ the distance from the stagnation plane where U_{cl} begins to decrease shortens at about $(z-z_{st})/(L/2)=0.22$. Neither of the k-ε or k-ω model predict accurately the mean flow streamwise velocity and both exhibit significant deviations from the experimental measurements. The k-ε model predicts a more gradual drop of velocity at the stagnation plane leading to smaller axial strain rate, while the k-ω model predicts a sharper velocity drop and strain. Interestingly, the k-ω model predicts the location of the slowing down of the flow in agreement with the experimental measurements while the k-ε model is in better agreement with the experimental measurements close to the stagnation plane.

In Table 5-1, the absolute, bulk and the normalized (by the bulk strain rate) values of the decay constants of U_{cl} are provided. The absolute and bulk decay constants correspond to the axial strain rates $\partial U/\partial z$. For Re≥5500 the values of the absolute and bulk strain rates (defined as $S_b=2U_e/L$) are proportional to the Re number for both L/d_e ratios. This linear increase in the strain rate with Re is verified by the fact that the normalized strain rate values remain nearly constant with the increase of

Re. Furthermore, it is observed that at L/d_e=7.5 the strain is about 1.75 times greater than at L/d_e=5. This contradicts the conventional quantification of the bulk strain rate of $S_b=2U_e/L$, which is larger for the smaller L/d_e ratio in every case. Moreover, a large deviation of the absolute strain rate from the bulk strain rate values is observed in every case, the measured strain rates emerging $>2S_b$ for L/d_e=5 and $>4S_b$ for L/d_e=7.5. An agreement with the bulk strain rate is expected for L/d_e ratios as in Korusoy and Whitelaw [4] lower than in the present cases. In such cases of very low L/d_e ratios the stagnating effect begins almost immediately after the jet exit and as a result yields a strain rate with value $U_e/(L/2)$.

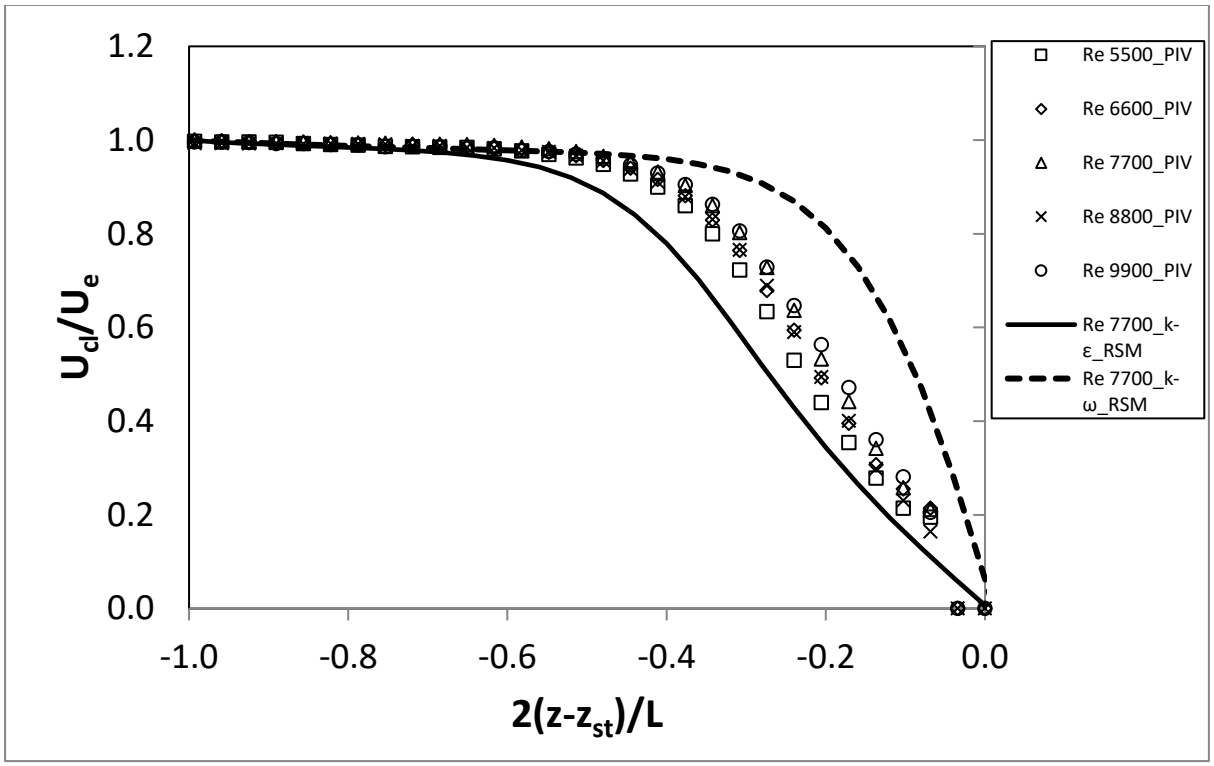

Figure 5-5: Mean streamwise (axial) velocity U along the opposed jets axis (centerline), L/d_e=5

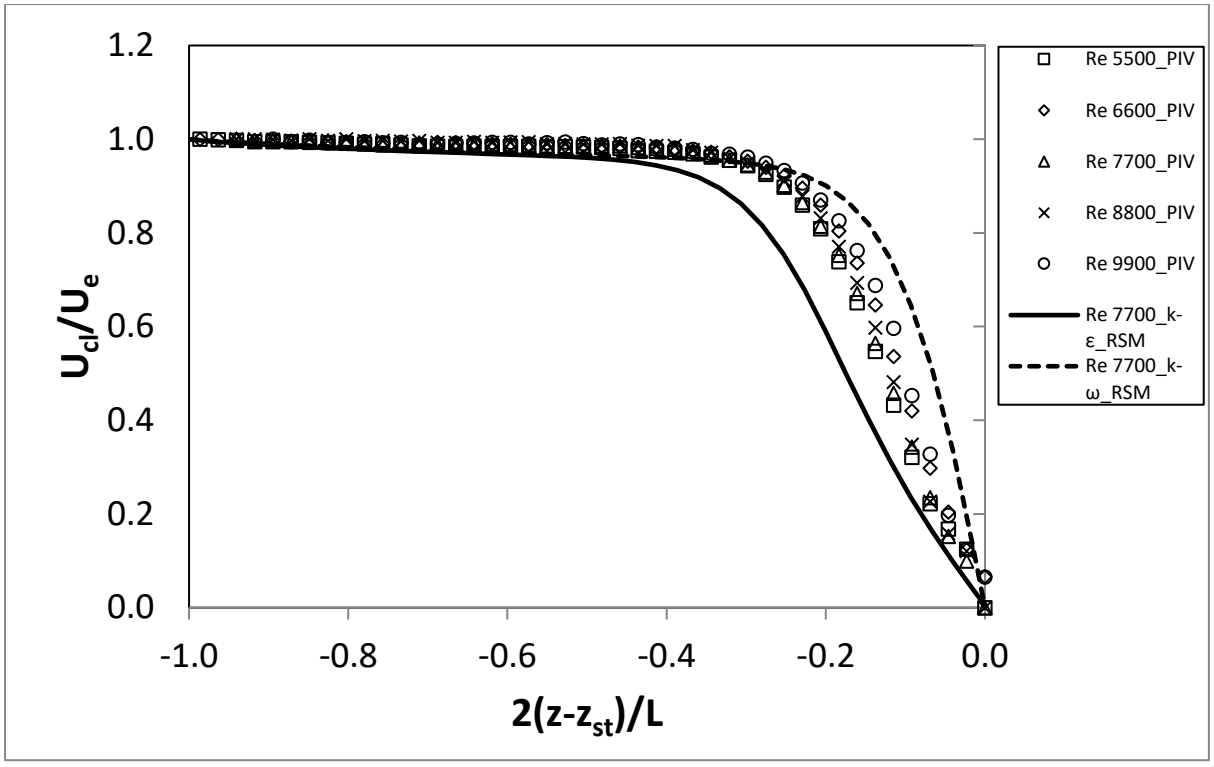

Figure 5-6: Mean streamwise (axial) velocity U along the opposed jets axis (centerline), L/d_e=7.5

Table 5-1: Linear axial decay constants (axial strain rates) at the stagnation region

	Re	5500	6600	7700	8800	9900
	Absolute	462.5	526.3	627.9	749.4	827.5
L/d_e=5	Normalized	2.47	2.43	2.43	2.46	2.49
	Bulk	187.2	216.5	255.6	304	332.3
	Absolute	536.2	658.8	726.8	834.3	1002.7
L/d_e=7.5	Normalized	4.24	4.45	4.31	4.45	4.68
	Bulk	126.4	147.8	168.5	187.2	214.2

The development of turbulence along the jet centerline is examined through the normalized (with the exit velocity U_e) quantities of u_{rms}, v_{rms} and tke for L/d_e=5 (Figure 5-7 through Figure 5-9) and L/d_e=7.5 (Figure 5-10 through Figure 5-12).

The trends of each property show good grouping among the Re numbers considered and follow similar but not identical development. In all cases, both the fluctuating velocities and the tke maintain the same values for some distance downstream the nozzle as those measured at the nozzle exit, since the

jet core is not disturbed by external influences. After a length of constant magnitude, both fluctuating velocities and the tke begin to increase, as the shear layer at the jet boundary starts to affect the jet core. The location of the increase agrees with the location where the streamwise velocity was found to begin to decrease in Figure 5-5 and Figure 5-6 which shows that the turbulence is caused by velocity fluctuations that occur in the stagnation region of the flow. These fluctuations result from the stagnation plane oscillations around the stagnation plane at $z=z_{st}$. This behavior can be described as a pitchfork bifurcation mode defined in section 2.4., where the stagnation plane position oscillates around a mean symmetry position located in the middle between the two exits.

All three properties reach maximum values ahead of the stagnation plane which are about 0.20 for $u_{rms,max}/U_e$, 0.05 for $v_{rms,max}/U_e$ and 0.025 for tke_{max}/U_e^2. The measured maximum values represent an increase of 7.5, 1.8 and 22 from the values at the nozzle exit for $u_{rms,max}/U_e$, $v_{rms,max}/U_e$ and tke_{max}/U_e^2 respectively. The maximum magnitude of the fluctuating velocities and tke are somewhat greater for $L/d_e=7.5$ than for $L/d_e=5$. The greater effect on $L/d_e=7.5$ can be attributed to the greater axial strain in this case as reported earlier. After the location of maximum magnitude, the value of the fluctuating velocities and tke starts to decrease as the stagnation plane is approached. However, the trends do not converge to zero at the stagnation plane for any of the three examined properties. Furthermore, large anisotropy $u_{rms}/v_{rms}=5$ is observed along the centerline, the reason being the small cross-stream (radial) velocity (nearly zero) along the axis, which characterizes the axisymmetric jet.

Concerning the CFD results, only the cases of Re=7700 are shown, since the normalized data have exhibited invariance with the Re number. Both k-ε and k-ω models succeed in predicting the elevated rms quantities around the stagnation point which is in agreement with the experimentally measured values. However, the overall trends of the fluctuating velocities and the tke predicted by both CFD models are in disagreement with the overall trends captured by the experimental measurements as the former fail to predict the turbulence maxima upstream of the stagnation plane captured by the latter.

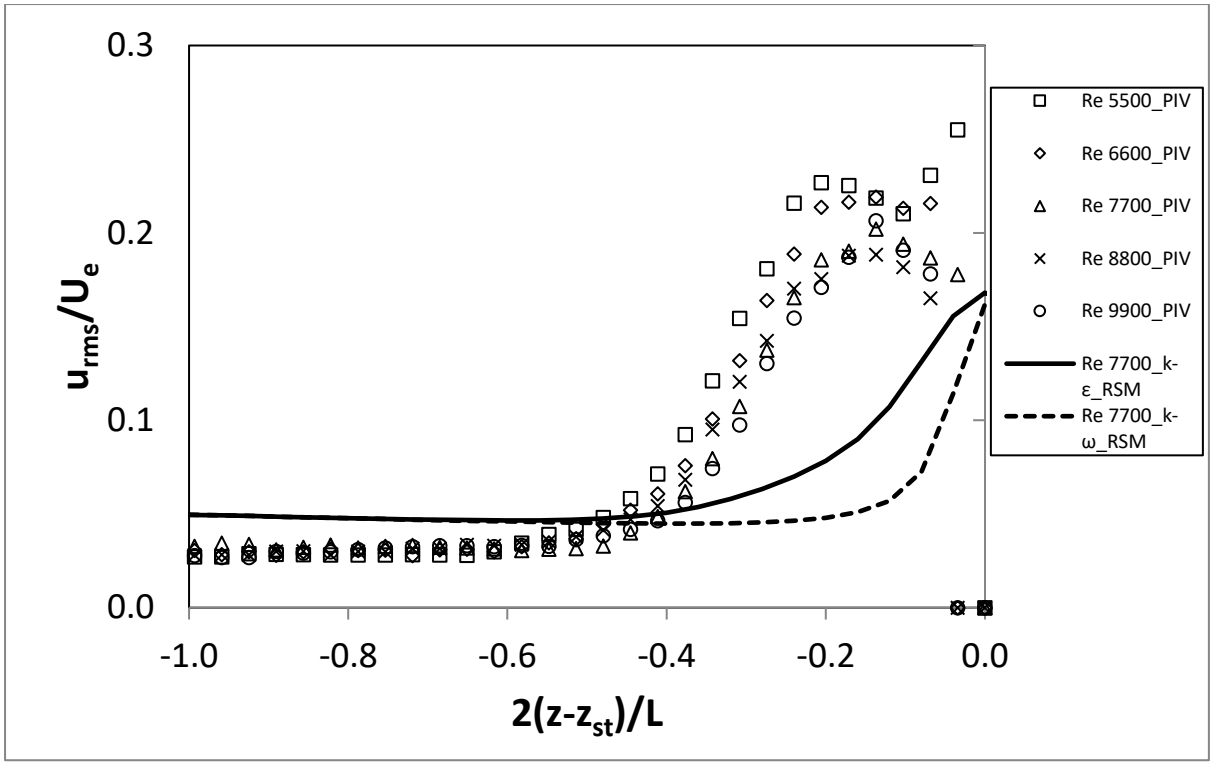

Figure 5-7: Normalized u_{rms} along the opposed jets axis (centerline), $L/d_e=5$

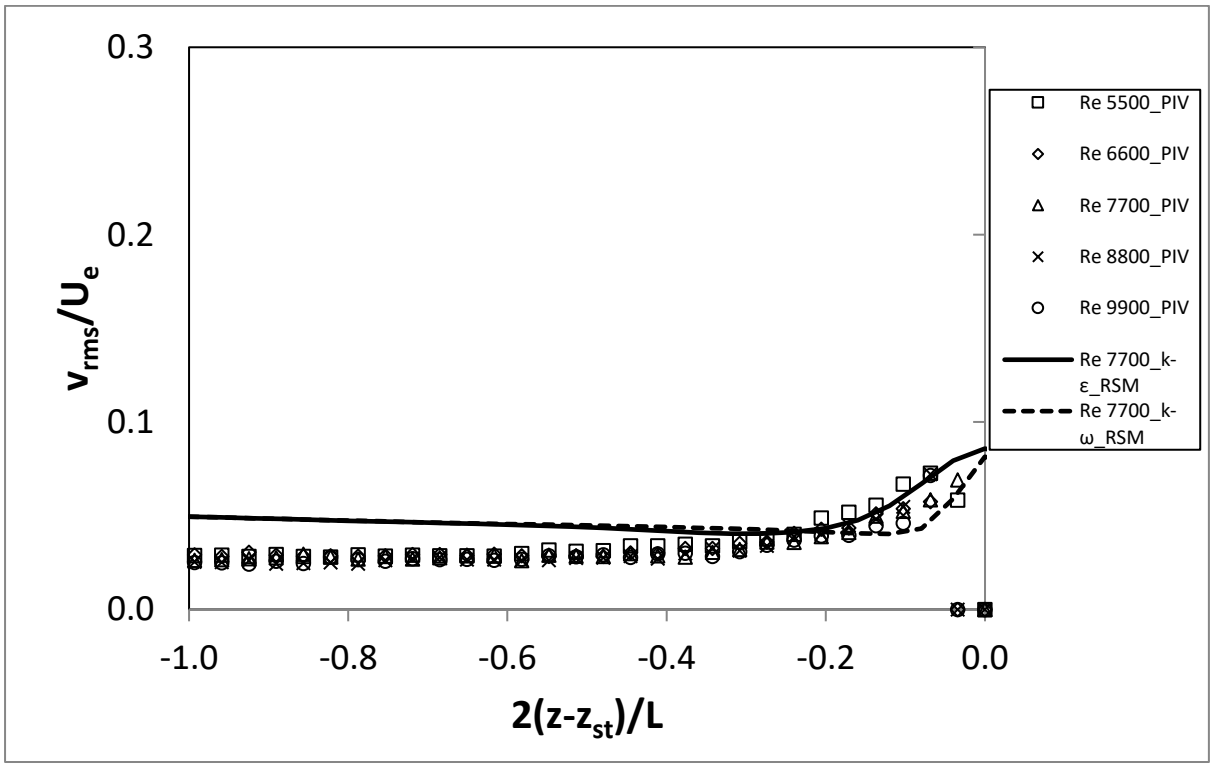

Figure 5-8: Normalized v_{rms} along the opposed jets axis (centerline), $L/d_e=5$

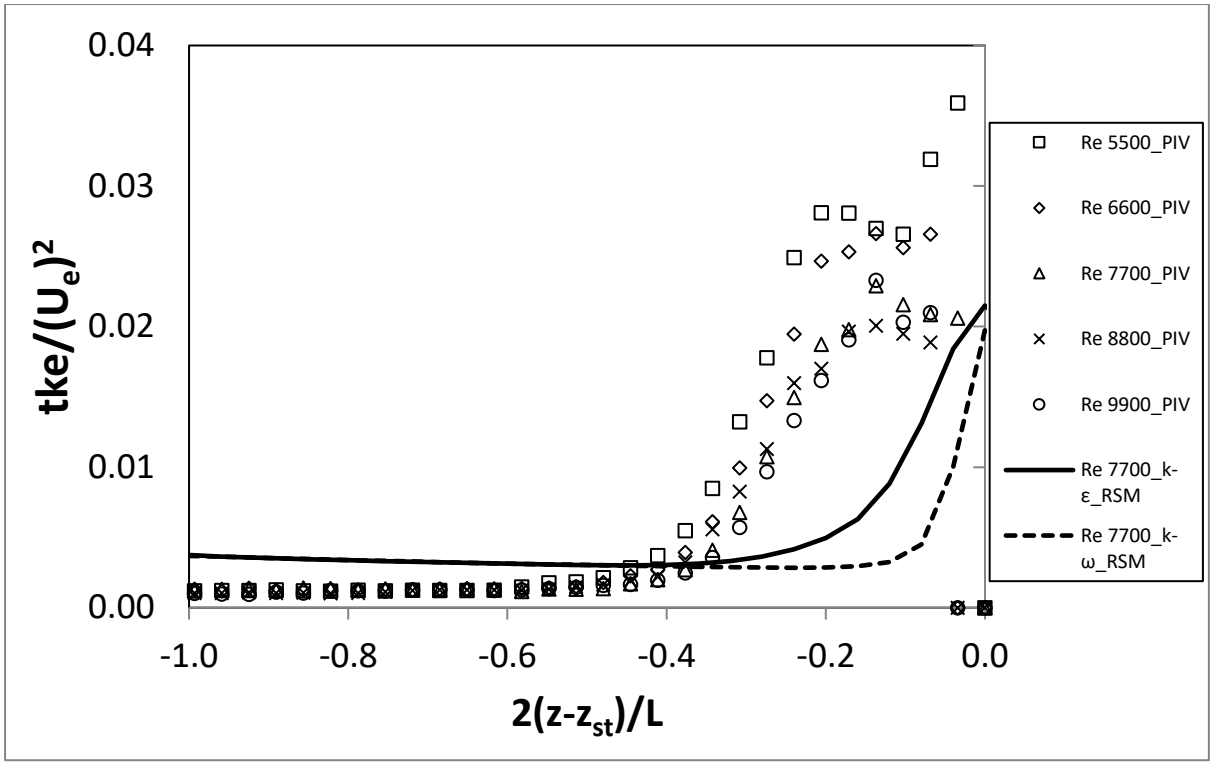

Figure 5-9: Normalized turbulent kinetic energy along the opposed jets axis (centerline), $L/d_e=5$

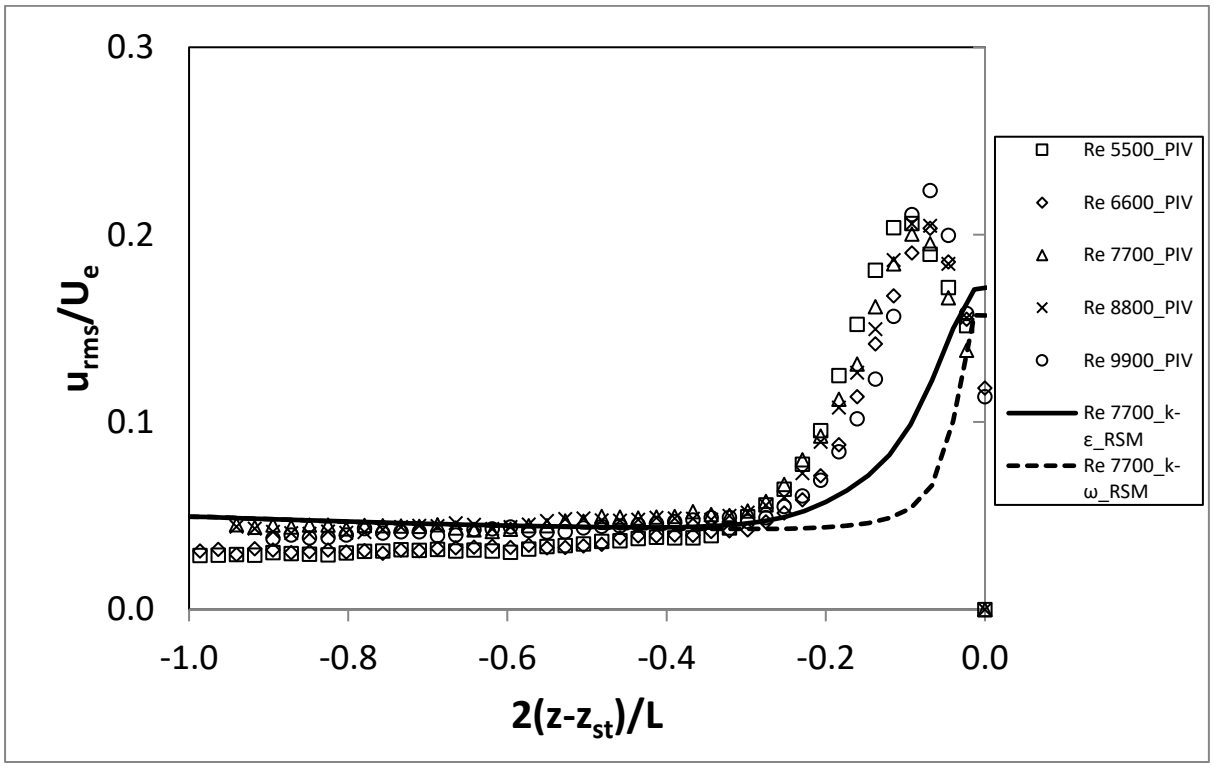

Figure 5-10: Normalized u_{rms} along the opposed jets axis (centerline), $L/d_e=7.5$

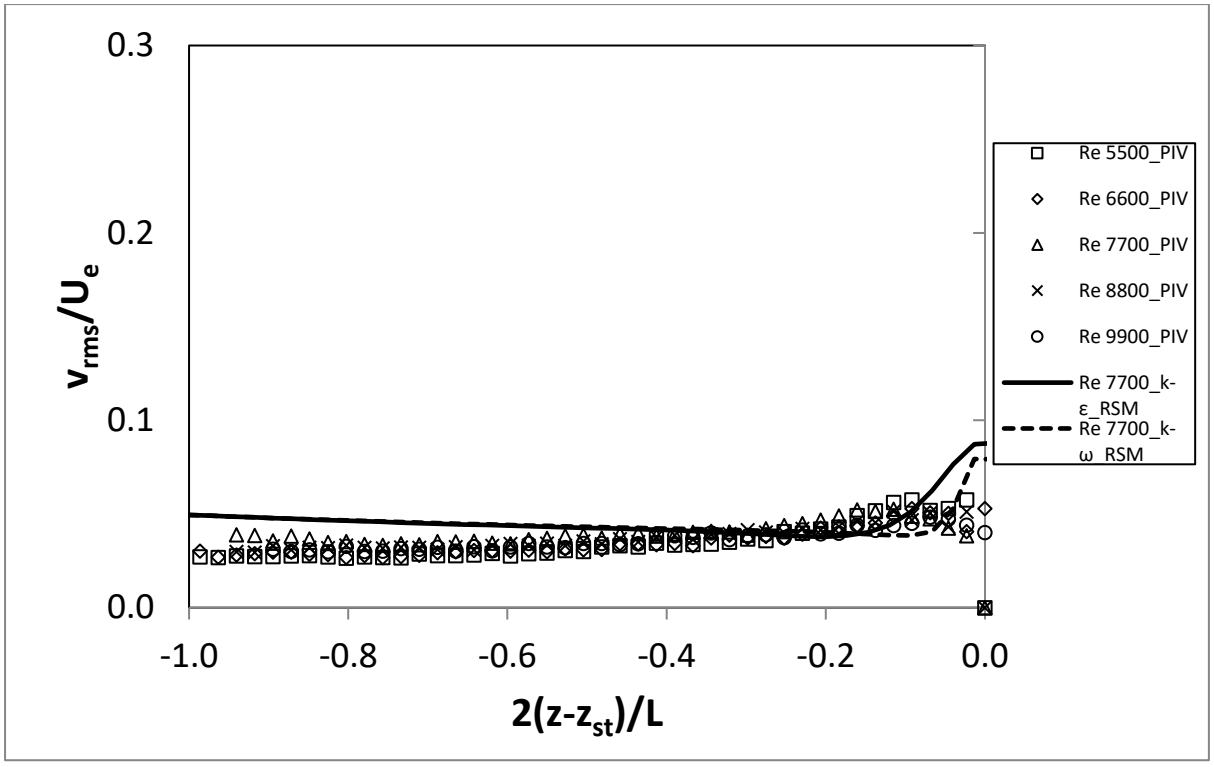

Figure 5-11: Normalized v_{rms} along the opposed jets axis (centerline), L/d_e=7.5

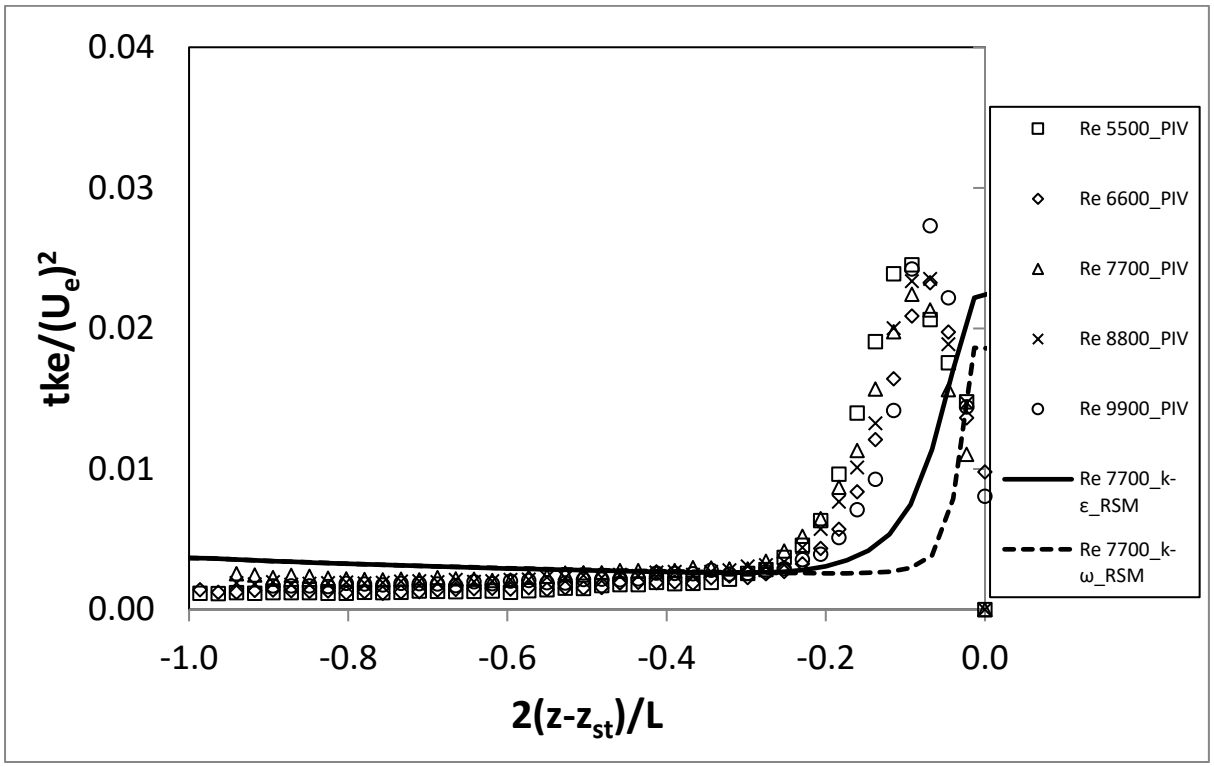

Figure 5-12: Normalized turbulent kinetic energy along the opposed jets axis (centerline), L/d_e=7.5

5.2 Opposed jets flow along the stagnation line without HIT

The evolution of the radial jets formed along the stagnation plane will be examined in this section in terms of V_{mean}, u_{rms}, v_{rms}, and tke. The phenomenon under investigation is three-dimensional. However, due to its axisymmetric nature, the description of the flow that is captured by the 2D PIV data provides general conclusions for the stagnation plane. The straight line perpendicular to centerline axis of the opposed jets that is crossing the centerline in the middle of the separation distance between the nozzles where the jet flow stagnates, will be called from now on "stagnation line".

The evolution of the streamwise component of the velocity from the jets exit till the stagnation plane for L/d_e=5 and L/d_e=7.5 is presented in Figure 5-13 and Figure 5-14 respectively. The normalization chosen is adapted from Korusoy & Whitelaw [4]. This permits the direct comparison of the radial component V developed at the stagnation plane with the exit boundary condition, giving an indication of the stretching of the flow. Moreover, the normalization of the radial coordinate with exit diameter d_e provides an easy way for locating the maximum value of V and how the flow evolves considering the geometrical setup.

Examining the evolution of V along the stagnation line, the following remarks can be made:

- As expected along the stagnation line the flow is symmetric around the origin.
- The velocity at the origin is zero and increases along the stagnation line towards the radial direction until a maximum value is reached. This shape is due to the conservation of mass since the axial flow is stagnated.
- The maximum value of the radial jet V occurs for both jet separations at about 0.75 d_e from the stagnation point after which the decrease of the velocity decreases exponentially with the radius as $V=ae^{-gy}$, with a=0.6, g=0.25 for L/d_e=5 and g=0.30 for L/d_e=7.5. The peak values of V are larger for the smaller separation ratio L/d_e=5.
- The normalized plots of Figure 5-13 and Figure 5-14 coincide for all Re numbers, exposing the analogous relationship between stretching of the flow in the cross-stream direction of the stagnation plane and the variation of Re.
- The rate of change of V with y, $\partial V/\partial y$, namely the radial strain rate is constant along the stagnation line within the central portion of the opposed jets, as described also in Wu et al [115] and Stan [135]. The values of the strain rates are provided in Table 5-2 for all Re along with the bulk strain rate defined from geometrical considerations as $S_b=2U_e/L$ and the normalized strain rate, which is the ratio of the absolute strain rate to the bulk strain rate. The normalized values tend to be constant regardless of Re for each L/d_e ratio, meaning that there is a proportional

increase of the radial strain rate to Re number for a certain L/d_e. The axial strain of the radial jet is greater for the smaller L/d_e ratio of $L/d_e=5$. Due to the smaller available space, the conservation principle forces the flow in the radial direction with higher momentum.

- The assumption of equation 1.73, stating that the axial strain rate is being twice the radial strain rate is not verified by Table 5-1 and Table 5-2. The deviation is attributed to the fact that the theoretical model of equation 1.73 was developed under the circumstances relating to Closely Spaced Opposed Jets, where the axial strain rate starts immediately from the jets exit.
- While both CFD models predict qualitatively correctly the development of the radial velocity along the stagnation line in terms of the overall shape and the location of the maximum V, neither is able to consistently match the experimental measurements. The k-ε model in general underestimates the stretching of the flow leading to both lower maxima of V and lower radial strain rate, although there is fair agreement in the case of $L/d_e=7.5$. In contrast, the k-ω model in general overestimates the linear slope of radial strain rate and the peak V component values.

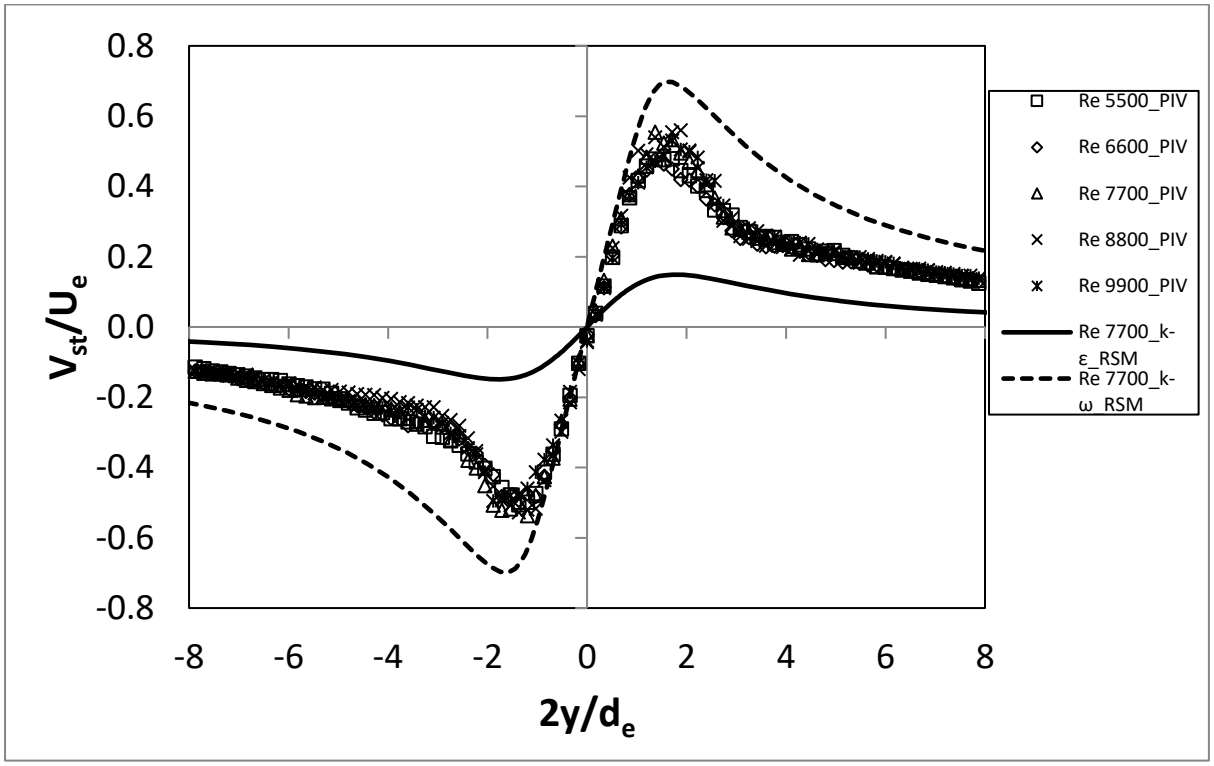

Figure 5-13: Normalized mean cross-stream (radial) V along the stagnation line, $L/d_e=5$

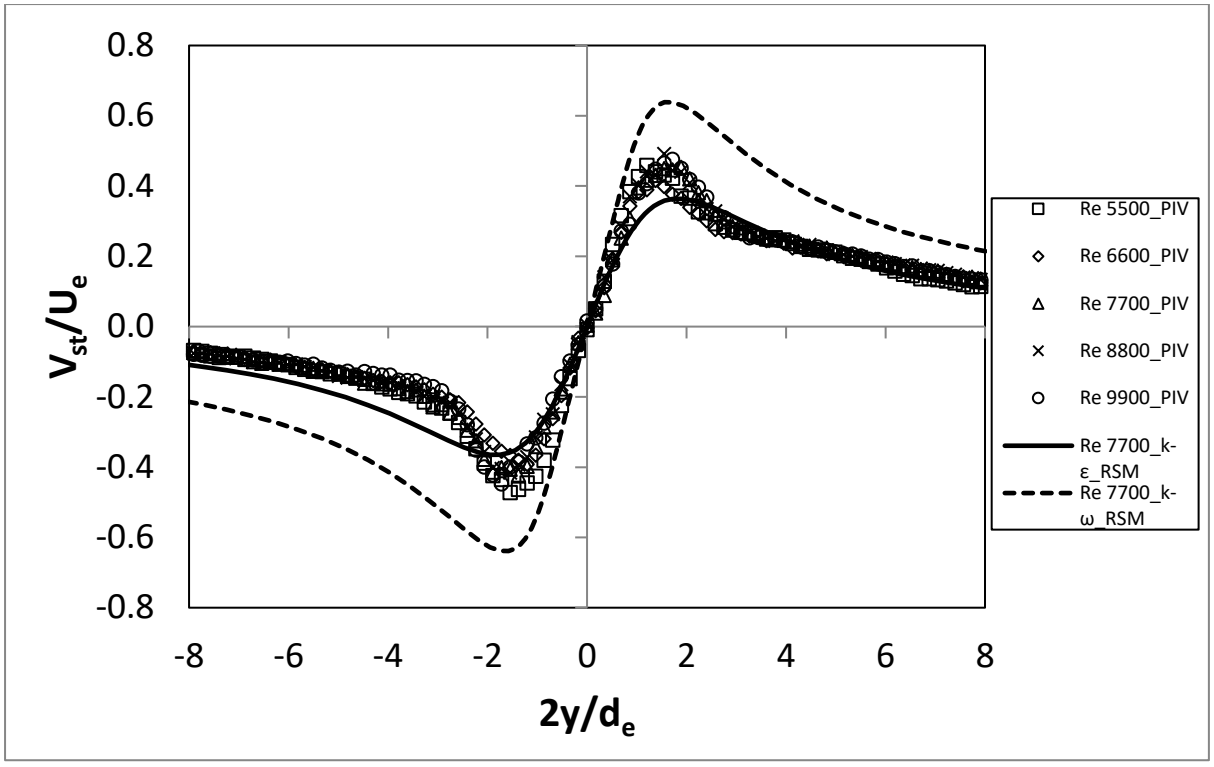

Figure 5-14: Normalized mean cross-stream (radial) V along the stagnation line, L/d_e=7.5

Table 5-2: Linear radial constants (radial strain rates) at the stagnation line

	Re	5500	6600	7700	8800	9900
	Absolute	405.5	466.0	570.6	701.3	710.6
L/d_e=5	Normalized	0.43	0.43	0.45	0.46	0.42
	Bulk	187.2	216.5	255.6	304	332.3
	Absolute	399.2	412.2	429.5	476.0	497.9
L/d_e=7.5	Normalized	0.42	0.37	0.33	0.33	0.31
	Bulk	126.4	147.8	168.5	187.2	214.2

The fluctuating velocity along the stagnation line v_{rms}, the fluctuating velocity normal to the stagnation line u_{rms}, and the tke, normalized with the velocity on the stagnation line, are presented in Figure 5-15 through Figure 5-20. The following remarks can be made regarding the turbulent quantities.

- The development of the normalized v_{rms}, u_{rms}, and tke along the stagnation line is quantitatively similar for both examined L/d_e ratios.

- For the range of Re numbers examined here, all the trends of the normalized quantities collapse to a single trend. Since the normalized plots coincide in general, it is deduced that the turbulent quantities are proportional to the Re number.
- The streamwise turbulent velocity along the stagnation line, $v_{rms,}$ is minimum on the centerline but increases until symmetrical peak values at about one diameter from the centerline. The location of the v_{rms} maxima corresponds to approximately the location where the shear layers of the opposed jets meet the stagnation line. The maximum value of v_{rms} is greater for L/d_e=5. This can be attributed to the shorter distance between the opposed jets resulting to a more energetic shear layer in this case that can perturb the stretching of the radial jets more significantly than the shear layer of the jets separated by L/d_e=7.5 where the shear layer had more distance to develop and attain lower shear rate. Beyond the maximum value, v_{rms} starts to decay exponentially as $v_{rms}=ae^{-fy}$, with a=0.3, f=0.22 for L/d_e=5 and f=0.17 for L/d_e=7.5 The development of the streamwise fluctuating velocity of radial jet is radically different from the development of the streamwise turbulent velocity observed for a single jet cylindrical discussed in section 4.3 and reported by Vouros and Panidis [83] Xu & Antonia [80]. This evolution of the v_{rms} along the stagnation line agrees with the LES data used by Wu et al. [115] for Re=4050 and L/d_e=12 exhibiting almost the same magnitude of maximum values [0.2-0.3]. The difference in the development between axial and radial jets can be attributed to the radial expansion of the jet along the stagnation plane which expands the jet rapidly in the normal direction, subsiding the fluctuations of the streamwise velocity in the latter case.
- The normal turbulent velocity along the stagnation line, u_{rms}, attains a maximum value on the centerline. The magnitude of u_{rms} quickly drops to a minimum at about one exit diameter from the centerline, which is the same location of maximum streamwise turbulent velocity along the stagnation line, v_{rms}, and coinciding approximately with the location were the shear layers of the opposed jets meet the stagnation line. The magnitude of the normal velocity fluctuations quickly recovers and further downstream starts to decrease exponentially, following the same exponential law with v_{rms}, producing isotropy for the turbulent flow. The inverse relationship between the streamwise and normal velocity fluctuations along the stagnation line within the region circumscribed by the shear layers of the opposed jets can be attributed to the change in the flow direction which enhances the velocity fluctuations in the streamwise direction where the flow is free to develop and suppresses velocity fluctuations in the normal direction where the flow is contained by the opposing jets.

- The magnitude of v_{rms} due the shape of u_{rms} prevails over its larger values. Consequently, the tke profile is similar to v_{rms} with a local minimum on the centerline and peak values at about one exit diameter from the centerline.
- In general, the smaller L/d_e distance results to elevated u_{rms}, since the opposed jets have less distance to develop radially causing the jet momentum to be contained within a narrower radius. Consequently, when the opposed jets meet on the stagnation plane the greater momentum flux in the case of L/d_e=5 results in greater fluctuating velocities.
- While there is agreement in the order of magnitude of the fluctuating velocities and the tke between the experimental measurements and the CFD simulations, the profiles of these quantities along the stagnation line are poorly matched. There is also poor agreement between the CFD simulations. The k-ε model fails to detect the maxima of v_{rms} and tke and the minima of u_{rms} while the overall magnitudes are generally lower, especially for the case of L/d_e=5. The k-ω model succeeds in predicting the maxima of v_{rms} and tke but not the minima of u_{rms} along the stagnation line. However, it cannot predict accurately their quantities and also does not predict accurately their locations along the stagnation line. Finally, both models estimate that the u_{rms} is larger than v_{rms}, within the region circumscribed by the shear layers of the opposed jets which contradicts the PIV results.

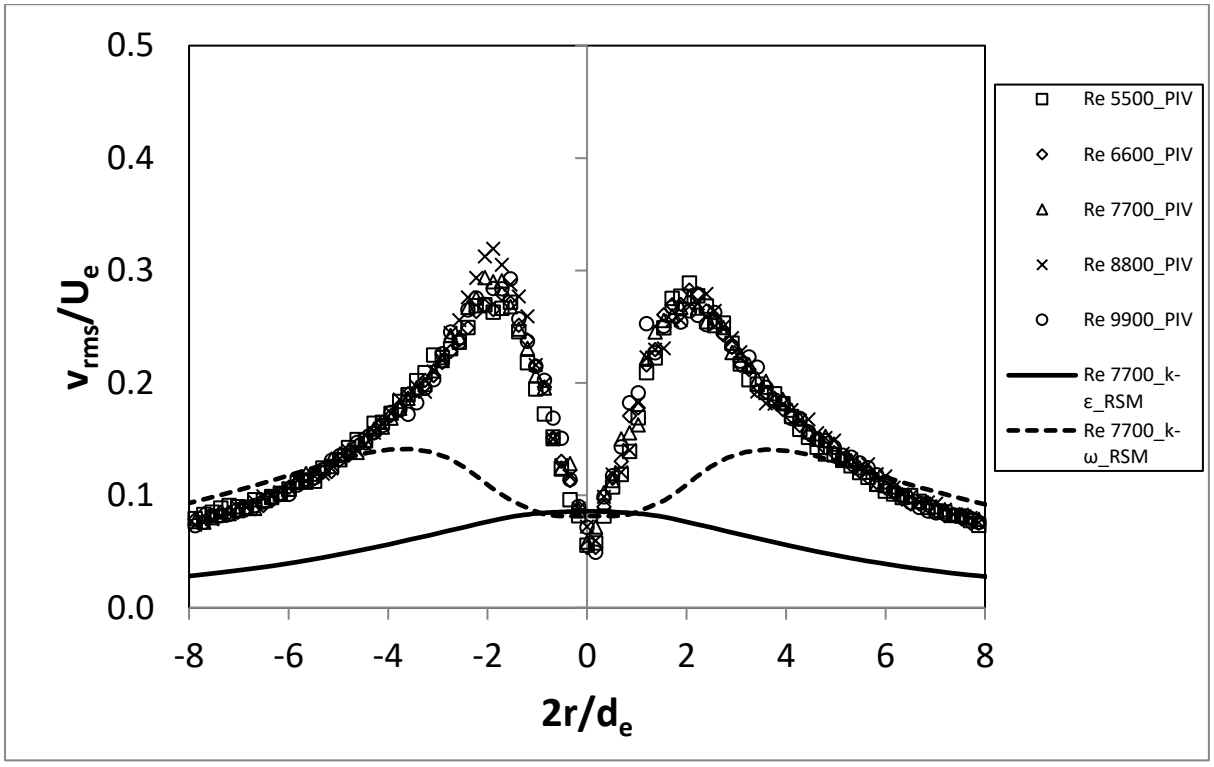

Figure 5-15: Normalized v_{rms} along the stagnation line, L/d_e=5

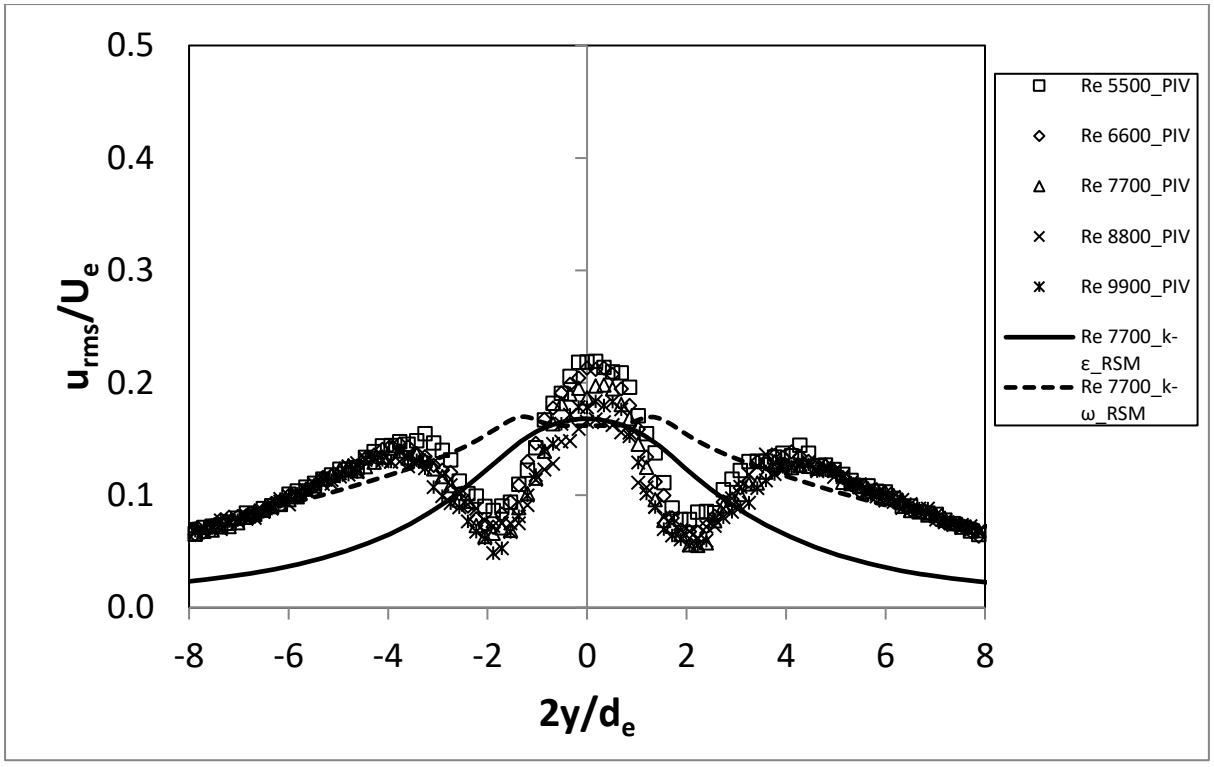

Figure 5-16: Normalized u_{rms} along the centerline $L/d_e=5$

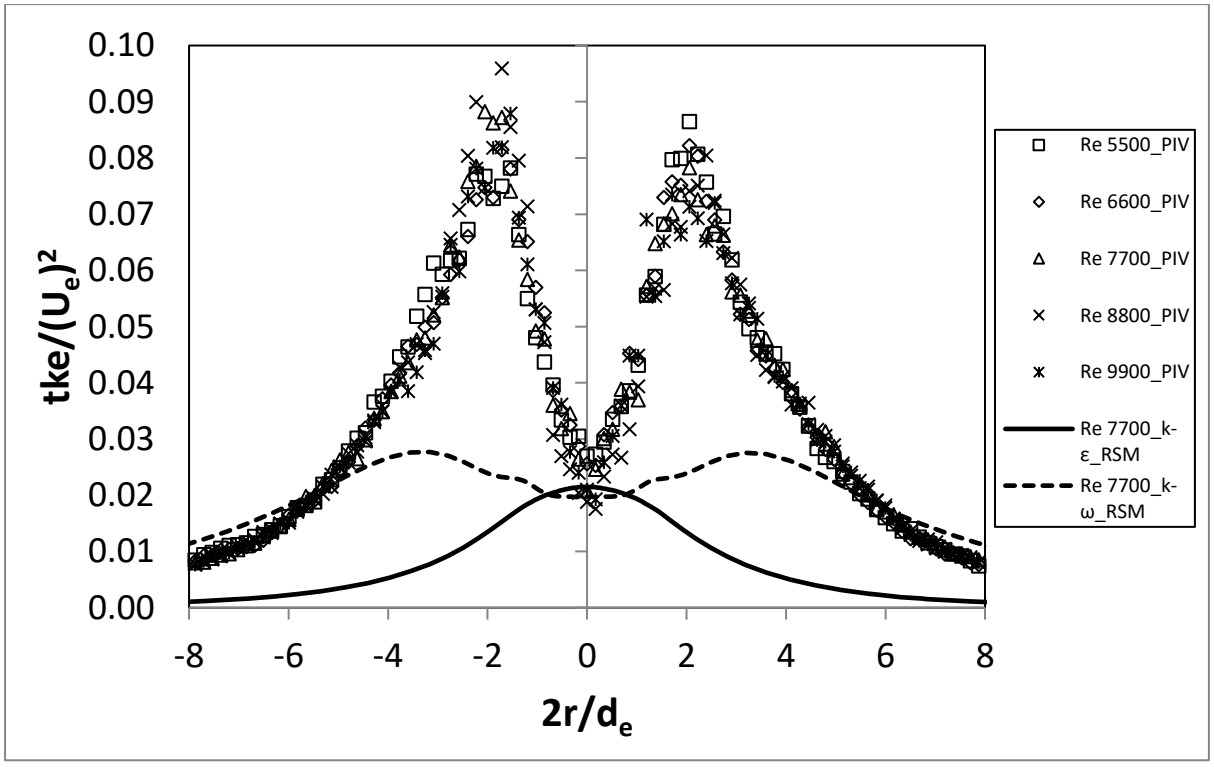

Figure 5-17: Normalized tke along the stagnation line, $L/d_e=5$

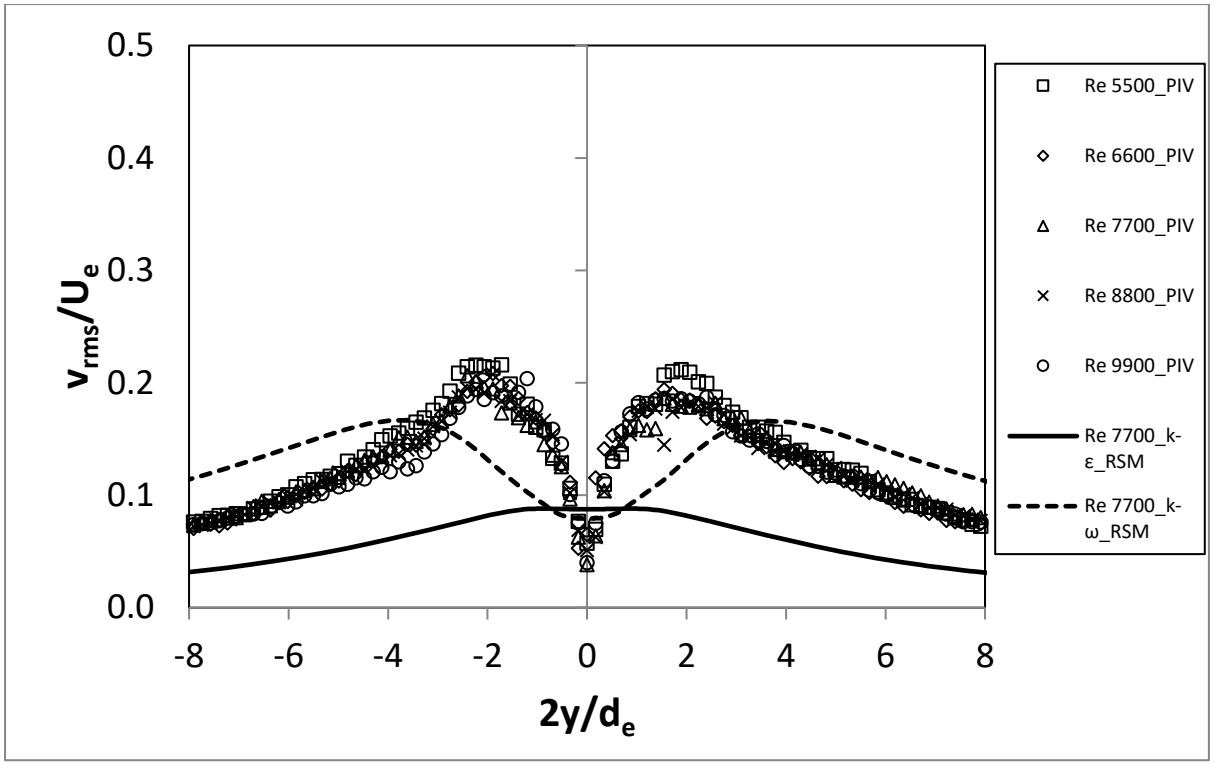

Figure 5-18: Normalized v_{rms} along the stagnation line, L/d_e=7.5

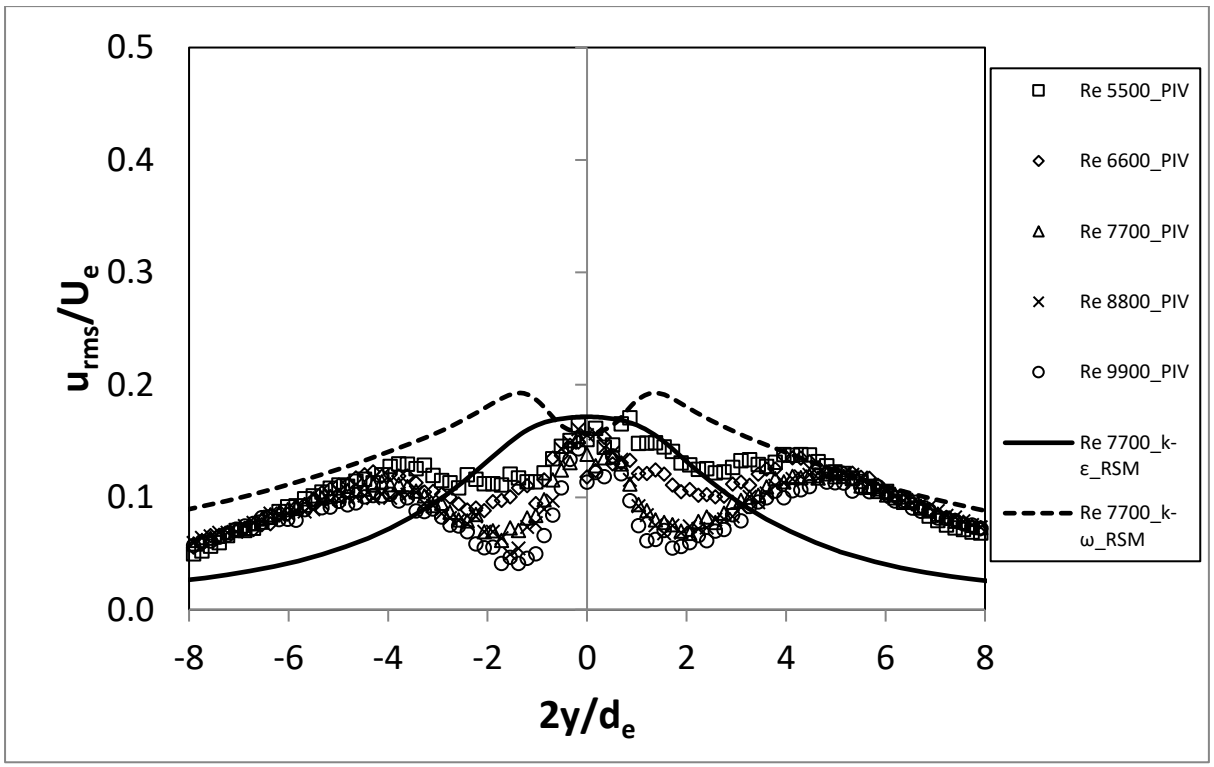

Figure 5-19: Normalized u_{rms} along the stagnation line, L/d_e=7.5

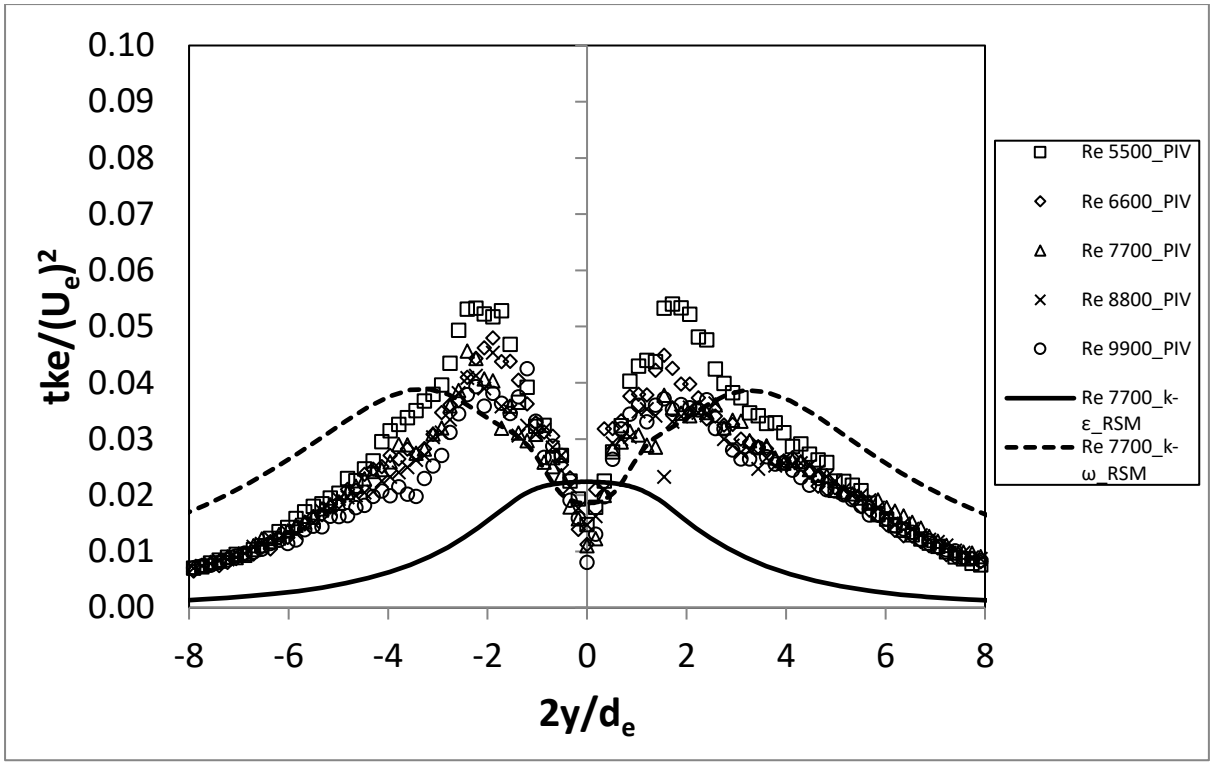

Figure 5-20: Normalized tke along the stagnation line, L/d_e=7.5

5.3 Free radial jet development without HIT

In this section, the concept of free radial jet as described in par 2.4 is examined. The main purpose of this analysis is to verify or not if two axisymmetric jets are developed around the stagnation line as shown in Figure 5-21 and if they attain self-similar properties in their developed region. The linear evolution of normalized velocity V/U_e as presented in Figure 5-13 and Figure 5-14 is an indication of a possible self-similar state. However, experimental data need to be plotted in the form of section 4.4 that will permit more insight in the nature of the radial flow produced in the stagnation region. The velocity data are normalized by the mean radial velocity along the stagnation line V_{st} which is a function of the distance y from the opposed jet centerline. The normalized velocity is plotted against the distance normal to the stagnation line $z-z_{st}$, normalized by y coordinate which is the direction of the radial jet spreading. It should be noted that the V velocity is the radial jet streamwise velocity of the radial jet and the U velocity is the cross-stream velocity of the radial jet.

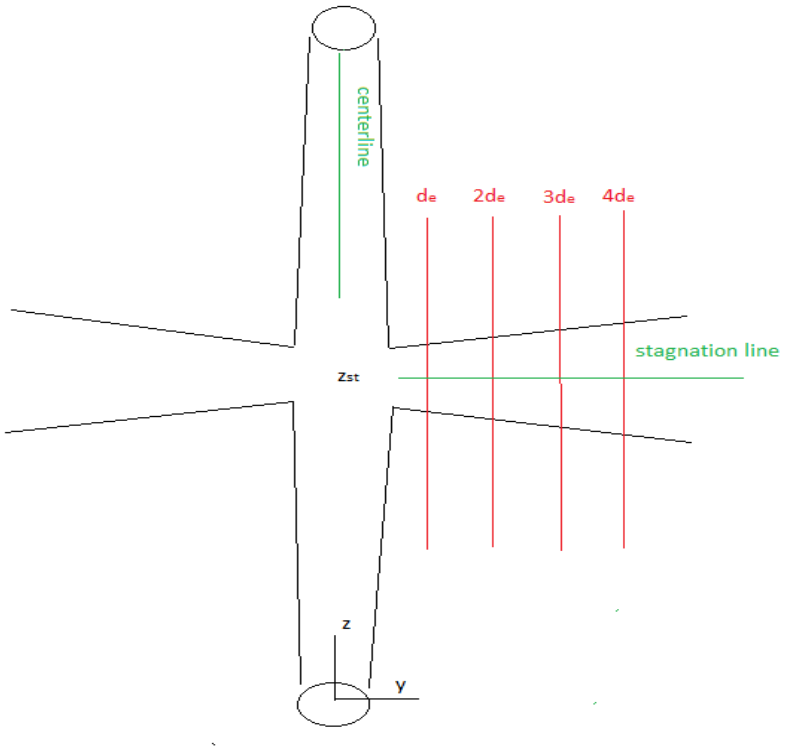

Figure 5-21: Schematic representation of the flow evolution and measurement locations

The development of the mean radial velocity V across the width of the radial jet is presented in Figure 5-22 through Figure 5-25 for distances of 1, 2, 3 and 4 d_e from the jet centerline. The development of the streamwise velocity for each Re is similar for L/d_e=5 and L/d_e=7.5. The gaussian profile indicates the presence of an axisymmetric jet. The gaussian profile is verified by the estimated skewness and kurtosis values summarized in Table 5-3, that rest very close to the ideal values of 0 for skewness and 3 for kurtosis. Moreover, after about a streamwise development of the radial jet for about $2d_e$, the streamwise velocity profiles collapse to a single trend demonstrating that the flow has become self-similar in respect to the streamwise velocity.

The CFD simulations also predict an axisymmetric radial jet that becomes self-similar after the jet has had sufficient distance to develop, as the experimental measurements do. For the k-ε model self-similarity of the radial jet is obtained after $3d_e$ while the k-ω model reveal that self-similarity of the radial jet occurs after $2d_e$ in agreement with the experimental measurements. Additionally, while the k-ε model predicts a radial jet width that is substantially greater than that measured experimentally while the k-ω model prediction is much closer to the experimental data.

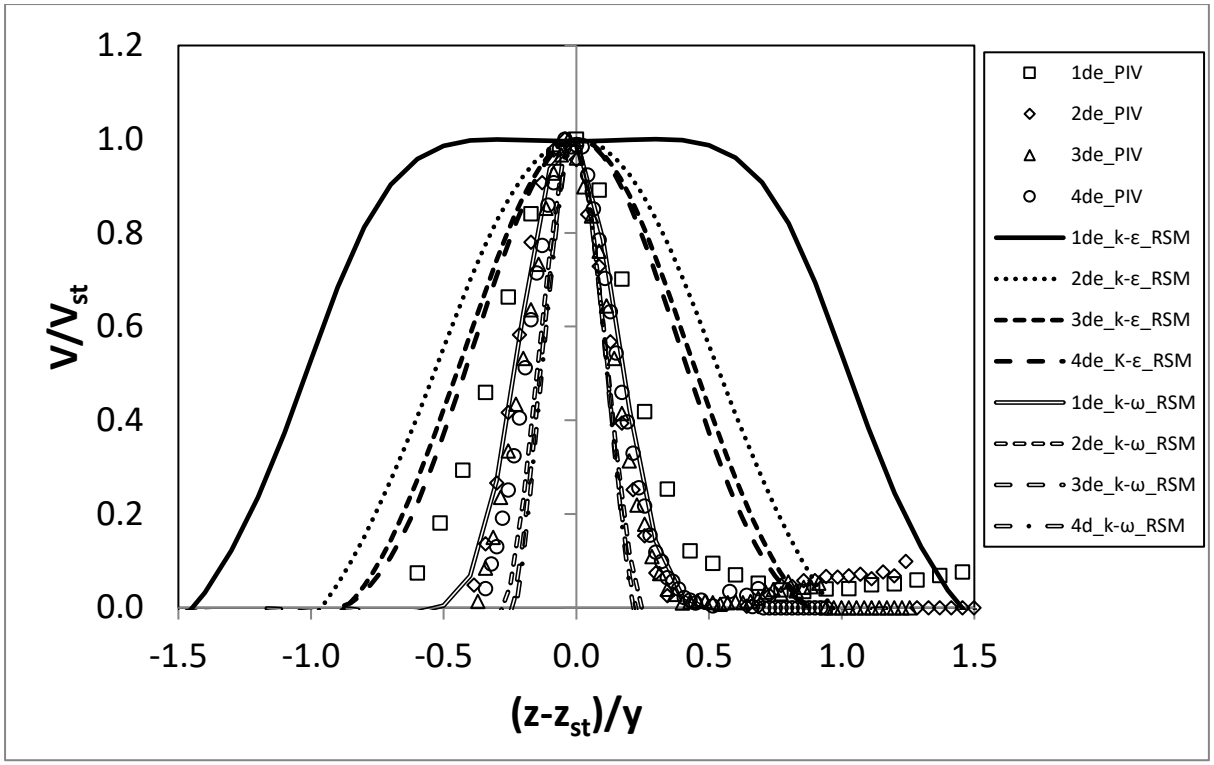

Figure 5-22: Normalized mean radial velocity V, Re=5500, L/d_e=5

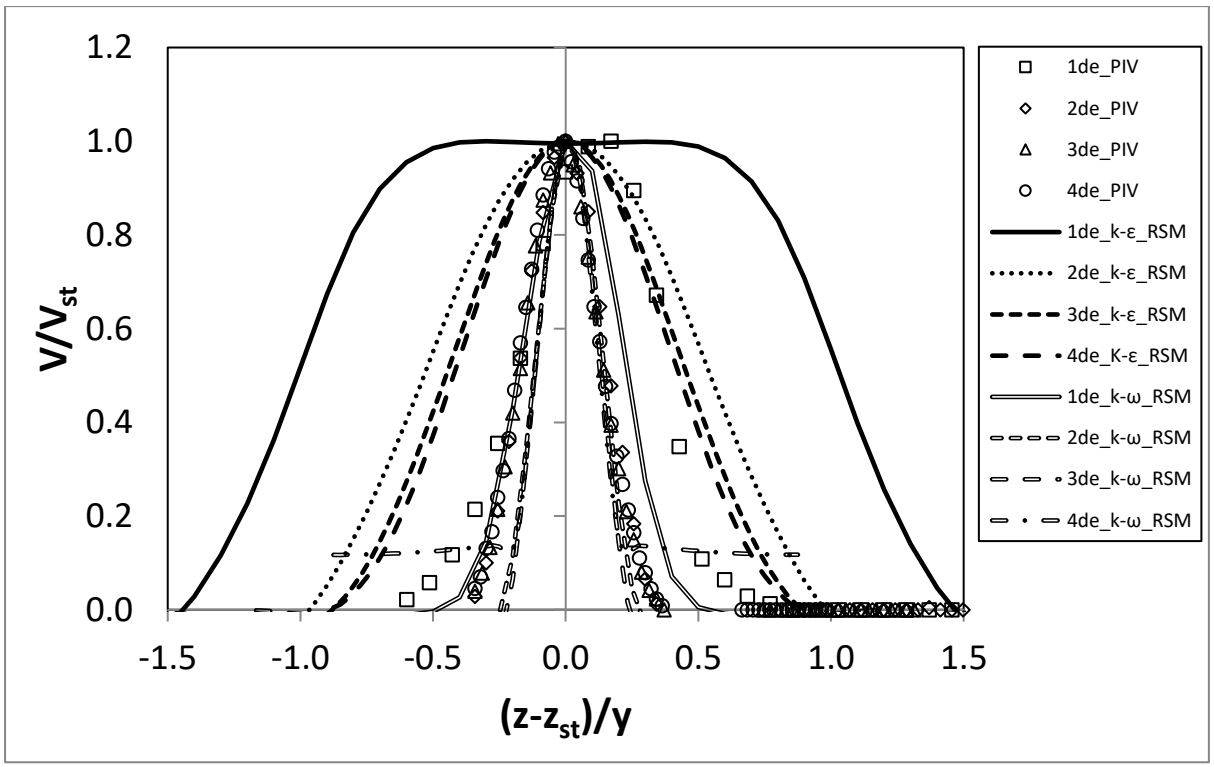

Figure 5-23: Normalized mean radial velocity V, Re=7700, L/d_e=5

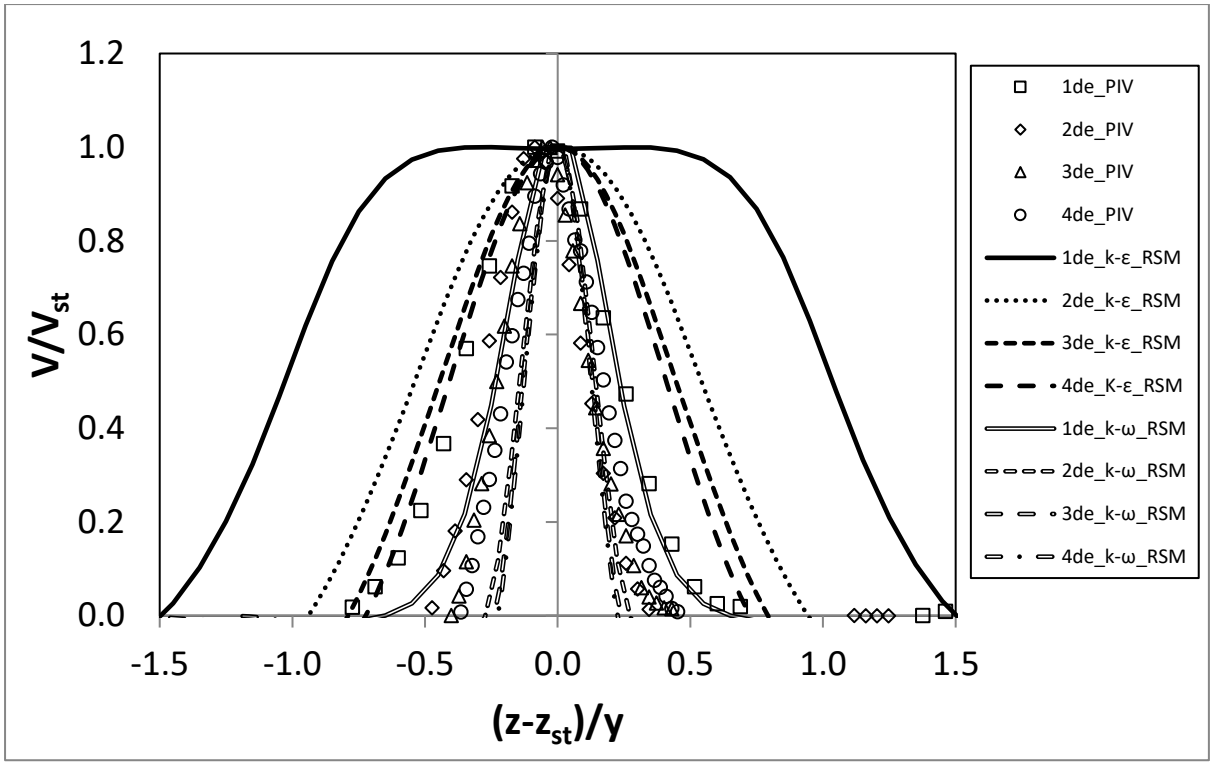

Figure 5-24: Normalized mean radial velocity V, Re=5500, L/d_e=7.5

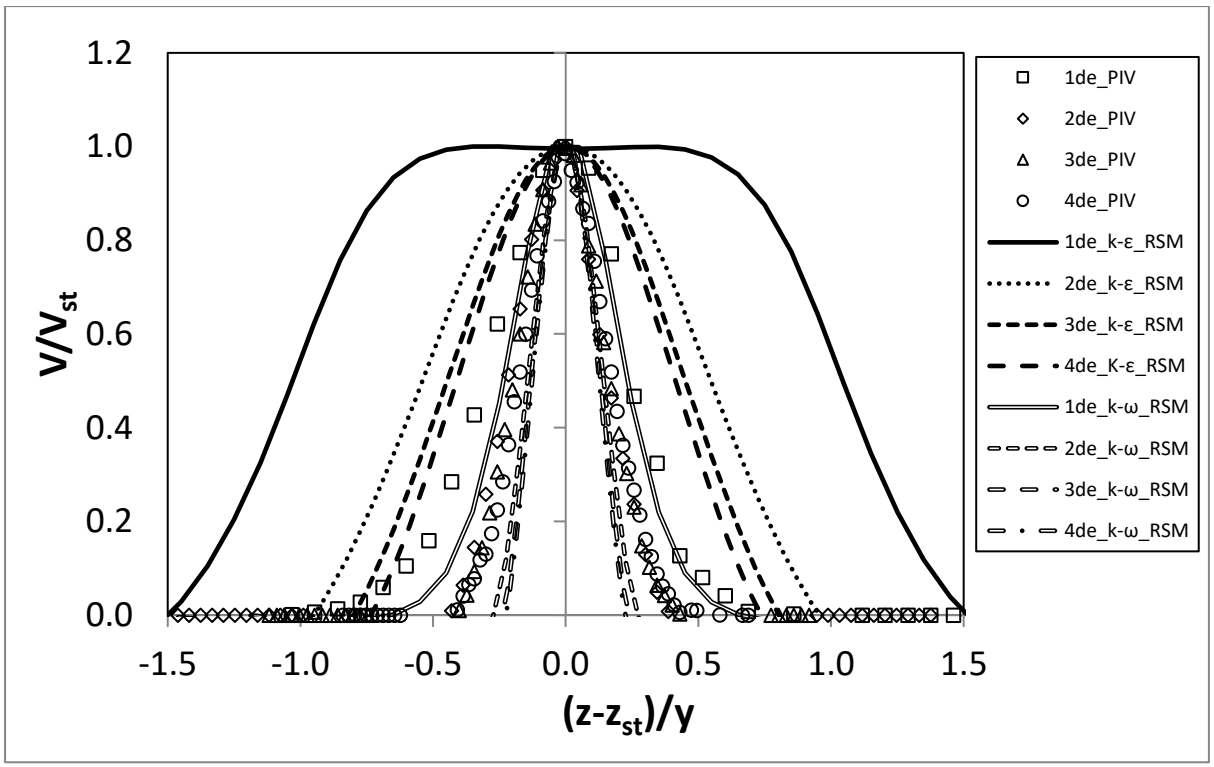

Figure 5-25: Normalized mean radial velocity V, Re=7700, L/d_e=7.5

Table 5-3: Skewness and kurtosis of normalized mean radial velocity V

	Skewness				Kurtosis			
	Re 5500 L/d_e=5	Re 7700 L/d_e=5	Re 5500 L/d_e=7.5	Re 7700 L/d_e=7.5	Re 5500 L/d_e=5	Re 7700 L/d_e=5	Re 5500 L/d_e=7.5	Re 7700 L/d_e=7.5
$1d_e$	0.001	-0.002	0.000	0.000	2.827	2.890	2.827	2.956
$2d_e$	0.001	0.000	0.001	0.001	2.951	2.814	3.080	2.893
$3d_e$	0.001	0.001	0.001	0.001	2.979	3.060	3.010	3.030
$4d_e$	0.001	0.001	0.001	0.001	3.035	2.984	2.858	2.957

The normalized streamwise fluctuating velocity v_{rms}/V_{st} is presented in Figure 5-26 through Figure 5-29. Nearly self-similarity is attained after the radial jet has developed for $2d_e$. The maximum streamwise velocity fluctuation is on the jet axis much like the case of a single jet, however for the radial jet its magnitude is much higher reaching about $0.6V_{st}$. Stan & Johnson [102] also reported values of $v_{rms}/V_{st} \geq 0.5$ for an opposed jets configuration of $L/d_e=0.5$ and radial distances up to $3d_e$. The corresponding streamwise fluctuating velocity on the central axis of a single jet in the self-similar region in section 4.4 is between $0.2U_{cl}$ to $0.3\ U_{cl}$ (similar values are obtained for a round jet by Vouros & Panidis [83]).

The normalized cross-stream fluctuating velocity u_{rms}/V_{st} is presented in Figure 5-30 through Figure 5-33. It is observed that the same level of intensity 0.6 is reached also in the self-similar region of the u_{rms}, verifying the observation of isotropic turbulence beyond $2d_e$ off-z-axis where the exponential decrease of both u_{rms} and v_{rms} occurs.

The profiles of both v_{rms}/V_{st} and u_{rms}/V_{st} obtained from the CFD models attain self-similarity after $3d_e$ for the k-ε model and $2d_e$ for the k-ω model, similarly to the mean velocity V profile. In the self-similar region, the k-ε model is able to offer a quantitatively reasonable match with the experimental measurements, while the k-ω model predicts lower values. However, neither model is able to match the experimental measurements in the region of flow establishment.

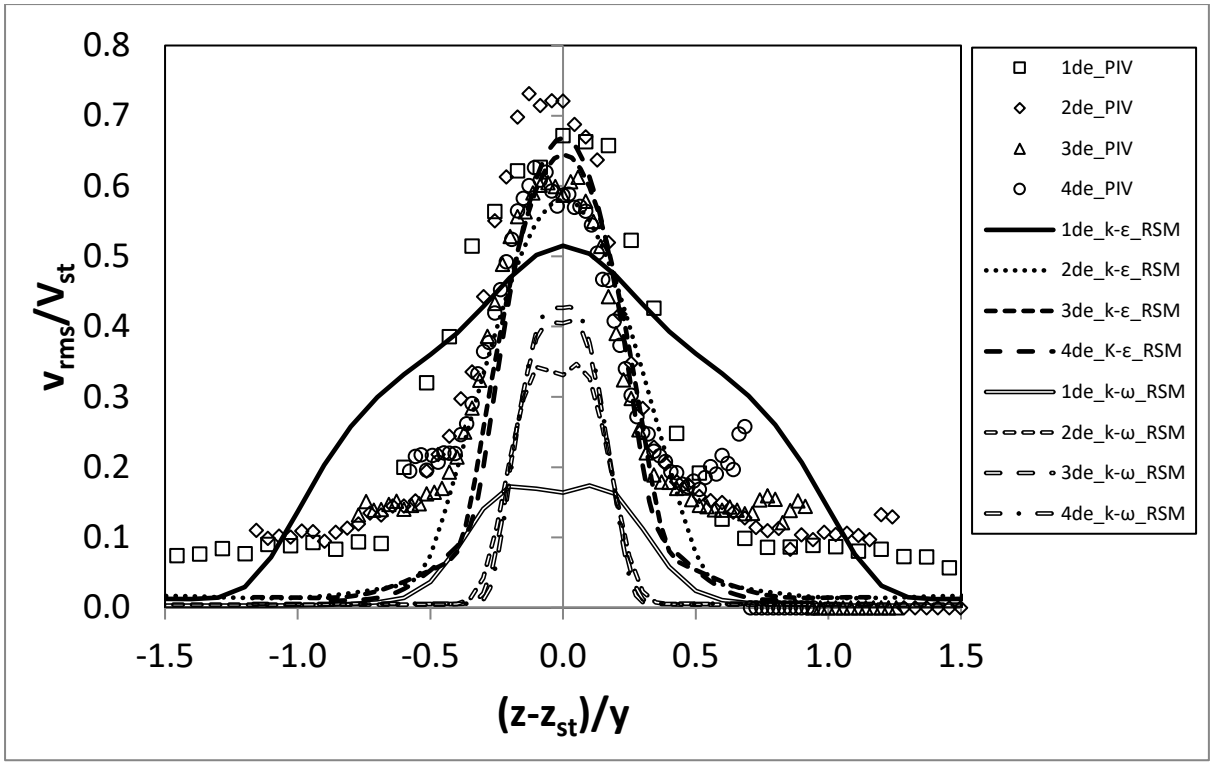

Figure 5-26: Normalized v_{rms}, Re=5500, L/d_e=5

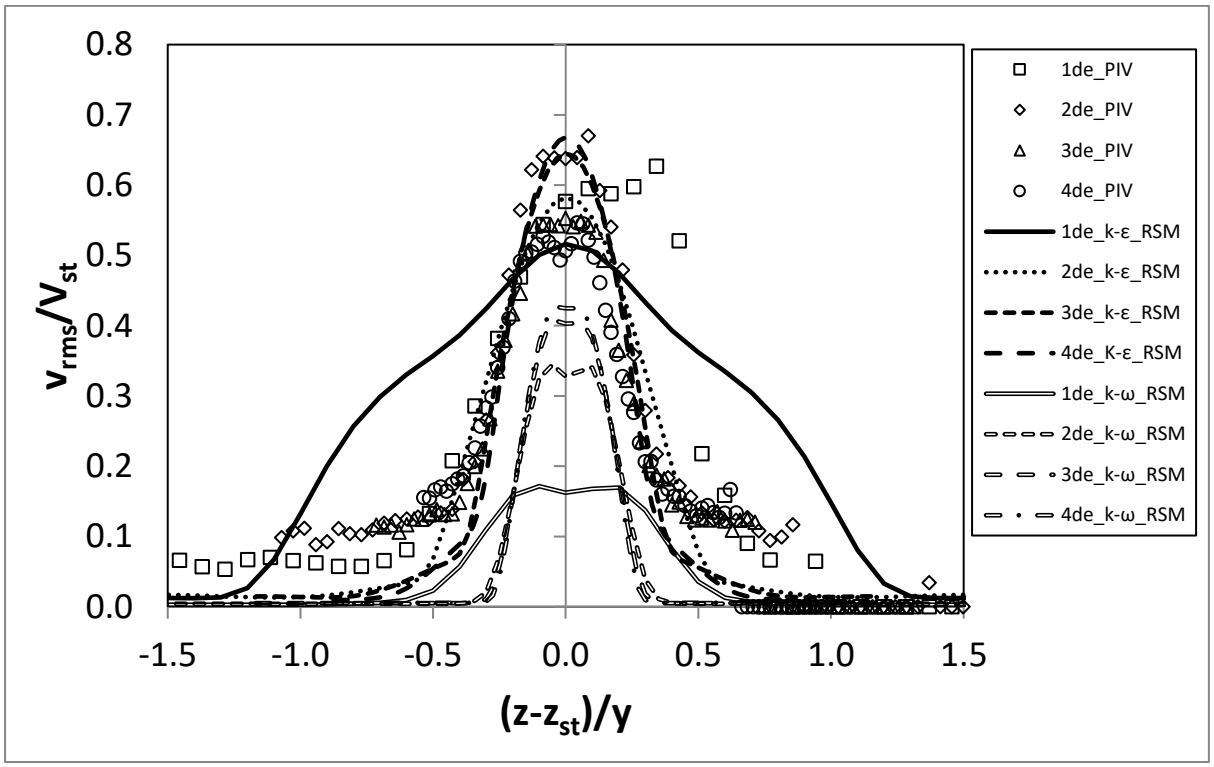

Figure 5-27: Normalized v_{rms}, Re=7700, L/d_e=5

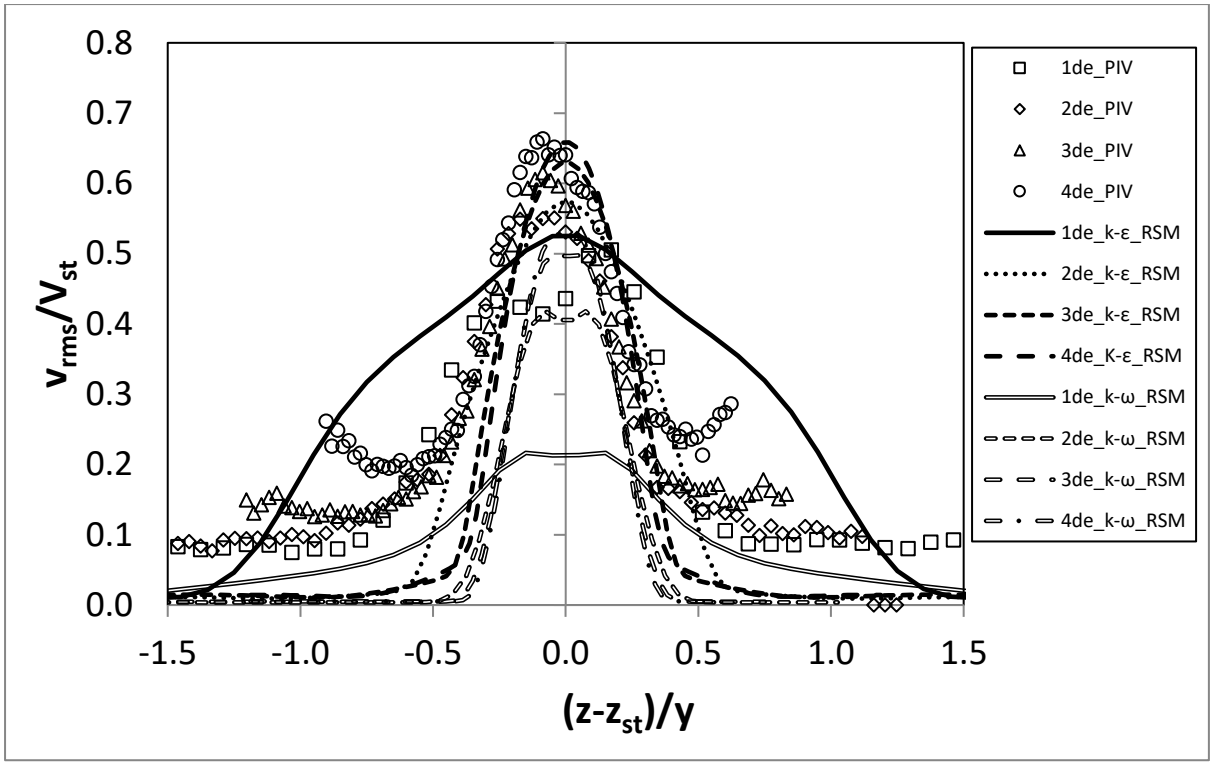

Figure 5-28: Normalized v_{rms}, Re=5500, L/d_e=7.5

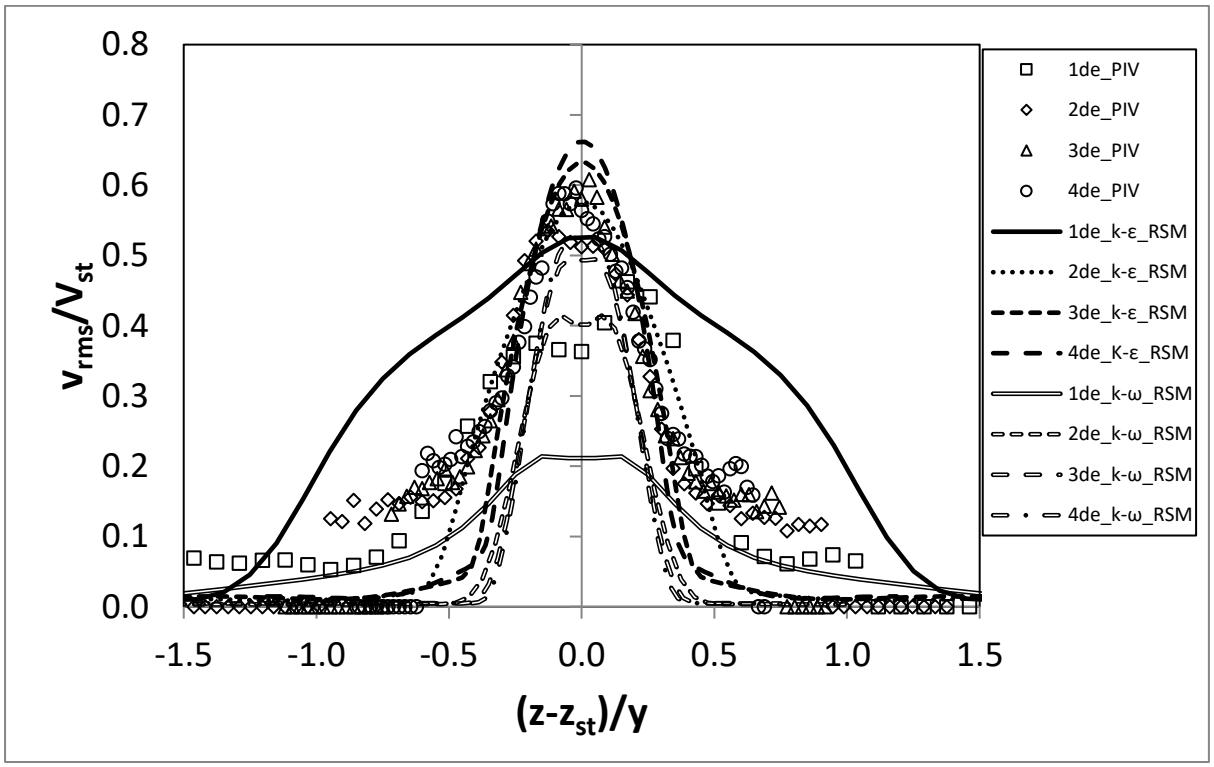

Figure 5-29: Normalized v_{rms}, Re=7700, L/d_e=7.5

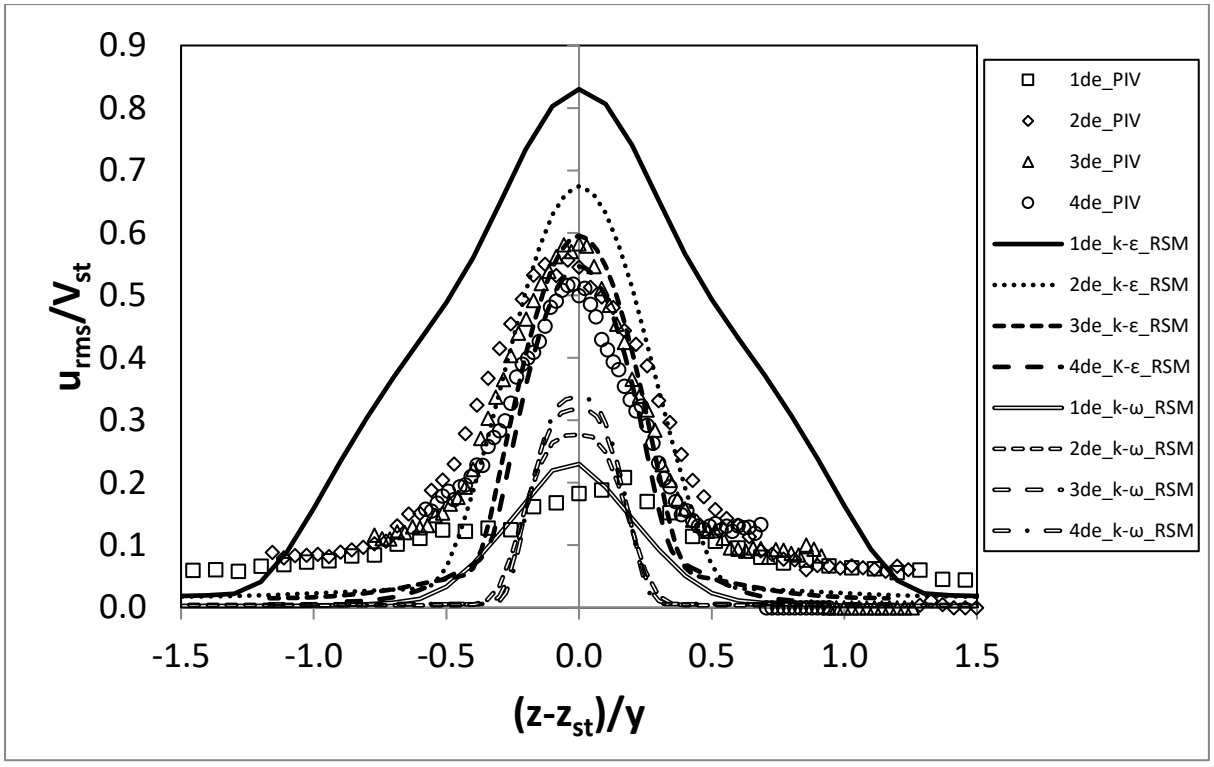

Figure 5-30: Normalized u_{rms}, Re=5500, L/d_e=5

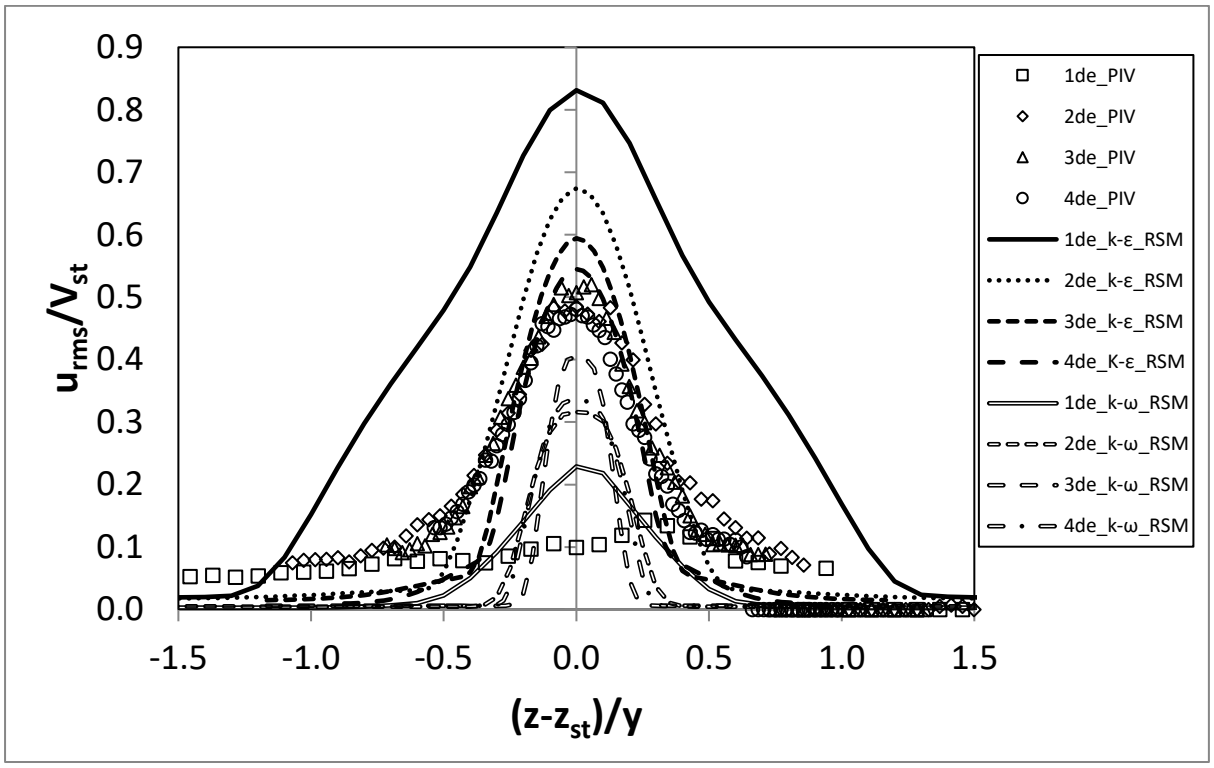

Figure 5-31: Normalized u_{rms}, Re=7700, L/d_e=5

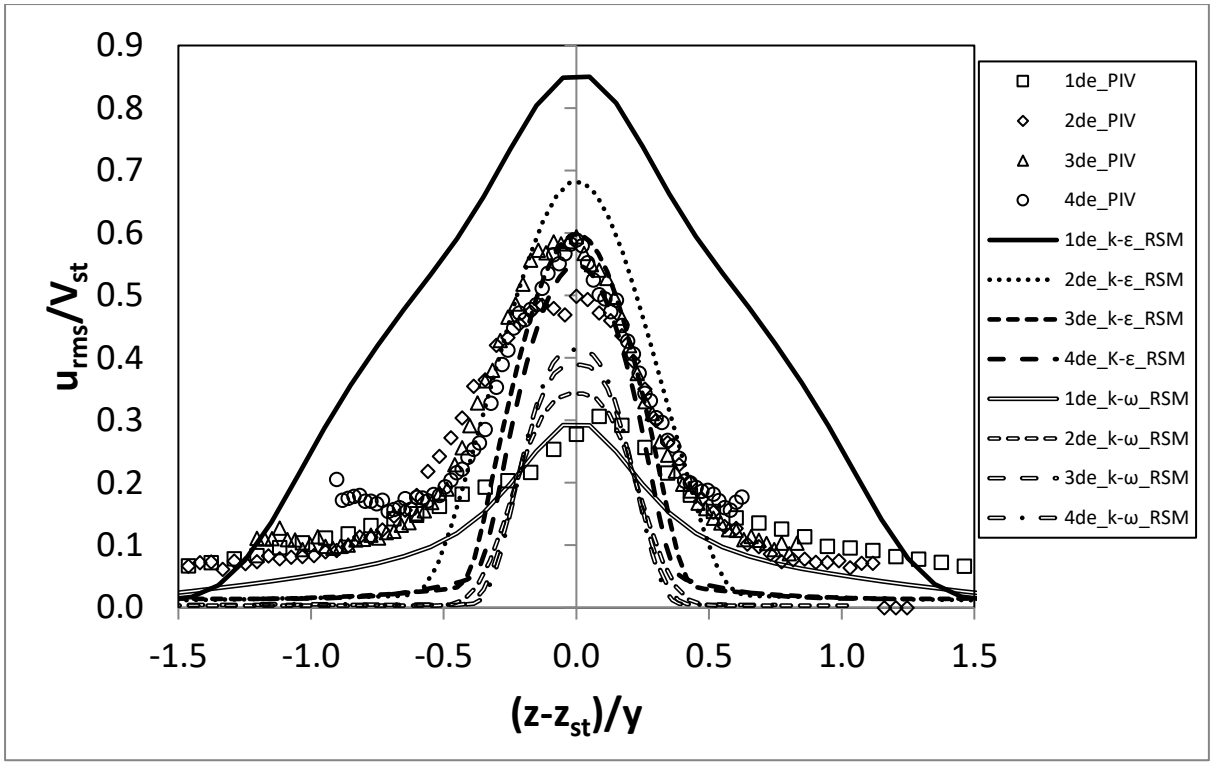

Figure 5-32: Normalized u_{rms}, Re=5500, L/d_e=7.5

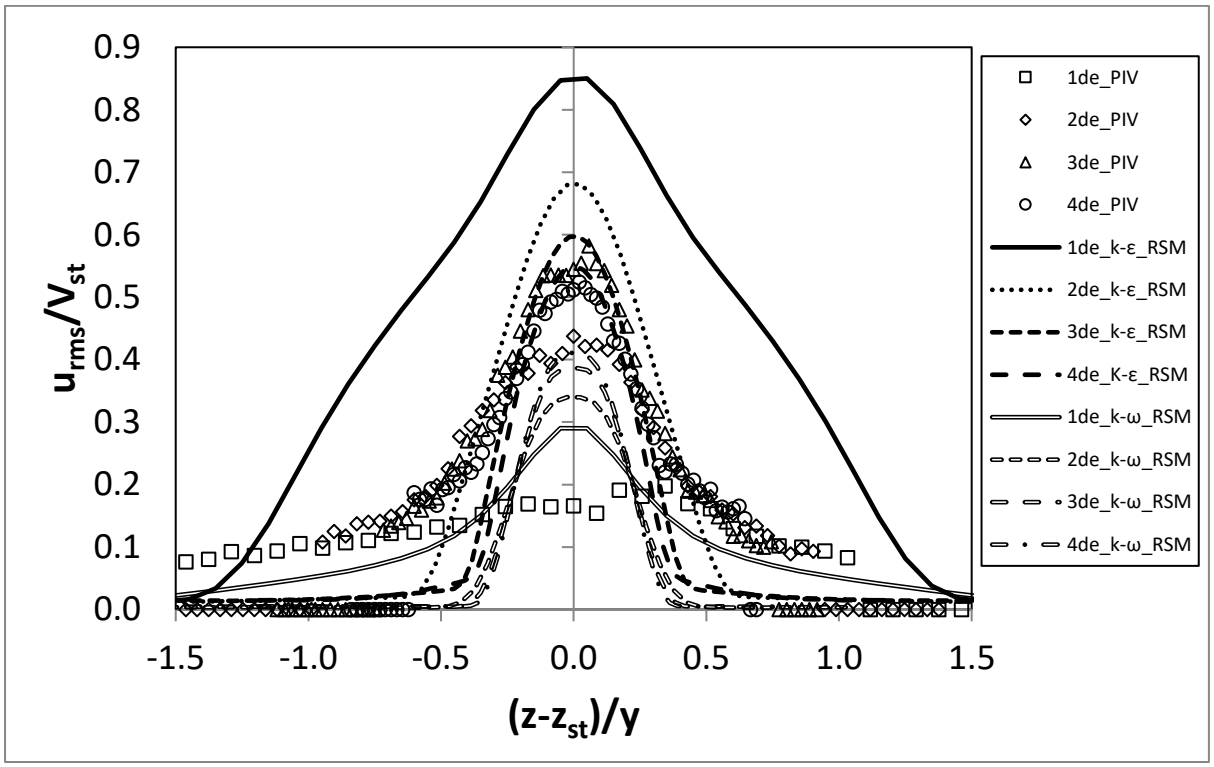

Figure 5-33: Normalized u_{rms}, Re=7700, L/d_e=7.5

The evolution of the jet half width normalized with the nozzle diameter is presented in Figure 5-34 and Figure 5-35 along the streamwise direction. The linear increase of jet half width validates the assumption for the existence of a symmetric free radial jet. In comparison with an axisymmetric single jet, the free radial jets present larger spreading rates according to Table 5-4 and recalling Table 4-2. It should be noted that L/d_e=7.5 presented larger spreading rates than L/d_e=5. As mentioned in section 5.2, in the case of the higher L/d_e ratio, the radial momentum is lower and consequently the flow velocity decays more easily resulting in larger spreading rates.

For both opposed jet separations, the k-ω model simulation predicts better the spreading rate in the radial direction in comparison with the k-ε model that significantly overestimates the spreading rate. The spreading rate predicted by the k-ω model is around 0.095, a value which matches the theory of turbulent jets (Table 2-2).

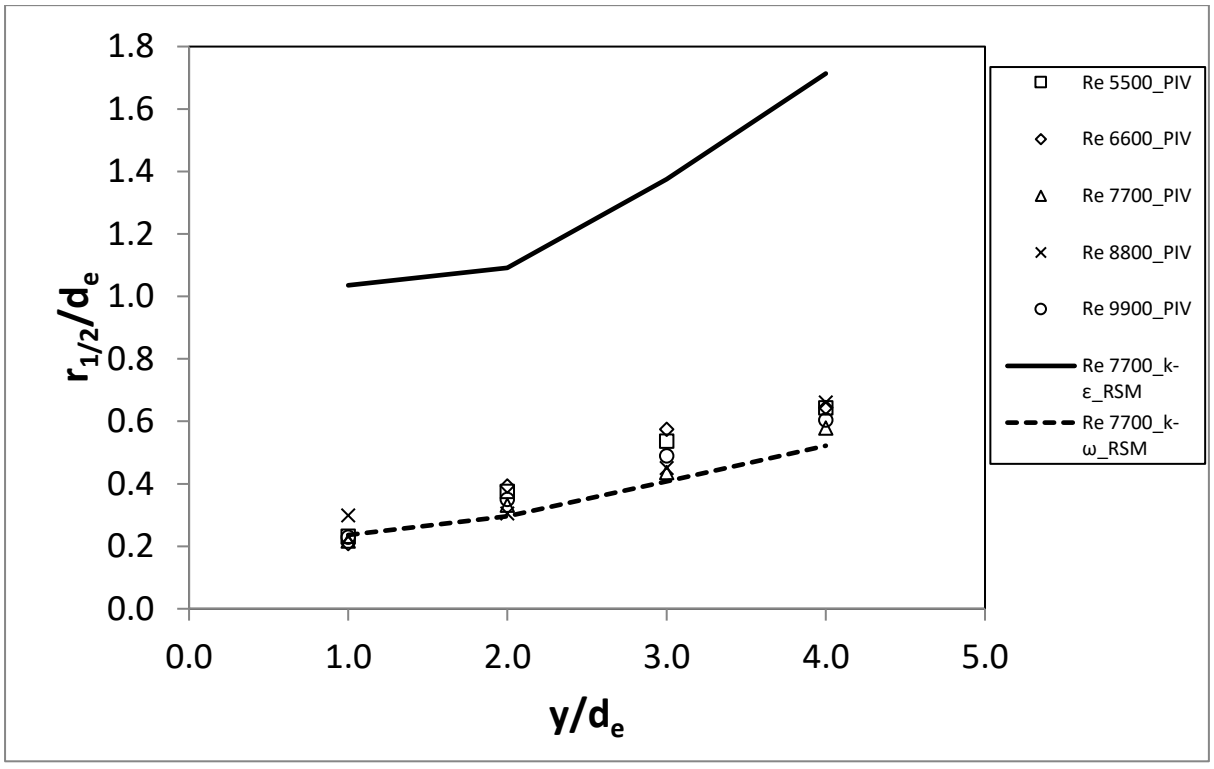

Figure 5-34: Jet half width $r_{1/2}$ of free radial jet, L/d_e=5

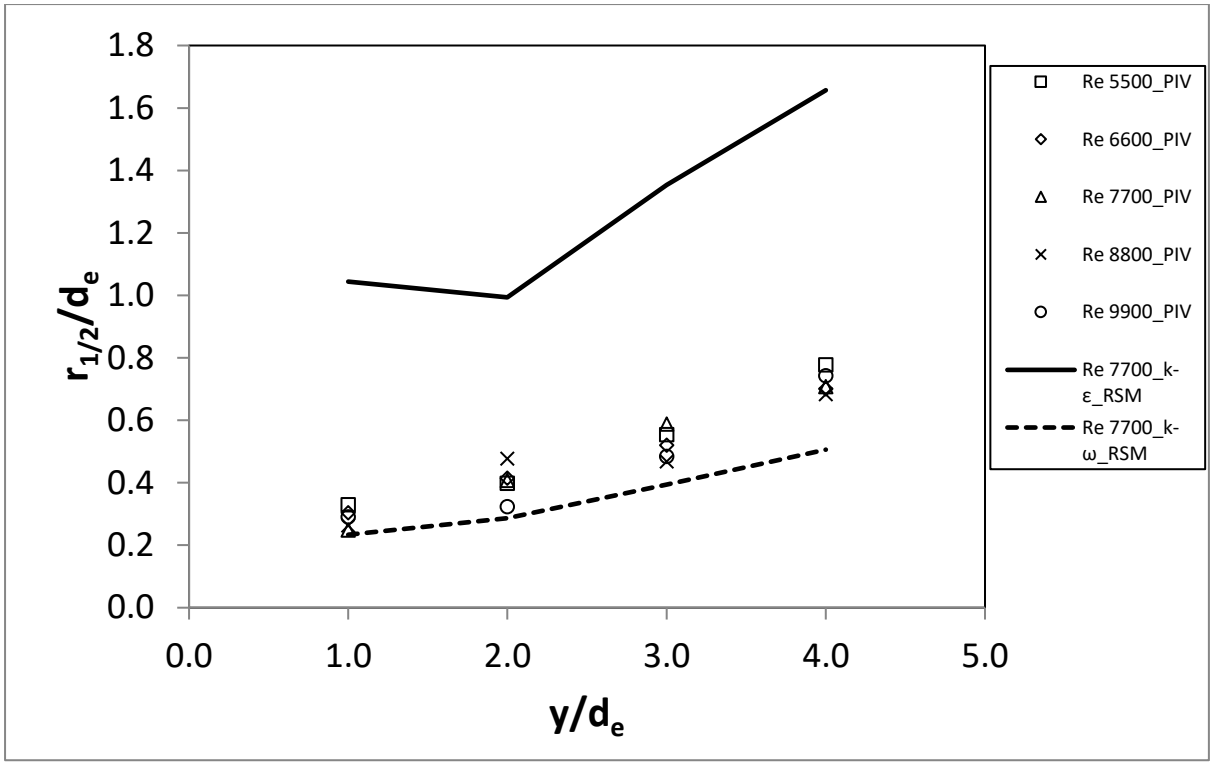

Figure 5-35: Jet half width $r_{1/2}$ of free radial jet, L/d_e=7.5

Table 5-4: Spreading rate of free radial jet (PIV results)

	Re	5500	6600	7700	8800	9900
Single jet	Spreading rate	0.084	0.076	0.074	0.065	0.063
L/d_e=5		0.139	0.148	0.119	0.123	0.126
L/d_e=7.5		0.150	0.129	0.155	0.125	0.151

5.4 Opposed jets flow along their centerline, under HIT

The PIV mean velocity maps of the opposed jets under the HIT presence, for L/d_e=5 is presented in Figure 5-36. A brief look at the figures shows us that there is a profound effect on the flow for Re≤4400, which deteriorates the opposed jets flow. The rest of the cases Re ≥5500 any deviations for the cases without HIT, shall be examined in the following paragraphs.

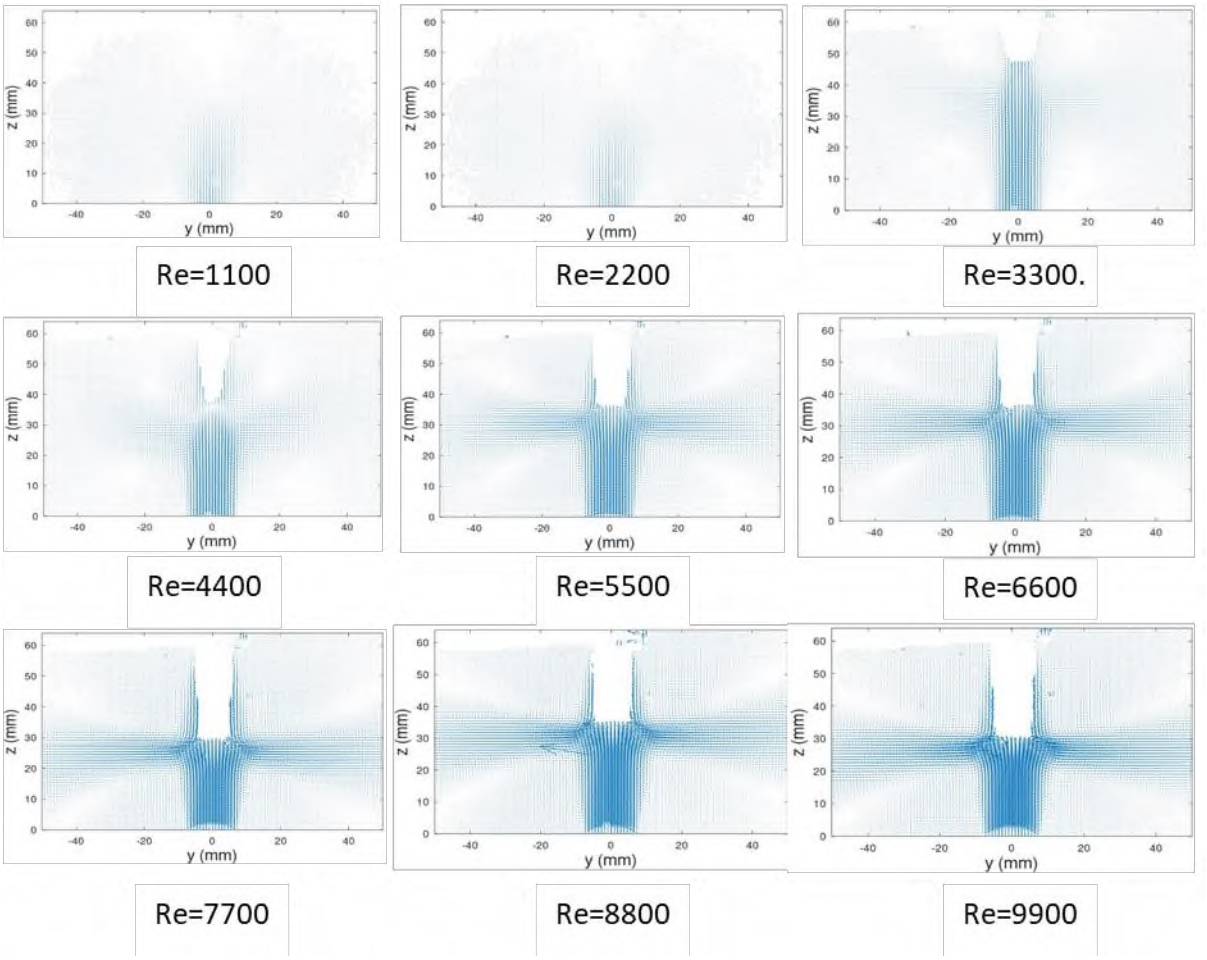

Figure 5-36: Mean velocity vector maps of opposed jets with HIT for each Re number, L/d_e=5

Following the same approach as in section 5.1, the evolution of the normalized streamwise component of the velocity along the centerline axis from the jets exit up to the stagnation plane is presented, for an initial assessment of the influence of HIT. The velocity fields for all Re ≥5500 and each combination of L/d_e ratio and turbulence conditions are presented in Figure 5-37 and Figure 5-38. Additionally, the axial strain rates are summarized in Table 5-5.

- The overall velocity profile is similar to the flow without HIT, namely the velocity is almost constant, near the value of U_e and there is a sharp decrease to zero in the stagnation plane. The potential core is unaffected by the HIT in this case.

- The fact that the flow is more strained around the stagnation plane for L/d_e=7.5, as noted in par. 5.1, reoccurs under the presence of HIT as well. The HIT domain is characterized by zero mean velocity and the absence of velocity gradients since the flow is homogeneous. On the other hand, the opposed jets have significant velocity magnitude that produce strong gradient in the stagnation region along the stagnation line. As a result, the qualitative characteristics of the opposed flow as described in the case of quiescent environment prevail over the HIT mean flow. However, the presence of HIT leads to smaller strain rates, as reported in Table 5-5. Examining the cases for Re≥5500, the average normalized value is L/d_e=5:1.89, and L/d_e=7.5: 3.57. The respective values in the absence of HIT are L/d_e=5: 2.45 and L/d_e=7.5: 4.43. This leads on average to approximately 20% reduction of the axial strain rate. The HIT environment being a stagnating flow itself enhances the velocity decay of the opposed jets in the early stages of the stagnation. Consequently, the final linear stagnation part, where the strain rated is estimated presents a more gradual drop until the zero magnitude at the stagnation point.

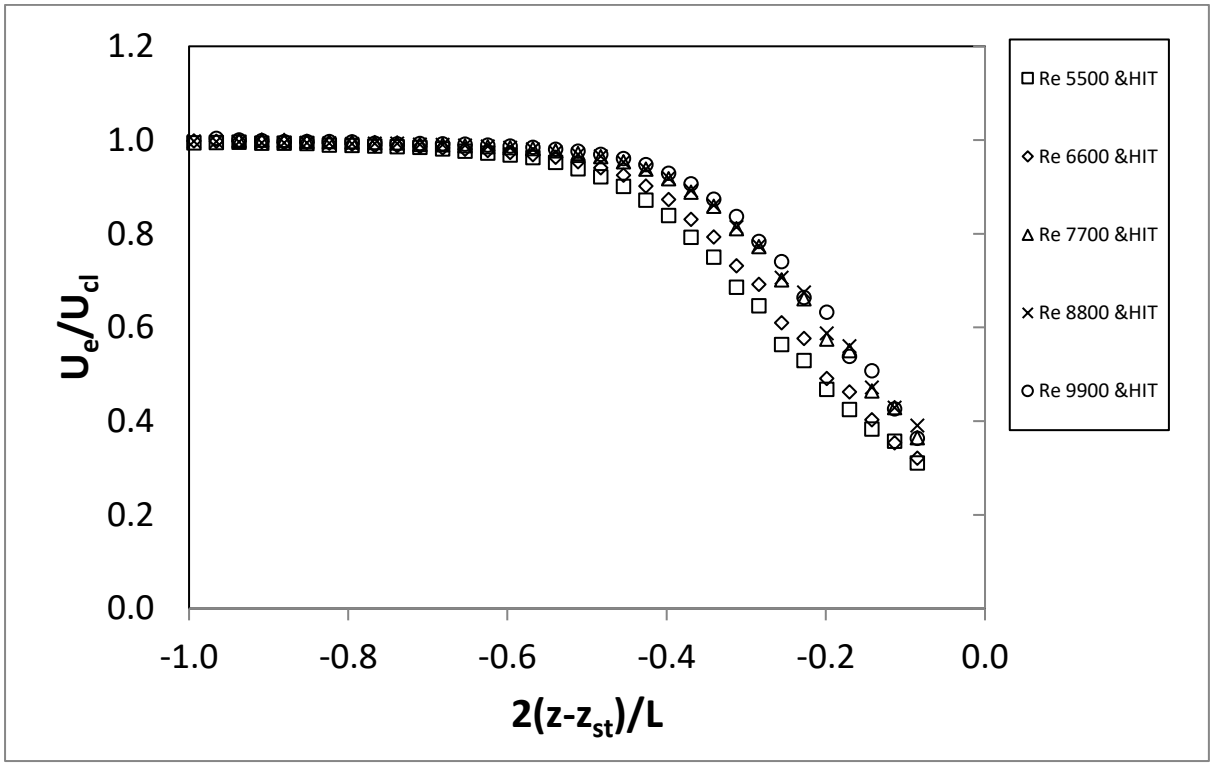

Figure 5-37: Mean streamwise (axial) velocity U along the opposed jets axis (centerline) under HIT, L/d_e=5

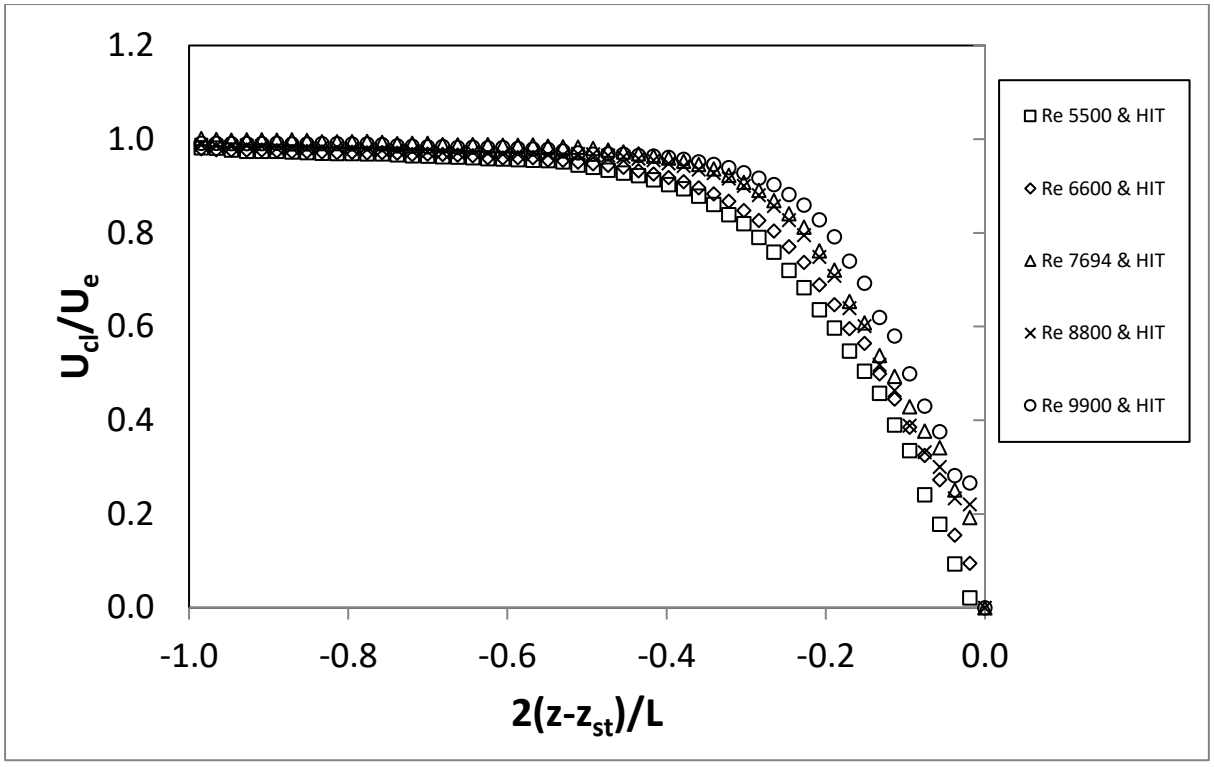

Figure 5-38: Mean streamwise (axial) velocity U along the opposed jets axis (centerline) under HIT, L/d_e=7.5

Table 5-5: Linear axial decay constants (axial strain rates) at the stagnation region, under HIT

	Re	5500	6600	7700	8800	9900
	Absolute	333.0	429.8	512.8	578.2	687.7
L/d_e=5 & HIT	Normalized	1.74	1.88	1.90	1.91	2.02
	Bulk	191.6	228.8	269.2	302.2	339.7
L/d_e=5	Normalized	2.47	2.43	2.43	2.46	2.49
	Absolute	528.4	667.8	579.9	624.3	780.6
L/d_e=7.5 & HIT	Normalized	4.14	4.23	3.16	3.02	3.32
	Bulk	127.6	157.5	183.4	206.2	234.8
L/d_e=7.5	Normalized	4.24	4.45	4.31	4.45	4.68

Examination of the development of the normalized turbulence quantities u_{rms}, v_{rms}, tke along the centerline axis of the opposed jet as plotted in Figure 5-39 through Figure 5-44 for the combinations

of Re, L/d_e ratios and turbulence Re number, the following conclusions can be drawn regarding the effect of HIT configuration.

- For Re≥5500, as depicted from the u_{rms} profiles in Figure 5-39 and Figure 5-40 the overall shape of the profiles resembles the corresponding shape of the profiles without HIT. The maximum values of u_{rms}/U_e are about 0.25 in a region ahead of the stagnation point which is somewhat elevated from the value of 0.2 measured for opposed jets in a quiescent environment demonstrating that the HIT is able to penetrate into the jet core. The penetration of the environmental turbulence into the jet core before the stagnation plane is also attested by the spreading of the u_{rms}/U_e profiles in the upstream direction, more so for the cases of Re=5500 and 6600. The effect of turbulence is more profound for the larger jet separation, of L/d_e=7.5, where the jets have more space to develop and turbulence has more time to perturb the jet core. The crossflow fluctuating velocity v_{rms}/U_e is also affected by the presence of environmental turbulence, as its profile is also spread in the upstream direction.
- The large anisotropy described in par. 5.1 is observed here as well, since the values of v_{rms}/U_e Figure 5-41 and Figure 5-42 are significantly lower than u_{rms}/U_e. This is the result of the nearly zero radial velocity V in the axis of the jets due to symmetry, the maximum values attained near the stagnation point being smaller than 0.05.
- The development of $tke/(U_e)^2$, follows mainly the development of u_{rms}/U_e, due to the aforementioned large anisotropy. Nevertheless, it can be added that in the case of L/d_e=7.5, the maximum values in the stagnation point are significantly larger than for the lower Re cases where the deviations are attenuated. This does not occur for the L/d_e=5. Consequently, it is deduced that external HIT elevates the turbulent intensity of the weaker Re opposed jets as the L/d_e increases.

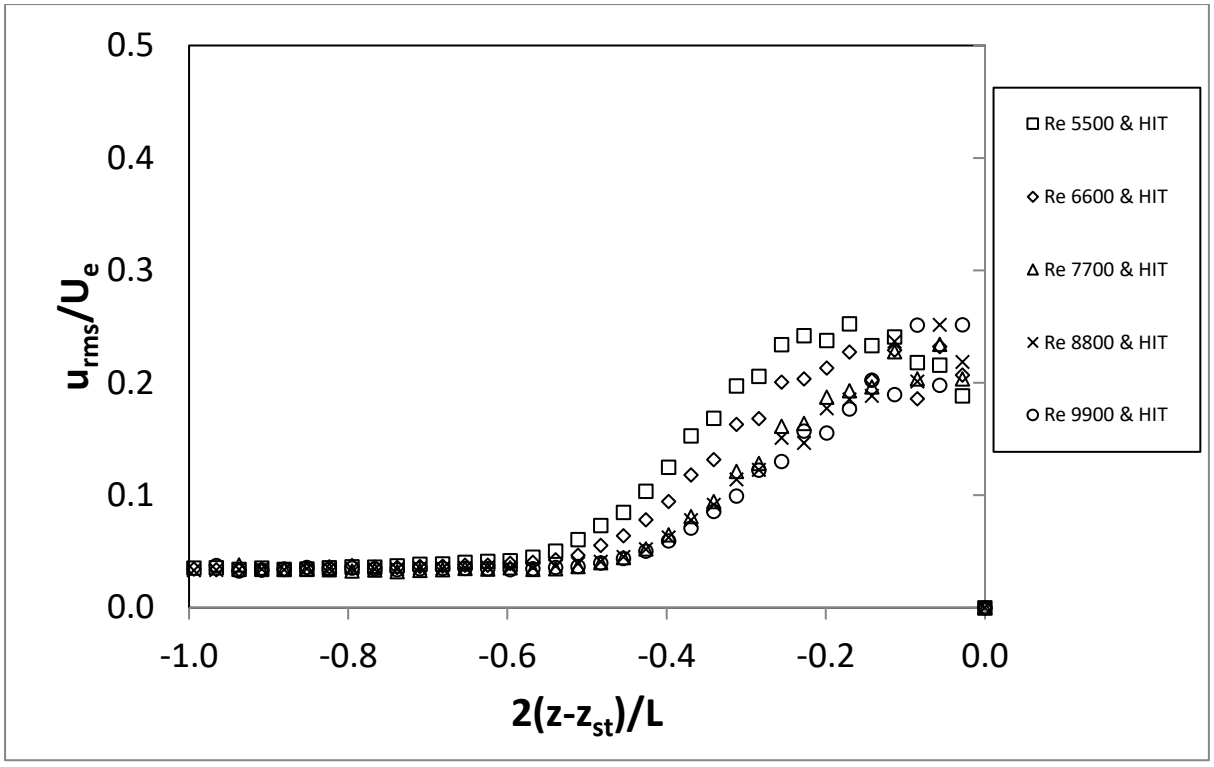

Figure 5-39: Normalized u_{rms} along the opposed jets axis (centerline) under HIT, L/d_e=5

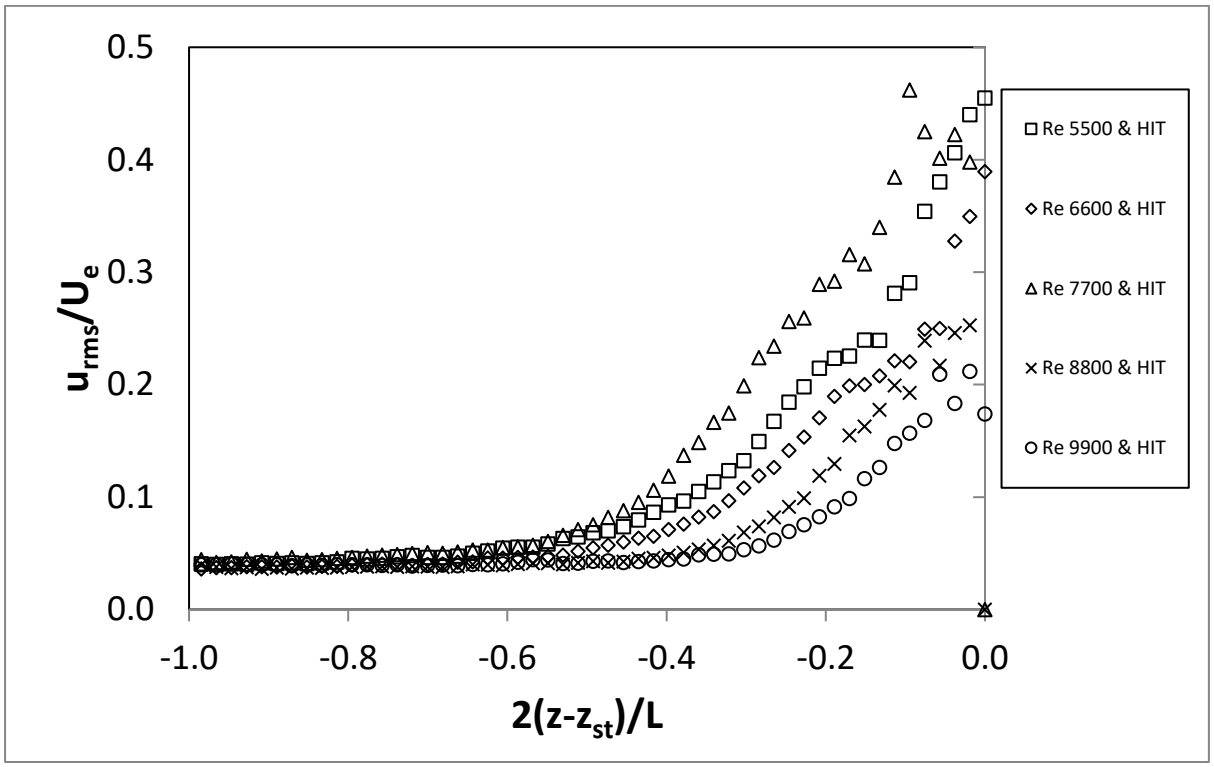

Figure 5-40: Normalized u_{rms} along the opposed jets axis (centerline) under HIT, L/d_e=7.5

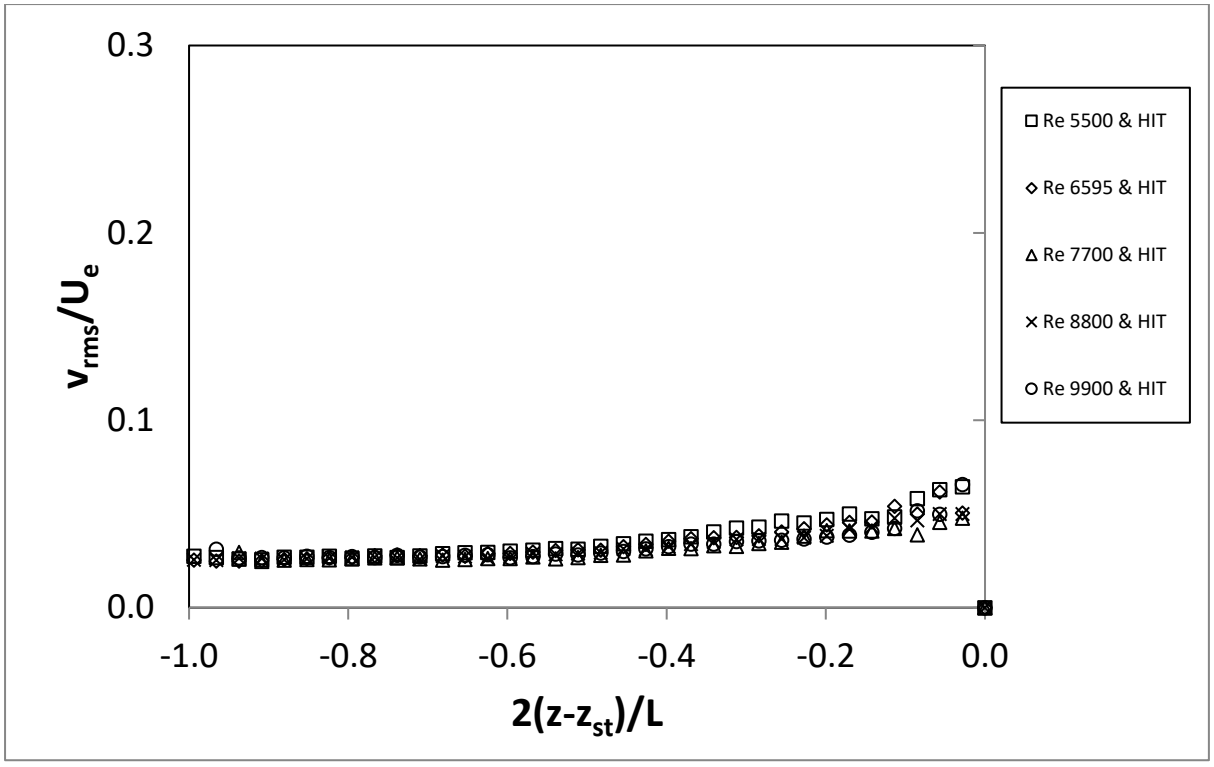

Figure 5-41: Normalized v_{rms} along the opposed jets axis (centerline) under HIT, L/d_e=5

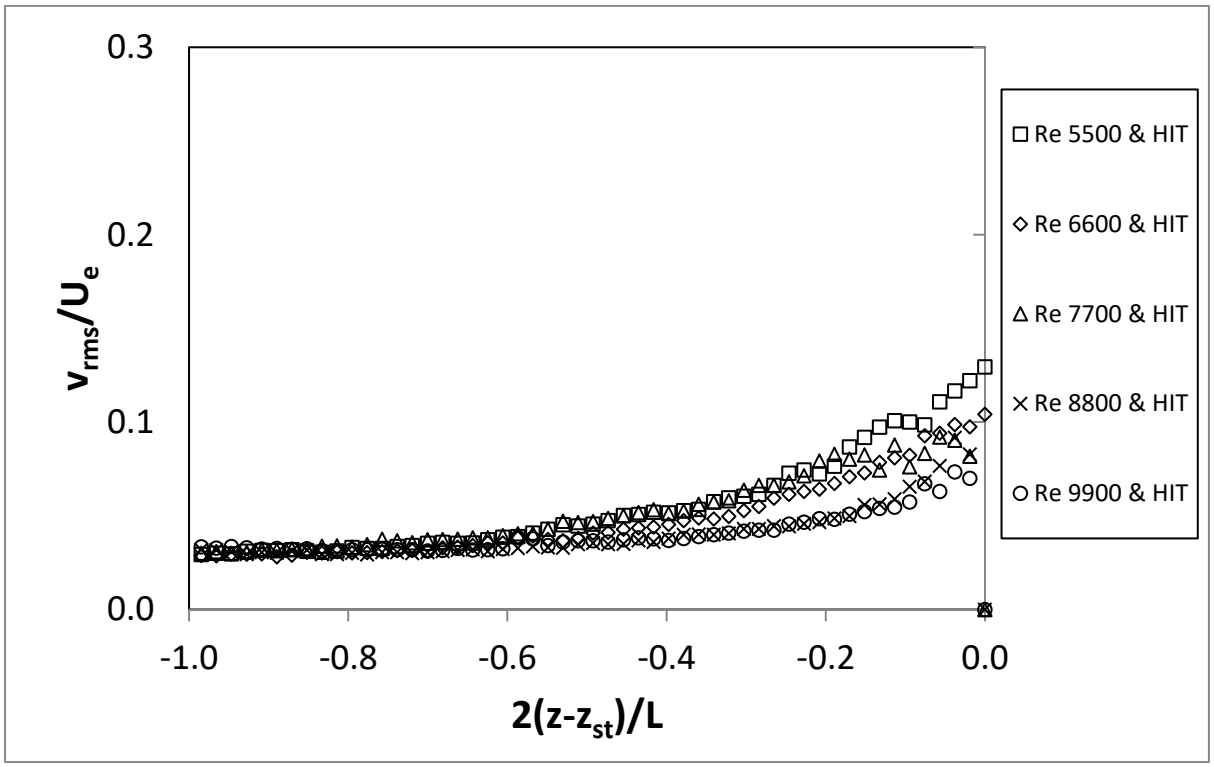

Figure 5-42: Normalized v_{rms} along the opposed jets axis (centerline) under HIT, L/d_e=7.5

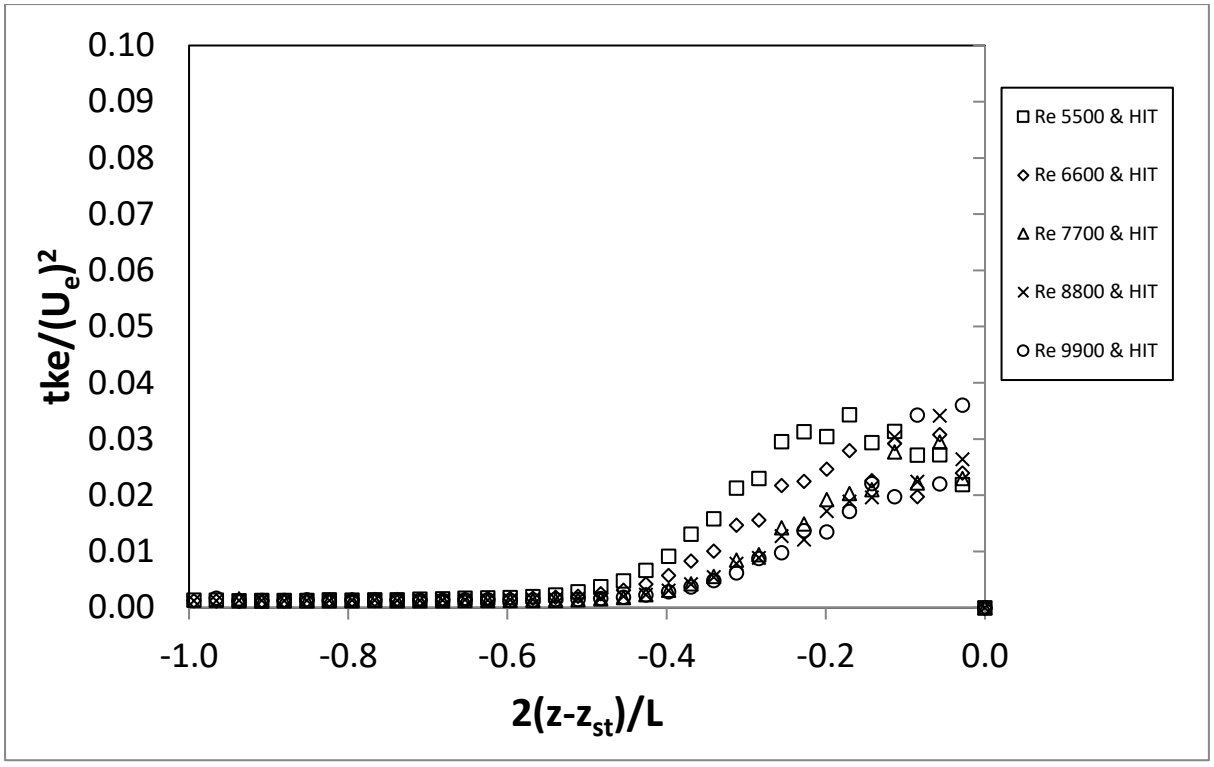

Figure 5-43: Normalized turbulent kinetic energy along the opposed jets axis (centerline) under HIT, $L/d_e=5$

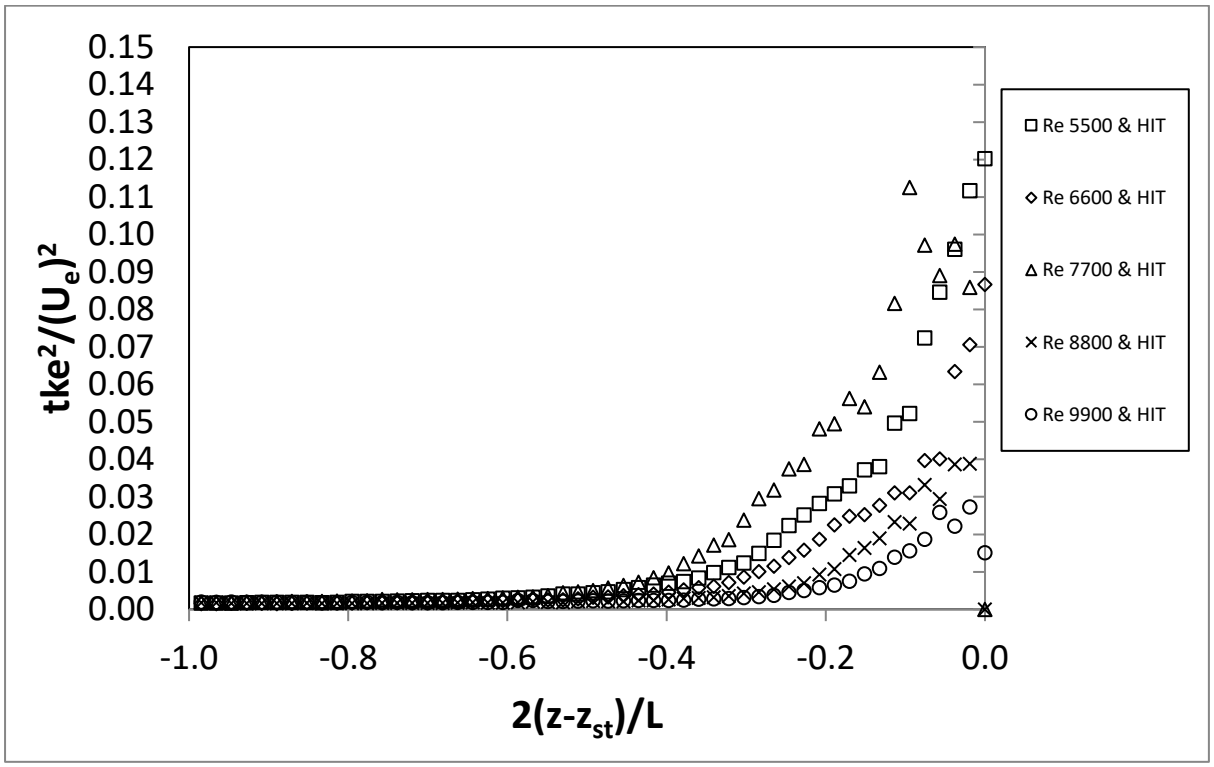

Figure 5-44: Normalized turbulent kinetic energy along the opposed jets axis (centerline) under HIT, $L/d_e=7.5$

5.5 Opposed jets flow along the stagnation line, under HIT

Following the approach of section 5.2, the mean and turbulent properties of the radial jets are examined along the stagnation line. First the mean value of the radial component V, which represents the streamline velocity of the radial jet, is presented in Figure 5-45 through Figure 5-46, for the combinations of L/d_e, jet Re used. The following observations can be noted:

- In the region of the stagnation point there is rapid linear increase of the radial velocity of V along the stagnation line until a maximum value is reached, as a result of the mass conservation. This phenomenon remains the same as in the case of opposed jets without the influence of HIT in the environment.
- In the case of L/d_e=5, (Figure 5-45) the velocity profiles almost coincide for all considered Re, leading to maximum values of V_{st}/U_e=0.5. This shows that the peak values along the stagnation line are largely unaffected by the presence of HIT in the surrounding environment when compared to the profiles of Figure 5-13.
- In the case of L/d_e=7.5 (Figure 5-46), for Re=5500 and 6600 lead to V_{st}/U_e peaks around 0.3, while for Re=7700, 8800 and 9900 the peak values reach the level of 0.5, which is the same for the cases without HIT. This leads us to the hypothesis that in the greater opposed jet distance, each jet flow becomes weaker and the HIT effect becomes more evident.
- The radial location of maximum V_{st}/U_e values remains about the same as in the cases without HIT, namely $0.75d_e$.
- An overall account is summarized in Table 5-6, where the stain rate is presented. It can be deduced from the normalized strain rates that the stain is approximately the same as in the case of the quiescent surrounding air (Table 5-2), regardless of L/d_e ratio.

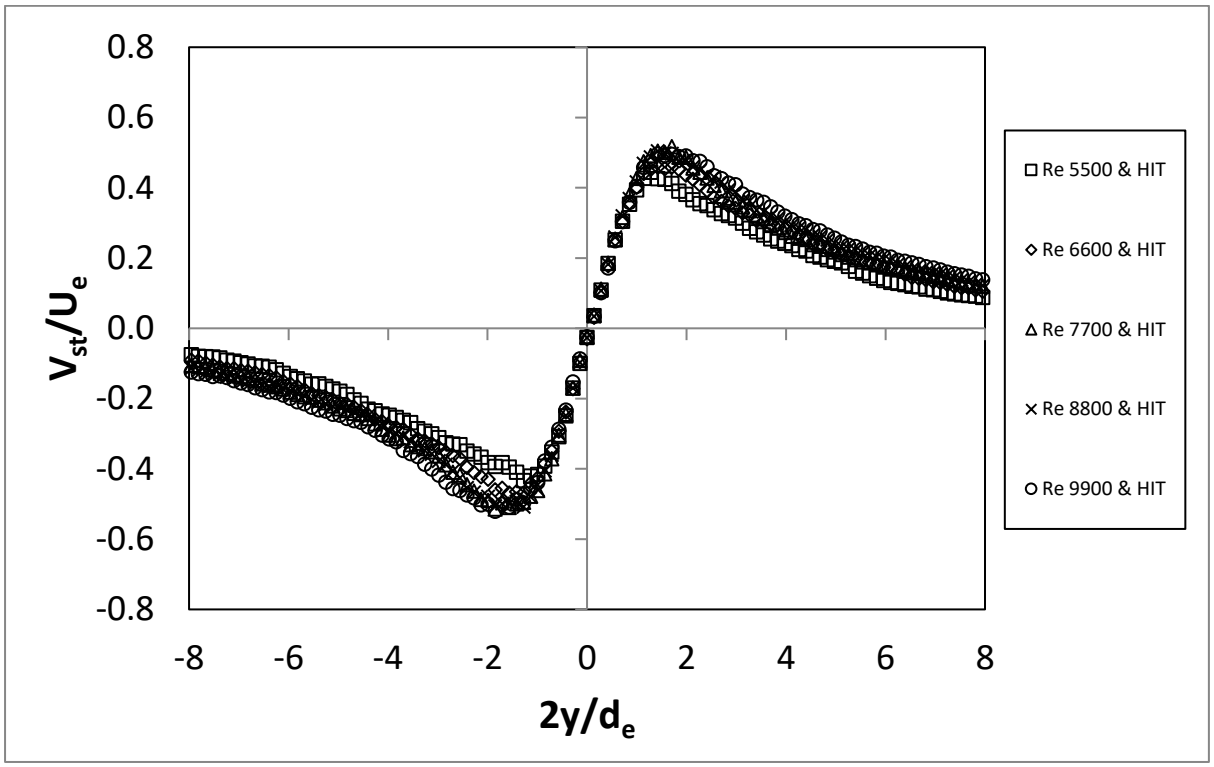

Figure 5-45: Normalized mean cross-stream (radial) V along the stagnation line under HIT, L/d_e=5

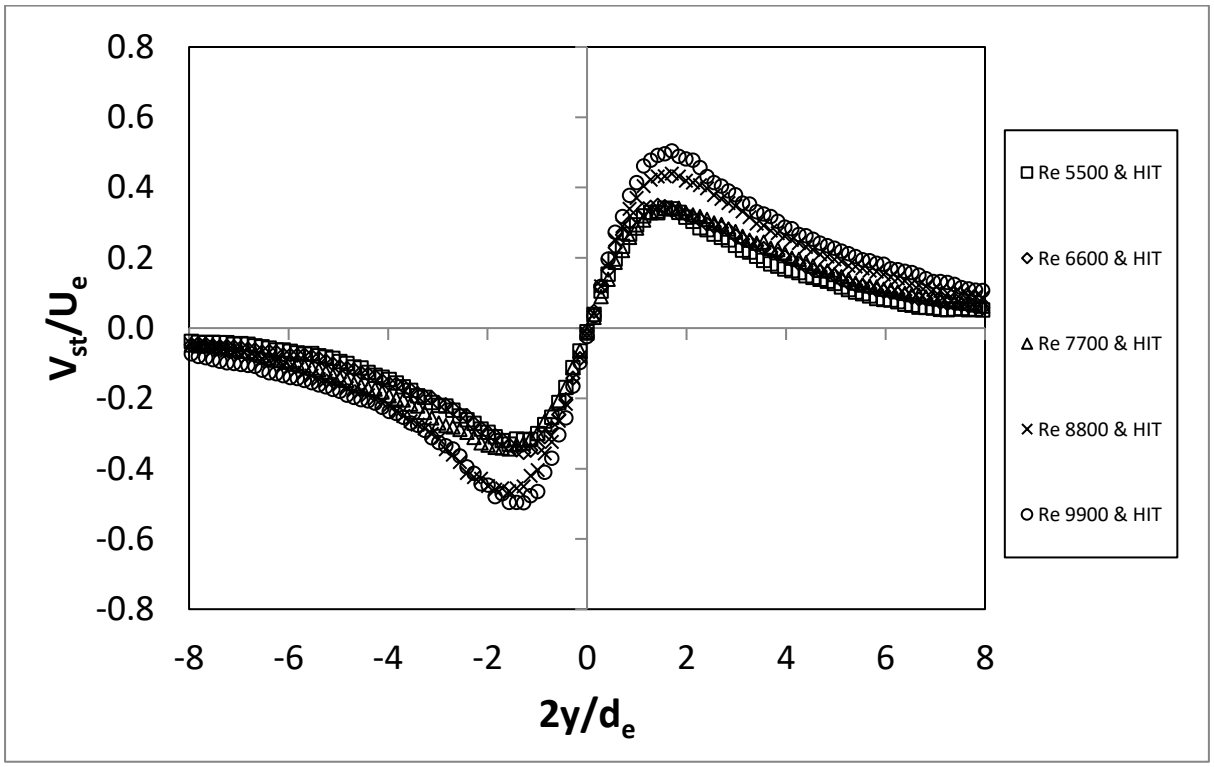

Figure 5-46: Normalized mean cross-stream (radial) V along the stagnation line under HIT, L/d_e=7.5

Table 5-6: Linear radial constants (radial strain rates) at the stagnation line, under HIT

	Re	5500	6600	7700	8800	9900
L/d_e=5 & HIT	Absolute	444.5	524.2	646.5	716.8	763.4
	Normalized	0.46	0.46	0.48	0.47	0.45
	Bulk	191.6	228.8	269.25	302.2	339.7
L/d_e=7.5 & HIT	Absolute	326.9	460.2	448.4	666.4	854.5
	Normalized	0.34	0.38	0.33	0.43	0.48
	Bulk	127.6	157.5	183.4	206.2	234.8

The turbulent quantities v_{rms}, u_{rms}, and the tke are presented in Figure 5-47 through Figure 5-52, for the combinations of Re and L/d_e ratios of interest. The following remarks can be made regarding the turbulent quantities:

- As in the case of opposed jets in quiescent air, the normalized streamline fluctuating velocity v_{rms} is minimum and nearly zero at the stagnation point and increases to maximum at a distance of about $1d_e$ from the axis of symmetry. The maximum values are about 0.3 for L/d_e=5 and 0.2 for L/d_e=7.5. The data into this Re regime collapses into identical trends. According to Table 5-7, for L/d_e=5, there is a constant decrease in the maximum v_{rms}, in the presence of HIT, whereas for L/d_e=7.5 in most cases the maximum value is increased.
- u_{rms} attains a maximum value on the centerline but presents also local maximums at about two exit diameters from the centerline. For L/d_e=5 all plots collapse onto a nearly identical curve, and there is an increase in the maximum values, which gradually drops towards the higher Re. On the other hand, for L/d_e=7.5, the increase of normalized u_{rms} is sustained until the higher Re and is significantly larger than the L/d_e=5 cases. This fact is attributed to the weaker mean flow of the opposed jets for the L/d_e case near the stagnation region.
- Taking into account the end result as expressed by the normalized tke, the conclusion that can be reached is that there is a gradual effect by external HIT as the Re decreases, which leads to elevation of tke intensity. These gradual effects are more profound for the L/d_e ratio=7.5.

Table 5-7: Variation of max u_{rms}, v_{rms} due to HIT

Re	5500	6600	7700	8800	9900
$\Delta(u_{rms}/U_e)\%$ $L/d_e=5$	10.80	-2.85	2.67	22.13	3.23
$\Delta(u_{rms}/U_e)\%$ $L/d_e=7.5$	80.22	85.88	71.78	25.04	49.91
$\Delta(v_{rms}/U_e)\%$ $L/d_e=5$	-2.33	-7.91	-10.79	-17.53	-16.69
$\Delta(v_{rms}/U_e)\%$ $L/d_e=7.5$	3.05	7.35	9.11	-3.02	9.21

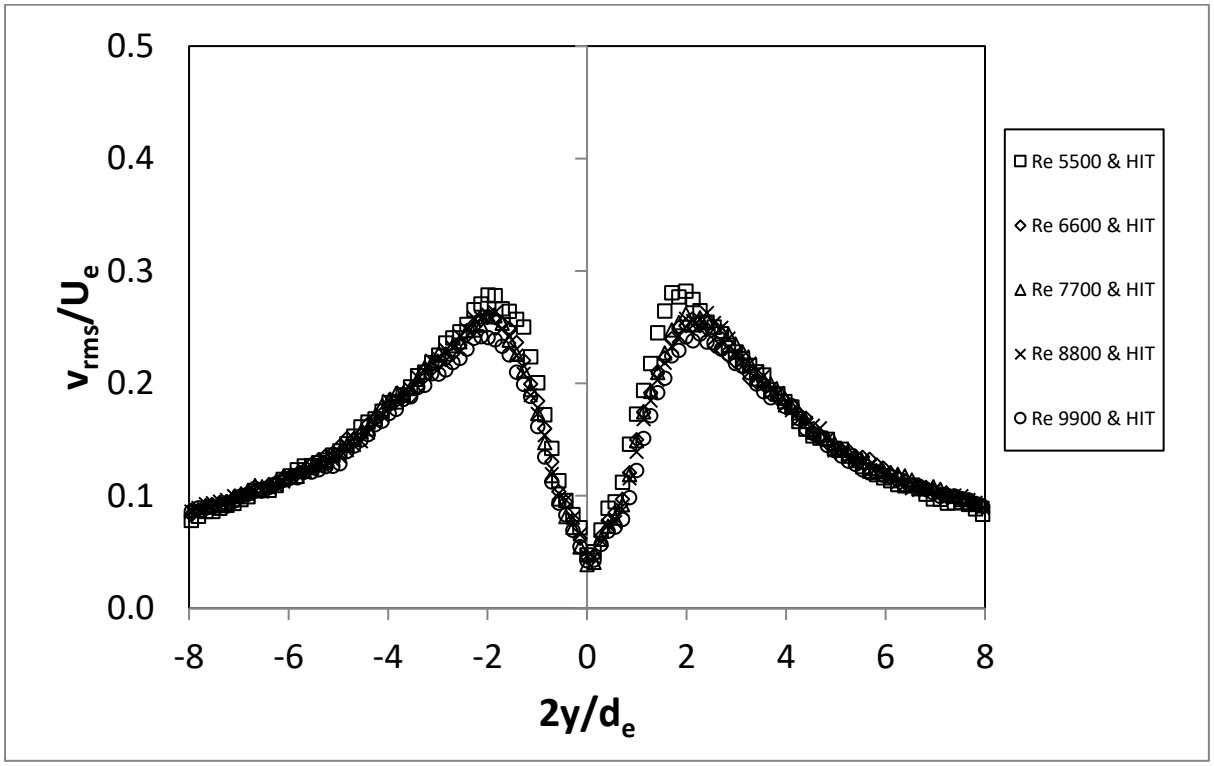

Figure 5-47: Normalized v_{rms} along the stagnation line under HIT , $L/d_e=5$

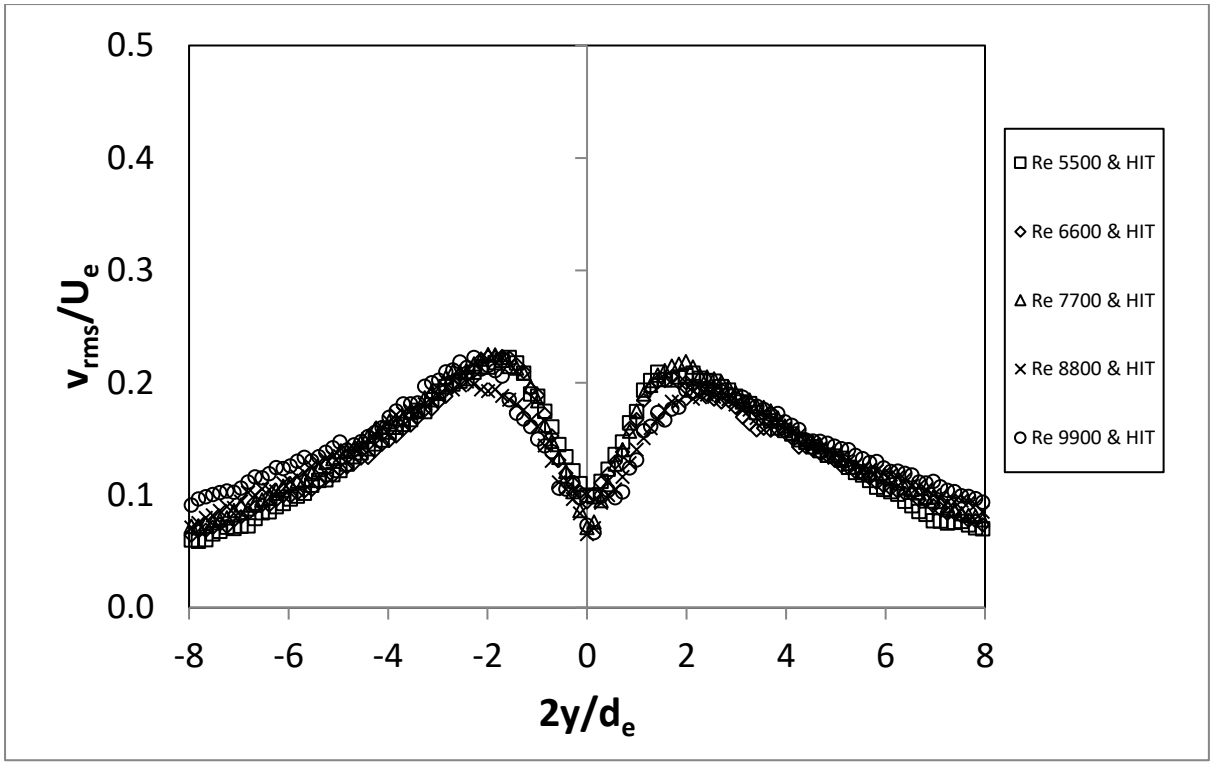

Figure 5-48: Normalized v_{rms} along the stagnation line under HIT, L/d_e=7.5

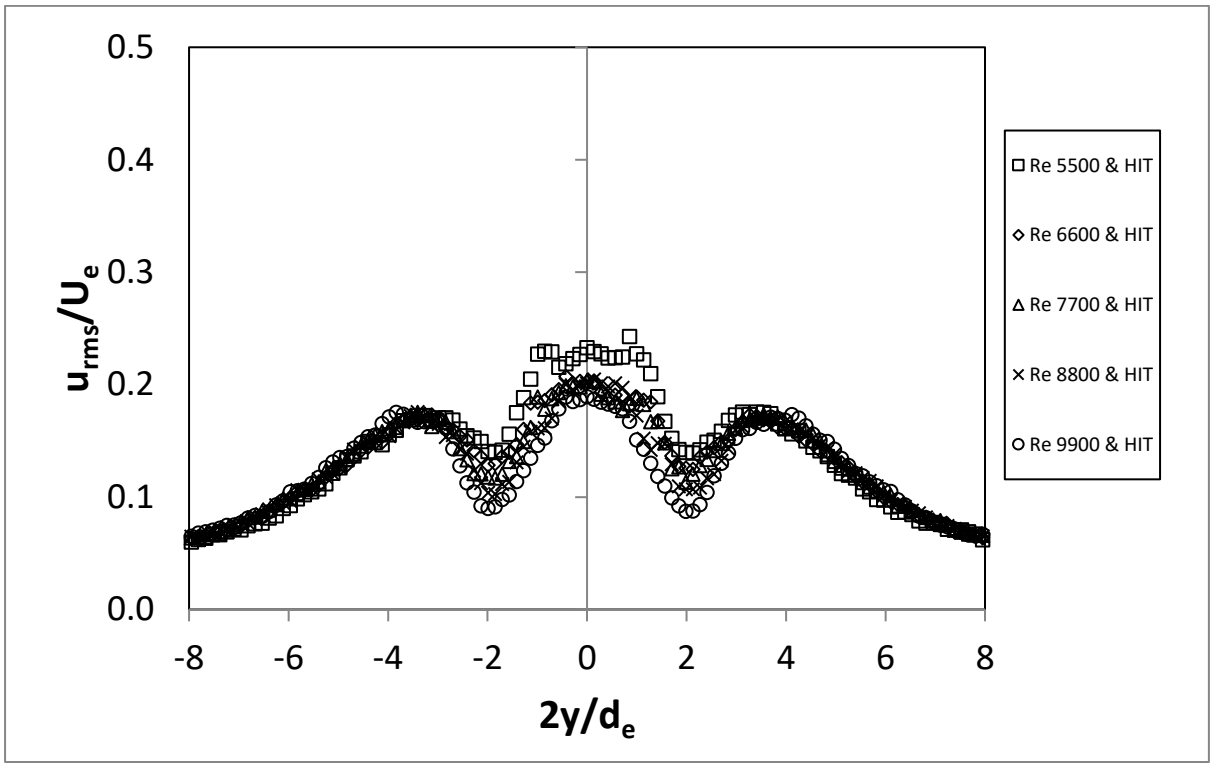

Figure 5-49: Normalized u_{rms} along the stagnation line under HIT, L/d_e=5

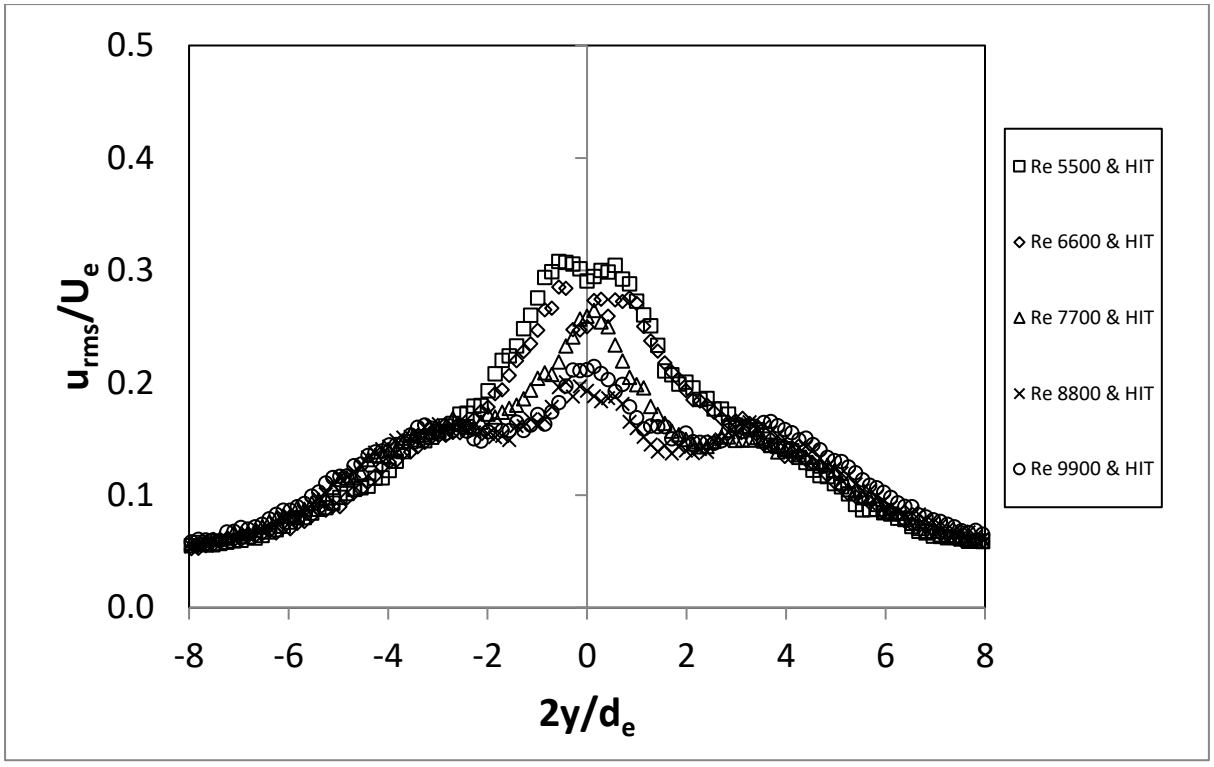

Figure 5-50: Normalized u_{rms} along the stagnation line under HIT, L/d_e=7.5

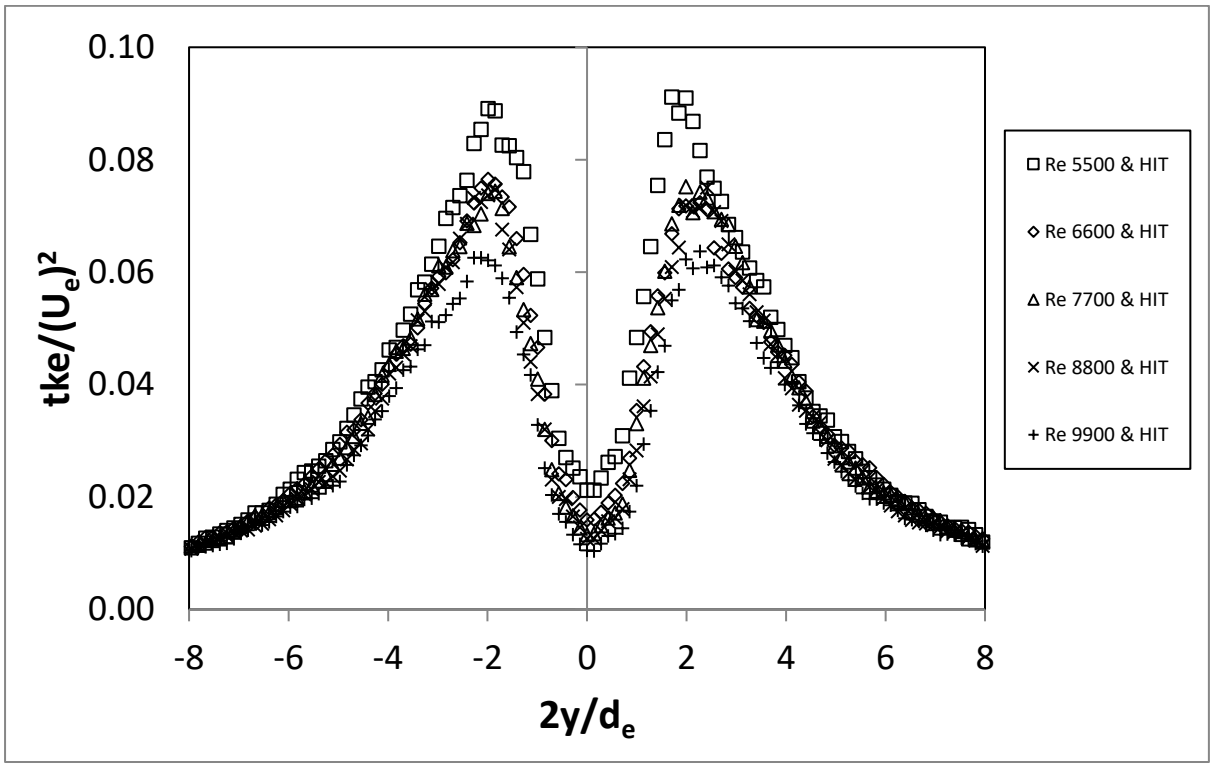

Figure 5-51: Normalized tke along the stagnation line under HIT, L/d_e=5

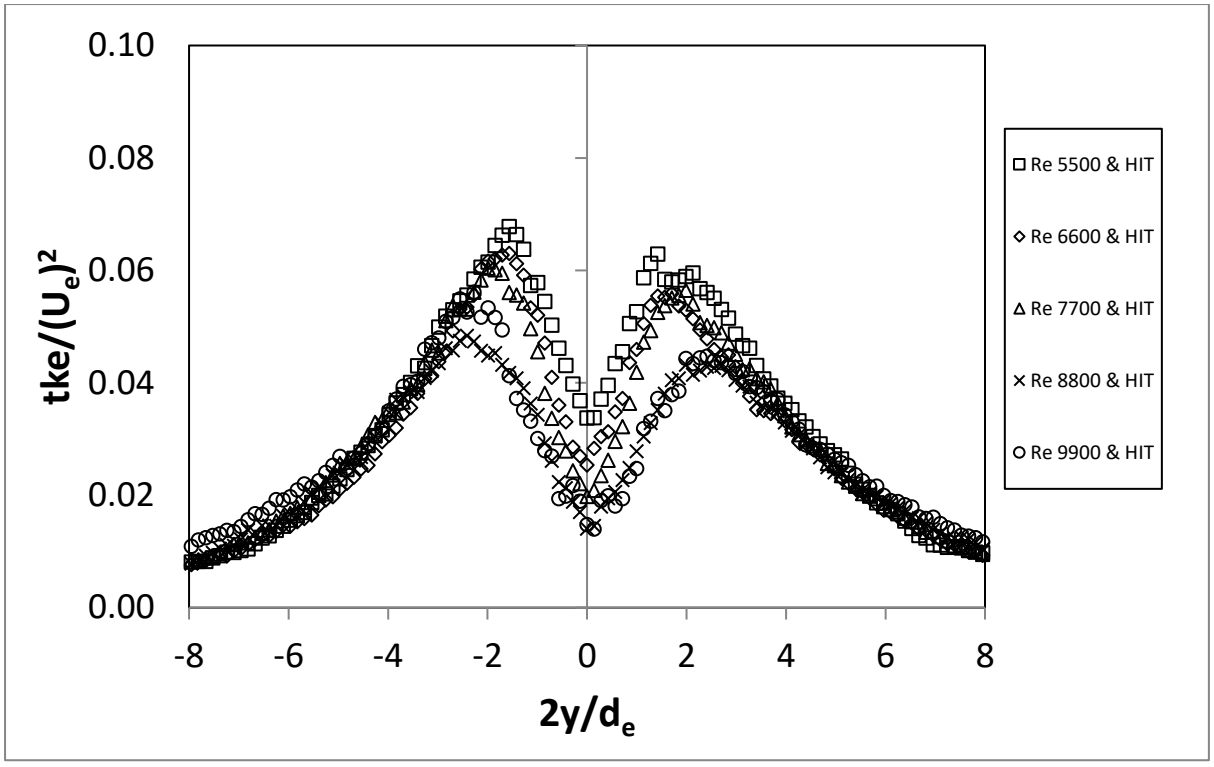

Figure 5-52: Normalized tke along the stagnation line under HIT, L/d_e=7.5

5.6 Free radial jet development under HIT

In this paragraph, the behavior of the radial jet developed around the stagnation line under the influence of HIT is investigated, in a same manner as the development of the redial jet from opposed jets in quiescent environment in section 5.3. The two cases of jet of Re=5500 and 7700 that were chosen in section 5.3 for illustration will be presented here for L/d_e=5 and L/d_e=7.5.

The development of the radial streamwise velocity, V, profile is examined first. Examining the effect of HIT on the mean radial velocity V, the following conclusions are drawn:

- For L/d_e=5, the development along the stagnation line of the normalized radial jet profile shown in Figure 5-53 and Figure 5-54 for Re=5500 and 7700 respectively, is not affected significantly by the surrounding air turbulence in comparison with the development of the profile in case of opposed jet in quiescent air, shown in Figure 5-22 and Figure 5-23. After the initial wider distribution for $1d_e$, a self-similar narrower profile is reached beyond $2d_e$. However, for the Re=5500 case, a small widening of the distribution may be observed due the presence of HIT. The same effect is minimal for jets with Re=7700, where the distributions are similar to the case without HIT, due to the increased jet momentum of the higher Re number jet.

- For L/d_e=7.5, where the jet separation increases and the jets have more time to develop and spread, resulting to decreased momentum flux at the stagnation plane, there is a notable influence of HIT for the jets of Re=5500 (Figure 5-55). The decreased momentum flux of the axial jets at the stagnation plane results to widening of the radial jet velocity profiles for all distances from the stagnation point up to $4d_e$ in comparison to the velocity profiles of the opposed jets in quiescent air, shown in Figure 5-24. Additionally, self-similarity is not attained within the measured region up to $4d_e$. In contrast, for the higher momentum jets of Re=7700, the environmental turbulence does not appear to have a significant effect on the development of the radial jet velocity profile, Figure 5-56, in comparison to the corresponding profile in a quiescent environment shown in Figure 5-25.

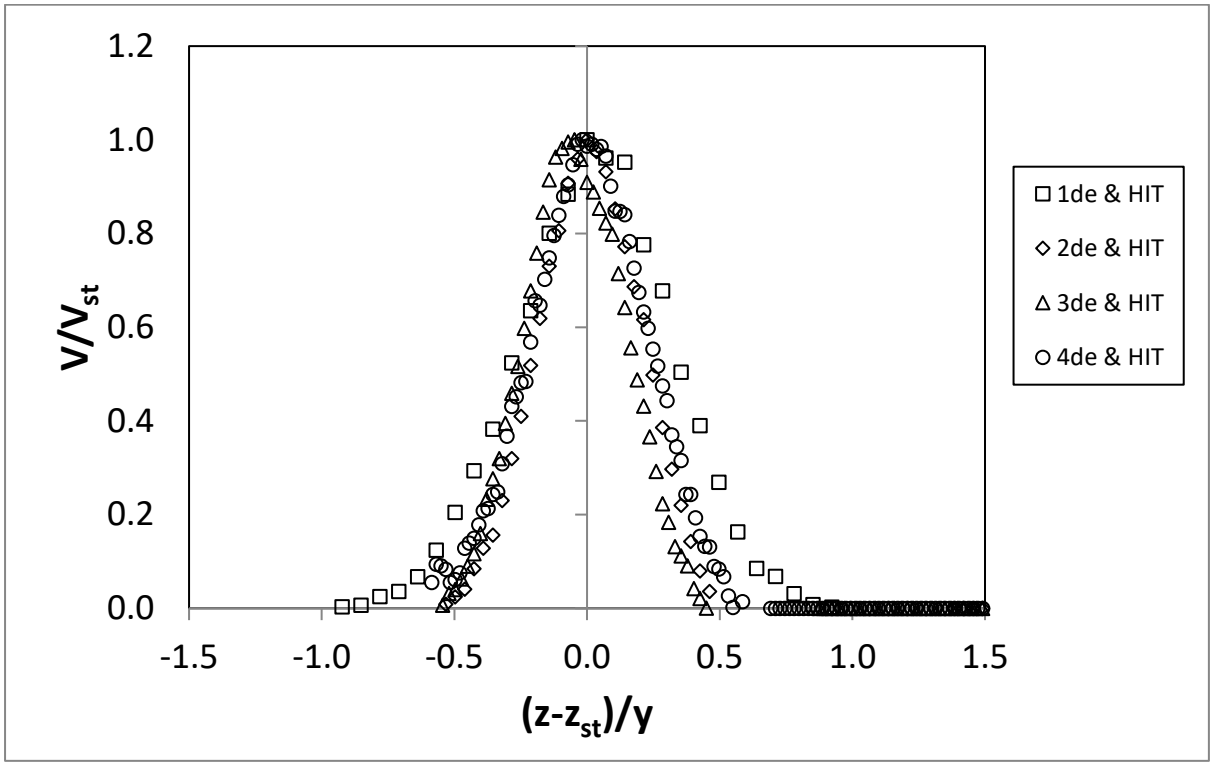

Figure 5-53: Normalized mean radial velocity V under HIT , Re=5500, L/d_e=5

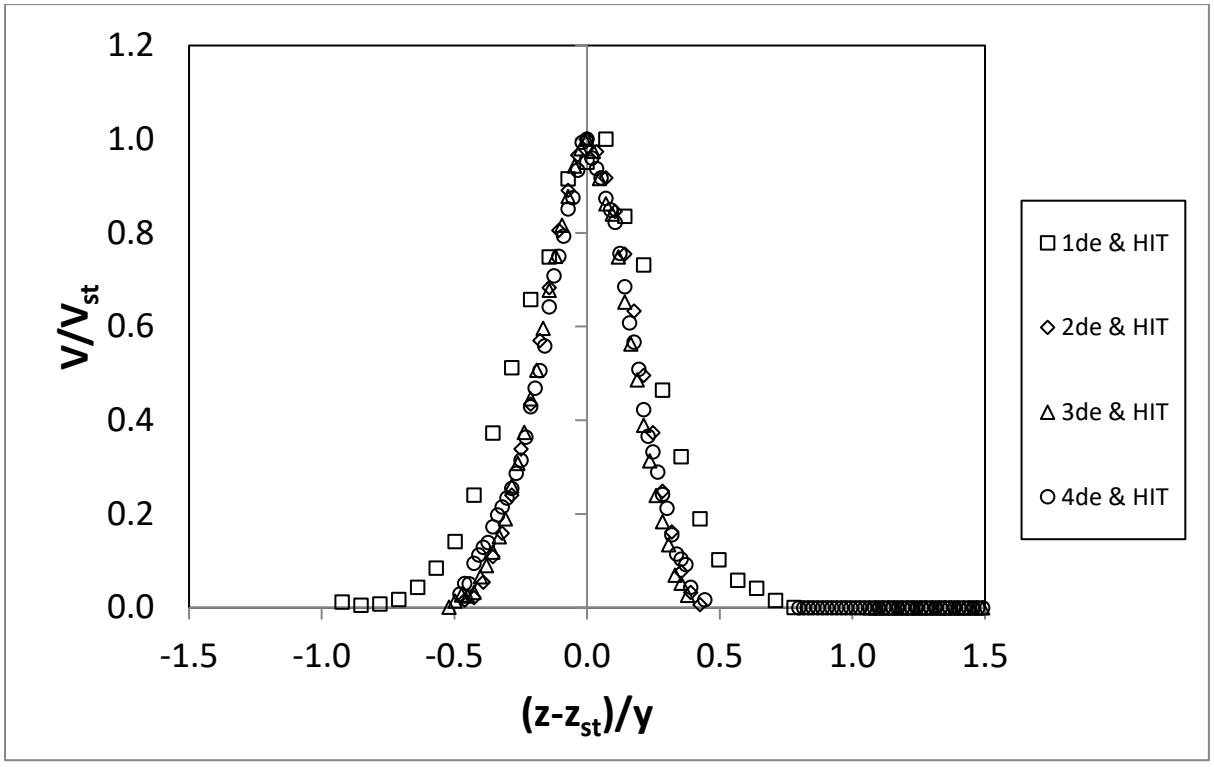

Figure 5-54: Normalized mean radial velocity V under HIT , Re=7700, L/d_e=5

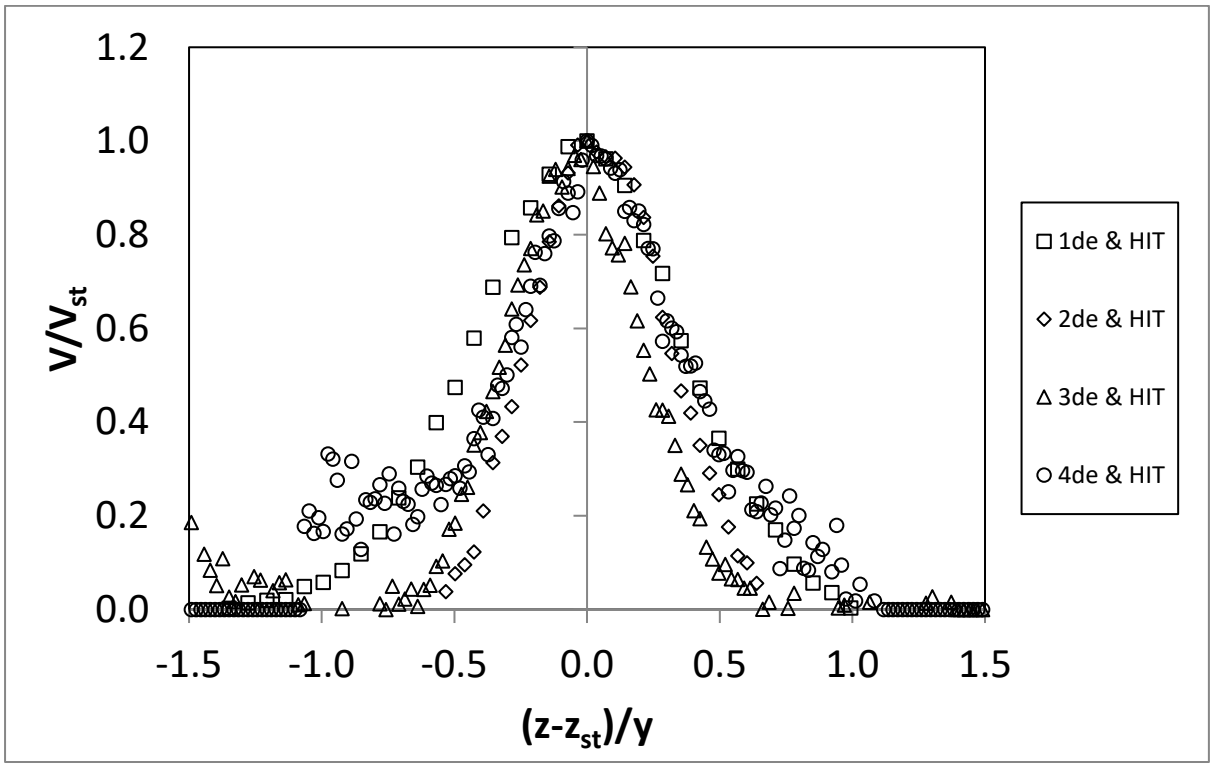

Figure 5-55: Normalized mean radial velocity V under HIT , Re=5500, L/d_e=7.5

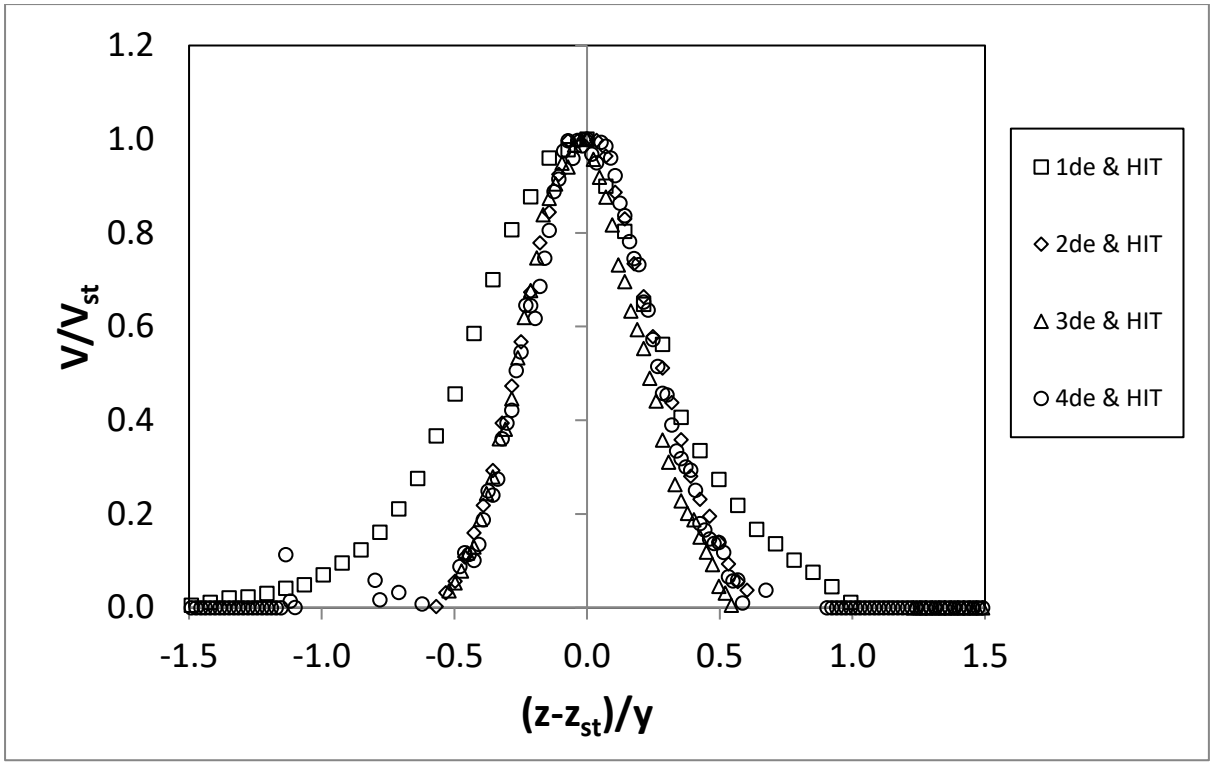

Figure 5-56: Normalized mean radial velocity V under HIT , Re=7700, L/d_e=7.5

The development of the normalized radial fluctuating velocity profile v_{rms}/V_{st} is presented in Figure 5-57 through Figure 5-60, for the two L/d_e ratios separately.

- For L/d_e=5 (Figure 5-57 and Figure 5-58 for Re=5500 and Re=7700 respectively) there is a clear effect of environmental turbulence both in the magnitude and the shape of the distribution of the v_{rms} intensity. In contrast to the corresponding cases of opposed jets in quiescent air (Figure 5-26 and Figure 5-27 for Re=5500 and Re=7700 respectively) where self-similar profiles are attained beyond $1d_e$ from the stagnation point, neither the centerline intensity not the intensity at the jet edges the turbulence intensity converge. The centerline intensity increases constantly as energy is fed to the radial jet from the background turbulence which appear to penetrate all the way to the radial jet core, while the intensity on the radial jet edges attains a plateau and does not decrease to zero as it would be the case for a radial jet in quiescent air. The magnitude of the intensity of the turbulence plateau is determined by the background turbulence which takes over and the stagnation line velocity which decreases with distance from the stagnation point. Additionally, the location where the transition between background turbulence of the environment and the radial jet turbulence profile takes place progressively approaches the stagnation line as the radial jet develops. Eventually the turbulence profile of the radial jet is expected to be dominated by the background turbulence, even if the velocity profile (shown in

Figure 5-53 and Figure 5-54 for Re=5500 and Re=7700 respectively up to $4d_e$,) persists as Figure 5-45 of the stagnation line velocity V_{st} suggests. In the case of the more energetic jets such as Re=7700, the effect of background turbulence is present but more limited. This can be attested by the more limited effect of turbulence along the stagnation line with maximum levels of around 0.6 observed for at $4d_e$, while the corresponding turbulence intensity for the lower jet momentum case of Re=5500 reaching values up to 1 at the same distance.

- For L/d_e=7.5 (Figure 5-59 and Figure 5-60 for Re=5500 and Re=7700 respectively), where the opposed jets have more time and distance to develop and the momentum flux is decreased at the stagnation plane, the background intensity has a more significant effect than at L/d_e=5. While ultimately the v_{rms} turbulence intensity profile is not wholly dominated within the examined region by the background turbulence as the peak of the jet profile still survives close to the stagnation line up to $4d_e$ from the stagnation point, the maximum v_{rms} levels are significantly higher ≥1.2 for both Re than the corresponding turbulence levels for the shorter jet separation. Comparison of the v_{rms} turbulence intensity profiles with the corresponding velocity profiles of the radial jets (Figure 5-55 and Figure 5-56 for Re=5500 and Re=7700 respectively) shows that for the lower momentum jet (Re=5500) the velocity profile is not fully self-similar explaining why it is almost dominated by the background turbulence, while in the other cases where the velocity profile does maintain a self-similar profile, the v_{rms} intensity profile is able to maintain for longer.

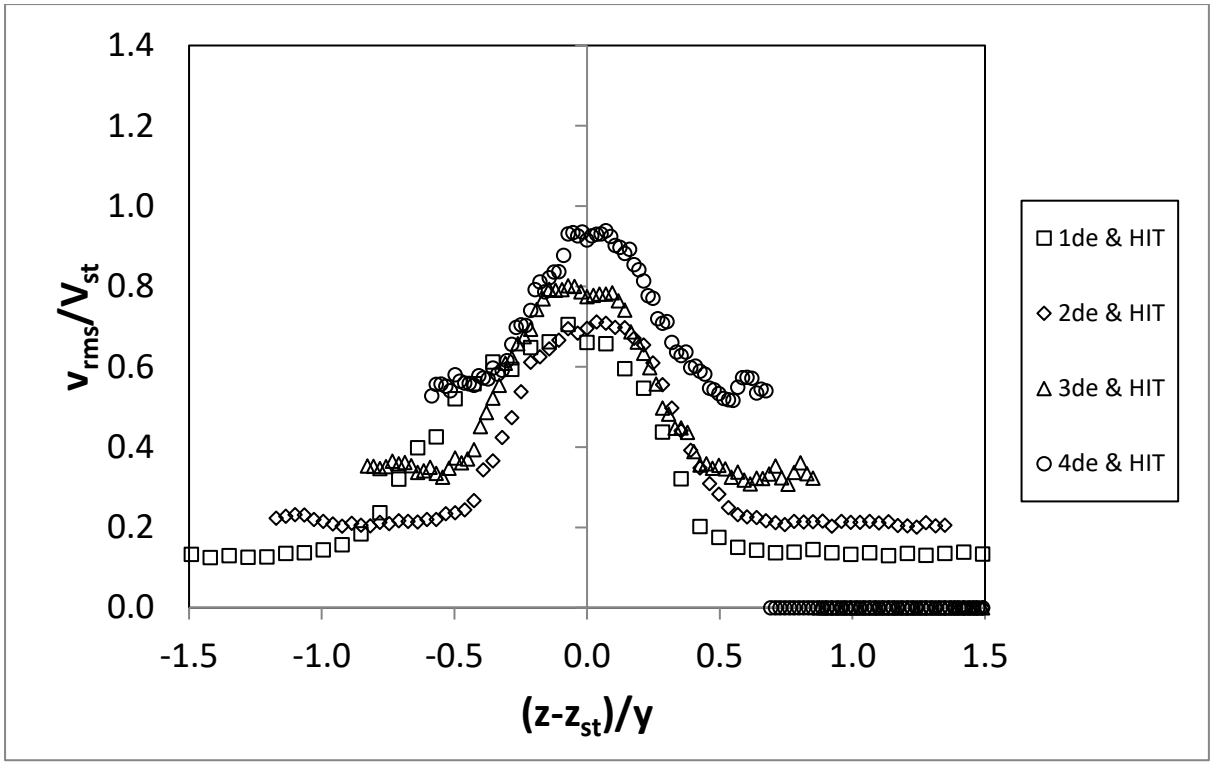

Figure 5-57: Normalized v_{rms}, Re=5500 under HIT , L/d_e=5

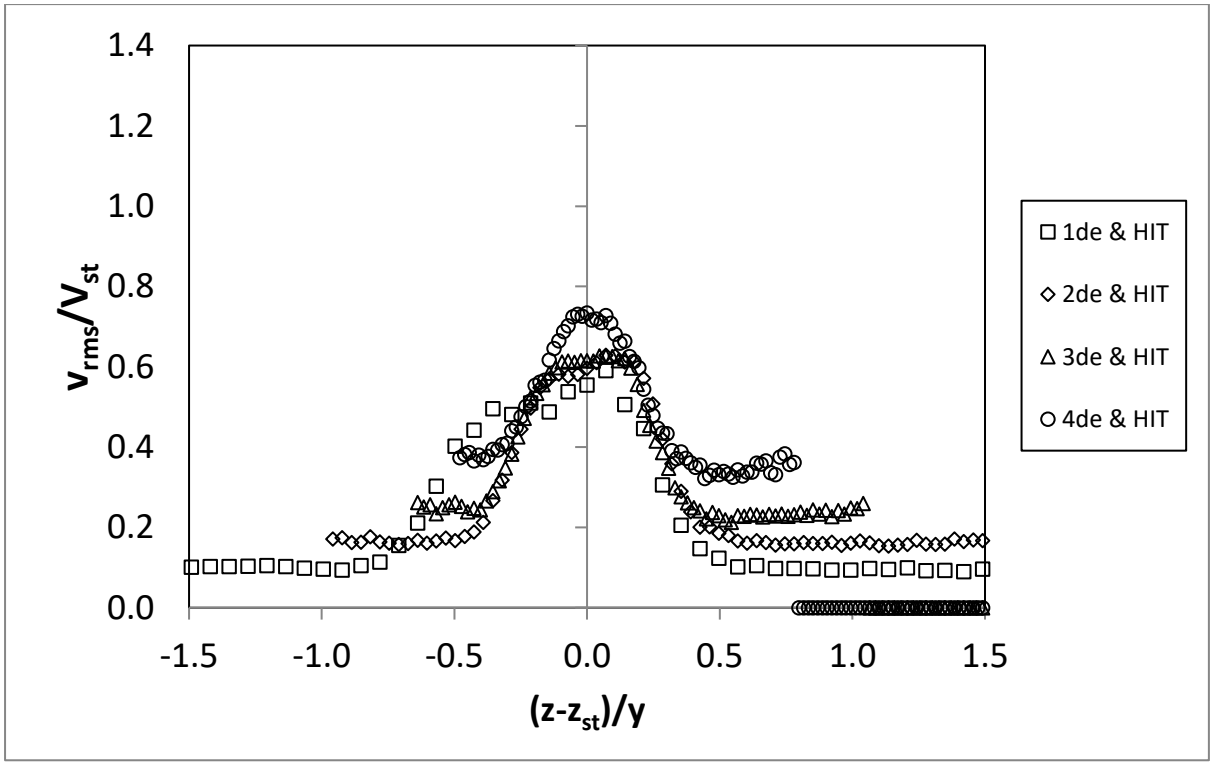

Figure 5-58: Normalized v_{rms}, Re=7700 under HIT , L/d_e=5

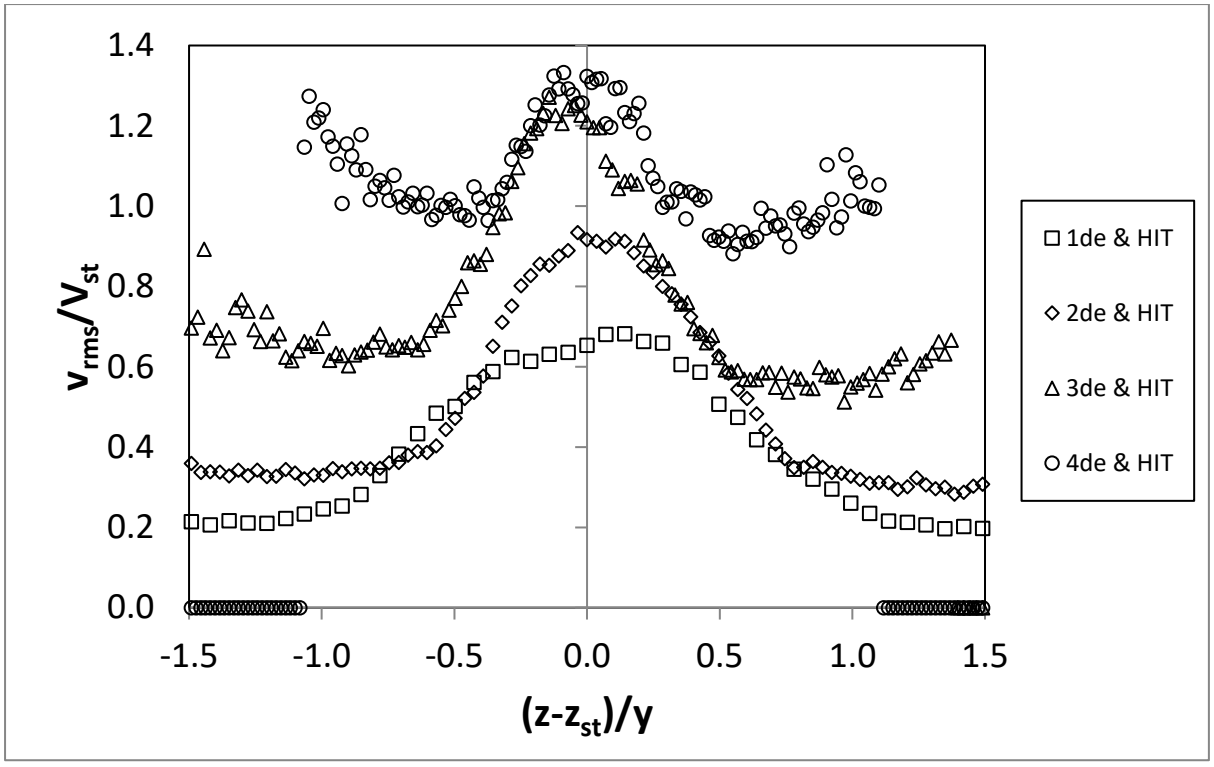

Figure 5-59: Normalized v_{rms}, Re=5500 under HIT , L/d_e=7.5

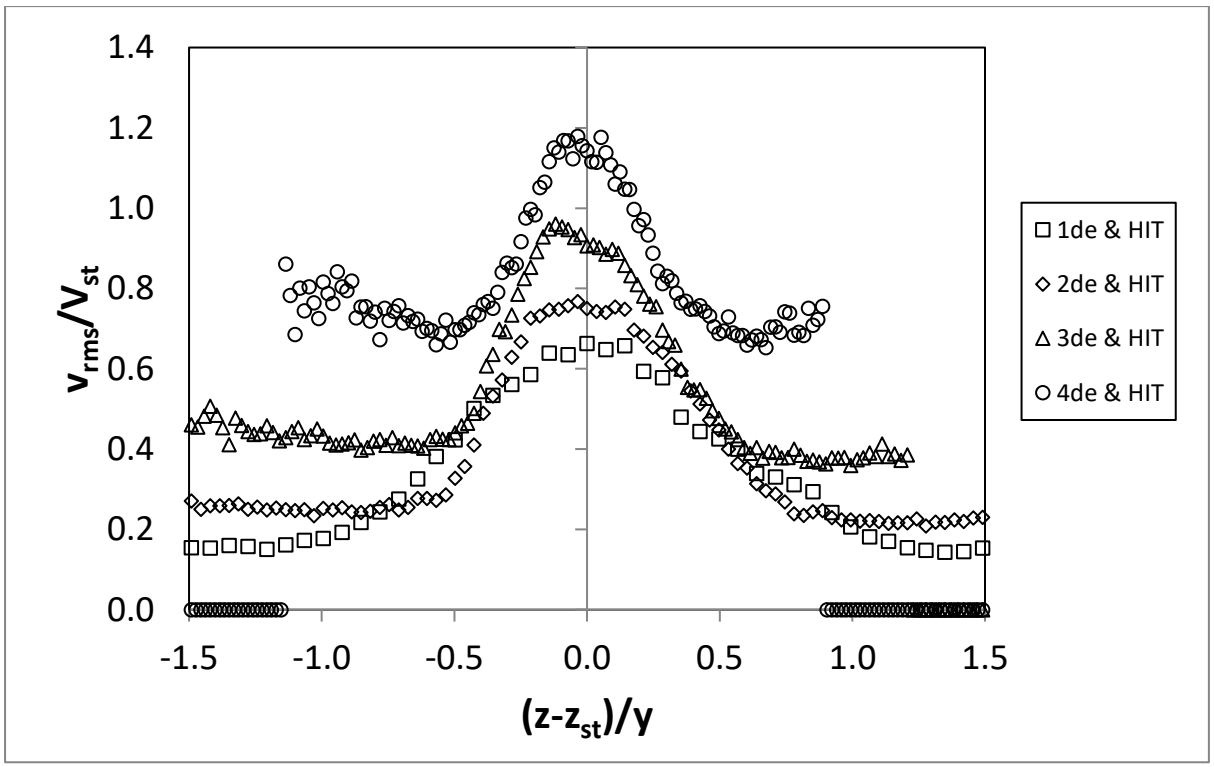

Figure 5-60: Normalized v_{rms}, Re=7700 under HIT , L/d_e=7.5

In order to examine the penetration of the background turbulence into the radial jet, the normalized u_{rms} profiles are presented (Figure 5-61 through Figure 5-64), for the two L/d_e ratios at Re=5500 and

Re=7700. In all cases the maximum u_{rms} turbulence intensity at the maximum measured extent of the radial jet development at $4d_e$ from the stagnation point is almost but not quite equal to v_{rms} intensity.

- Even for $L/d_e=5$ (Figure 5-61 and Figure 5-62, for Re=5500 and Re=7700 respectively) where the opposed jets have less distance to develop and the momentum flux of the axial jet is greater on the stagnation plane, the u_{rms} velocity profile of the radial jets is dominated by the background turbulence, although the streamwise velocity profile (shown in Figure 5-53 and Figure 5-54 for Re=5500 and Re=7700) clearly shows that the radial jet is largely intact and self-similar all the way up to that maximum measured distance. The more energetic jet (Re=7700) in not completely absorbed by the background turbulence, as the u_{rms} velocity profile manages to maintain a peak over the background turbulence and obtain a steady magnitude along the stagnation line up to $4d_e$ from the stagnation point.
- For $L/d_e=7.5$ (Figure 5-63 and Figure 5-64, for Re=5500 and Re=7700 respectively) where the opposed jets are less energetic by the time they reach the stagnation plane the u_{rms} velocity profile of both jets has been dominated by the background turbulence even though the corresponding velocity profiles of the radial jets (Figure 5-55 and Figure 5-56 for Re=5500 and Re=7700 respectively) are preserved
- A comparison of the value of the u_{rms} and v_{rms} turbulence intensities between Figure 5-61 through Figure 5-64 and Figure 5-57 through Figure 5-60, shows that the value of u_{rms} and v_{rms} at the jet edges at $4d_e$.is approximately the same in both cases. This confirms the idea that it is the background turbulence that is measured at the jet edges and that it controls the turbulence profile of the radial jets.

  While the velocity profiles of the radial jets (Figure 5-53 and Figure 5-56 for Re=5500 and Re=7700 respectively) and of v_{rms} (Figure 5-57 through Figure 5-60) do persevere throughout the measured length of the radial jet, the effect of background turbulence on u_{rms} is greater as the turbulence intensity of u_{rms} close to the stagnation point is lower than the corresponding intensity of v_{rms}. As such, background turbulence is able to overtake u_{rms} faster than it is able to overtake v_{rms}.

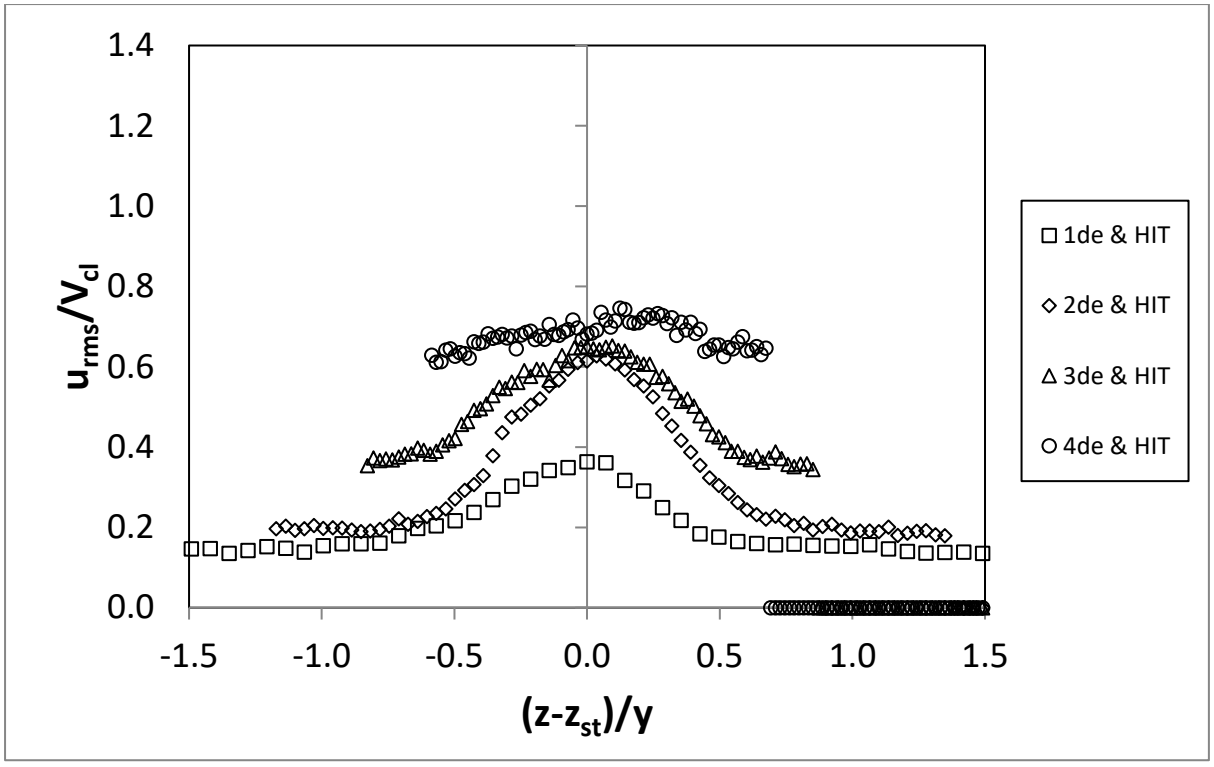

Figure 5-61: Normalized u_{rms}, Re=5500 under HIT , L/d_e=5

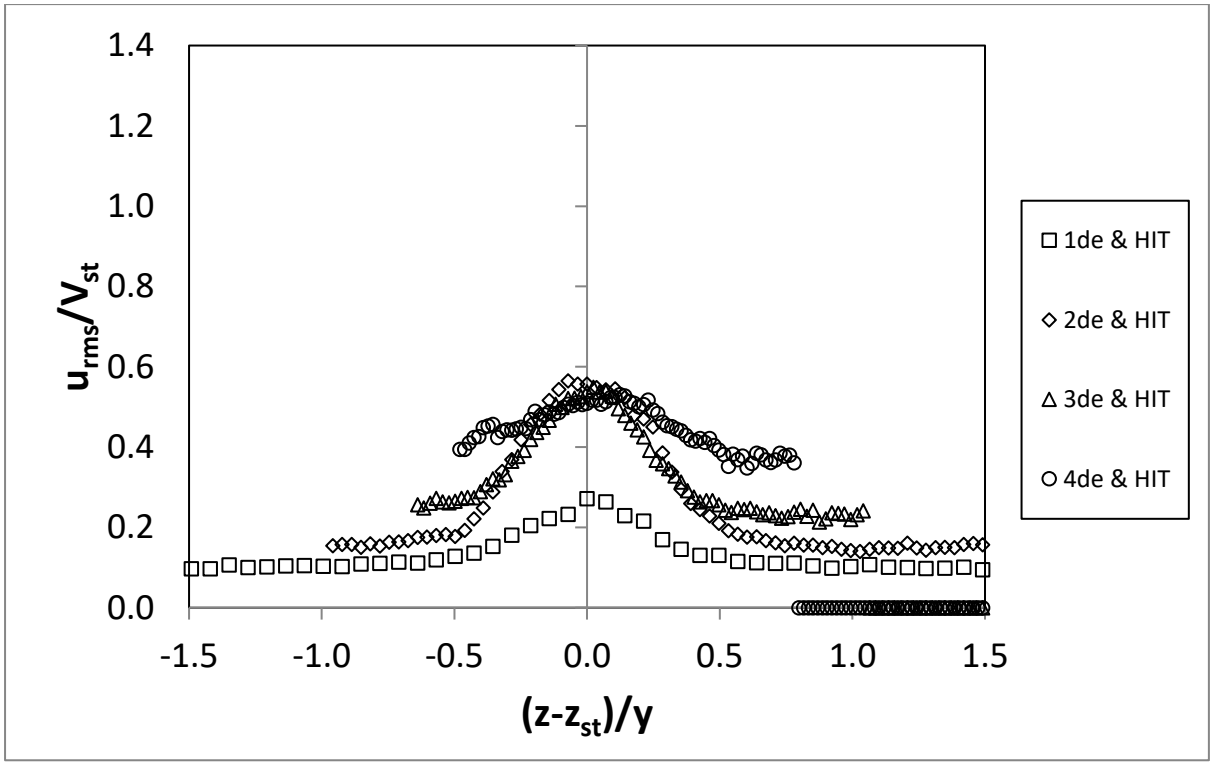

Figure 5-62: Normalized u_{rms}, Re=7700 under HIT , L/d_e=5

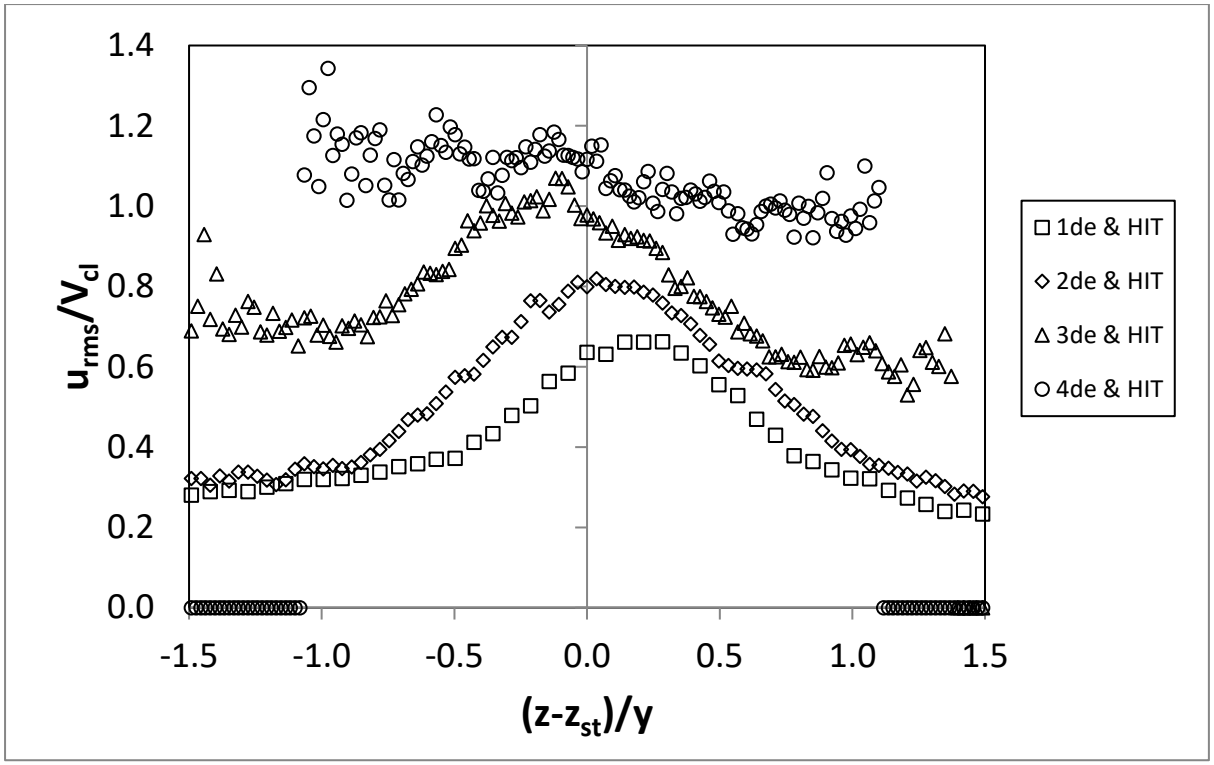

Figure 5-63: Normalized u_{rms}, Re=5500 under HIT , L/d_e=7.5

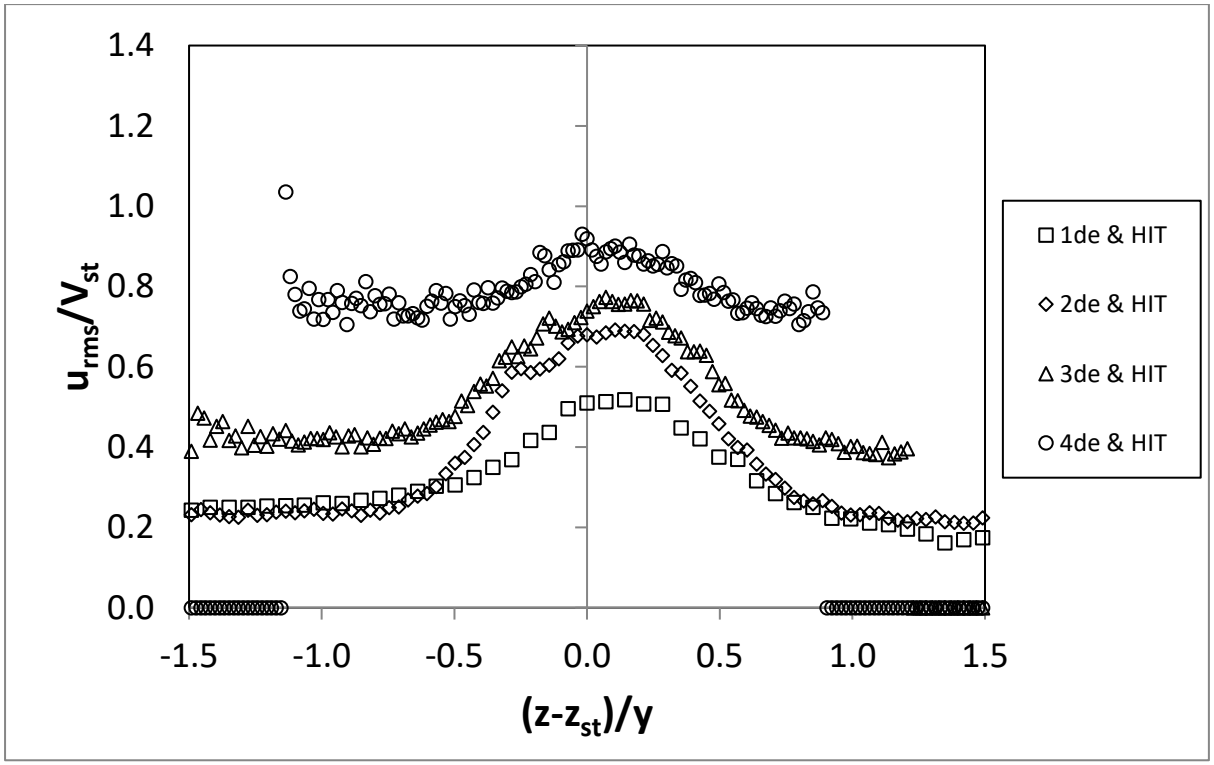

Figure 5-64: Normalized u_{rms}, Re=7700 under HIT , L/d_e=7.5

The spreading rate of the jets, estimated by the jet half-width $r_{1/2}$ of V component is presented in Figure 5-65 through Figure 5-66. The radial jet spread rate obtained from the figures is summarized in

Table 5-8. It is observed that $r_{1/2}$ evolves in a nearly linear fashion with distance having the same quantitative behavior as in Figure 5-34 and Figure 5-35 for a radial jet in quiescent background, indicating that the free radial jet structure is maintained under HIT. However, the normalized values of $r_{1/2}$ attain higher values in comparison with the corresponding cases of opposed jets in quiescent air shown in Figure 5-34 and Figure 5-35. This means that HIT increases the radial jet width for both L/d_e ratios, with the effect being more profound for L/d_e=7.5, where the opposed jets have less momentum flux at the stagnation plane and are more susceptible to the effects of turbulence. Furthermore, as it can be observed in Table 5-8, the radial jet spreading rate also increases with L/d_e ratio. This can be attributed also to the additive effect that the HIT Taylor scale λ has on the radial jet eddy sizes. It is evident from the Figure 5-65 and Figure 5-66, that the Taylor length λ scale is of the same order of the jet half width and as a result the HIT eddies interact with the jet enhancing the spreading rate of the jet. Finally, it can be stated that the effect of turbulence on the spreading rate is less significant for the higher momentum jets Re≥7700.

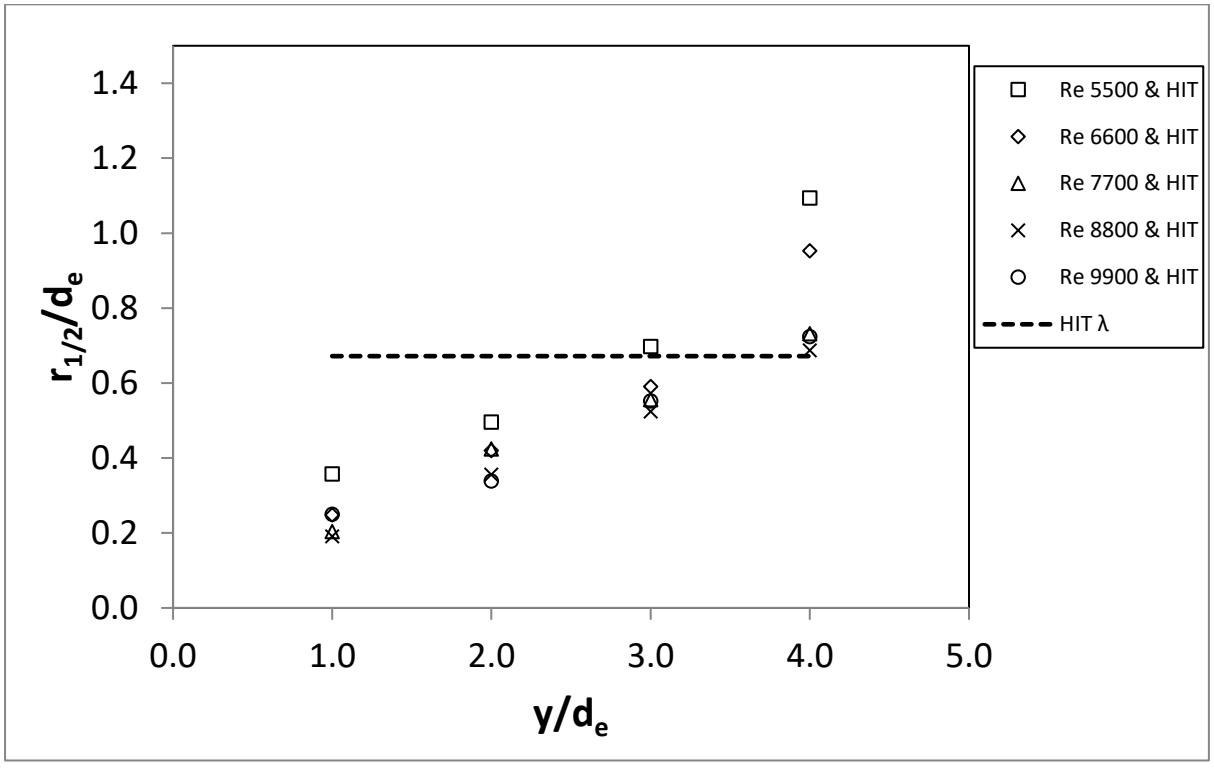

Figure 5-65: Jet half width $r_{1/2}$ of free radial jet under HIT, L/d_e=5

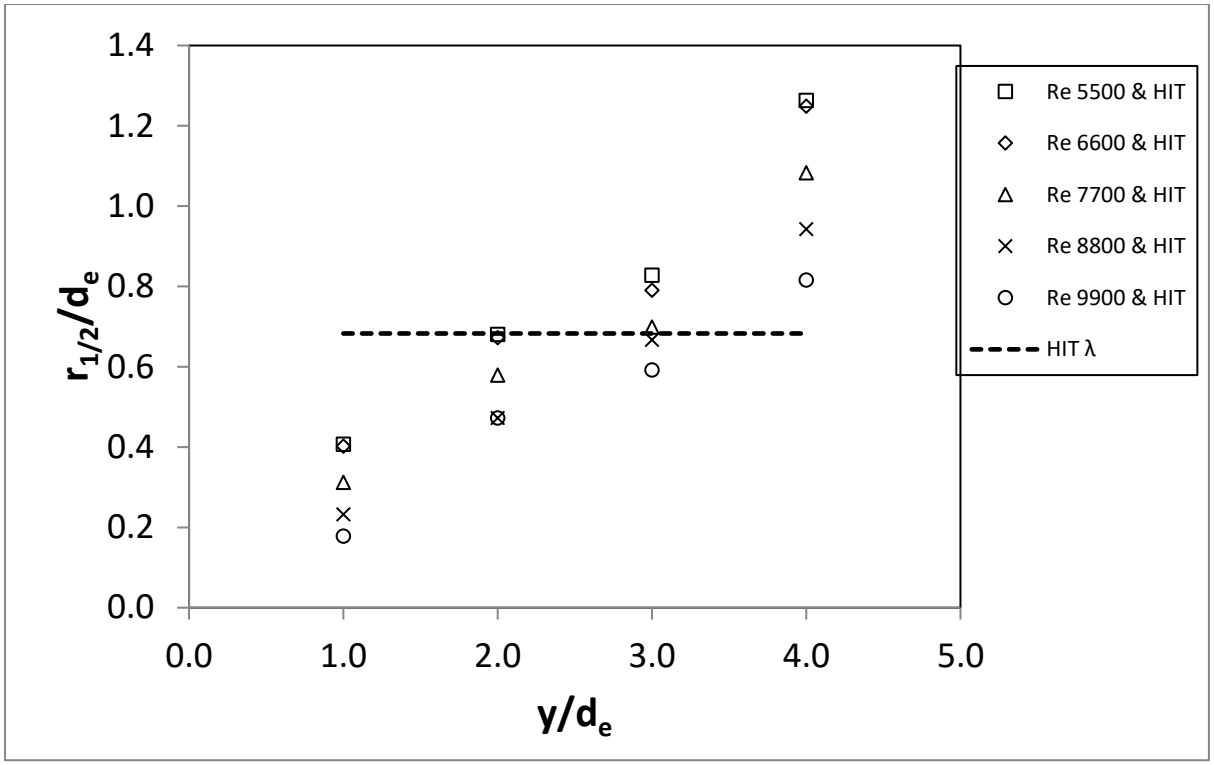

Figure 5-66: Jet half width $r_{1/2}$ of free radial jet under HIT , L/d_e=7.5

Table 5-8: Spreading rate of free radial jet under HIT

	Re	5500	6600	7700	8800	9900
L/d_e=5	Spreading	0.241	0.228	0.171	0.165	0.163
L/d_e=7.5	rate	0.272	0.255	0.243	0.232	0.203

6. Conclusions and recommendations for future work

6.1 Conclusions

A Box of Turbulence facility using synthetic jets was implemented in order to study the influence of Homogeneous and Isotropic Turbulence (HIT) with zero mean velocity on the development of opposed jets. As a first step, it was judged necessary to investigate the influence of HIT on a single axisymmetric jet first. The flow development between the opposed jets was examined for two separation distances of 5 and 7.5 exit diameters and for Re numbers in the range of 10^3 to 10^4.

The experimental investigation was conducted by 2D PIV since both single and opposed jets configurations produced axisymmetric flow fields. Furthermore, an assessment of the performance of RANS CFD models was attempted in the cases where the flow was developed in a quiescent background. The k-ε realizable and k-ω SST models were used for the initial calculation of the mean and turbulent flow properties, while the turbulent properties were recalculated using the Reynolds Stress Model (RSM).

The main findings of the present study are summarized as follows:

Single Axisymmetric jet in a quiescent environment

1) In the current thesis it was shown by the PIV measurements that the jet became turbulent above Re ~3000. The potential core of the jet extended approximately to four exit diameters and beyond this distance a z^{-1} decay of the normalized mean centerline velocity took place. Nevertheless, in the near field examined the jet decayed at a slower rate in comparison to the majority of the results provided in the literature review taken in the far field. This was in agreement with data extracted from the studies containing data in the near field such as Xu & Antonia [80] and Vouros and Panidis [83]. The k-ε realizable model considered suitable for the study of axisymmetric jets exposed faster decay rates when compared with the PIV measurements. Furthermore, the experimental results showed that as the Re increased, the jet decayed more slowly in this initial zone.
2) The centerline normalized velocity fluctuations in terms of u_{rms}/U_{cl} and v_{rms}/U_{cl} evolved towards an asymptotic state, although the values reached were lower than anticipated. This observation is explained by the fact that the distance covered ended before the ZFE was terminated. The smaller decay of U_{cl} was an additional factor contributing to this behavior. The anisotropy u_{rms}/v_{rms}

of the flow was verified by the PIV measurements and also captured by the incorporation of the RSM model after the mean flow was calculated by the k-ε realizable in the simulations.

3) The profiles of the mean and turbulent quantities in the radial direction showed that the flow approached self-similarity after ten exit diameters. The spreading rate of the jet was constant and rested in the range [0.063, 0.084], with the smaller values emerging from the larger Re, which agreed with the smaller velocity decay rate. The entrainment rate was linear and estimated near the anticipated value of 0.32 for a jet in the development region. However, the k-ε realizable underestimated the flow entrainment constants, giving 0.23.

Single axisymmetric jet in Homogeneous and Isotropic Turbulence (HIT)

1) In the presence of HIT, the jet maintained a z^{-1} decay of the mean centerline velocity. However, the decay rate increased significantly especially for the lower jet Re cases. The lower momentum in these cases made the jets more prone to the influence of the surrounding turbulent environment.
2) There was a significant increase in the turbulent intensity in terms of u_{rms}/U_{cl} and v_{rms}/U_{cl} along the centerline by the ambient HIT and an asymptotic value was not reached, which was the result of both the increased fluctuations and the decay of mean velocity. However, the anisotropy u_{rms} and v_{rms} was maintained.
3) From the profiles of the mean and turbulent quantities in the cross-stream direction, it became evident that the self-similar behavior of the jet ceased to exist in the presence of HIT. Furthermore, the spreading and entrainment rates increased in the presence of HIT. Specifically, the spreading rate did not exhibit a linear behavior, but an exponential law captured better the experimental measurements. The jet half width, which is a measure of the integral length scale of the jet interacted with the Taylor length scale of HIT, since it was found that both were of the same order of magnitude.

Opposed jets in a quiescent environment

1) The two principal characteristics of the opposed jets flow were the sharp linear streamwise velocity decay rate or axial strain rate and the radial jets that were formed around the stagnation plane. It was noted that the flow presented consistent turbulent characteristics both in axial and radial direction for Re>5000, while the turbulent exit profile was unaffected in contrast with Closely Spaced Opposed Jets (CSTOs) configurations with L/d_e~1, Korusoy and Whitelaw [4].
2) For Re>5000 the axial strain rate $\partial U/\partial z$ increased in proportion to Re. The larger L/d_e ratio presented larger strain rate constants, while in both cases the decay constants were significantly larger than the theoretical bulk strain rate $S_b=2U_e/L$, which better suits CSTOs configurations. The

k-ε realizable model underpredicted the straining of the flow near the stagnation region, whereas the SST k-ω model overpredicted it.

3) The u_{rms}, v_{rms} normalized by the exit velocity U_e increased as the stagnation plane was approached, presenting peaks around it. This rise was attributed to the symmetric pitchfork mode oscillations of the stagnation plane around the middle of the configuration. There was also large anisotropy u_{rms}/v_{rms} (in the order of 5) due to the fact that the V component was very small along the centerline. The CFD models succeeded in predicting the increased turbulent intensity, although in a narrower region around the stagnation plane.
4) The radial jet velocity that was produced along the stagnation line of the jets reached values of approximately 0.5 times the exit velocity of the jets at a radial distance about 0.75 exit diameters from the stagnation point. Nearly constant values of the normalized radial strain rate ∂V/∂y were produced in proportion to the axial strain rate, indicating that there was a linear relationship between the stretching of the flow and the Re number. The SST k-ω model performed better than the k-ε realizable model in estimating both the straining of the flow and the maximum values of the radial velocity along the stagnation line.
5) The v_{rms} fluctuations presented off centerline peaks about one diameter away from the centerline, a distance characterized by the energetic interaction of the shear layers of the axial jets. Beyond this distance the fluctuations decayed exponentially. The u_{rms} presented maxima at the centerline and subsequently minimized at about the same location where the v_{rms} maximized. This resulted from the change in the flow direction which enhanced the velocity fluctuations in the streamwise direction where the flow was free to develop and suppressed velocity fluctuations in the normal direction where the flow was contained by the opposing jets. The smaller separation distance presented larger maximum turbulent intensities, since the flow containment created a more energetic interaction of the shear layers and stretching of the flow. The SST k-ω simulation of the v_{rms} was found to be the only case where a CFD simulation approached the behavior extracted by the PIV measurements.
6) The formation of free radial jets was verified, exhibiting self-similarity beyond two exit diameters, while presenting larger turbulent quantities and spreading rates in comparison with a simple axisymmetric jet. The intensities of the normalized u_{rms}/U_e reached values of 0.6 beyond this distance, while the turbulent flow was found to be isotropic. In addition, the free radial jet was characterized by larger spreading rates in comparison to a simple axisymmetric jet.

Opposed jets in Homogeneous and Isotropic Turbulence (HIT)

1) For Re<5000, i.e. in the laminar and transitional range of the opposed flow, the HIT had a dominant effect, since the presence of well-defined symmetric stagnation plane vanished gradually as the Re decreased.
2) For Re>5000, the qualitative characteristics of the opposed jets flow prevailed over the background HIT. However, the linear axial strain rate around the stagnation plane decreased about 20%, due to the earlier origin of the velocity decay upstream of the stagnation plane, as a result of the mixing and homogenizing properties of turbulence. The high levels of turbulence intensity were also spread more away from the stagnation line of symmetry.
3) The maximum values of the radial velocity V in the stagnation line were affected, giving reduced values for smaller jet's Re and larger jets separation. However, the location ($0.75d_e$) of these peak values was not influenced. Furthermore, the radial strain rate presented small deviations from the cases without the presence of HIT.
4) Regarding the normalized turbulence velocities values along the stagnation line, a small reduction was observed for v_{rms} in the case of $L/d_e=5$ and an increase in u_{rms} for $L/d_e=7.5$. In general, the effect was greater for the larger L/d_e ratio and smaller Re number.
5) The radial jet velocity profiles along the stagnation line were mostly affected for the lower Re and the larger separation distance, increasing in width and losing the self-similar behavior. The self-similar behavior, that existed for the greater Re deteriorated as the distance from the centerline increased. The widening of the mean velocity profiles resulted in increased spreading rate. Furthermore, in the cases of low Re and large separation, the turbulence intensity profiles became wider with elevated maximum turbulent velocity values.

6.2 Recommendations for future work

The results of the present study identified several potential directions for future work, which are suggested below:

1) Homogenous and isotropic turbulence is a special case of turbulence which was considered in this investigation and caused symmetric perturbation of the jets. Further insight on the jet-environmental turbulence interaction may be obtained by the generation of non-isotropic turbulence which will cause non-symmetric jet perturbation.
2) Opposed jets configurations of varying geometries are found in many industrial applications such as burners and chemical reactors. The introduction of an offset between the opposed jets centerline or an angle between the jets will broaden the scope of the research to a greater range of practical applications.

3) The loading of the jets with an inertial phase such as solid particles or droplets that do not follow the gas flow perfectly will, allow the study of the formation of clusters in single and opposed jet configurations which are important in practical applications as they can affect the evaporation rate of droplets or affect the size distribution due to collisions between particles and if sufficiently dense the carrier flow development.
4) In many practical applications the flow is not isothermal. The use of heated jets can be useful for the evaluation of the effects of jet temperature on jet environmental turbulence interaction.
5) The introduction of a scalar tracer in the jets can provide valuable insight on the mechanisms of the mixing process and allow correlation of the concentration field with the flow field.
6) The exploratory numerical simulations carried out in this thesis assisted in the description of the flow field only for the case of a quiescent environment. The implementation of CFD simulations by introducing a source of homogeneous and isotropic turbulence energy in the surrounding environment will supplement the current results and test the performance of the existing RANS models.

7. References

[1] I. Wygnanski and H. Fiedler, “Some measurements in the self-preserving jet,” *J. Fluid Mech.*, vol. 38, no. 3, pp. 577–612, 1969, doi: 10.1017/S0022112069000358.

[2] N. R. Panchapakesan and J. L. Lumley, “Turbulence Measurements in Axisymmetric Jets of Air and Helium. Part 2. Helium Jet,” *J. Fluid Mech.*, vol. 246, pp. 225–247, 1993, doi: 10.1017/S0022112093000102.

[3] A. Abdel-Rahman, “A review of effects of initial and boundary conditions on turbulent,” *WSEAS Trans. Fluid Mech.*, vol. 5, no. 4, pp. 257–275, 2010.

[4] E. Korusoy and J. H. Whitelaw, “Opposed jets with small separations and their implications for the extinction of opposed flames,” *Exp. Fluids*, vol. 31, no. 1, pp. 111–117, 2001, doi: 10.1007/s003480000265.

[5] H. F. Zhao, “Application of multiple opposed jets to coal flame stabilization,” *Combust. Flame*, vol. 99, no. 3–4, pp. 653–659, 1994, doi: 10.1016/0010-2180(94)90059-0.

[6] B. K. Johnson and R. K. Prud’homme, “Chemical processing and micromixing in confined impinging jets,” *AIChE J.*, vol. 49, no. 9, pp. 2264–2282, 2003, doi: 10.1002/aic.690490905.

[7] C. L. Tucker and N. P. Suh, “No TitleMixing for Reaction Injection Molding. 1. Impingement Mixing of Liquids,” *Polym. Eng. Sci*, vol. 20, pp. 875–886, 1980, doi: doi.org/10.1002/pen.760201307.

[8] P. E. Dimotakis, “The mixing transition in turbulent flows,” *J. Fluid Mech.*, vol. 409, pp. 69–98, 2000, doi: 10.1017/S0022112099007946.

[9] P. A. Davidson, *Turbulence: an introduction for scientists and engineers*. Oxford University Press, 2015.

[10] P. Kundu, I. Cohen, and D. Dowling, “Turbulence,” in *Fluid Mechanics*, 6th ed., Academic Press, 2016, pp. 603–697.

[11] C. Bailly and G. Comte-Bellot, *Experimental Fluid Mechanics: Turbulence*. 2015.

[12] M. S. Uberoi and S. Wallis, “Effect of grid geometry on turbulence decay,” *Phys. Fluids*, vol. 10, no. 6, pp. 1216–1224, 1967, doi: 10.1063/1.1762265.

[13] G. Comte-Bellot and S. Corrsin, “The use of a contraction to improve the isotropy of grid-generated turbulence,” *J. Fluid Mech.*, vol. 25, no. 4, pp. 657–682, 1966, doi:

10.1017/S0022112066000338.

[14] R. E. Britter, “Structure of the temperature field downwind of a line source in grid turbulence,” *J. Fluid Mech.*, vol. 165, pp. 401–424, 1986, doi: 10.1017/S0022112086003154.

[15] C. Goepfert, J. L. Marié, D. Chareyron, and M. Lance, “Characterization of a system generating a homogeneous isotropic turbulence field by free synthetic jets,” *Exp. Fluids*, vol. 48, no. 5, pp. 809–822, 2010, doi: 10.1007/s00348-009-0768-5.

[16] S. M. Thompson and J. S. Turner, “Mixing across an interface due to turbulence generated by an oscillating grid,” *J. Fluid Mech.*, vol. 67, no. 2, pp. 349–368, 1975, doi: 10.1017/S0022112075000341.

[17] E. J. Hopfinger and J. A. Toly, “Spatially decaying turbulence and its relation to mixing across density interfaces,” *J. Fluid Mech.*, vol. 78, no. 1, pp. 155–175, 1976, doi: 10.1017/S0022112076002371.

[18] E. Villermaux, B. Sixou, and Y. Gagne, “Intense vortical structures in grid-generated turbulence,” *Phys. Fluids*, vol. 7, no. 8, pp. 2008–2013, 1995, doi: 10.1063/1.868512.

[19] S. S. Shy, R. H. Jang, and C. Y. Tang, “Simulation of turbulent burning velocities using aqueous autocatalytic reactions in a near-homogeneous turbulence,” *Combust. Flame*, vol. 105, no. 1–2, pp. 54–62, 1996, doi: 10.1016/0010-2180(95)00159-X.

[20] S. S. Shy, C. Y. Tang, and S. Y. Fann, “A Nearly Isotropic Turbulence Generated by a Pair of Vibrating Grids,” *Exp. Therm. Fluid Sci.*, vol. 14, no. 3, pp. 251–262, 1997, doi: 10.1016/S0894-1777(96)00111-2.

[21] I. P. D. De Silva and H. J. S. Fernando, “Oscillating grids as a source of nearly isotropic turbulence,” *Phys. Fluids*, 1994, doi: 10.1063/1.868193.

[22] H. Schlichting and K. Gersten, *Boundary-Layer Theory*. 2016.

[23] W. Li, P. Zhang, S. Yang, X. Fu, and Y. Xiao, “An experimental method for generating shear-free turbulence using horizontal oscillating grids,” *Water (Switzerland)*, vol. 12, no. 2, pp. 29–34, 2020, doi: 10.3390/w12020591.

[24] E. A. Variano, E. Bodenschatz, and E. A. Cowen, “A random synthetic jet array driven turbulence tank,” *Exp. Fluids*, vol. 37, no. 4, pp. 613–615, 2004, doi: 10.1007/s00348-004-0833-z.

[25] E. A. Variano and E. A. Cowen, “A random-jet-stirred turbulence tank,” *J. Fluid Mech.*, vol. 604, pp. 1–32, 2008, doi: 10.1017/S0022112008000645.

[26] J. F. Krawczynski, B. Renou, and L. Danaila, “The structure of the velocity field in a confined flow

driven by an array of opposed jets," *Phys. Fluids*, vol. 22, no. 4, pp. 1–17, 2010, doi: 10.1063/1.3371820.

[27] G. Bellani and E. A. Variano, "Homogeneity and isotropy in a laboratory turbulent flow," *Exp. Fluids*, vol. 55, no. 1, 2014, doi: 10.1007/s00348-013-1646-8.

[28] M. Amitay, A. Honohan, M. Trautman, and A. Glezer, "Modification of the aerodynamic characteristics of bluff bodies using fluidic actuators," *28th Fluid Dyn. Conf.*, 1997, doi: 10.2514/6.1997-2004.

[29] D. You and P. Moin, "Active control of flow separation over an airfoil using synthetic jets," *J. Fluids Struct.*, vol. 24, no. 8, pp. 1349–1357, 2008, doi: 10.1016/j.jfluidstructs.2008.06.017.

[30] A. E. Washburn and M. Amitay, "Aiaa 2004-745," no. January, pp. 1–15, 2004.

[31] G. Krishan, K. C. Aw, and R. N. Sharma, "Synthetic jet impingement heat transfer enhancement – A review," *Appl. Therm. Eng.*, vol. 149, no. October 2018, pp. 1305–1323, 2019, doi: 10.1016/j.applthermaleng.2018.12.134.

[32] W. Hwang and J. K. Eaton, "Creating homogeneous and isotropic turbulence without a mean flow," *Exp. Fluids*, vol. 36, no. 3, pp. 444–454, 2004, doi: 10.1007/s00348-003-0742-6.

[33] H. Lian, G. Charalampous, and Y. Hardalupas, "Preferential concentration of poly-dispersed droplets in stationary isotropic turbulence This article is part of the Topical Collection on Application of Laser Techniques to Fluid Mechanics 2012," *Exp. Fluids*, vol. 54, no. 5, 2013, doi: 10.1007/s00348-013-1525-3.

[34] P. F. Zhang, J. J. Wang, and L. H. Feng, "Review of zero-net-mass-flux jet and its application in separation flow control," *Sci. China, Ser. E Technol. Sci.*, vol. 51, no. 9, pp. 1315–1344, 2008, doi: 10.1007/s11431-008-0174-x.

[35] K. Toyoda and R. Hiramoto, "Manipulation of vortex rings for flow control," *Fluid Dyn. Res.*, vol. 41, no. 5, 2009, doi: 10.1088/0169-5983/41/5/051402.

[36] J. J. Wang and L. H. Feng, "Synthetic Jet," in *Flow Controls and Applications*, Cambridge University Press, 2018, pp. 168–205.

[37] A. Glezer, "The formation of vortex rings," *Phys. Fluids*, vol. 31, no. 12, p. 3532, 1988, doi: 10.1063/1.866920.

[38] B. L. Smith and A. Glezer, "The formation and evolution of synthetic jets," *Phys. Fluids*, vol. 10, no. 9, pp. 2281–2297, 1998, doi: 10.1063/1.869828.

[39] B. L. Smith and G. W. Swift, "A comparison between synthetic jets and continuous jets," *Exp.*

Fluids, vol. 34, no. 4, pp. 467–472, 2003, doi: 10.1007/s00348-002-0577-6.

[40] J. C. Béra, M. Michard, N. Grosjean, and G. Comte-Bellot, "Flow analysis of two-dimensional pulsed jets by particle image velocimetry," *Exp. Fluids*, vol. 31, no. 5, pp. 519–532, 2001, doi: 10.1007/s003480100314.

[41] J. E. Cater and J. Soria, "The evolution of round zero-net-mass-flux jets," *J. Fluid Mech.*, no. 472, pp. 167–200, 2002, doi: 10.1017/S0022112002002264.

[42] M. O. Muller *et al.*, "Flow Structure and Performance of Axisymmetric Synthetic Jets," *39th Aerosp. Sci. Meet. Exhib.*, no. January, pp. 1–11, 2001.

[43] S. G. Mallinson, G. Hong, and J. A. Reizes, "Some characteristics of synthetic jets," *30th Fluid Dyn. Conf.*, no. c, 1999, doi: 10.2514/6.1999-3651.

[44] S. Lardeau and M. A. Leschziner, "The interaction of round synthetic jets with a turbulent boundary layer separating from a rounded ramp," *J. Fluid Mech.*, vol. 683, pp. 172–211, 2011, doi: 10.1017/jfm.2011.258.

[45] W. Hwang and J. K. Eaton, "Homogeneous and isotropic turbulence modulation by small heavy (St∼50) particles," *J. Fluid Mech.*, vol. 564, pp. 361–393, 2006, doi: 10.1017/S0022112006001431.

[46] A. Eidelman, T. Elperin, N. Kleeorin, I. Rogachevskii, and I. Sapir-Katiraie, "Turbulent thermal diffusion in a multi-fan turbulence generator with imposed mean temperature gradient," *Exp. Fluids*, vol. 40, no. 5, pp. 744–752, 2006, doi: 10.1007/s00348-006-0111-3.

[47] H. Stapountzis, G. Charalampous, D. Tziourtzioumis, and A. Stamatelos, "Diffusion in Synthetic Jet Generated Turbulence," in *The Proceedings of the International Conference on Jets, Wakes and Separated Flows (ICJWSF)*, 2013, vol. 2013.4, no. 0, p. _1202-1_-_1202-6_, doi: 10.1299/jsmeicjwsf.2013.4._1202-1_.

[48] T. D. Fansler and E. G. Groff, "Turbulence characteristics of a fan-stirred combustion vessel," *Combust. Flame*, 1990, doi: 10.1016/0010-2180(90)90110-D.

[49] B. Galmiche, N. Mazellier, F. Halter, and F. Foucher, "Turbulence characterization of a high-pressure high-temperature fan-stirred combustion vessel using LDV, PIV and TR-PIV measurements," *Exp. Fluids*, vol. 55, no. 1, 2014, doi: 10.1007/s00348-013-1636-x.

[50] Y. Sung, G. Charalampous, Y. Hardalupas, and G. Choi, "Laser ignition and flame characteristics of pulsed methane jets in homogeneous isotropic turbulence without mean flow," *Proc. Combust. Inst.*, vol. 36, no. 2, pp. 1653–1660, 2017, doi: 10.1016/j.proci.2016.07.117.

[51] M. Birouk, C. Chauveau, B. Sarh, A. Quilgars, and I. Gökalp, “Turbulence effects on the vaporization of monocomponent single droplets,” *Combust. Sci. Technol.*, vol. 113–114, no. October 2014, pp. 413–428, 1996, doi: 10.1080/00102209608935506.

[52] T. Fallon and C. B. Rogers, “Turbulence-induced preferential concentration of solid particles in microgravity conditions,” *Exp. Fluids*, vol. 33, no. 2, pp. 233–241, 2002, doi: 10.1007/s00348-001-0394-3.

[53] M. Gibert, H. Xu, and E. Bodenschatz, “Where do small, weakly inertial particles go in a turbulent flow?,” *J. Fluid Mech.*, vol. 698, pp. 160–167, 2012, doi: 10.1017/jfm.2012.72.

[54] B. J. Rothschild and T. R. Osborn, “Small-scale turbulence and plankton contact rates,” *J. Plankton Res.*, 1988, doi: 10.1093/plankt/10.3.465.

[55] E. S. Semenov, “Measurement of turbulence characteristics in a closed volume with artificial turbulence,” *Combust. Explos. Shock Waves*, vol. 1, no. 2, pp. 57–62, 1965, doi: 10.1007/BF00757231.

[56] G. E. Andrews, D. Bradley, and S. B. Lwakabamba, “Measurement of turbulent burning velocity for large turbulent Reynolds numbers,” *Symp. Combust.*, vol. 15, no. 1, pp. 655–664, 1975, doi: 10.1016/S0082-0784(75)80336-5.

[57] M. Birouk, B. Sarh, and I. Gökalp, “An Attempt to Realize Experimental Isotropic Turbulence at Low Reynolds Number,” *Flow, Turbul. Combust.*, vol. 70, no. 1–4, pp. 325–348, 2003, doi: 10.1023/B:APPL.0000004974.74706.6d.

[58] J. De Jong, L. Cao, S. H. Woodward, J. P. L. C. Salazar, L. R. Collins, and H. Meng, “Dissipation rate estimation from PIV in zero-mean isotropic turbulence,” *Exp. Fluids*, vol. 46, no. 3, pp. 499–515, 2009, doi: 10.1007/s00348-008-0576-3.

[59] J. P. L. C. Salazar, J. De Jong, L. Cao, S. H. Woodward, H. Meng, and L. R. Collins, “Experimental and numerical investigation of inertial particle clustering in isotropic turbulence,” *J. Fluid Mech.*, vol. 600, pp. 245–256, 2008, doi: 10.1017/S0022112008000372.

[60] D. R. Webster, A. Brathwaite, and J. Yen, “a Novel Laboratory Apparatus for Simulating,” no. February, pp. 1–12, 2004.

[61] G. Bertens, D. van der Voort, H. Bocanegra-Evans, and W. van de Water, “Large-eddy estimate of the turbulent dissipation rate using PIV,” *Exp. Fluids*, vol. 56, no. 5, pp. 1–9, 2015, doi: 10.1007/s00348-015-1945-3.

[62] H. Bocanegra Evans, N. Dam, G. Bertens, D. Van Der Voort, and W. Van De Water, “Dispersion

of droplet clouds in turbulence," *Phys. Rev. Lett.*, vol. 117, no. 16, pp. 1–5, 2016, doi: 10.1103/PhysRevLett.117.164501.

[63] H. Bocanegra Evans, N. Dam, G. Bertens, and W. Van De Water, "Making droplets glow in turbulence," *Phys. Rev. Fluids*, vol. 5, no. 4, pp. 1–13, 2020, doi: 10.1103/PhysRevFluids.5.044303.

[64] K. Chang, G. P. Bewley, and E. Bodenschatz, "Experimental study of the influence of anisotropy on the inertial scales of turbulence," *J. Fluid Mech.*, vol. 692, pp. 464–481, 2012, doi: 10.1017/jfm.2011.529.

[65] G. P. Bewley, K. Chang, and E. Bodenschatz, "On integral length scales in anisotropic turbulence," *Phys. Fluids*, vol. 24, no. 6, 2012, doi: 10.1063/1.4726077.

[66] J. Lu, J. P. Fugal, H. Nordsiek, E. W. Saw, R. A. Shaw, and W. Yang, "Lagrangian particle tracking in three dimensions via single-camera in-line digital holography," *New J. Phys.*, vol. 10, 2008, doi: 10.1088/1367-2630/10/12/125013.

[67] Z. Dou, Z. K. Pecenak, L. Cao, S. H. Woodward, Z. Liang, and H. Meng, "PIV measurement of high-Reynolds-number homogeneous and isotropic turbulence in an enclosed flow apparatus with fan agitation," *Meas. Sci. Technol.*, vol. 27, no. 3, 2016, doi: 10.1088/0957-0233/27/3/035305.

[68] D. R. Webster, A. Brathwaite, and J. Yen, "A novel laboratory apparatus for simulating isotropic oceanic turbulence at low Reynolds number," *Limnol. Oceanogr. Methods*, vol. 2, no. 1, pp. 1–12, 2004, doi: 10.4319/lom.2004.2.1.

[69] T. A. Warnaars, M. Hondzo, and M. A. Carper, "A desktop apparatus for studying interactions between microorganisms and small-scale fluid motion," *Hydrobiologia*, vol. 563, no. 1, pp. 431–443, 2006, doi: 10.1007/s10750-006-0030-6.

[70] B. Cushman-Roisin and Dartmouth College, "Chapter 9: Turbulent Jets," *Environ. Fluid Dyn.*, vol. 5, pp. 153–161, 2014.

[71] F. H. Clauser, "The structure of turbulent shear flow," *Nature*, vol. 179, no. 4550. p. 60, 1957, doi: 10.1038/179060a0.

[72] G. N. Abramovich and L. Schindel, "Turbulent Jets of Incompressible Fluid," *Theory Turbul. Jets*, p. 671, 2003.

[73] Tennekes and Lumley, *A fisrt course in Turbulence*. THE MIT PRESS, 1972.

[74] H. Fellouah, C. G. Ball, and A. Pollard, "Reynolds number effects within the development region

of a turbulent round free jet," *Int. J. Heat Mass Transf.*, vol. 52, no. 17–18, pp. 3943–3954, 2009, doi: 10.1016/j.ijheatmasstransfer.2009.03.029.

[75] C. G. Ball, H. Fellouah, and A. Pollard, "The flow field in turbulent round free jets," *Prog. Aerosp. Sci.*, vol. 50, pp. 1–26, 2012, doi: 10.1016/j.paerosci.2011.10.002.

[76] Stephen B. Pope, *Turbulent Flows*. Cambridge University Press.

[77] G. Lipari and P. K. Stansby, "Review of experimental data on incompressible turbulent round jets," *Flow, Turbul. Combust.*, vol. 87, no. 1, pp. 79–114, 2011, doi: 10.1007/s10494-011-9330-7.

[78] H. B. Squire and J. Trouncer, "Round Jets in a General Stream," 1944. [Online]. Available: https://apps.dtic.mil/sti/citations/ADB039248.

[79] H. J. Hussein, S. P. Capp, and W. K. George, "Velocity measurements in a high-Reynolds-number, momentum-conserving, axisymmetric, turbulent jet," *J. Fluid Mech.*, vol. 258, no. February, pp. 31–75, 1994, doi: 10.1017/S002211209400323X.

[80] G. Xu and R. A. Antonia, "Effect of different initial conditions on a turbulent round free jet," *Exp. Fluids*, vol. 33, no. 5, pp. 677–683, 2002, doi: 10.1007/s00348-002-0523-7.

[81] C. Fukushima, L. Aanen, and J. Westerweel, "Investigation of the Mixing Process in an Axisymmetric Turbulent Jet Using PIV and LIF," *Laser Tech. fluid Mech.*, pp. 1–11, 2002, doi: 10.1007/978-3-662-08263-8.

[82] W. R. Quinn, "Upstream nozzle shaping effects on near field flow in round turbulent free jets," *Eur. J. Mech. B/Fluids*, vol. 25, no. 3, pp. 279–301, 2006, doi: 10.1016/j.euromechflu.2005.10.002.

[83] A. P. Vouros and T. Panidis, "Turbulent properties of a low Reynolds number, axisymmetric, pipe jet," *Exp. Therm. Fluid Sci.*, vol. 44, pp. 42–50, 2013, doi: 10.1016/j.expthermflusci.2012.05.012.

[84] J.O.Hinze, *Turbulence*. McGraw-Hill Mechanical Engineering.

[85] William K. George, "The Self-Preservation of turbulent flows and its relation to the initial conditions and coherent structures," *Advances in Turbulence*. pp. 39–73, 1989.

[86] L. P. Xia and K. M. Lam, "Velocity and concentration measurements in initial region of submerged round jets in stagnant environment and in coflow," *J. Hydro-Environment Res.*, vol. 3, no. 1, pp. 21–34, 2009, doi: 10.1016/j.jher.2009.03.002.

[87] S. J. Kwon and I. W. Seo, "Reynolds number effects on the behavior of a non-buoyant round

jet," *Exp. Fluids*, vol. 38, no. 6, pp. 801–812, 2005, doi: 10.1007/s00348-005-0976-6.

[88] J. Mi, G. J. Nathan, and D. S. Nobes, "Mixing characteristics of axisymmetric free jets from a contoured nozzle, an orifice plate and a pipe," *J. Fluids Eng. Trans. ASME*, vol. 123, no. 4, pp. 878–883, 2001, doi: 10.1115/1.1412460.

[89] N. B. Hugo Fischer, John List, C. Koh, Jorg Imberger, *Mixing in Inland and Coastal Waters*. .

[90] C. M. Or, K. M. Lam, and P. Liu, "Potential core lengths of round jets in stagnant and moving environments," *J. Hydro-Environment Res.*, vol. 5, no. 2, pp. 81–91, 2011, doi: 10.1016/j.jher.2011.01.002.

[91] F. P. Ricou and D. B. Spalding, "Measurements of entrainment by axisymmetrical turbulent jets," *J. Fluid Mech.*, vol. 11, no. 1, pp. 21–32, 1961, doi: 10.1017/S0022112061000834.

[92] H. Bj, "Soa," vol. 51, 1973.

[93] L. Bogusławski and C. O. Popiel, "Flow structure of the free round turbulent jet in the initial region," *J. Fluid Mech.*, vol. 90, no. 3, pp. 531–539, 1979, doi: 10.1017/S0022112079002378.

[94] N. T. Obot, M. L. Graska, and T. A. Trabold, "The near field behavior of round jets at moderate reynolds numbers," *Can. J. Chem. Eng.*, vol. 62, no. 5, pp. 587–593, 1984, doi: 10.1002/cjce.5450620503.

[95] B. Khorsandi, S. Gaskin, and L. Mydlarski, "Effect of background turbulence on an axisymmetric turbulent jet," *J. Fluid Mech.*, vol. 736, pp. 250–286, 2013, doi: 10.1017/jfm.2013.465.

[96] Y. Guo, P. A. Davies, H. J. S. Fernando, and C. Y. Ching, "Influence of Background Turbulence on the," no. 1994, p. 2012, 2012.

[97] Y. Guo, D. Malcangio, P. A. Davies, and H. J. S. Fernando, "A laboratory investigation into the influence of a localized region of turbulence on the evolution of a round turbulent jet," *Fluid Dyn. Res.*, vol. 36, no. 2, pp. 75–89, 2005, doi: 10.1016/j.fluiddyn.2005.01.001.

[98] S. Wright, "The effect of ambient turbulence in jet mixing," *Recent Res. Adv. Fluid Mech. Turbul. Jets Plumes, NATO ASI Ser.*, vol. 255, pp. 13–27, 1994, doi: 10.1007/978-94-011-0918-5.

[99] R. Sahebjam, K. F. Kohan, and S. Gaskin, "The dynamics of an axisymmetric turbulent jet in ambient turbulence interpreted from the passive scalar field statistics," *Phys. Fluids*, vol. 34, no. 1, 2022, doi: 10.1063/5.0071023.

[100] A. Tamir and A. Kitron, "Applications of impinging-streams in chemical engineering processes," *Chem. Eng. Commun.*, vol. 50, no. 1–6, pp. 241–330, 1987, doi: 10.1080/00986448708911828.

[101] I. Between *et al.*, “No Title,” no. 6, pp. 165–167, 1978.

[102] G. Stan and D. A. Johnson, “Experimental and numerical analysis of turbulent opposed impinging jets,” *AIAA J.*, vol. 39, no. 10, pp. 1901–1908, 2001, doi: 10.2514/2.1205.

[103] R. P. Pawlowski, A. G. Salinger, J. N. Shadid, and T. J. Mountziaris, “Bifurcation and stability analysis of laminar isothermal counterflowing jets,” *J. Fluid Mech.*, vol. 551, pp. 117–139, 2006, doi: 10.1017/S0022112005008396.

[104] L. W. Kostiuk, K. N. C. Bray, and R. K. Cheng, “Experimental study of premixed turbulent combustion in opposed streams. Part II-Reacting flow field and extinction,” *Combust. Flame*, vol. 92, no. 4, pp. 396–409, 1993, doi: 10.1016/0010-2180(93)90151-R.

[105] J. C. Rolon, D. Veynante, J. P. Martin, and F. Durst, “Counter jet stagnation flows,” *Exp. Fluids*, vol. 11, no. 5, pp. 313–324, 1991, doi: 10.1007/BF00194863.

[106] L. W. Kostiuk, I. G. Shepherd, and K. N. C. Bray, “Experimental study of premixed turbulent combustion in opposed streams. Part III - Spatial structure of flames,” *Combust. Flame*, vol. 118, no. 1–2, pp. 129–139, 1999, doi: 10.1016/S0010-2180(98)00155-2.

[107] R. P. Lindstedt, D. S. Luff, and J. H. Whitelaw, “Velocity and strain-rate characteristics of opposed isothermal flows,” *Flow, Turbul. Combust.*, vol. 74, no. 2, pp. 169–194, 2005, doi: 10.1007/s10494-005-4130-6.

[108] Z. Dai, X. Gong, X. Guo, H. Liu, F. Wang, and Z. Yu, “Pilot-trial and modeling of a new type of pressurized entrained-flow pulverized coal gasification technology,” *Fuel*, vol. 87, no. 10–11, pp. 2304–2313, 2008, doi: 10.1016/j.fuel.2007.12.005.

[109] J. Ni, Q. Liang, Z. Zhou, Z. Dai, and G. Yu, “Numerical and experimental investigations on gas-particle flow behaviors of the Opposed Multi-Burner Gasifier,” *Energy Convers. Manag.*, vol. 50, no. 12, pp. 3035–3044, 2009, doi: 10.1016/j.enconman.2009.07.023.

[110] W. Li, Z. Sun, H. Liu, F. Wang, and Z. Yu, “Experimental and numerical study on stagnation point offset of turbulent opposed jets,” *Chem. Eng. J.*, vol. 138, no. 1–3, pp. 283–294, 2008, doi: 10.1016/j.cej.2007.05.039.

[111] and F.-C. W. Wei-Feng Li, Tian-Liang Yao, “Study on Factors Influencing Stagnation Point Offset of Turbulent Opposed Jets,” *Am. Inst. Chem. Eng. AIChE J*, vol. 56, pp. 4828–4838, 2010, doi: 10.1002/aic.12188.

[112] Z. Qiao, Z. Wang, C. Zhang, S. Yuan, Y. Zhu, and J. Wang, “PVAm–PIP/PS composite membrane with high performance for CO_2/N_2 separation,” *AIChE J.*, vol. 59, no. 4, pp. 215–228, 2012, doi:

10.1002/aic.

[113] and F.-C. W. Wei-Feng Li, Guo-Feng Huang, Gong-Yi Tu, Hai-Feng Liu, “Experimental Study of Oscillation of Axisymmetric Turbulent Opposed Jets with Modulated Airflow,” *Am. Inst. Chem. Eng. AIChE J*, vol. 59, pp. 4828–4838, 2013, doi: 10.1002/aic.14190.

[114] J. Li, H. Wang, Y. Xiong, G. Jiang, Z. Liu, and C. Zheng, “Experimental investigation on turbulence modification in a dilute gas-particle axisymmetric opposed jets flow,” *Chem. Eng. J.*, vol. 286, pp. 76–90, 2016, doi: 10.1016/j.cej.2015.10.056.

[115] D. Wu, J. Li, Z. Liu, Y. Xiong, C. Zheng, and P. R. Medwell, “Eulerian and Lagrangian stagnation plane behavior of moderate Reynolds number round opposed-jets flow,” *Comput. Fluids*, vol. 133, pp. 116–128, 2016, doi: 10.1016/j.compfluid.2016.05.001.

[116] D. Wu, J. Li, Z. Liu, W. Luo, and C. Zheng, “Penetration, accumulation, and swing characteristics of particle cloud in a turbulent axisymmetric opposed-jet flow,” *Powder Technol.*, vol. 329, pp. 33–46, 2018, doi: 10.1016/j.powtec.2018.01.071.

[117] Y. Liu and R. O. Fox, “CFD predictions for chemical processing in a confined impinging-jets reactor,” *AIChE J.*, vol. 52, no. 2, pp. 731–744, 2006, doi: 10.1002/aic.10633.

[118] Y. Liu, M. G. Olsen, and R. O. Fox, “Turbulence in a microscale planar confined impinging-jets reactor,” *Lab Chip*, vol. 9, no. 8, pp. 1110–1118, 2009, doi: 10.1039/b818617k.

[119] E. Gavi, D. L. Marchisio, and A. A. Barresi, “CFD modelling and scale-up of Confined Impinging Jet Reactors,” *Chem. Eng. Sci.*, vol. 62, no. 8, pp. 2228–2241, 2007, doi: 10.1016/j.ces.2006.12.077.

[120] and A. A. B. Daniele L. Marchisio, Liliana Rivautella, “Design and Scale-Up of Chemical Reactors for Nanoparticle Precipitation,” *2006 Am. Inst. Chem. Eng. AIChE J*, vol. 52, pp. 1877–1887, 2006, doi: 0.1002/aic.10786.

[121] E. Gavi, D. L. Marchisio, A. A. Barresi, M. G. Olsen, and R. O. Fox, “Turbulent precipitation in micromixers: CFD simulation and flow field validation,” *Chem. Eng. Res. Des.*, vol. 88, no. 9, pp. 1182–1193, 2010, doi: 10.1016/j.cherd.2010.01.025.

[122] M. Icardi *et al.*, “Investigation of the flow field in a three-dimensional Confined Impinging Jets Reactor by means of microPIV and DNS,” *Chem. Eng. J.*, vol. 166, no. 1, pp. 294–305, 2011, doi: 10.1016/j.cej.2010.09.046.

[123] C. L. Tucker and N. P. Suh, “Mixing for reaction injection molding II. Impingement mixing of fiber suspensions,” *Polym. Eng. Sci.*, vol. 20, no. 13, pp. 887–898, 1980, doi:

10.1002/pen.760201308.

[124] P. Wood, A. Hrymak, R. Yeo, D. Johnson, and A. Tyagi, “Experimental and computational studies of the fluid mechanics in an opposed jet mixing head,” *Phys. Fluids A*, vol. 3, no. 5, pp. 1362–1368, 1991, doi: 10.1063/1.858205.

[125] D. A. Johnson, P. E. Woods, A. N. Hrymak, C. Engineering, and U. S. Canada, “Flow Field of an Omosed Jet RIM Mix Head :,” vol. 74, no. 1985, 1989.

[126] D. A. Johnson and P. E. Wood, “Self-sustained oscillations in opposed impinging jets in an enclosure,” *Can. J. Chem. Eng.*, vol. 78, no. 5, pp. 867–875, 2000, doi: 10.1002/cjce.5450780503.

[127] A. M. Teixeira, R. J. Santos, M. R. P. F. N. Costa, and J. C. B. Lopes, “Hydrodynamics of the mixing head in RIM: LDA flow-field characterization,” *AIChE J.*, vol. 51, no. 6, pp. 1608–1619, 2005, doi: 10.1002/aic.10454.

[128] L. Xiaojin, R. J. Santos, and J. C. B. Lopes, “Modelling of self-induced oscillations in the mixing head of a RIM machine,” *Can. J. Chem. Eng.*, vol. 85, no. 1, pp. 45–54, 2007, doi: 10.1002/cjce.5450850104.

[129] G. K. Batchelor, *The theory of homogeneous turbulence*, vol. 256, no. 2. 1953.

[130] E. J. Stamhuis, “Basics and principles of particle image velocimetry (PIV) for mapping biogenic and biologically relevant flows,” *Aquat. Ecol.*, vol. 40, no. 4, pp. 463–479, 2006, doi: 10.1007/s10452-005-6567-z.

[131] J. K. Markus Raffel, Christian E. Willert, Fulvio Scarano, Christian J. Kähler, Steve T. Wereley, *Particle Image Velocimetry*. .

[132] Ansys Fluent Theory Guide, “Ansys Fluent Theory Guide,” *ANSYS Inc., USA*, vol. 15317, no. November, pp. 724–746, 2021, [Online]. Available: http://scholar.google.com/scholar?hl=en&btnG=Search&q=intitle:ANSYS+FLUENT+Theory+Guide#0.

[133] M. Ozen, “Meshing Workshop,” *Ozen Eng. Inc.*, p. 116, 2014, [Online]. Available: https://www.google.com/url?sa=t&rct=j&q=&esrc=s&source=web&cd=1&cad=rja&uact=8&ved=0ahUKEwjLm6XbkuzQAhUiSo8KHbt-BfQQFggZMAA&url=https%3A%2F%2Fwww.ozeninc.com%2Fwp-content%2Fuploads%2F2014%2F11%2FMESHING_WORKSHOP_2014.pdf&usg=AFQjCNF9XlppoNnerRk9_TntOF_IfH.

[134] E. Mastorakos, “Turbulent combustion in opposed jet flows,” Imperial College of Science, 1993.

[135] G. Stan, “Fundamental characteristics of turbulent opposed Impinging jets,” 2000.